



**Synthesis, structural characterization, and  
mechanical properties of advanced ceramics  
prepared via sol-gel**

(Síntesis, caracterización estructural y propiedades mecánicas de  
cerámicas avanzadas preparadas mediante sol-gel)

**Pedro Rivero Antúnez, BSc, MSc**

Departamento de Física de la Materia Condensada

Universidad de Sevilla

A thesis submitted for the degree of

*Doctor of Philosophy*

May, 2023



*A mi abuelo. Me acuerdo de ti todos los días. Sin excepción.*

# Synthesis, structural characterization, and mechanical properties of advanced ceramics prepared via sol-gel

Pedro Rivero Antúnez, BSc, MSc.

Department of Condensed Matter Physics, University of Seville

A thesis submitted for the degree of *Doctor of Philosophy*. May, 2023.

## Abstract

This doctoral thesis comprises a series of articles focused on the fabrication of ceramic materials (mainly alumina, but also zirconia) reinforced with carbon nanophases (graphene and carbon nanotubes). The backbone of the thesis consists of the preparation of advanced ceramics by the sol-gel technique and their structural and mechanical characterization. Specifically, the research focuses on the preparation of alumina ceramics reinforced with different embedded phases as carbon nanotubes or graphene. The objective was to determine the preparation conditions of ceramic composites that lead to the improvement of certain mechanical properties, such as the reduction of inherent ceramic fragility.

The experimental work included the synthesis of ceramic powders via sol-gel and other conventional techniques, traditional and advanced forms of sintering, structural characterization of the samples at different stages, and the measurement of mechanical properties. For all this, a wide variety of techniques have been employed, including optimal sol-gel processing routes to maximize the dispersion of carbon nanophases, densification via Spark Plasma Sintering (SPS), scanning and transmission electron microscopy (SEM and TEM), X-ray diffraction, Raman spectroscopy, Vickers indentation and nanoindentation. Additionally, an structural simulation approach was also considered in order to explore and discuss, from a geometrically point of view, the spatial distribution of the reinforcing phase within the matrix, and the viability of achieving perfect distributions of embedded nanostructured carbon allotropes in a ceramic matrix as a function of the carbon

content.

The experimental and theoretical results suggest that a boehmite-based sol-gel route followed by a reactive-SPS sintering is an effective, cheap and fast method for producing  $\alpha$ -Al<sub>2</sub>O<sub>3</sub> with high density. Moreover, it was also observed that the amounts of carbon nanophases typically used by the research community to reinforce the ceramic matrix cannot lead to homogeneous dispersions of the reinforcing phases, making impossible to achieve significant increases in the mechanical properties of fully densified ceramic compounds. Furthermore, it was found that the microstructure of the ceramics was crucial to their mechanical properties. Overall, this research has contributed to the doctoral candidate's understanding of the preparation, microstructural and mechanical characterization, and structural simulation of advanced ceramic matrix composites.

# Síntesis, caracterización estructural y propiedades mecánicas de cerámicas avanzadas preparadas mediante sol-gel

Pedro Rivero Antúnez, BSc, MSc.

Departamento de Física de la Materia Condensada, Universidad de Sevilla.

Tesis presentada para optar al grado de *Doctor*.

Marzo de 2023.

## Resumen

Esta tesis doctoral comprende una serie de artículos enfocados en la fabricación de materiales cerámicos (principalmente alúmina, pero también zircona) reforzados con nanofases de carbono (grafeno y nanotubos de carbono). La base de la tesis consiste en la preparación de cerámicas avanzadas mediante la técnica sol-gel, y su caracterización estructural y mecánica. En concreto, la investigación se centra en la preparación de cerámicas de alúmina reforzadas con diferentes fases carbonosas, como nanotubos de carbono o grafeno. El objetivo era determinar las condiciones de preparación de los compuestos cerámicos que conduzcan a la mejora de ciertas propiedades mecánicas, como la reducción de la inherente fragilidad de las cerámicas.

El trabajo experimental incluye la síntesis de polvos cerámicos mediante el método sol-gel y otras técnicas convencionales, así como formas tradicionales y avanzadas de sinterización. Se realizaron caracterizaciones estructurales de las muestras en diferentes etapas y se midieron sus propiedades mecánicas. Para todo esto, se empleó una amplia variedad de técnicas, que incluyen rutas óptimas de procesamiento sol-gel para maximizar la dispersión de nanofases de carbono, densificación mediante Sinterización de Chispa de Plasma (SPS), microscopía electrónica de barrido y transmisión (SEM y TEM), difracción de rayos X, espectroscopía Raman, indentación Vickers y nanoindentación. Además, también se consideró un enfoque de simulación estructural para explorar y discutir, desde un punto de vista geométrico, la distribución espacial de la fase de refuerzo dentro de

la matriz y la viabilidad de lograr distribuciones perfectas de alótopos de carbono nanoestructurados incrustados en una matriz cerámica en función del contenido de carbono.

Los resultados experimentales y teóricos sugieren que una ruta basada en sol-gel de boehmita seguida de una sinterización reactiva-SPS es un método efectivo, económico y rápido para producir piezas de  $\alpha$ -Al<sub>2</sub>O<sub>3</sub> de alta densidad. Además, también se observó que las cantidades de nanofases de carbono típicamente utilizadas por la comunidad científica para reforzar matrices cerámicas no pueden generar dispersiones homogéneas de las fases de refuerzo, lo que hace imposible lograr aumentos significativos en las propiedades mecánicas de los compuestos cerámicos completamente densificados. Además, se encontró que la microestructura de las cerámicas era crucial para sus propiedades mecánicas. En general, esta investigación ha contribuido a la comprensión del candidato sobre la preparación, caracterización microestructural y mecánica, y simulación estructural de compuestos de matriz cerámica avanzada.

## Acknowledgements

Firstly, I would like to thank my thesis supervisor, Dr. Víctor Morales Flórez, for his guidance and dedication in the development of this research. Thank you for your patience, your passion, your valuable suggestions, and for sharing your experience with me. It has been a true honor to work alongside you. You have not only been a source of scientific curiosity and inspiration but also of teaching, politics, personal life, gastronomy, music, literature, and culture in general. Without a doubt, one of the reasons why these years of doctoral studies have been worth it.

To Professor Arturo Domínguez, who gave me two pieces of advice that I will never forget. I would have remembered him for any of them, but the first one, which fits here, has always been a source of motivation for feeling the love I have for what I do.

To Professors Luis Esquivias, PacoLuis Cumbreira, and Diego Gómez, who were my professors during my undergraduate studies, who left a mark, and with whom I am lucky enough to share a research group. I hope I never have to stop enjoying their vast knowledge, closeness, and sense of humor.

To my team, Mali, J.A. Bejarano, Chico Martínez, Francisco Jiménez, and of course, to Rafa, Dr. Cano, Manuela G, Jesús L, and Morgado, who have put up with me more closely, who have been there for everything. To all of them, and to all those mentioned before, thank you for your patience and for being the best team one could have. I cannot leave out the part of the group that stayed on the other side of the wall after the divorce, especially Carmen and Cristina, who have been putting up with me since day one and have never failed me. To the close collaborators without whom the publications presented here would not be possible: Florentino Sánchez and Juan Carlos Moreno, brilliant colleagues and scientists, and to Eric Anglaret and Richard Todd, magnificent professionals and mentors. And, of course, to Camilo Zamora, the best colleague, collaborator, and mentor one could have. Thank you for your vital and scientific wisdom, for welcoming me as one more in your home, in Ecuador, in Seville, and in Murcia. I wish you and your family all



the best. I hope we never stop collaborating and laughing as we do.

When I think about how lucky I am to be in the group I am in, I have to remember Juan Carlos García, the encouragement he gave me about what to do in the future, and his advice on what to prioritize, whether the how much, what, where, or rather: with whom. Friend, mentor, analysis professor, and undergraduate thesis tutor who made a lasting impression with his passion for mathematics, reason, and love of teaching. I cannot help but remember all the other teachers who, in one way or another, taught me something that sparked my curiosity. Fortunately, they were not few.

To the colleagues of the general services, especially to Consuelo and Olivia, for their professionalism and kindness. To José Hidalgo and the colleagues from the machining workshop, José Luis and Enrique, whose meticulous work and expertise we all have to be grateful for. They know how much I love tools, how fascinated I am by their work and experience, and how much I enjoy watching them in action among lathes and milling machines. They have always welcomed me with open doors to their workshops. I wish them all the best, especially those who are starting a new stage outside the Faculty.

My gratitude to my colleagues and friends from the University, from those who accompanied me in my early years as an undergraduate and master's student, Juan, Tere, Ana, Inés, Juanjo, Chema, Ayoub, Isamar, Manolo Yi, and to those who have put up with me during my stay in England: Shenghuan, Christian Bechteler, and David Guo, for their help, support, and good work. I hope we never stop laughing and collaborating now and in the future.

To my friends, the others, the lifelong ones, and the most recent but indispensable ones, those who are here and those who are no longer with us. Fernando, Librero, Juan, Álvaro, Mario, Dani, Bea, Carlos, Toni, Álvaro Guitarra. Each one knows how much I have to be grateful for. As Jacinto Benavente used to say, or maybe Pio Baroja, who knows, *books are like friends, not always is the best one the one we like the most*. You, in addition, are the best.

To Helen and Joe, for everything they have helped me with, for everything we have shared. For how much they love my father.

To Martina A. G., the best companion one can imagine for this and for anything. Thank you for making everything so easy and beautiful, for being there from the beginning to the end, making me smile and, like now, leaving me speechless.

Finally, my family. Thank you for your support, discussions, and constant motivation. And occupying a privileged place, Mom, for your willpower and perseverance, for being that tireless engine without which none of this would have been possible. Dad, for always pushing me to do what I like the most, for teaching me so much about everything, for awakening my curiosity about everything around me, for your time and patience. Pablo, my brother, with whom I have grown up and who has given me so much and supported me. For his love, patience, and understanding throughout the path that has led me here, and the one that remains. For everything they have forgiven me. Thank you for always being by my side, for your unconditional support, and for motivating me to move forward.

## Agradecimientos

En primer lugar, agradezco a mi director de tesis, Víctor Morales Flórez, su orientación y dedicación en el desarrollo de esta investigación. Gracias por su paciencia, por su pasión, por sus valiosas sugerencias y por compartir su experiencia conmigo. Ha sido un verdadero honor trabajar a su lado. No solo ha sido fuente de curiosidad e inspiración científica, sino docente, política, personal, gastronómica, musical, literaria y cultural en general. Sin duda, uno de los motivos para decir que estos años de doctorado han merecido la pena.

Al profesor Arturo Domínguez, que me dio un par de consejos que no olvidaré en mi vida. Por cualquiera de ellos lo habría recordado, pero el primero de ellos, el que tiene cabida aquí, siempre ha sido fuente de motivación para sentir el cariño que siento por lo que hago.

A los profesores Luis Esquivias, Paco Luis Cumbreira y Diego Gómez, que fueron mis profesores durante la carrera, que dejaron huella, y con los que tengo la suerte de compartir grupo de investigación. Espero no tener que dejar de disfrutar de su vasto conocimiento, cercanía y sentido del humor.

A mi equipo, Mali, J.A. Bejarano, Chico Martínez, Francisco Jiménez, y por supuesto, a Rafa, el Dr. Cano, Manuela G, Jesús L, y Morgado, que me aguantan o me han aguantado más de cerca, que han estado ahí para todo. A todos ellos, y a todos los que he mencionado antes, gracias, por vuestra paciencia, y porque son el mejor equipo que se puede tener. No puedo dejarme fuera a la parte del grupo que quedó al otro lado del muro tras el divorcio, en especial Carmen y Cristina, que me llevan soportando desde el primer día y que no me han fallado nunca. A los estrechos colaboradores sin los que las publicaciones aquí presentadas no serían posibles: Florentino Sánchez y Juan Carlos Moreno, geniales colegas y científicos, así como a Eric Anglaret y Richard Todd, magníficos profesionales y mentores. Y, por supuesto, a Camilo Zamora, el mejor colega, colaborador y mentor que uno puede tener. Gracias por su sabiduría vital y científica, por acogerme como a uno más en su casa, en Ecuador, en Sevilla y en Murcia. Le deseo lo mejor, a él y a

su familia. Espero que nunca dejemos de colaborar y de echarnos las risas que nos echamos.

Cuando pienso en la suerte de estar en el grupo que estoy, me tengo que acordar de Juan Carlos García, los ánimos que me dio sobre qué hacer en el futuro, y su consejo sobre qué priorizar, si el cuánto, el qué, el dónde, o más bien: con quién. Amigo, mentor, profesor de análisis y tutor de TFG que me dejó grabada su pasión por las matemáticas, la razón y el amor a la docencia. No puedo dejar de acordarme aquí de todos los demás profesores que de una forma u otra me enseñaron algo que despertó mi curiosidad. Por suerte no han sido pocos.

A los compañeros de los servicios generales, en especial a Consuelo y Olivia, por su profesionalidad y amabilidad. A José Hidalgo, y los compañeros del taller de mecanizado, José Luis y Enrique, cuya minuciosa labor y saber hacer tenemos que agradecer todos. Que saben lo que me gusta una herramienta, y lo que me fascina su trabajo, experiencia, y verlos en acción entre tornos y fresadoras, y que siempre me han recibido con las puertas de sus talleres abiertas. Les deseo lo mejor, en especial a los que van a empezar una nueva etapa fuera de la Facultad.

Mi gratitud a mis colegas y amigos de la Universidad, desde los que me acompañaron en mis primeros años de estudiante de grado y máster, Juan, Tere, Ana, Inés, Isamar, Juanjo, Chema, Ayoub, Manolo Yi, y a los que me han aguantado en mi estancia en Inglaterra: Shenghuan, Christian Bechteler y David Guo, por su ayuda, apoyo y buen hacer. Espero que no dejemos de reír y de colaborar ahora y en el futuro.

A mis amigos, los demás, los de toda la vida y los más recientes pero imprescindibles, los que están y los que ya no están. Fernando, Libroero, Juan, Álvaro, Mario, Dani, Bea, Carlos, Toni, Álvaro Guitarra. Cada uno sabrá qué es lo mucho que tengo que agradecer. Como decía Jacinto Benavente, o Pío Baroja, quién sabe, *los libros son como los amigos, no siempre es el mejor el que más nos gusta*. Vosotros, además, sois los mejores.

A Helen y a Joe, por todo lo que me han ayudado, por todo lo que hemos

compartido. Por todo lo que quieren a mi padre.

A Martina A. G., la mejor compañera que uno puede imaginarse para esto y para cualquier cosa. Gracias por hacerlo todo tan fácil y bonito, por estar ahí desde el principio hasta el final sacándome una sonrisa y, como ahora, dejándome sin palabras.

Por último, mi familia. Gracias por vuestro apoyo, discusiones y constante motivación. Y ocupando un lugar privilegiado, Mamá, por tu fuerza de voluntad y tesón, por ser ese motor incansable sin el que nada de esto habría sido posible. Papá, por empujarme siempre a hacer lo que más me gustase, por enseñarme tanto de todo, por leernos libros, por despertar mi curiosidad por todo lo que me rodea, por tu tiempo, por tu paciencia. Pablo, mi hermano, con el que he crecido y tanto me ha aportado y soportado. Por su amor, paciencia y comprensión durante todo el camino que ha habido hasta aquí y el que quede. Por todo lo que me han perdonado. Gracias por estar siempre a mi lado, por vuestro apoyo incondicional y por motivarme a seguir adelante.

# Contents

1	Statement of purpose	1
2	Introduction: a brief state of the art	3
3	Intragranular carbon nanotubes in alumina-based composites for reinforced ceramics	18
4	Mechanical characterization of sol-gel alumina-based ceramics with intragranular reinforcement of multiwalled carbon nanotubes	30
5	Reactive SPS for sol-gel alumina samples: Structure, sintering behavior, and mechanical properties	40
6	Sol-gel method and reactive SPS for novel alumina-graphene ceramic composites	52
7	The dispersion of carbon nanotubes in composite materials studied by computer simulation of Small Angle Scattering	68
8	The Possible Detriment of Oxygen in Creep of Alumina and Zirconia Ceramic Composites Reinforced with Graphene	80
9	Rietveld analysis and mechanical properties of in situ formed La- $\beta$ -Al <sub>2</sub> O <sub>3</sub> /Al <sub>2</sub> O <sub>3</sub> composites prepared by sol-gel method	99
10	General conclusions	110

# Chapter 1

## Statement of purpose

This thesis by compilation of publications is devoted to the papers published along the time as a PhD student in the Department of Condensed Matter Physics of the University of Seville. Despite that the main focus are the scientific articles, two chapters has been added for sake of clarity. The first of them, the introduction, is just a contextualization at the world of ceramics, a frame of work accessible to every reader non-specialized in the topics of the thesis, but with enough references to complete and enlarge the knowledge on this area. An extensive specific introduction for the whole document would be just a reiteration of the detailed introductions available at the beginning of every presented paper. On the other hand, the thesis concludes with a section of general conclusions that gathers the knowledge derived from the set of published articles, and provides a different and complementary overview to the conclusion sections of each individual article.

The primary aim of this Doctoral Thesis is precisely to progress in knowledge in order to address the following challenges and achieve the following objectives:

1. Exploiting the sol-gel technique to achieve a good dispersion and homogenization of second phases into the ceramic matrix
2. To determine if it is possible to place the reinforcing phases in an intragranular position within the ceramic matrix

3. To study the effects of the inclusion process of carbonaceous nanophases on the structural and mechanical properties of the obtained composites



## Chapter 2

# Introduction: a brief state of the art

Ceramics, from the Greek “κεραμικός”, made of clay [1], have evolved significantly from their humble beginnings 25,000 years ago as basic pottery and figurines made from fired clay and other minerals. From the Paleolithic Age, the Venus of Vestonice [2], may be the earliest example of an “artificial” material. This refers to a ceramic statuette made by molding and baking powdered minerals that were transformed into a dense consolidated ceramic body through a process known as sintering, from the German word *Sinter* meaning “scoria, ash” [1]. It can be argued that “materials technology started with sintering” [3]. Today, ceramics come in a variety of modern forms and variations. The term “ceramic”, refers to non-metallic and inorganic mineral materials formed by heat that are hard and brittle. Ceramics are known for their ability to withstand high temperatures and chemical erosion, among other properties. A broad range of ceramic materials can be processed to exhibit different characteristics suitable for various applications, from everyday items to advanced technical materials. As a thriving industry in continuous growth, the global market value of ceramics is projected to reach €375 billion by 2025 [4], encompassing all branches: from pottery and classical tile production to pioneering space engineering and advanced research.

Ceramics exhibit outstanding properties, particularly in terms of thermal and mechanical. Focusing our attention on mechanical properties, stiffness and strength ( $\sigma_f$ ) are essential for designs that involve moving components while also trying to minimize weight or density ( $\rho$ ). This concept can be perfectly summarized by representing  $E/\rho$  against  $\sigma_f/\rho$  for each material (see Fig. 2.1-top), where  $E/\rho$  and  $\sigma_f/\rho$  are measures of the “mechanical efficiency” [5], i.e., dividing by density, this graph shows how much structural work can be achieved using the least amount of material. In this regard, ceramics presents remarkable stiffness-to-weight ratio, and their strength-to-weight ratio is comparable to that of metals. However, not all of their mechanical properties are equally impressive: the usefulness of increasing the strength of a material is limited to its plastic state and must not lead to brittleness. Once the material turns brittle, even the slightest crack or defect can trigger fast fracture, leading to failure. This is why, due to their brittleness, ceramics are not widely utilized for many structural purposes (Fig. 2.1-bottom).

The inherently brittleness of ceramics is due to the ionic-covalent character of the bonding of hard materials, which has limited their use in many structural applications. As a result, researchers have been motivated to explore new approaches aimed at improving their fracture toughness. Nature, which is a great source of inspiration for engineering solutions, has already tackled this challenge by creating composite microstructured materials like nacre. To emulate nature, numerous new ceramic-matrix micro- or nanostructured composites have been proposed. Mud bricks have been reinforced with straw as early as 4000 BC [6], which nowadays can be understood as the use of pseudo one-dimensional fillers as reinforcing agents. New words, old ideas, but the same goal: promoting new toughening mechanisms, such as increasing the tortuosity of crack propagation or the work of fracture.

For many years, there has been a considerable focus on investigating novel methods to produce ceramic matrix composites with enhanced fracture toughness or flexural strength, among many others mechanical properties. A popular strategy involves the use of allotropic carbon phases such as carbon nanotubes or graphene,

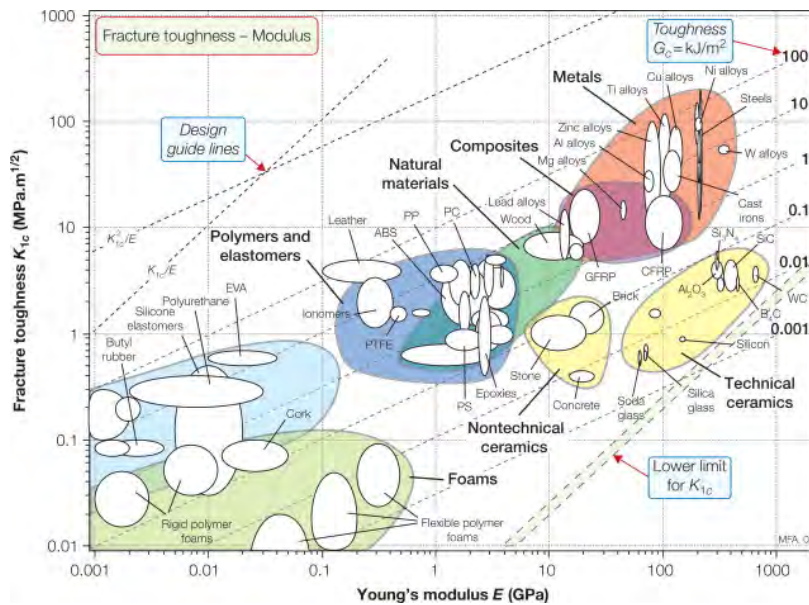
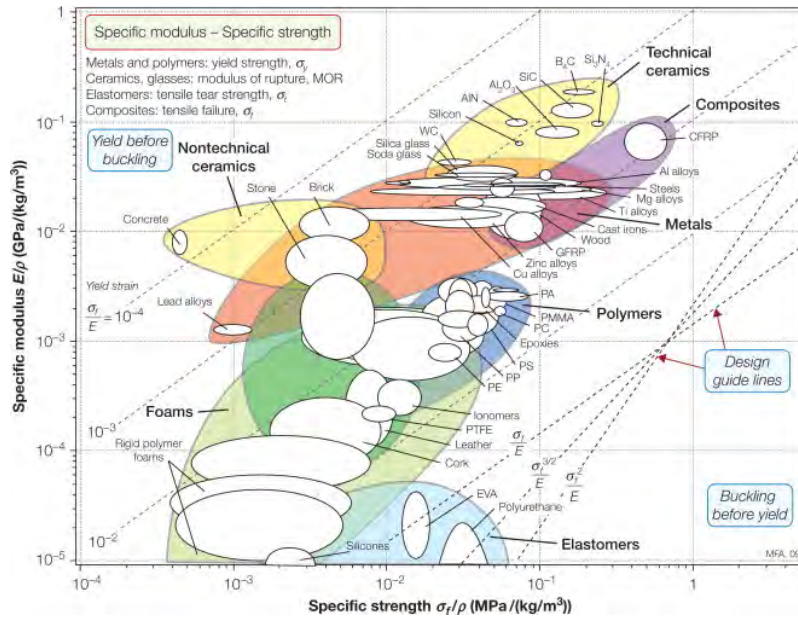


Figure 2.1: Ashby properties charts, reproduced from [5] with permission. In general, ceramics (represented by the light yellow ellipse) and especially technical ceramics like  $Al_2O_3$ , have the highest Young's modulus and strength values (**top**). Nevertheless, it is evident that ceramics have significantly lower fracture toughness values when compared to metals (**bottom**).

due to their wide variety of exceptional properties, and many literature has been produced on the primary fabrication techniques used to create ceramic composites based on alumina and zirconia. This literature discusses the mechanical properties and changes achieved through the addition of carbon allotropes, which have resulted in some improvements, such as wear resistance at low temperatures, or creep behavior and superplasticity at high temperatures [7, 8]. However, despite decades of research, there is still uncertainty and lack of agreement on the role of carbon allotropes as reinforcing agents of ceramic matrix composites. In addition, there are multiple studies that raise doubts about the expected enhancements in mechanical properties and suggest that the inclusion of carbon allotropes into ceramic matrixes has limitations, which lead to significant dispersion in the reported results [7]. See, e.g., Fig. 2.2, where the messy behavior of the hardness and fracture toughness of alumina composites versus the content of CNT (left) and graphene (right) are represented.

Despite this large discrepancy in the reported results, it is widely agreed that the controversy surrounding mechanical reinforcement can be attributed to three primary causes, all of which are connected to the preparation procedures:

1. **Dispersion and homogenization:** obtaining homogeneous composites at the microscale is challenging, resulting in carbon allotropes that are poorly dispersed and tend to form aggregates or bundles rather than individualized entities. CNTs pose significant dispersion difficulties due to their van der Waals interactions, which lead to entanglement and bundle formation, hindering the preparation of stable suspensions required for creating homogeneous composites. Furthermore, graphene-doped composites may experience a decrease in mechanical strength due to residual pores caused by the agglomeration of graphene nanoplatelets (GNPs), resulting in defects.
2. **Inter/intragranular location:** multiple studies indicate that carbon allotropes are usually situated within the grain boundaries of the ceramic matrix [9, 10]. However, it has been proposed that this location might not be the most effective

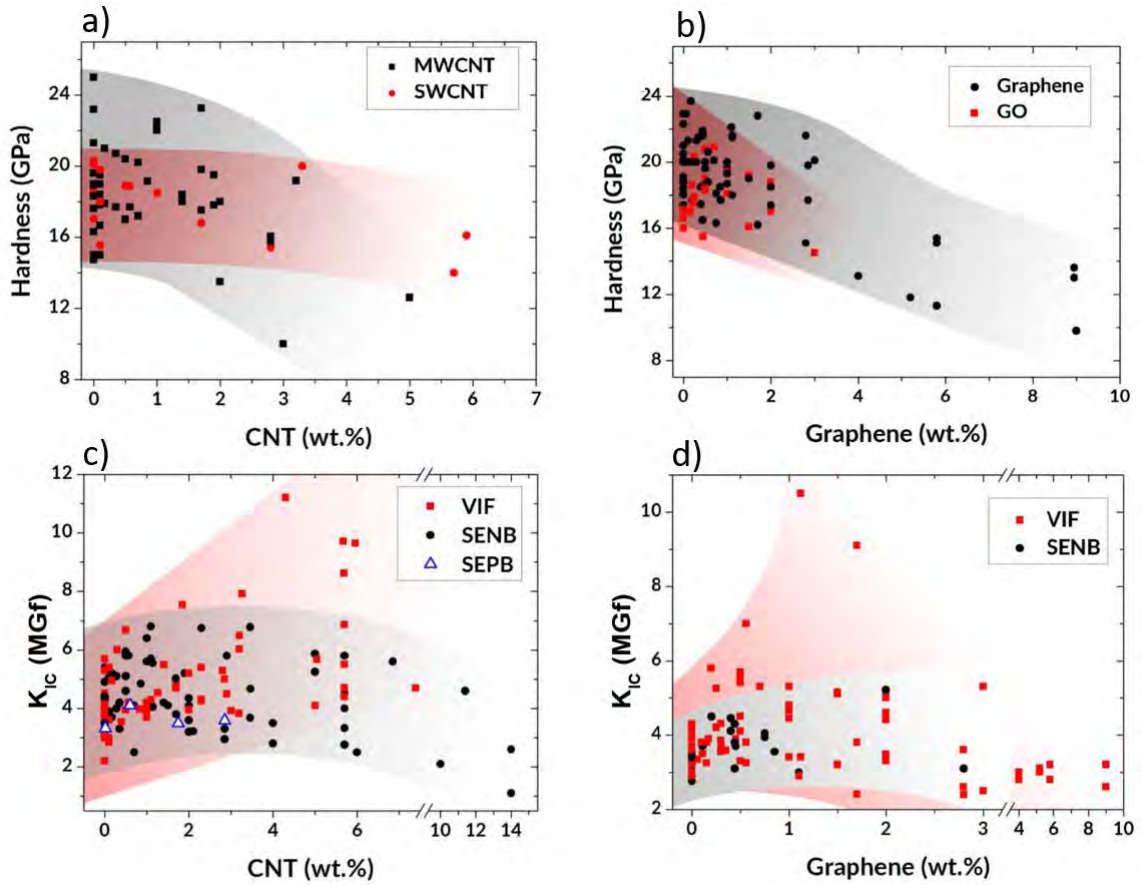


Figure 2.2: Hardness of alumina composites versus the content of **a)** CNTs and **b)** graphene. Fracture toughness of alumina composites versus the content of **c)** CNTs and **d)** graphene, measured by different methods: VIF (Vickers Indentation Fracture), SEPB (Single-edged pre-cracked beam), and SENB (Single-edged notched beam). Shadows serve as a mere visual aid to indicate trends, without providing precise measurements. Adapted with permission from [7].

way to mechanically reinforce the composite material. On the contrary, an intragranular position could be suggested as a more efficient reinforcement strategy. This is because toughening mechanisms like bridging or pullout could potentially occur, leading to a significant increase in fracture energy and impeding crack propagation.

- 3. Strength and nature of bonds:** the bonding between the ceramic matrix grains and carbon allotropes is not consistently adequate. For example, there has been reports of unsuccessful reinforcement of 3YTZP with CNTs because of insufficient bonding between the matrix and the CNTs [11].

Hence, dispersion, location, and bonding, are the key concepts in the search of a true mechanical reinforcement. Many methods have been employed along 20 years to disperse second phases in ceramic matrix. Among the known as “conventional processes”, we can find the direct mixing of the precursors, i.e., in a conventional manual mortar or through ball milling, both dry or in solution. In this last cases, where the powders are partially dispersed in an aqueous/alcoholic system, many alternatives have been added to the process, such as the application of ultrasonication, the addition of dispersants, or vigorous magnetic stirring [12, 13]. The problem of these routes that use long steps of mechanical milling is that they have the potential to harm the carbonaceous second phases, like causing carbon nanotubes to shorten, or stacking graphene platelets, thereby reducing their effectiveness as reinforcement and negatively impacting the physical properties of the ceramic-matrix composites. However, in the light of the reported results, the success of these methods for achieving good dispersion of the reinforcing phase is questionable. On the other hand, there exist other promising mixing techniques that claim to achieve improvements on the dispersion, at the same time that they keep unharmed the original structure of the carbonaceous phases, like the sol-gel method, which has been previously attempted a few times [14, 15].

In this work, the attention is devoted to the cited sol-gel method, which offers a promising and alternate approach for achieving an uniform and evenly dispersed

---

distribution of CNTs or graphene within the ceramic matrix. This process involves creating a solid, three-dimensional solid network of metal oxide or hydroxide, from liquid precursors such as colloidal suspensions (sol). These nanoparticles can be disturbed so they aggregate and grow, forming a solid three-dimensional network that spreads throughout the entire liquid system (gel). After drying the gel, the ceramic precursor powders are obtained. This technique is promising for creating ceramic matrix composites with carbon allotropes, as these second phases can be dispersed in the liquid precursor system, where the stability of the gelation kinetics of the system can be controlled by adjusting the pH, using high-power ultrasound or surfactants. This technique allows for the carbon allotropes to be perfectly dispersed in the liquid sol and then quickly trapped by the solid three-dimensional network, preventing any re-aggregation that may occur during long processing times or in subsequent steps of the synthesis route. In addition, the sol-gel technique is a cost-effective and straightforward process that can be used to produce CMCs on an industrial scale.

The next step after the gel formation (gelation) would be to extract the liquid from the gel. This drying process will leave a cloud of precursor nanoparticles (boehmite) surrounding the second phases [16]. After the coalescence of these nanoparticles during sintering, the graphene or CNTs could become trapped inside the ceramic grains, potentially enhancing the intragranular distribution of the reinforcing phase inside the matrix. In addition, the sol-gel method may have the ability to improve the existence of bonds between the between the matrix and the reinforcing phase, and enhance its strength: the presence of hydroxyl groups in the carbonaceous secondary phase during the condensation process is anticipated to enhance the formation of bonds by creating oxygen bridges between the matrix and the reinforcing phase [15].

After the powder processing, when a well-dispersed composite powder is obtained, the following step towards the production of a solid ceramic piece is the sintering. Although sintering has been extensively used for millenia, any major

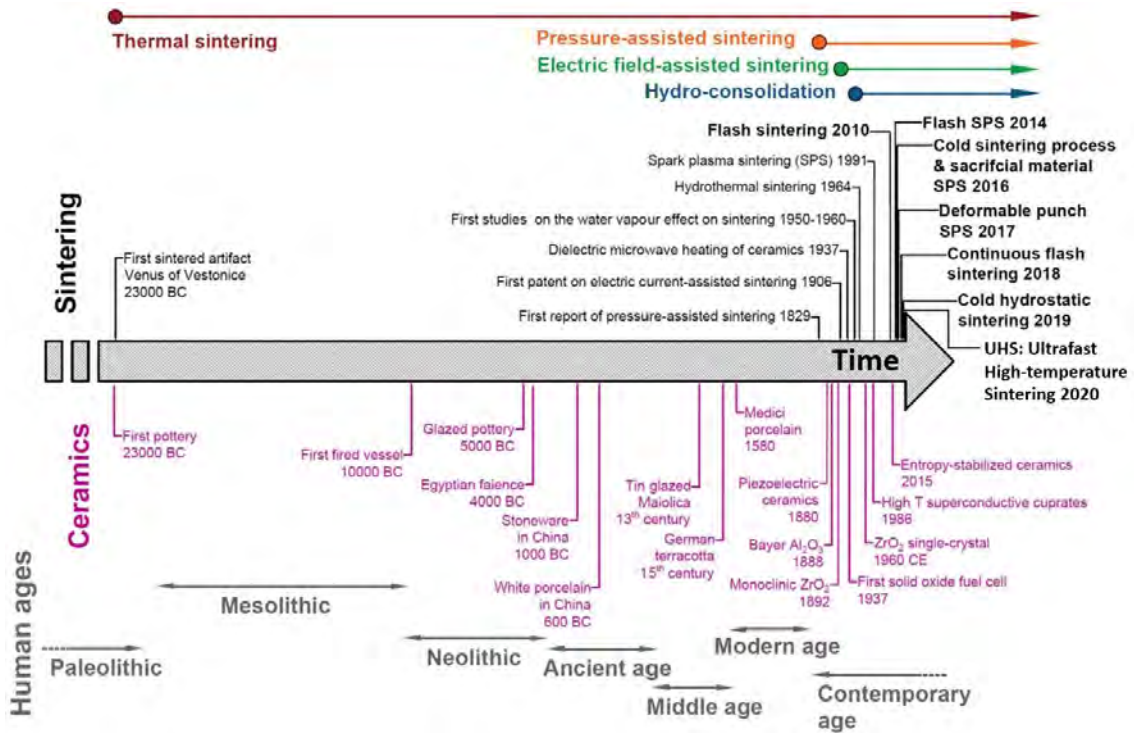


Figure 2.3: When looking at the history of sintering in relation to the evolution of ceramics and human history, it becomes evident that unconventional sintering techniques have mainly emerged over the past 115 years. However, there has been a significant surge in development in this area in the last ten years. Adapted with permission from [3].

breakthroughs in the field is hardly found, except for the development of more efficient and high-temperature furnaces or the use of new material compositions [3]. It was not until 1829, when W. Wollaston [17] conducted the first experiment on pressure-assisted sintering, that a significant advancement was made. Research on sintering only began to gain momentum in the early 20<sup>th</sup> century when scientists and engineers started considering the use of electromagnetic fields, currents, and radiations as possible enhancers of material consolidation (see Fig. 2.3).

Out of all the available sintering methods, this thesis has focused on the Spark Plasma Sintering (SPS) technique, also known as Pulsed Electric Current Sintering (PECS) or Field Assisted Sintering (FAST). This technique provides numerous benefits, such as reduced sintering temperatures, shorter hold times, and significant enhancements in the properties of the materials that are consolidated



---

using this approach. As a result of the lower temperatures and shorter hold times, it is now feasible to sinter nanometric powders to almost theoretical maximum density values with minimal grain growth [18]. Although this method was experimentally developed between 1950 and 1980, and commercialized in 1990 [3, 18], its fundamental principles were patented more than 100 years ago, and involve pressure-assisted sintering and electrically-induced heating. The most commonly used setup for SPS involves a graphite mold and a pair of conductive punches through which a pulsed DC current of approximately  $\sim 150$  MPa is applied [19]. The DC provides heat through the Joule effect (see Fig. 2.4). If the material being sintered is resistive, the current is forced to flow through the graphite mold, and heat is then transferred to the powder through conduction. If the sample is more conductive than graphite, such as in metals or conductive ceramics, the current flows through the sample and generates some internal heat. However, most of the heat generation occurs in the punches/mold assembly due to their larger mass compared to the sample, meaning that only a fraction of the heat needed to increase the sample's temperature is actually generated in the powder compact [3].

For alumina samples, for example, graphite foil is utilized to isolate the powders from the direct contact with the graphite die, and to concentrate all current lines around the targeted sample [20]. This results in higher temperatures being generated at the edges of the sample, but the heat rapidly diffused into the the sample, which, including the typically imposed dwell times at maximum temperatures, ensures the uniformity of densification [21]. Direct current is used with low applied voltages, generally under 25 V and below 1000 A, either in constant or pulsing mode. During sintering, the chamber atmosphere is adjusted, usually vacuum or by introducing an inert gas like Ar, to reduce corrosion and avoid the consumption of carbonaceous pieces. As a result, SPS guarantees the preservation of the CNTs and graphene [22], as demonstrated through many techniques such as Raman spectroscopy [23, 24].

After the sintering of the samples, the ultimate step of this research is the structural and mechanical characterization, given that a detailed understanding of

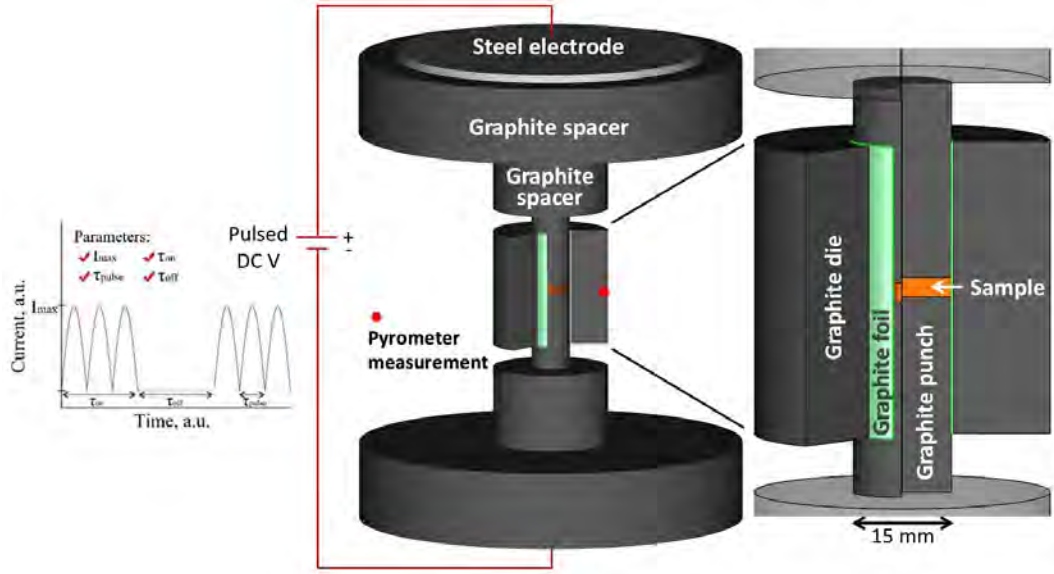


Figure 2.4: Ordinary setup for SPS sintering (adapted from [20]). Left inset: conventional electric current waveform used in SPS processes, with the typical adjustable parameters (adapted from [19]).

a material's structure and microstructure is essential for understanding its behavior and properties, and can help optimize its performance in various technological applications. The study of the microstructure of the samples consists mainly of the analysis of grain size, which is the average size of the crystallographic domains present in the material, as well as the identification of the crystalline phases and the determination of any preferential orientation of the grain growth. To carry out this structural characterization, techniques such as X-ray diffraction, scanning and transmission electron microscopy, and Raman spectroscopy are commonly used.

X-ray diffraction is a widely used technique for determining the crystal structure of solid materials. This technique is based on the fact that X-rays are diffracted when they interact with a periodic structure of atoms, which produces a characteristic diffraction pattern that can be analyzed to determine the crystal structure of the material. Electron microscopy, on the other hand, allows for direct observation of the material's microstructure and determination of crystal orientation. Raman spectroscopy, in turn, is a technique used to study the vibration of atoms in a sample

---

and can provide information on the crystalline phases present in the material.

In summary, all the fabrication and characterization processes present a significant challenge, and many techniques have been employed along the years. This work is focused in the sol-gel procedure as the initial hypothesis is that this method can achieve a good homogenization of CNTs, improve the chemical bonding between CNTs and the matrix, and promote the intragranular location of the nanophases, with the ultimate goal of transferring the exceptional micromechanical properties of carbon allotropes to the macroscopic scale of the composites, to create compounds with new and improved physical properties, specifically the fracture toughness.

# Bibliography

- [1] Real Academia Española, Diccionario de la lengua española, 23rd ed., 2022. URL: <https://dle.rae.es/ceramico>.
- [2] C. B. Carter, M. G. Norton, Ceramic materials: Science and engineering, Springer New York, 2013.
- [3] M. Biesuz, S. Grasso, V. M. Sglavo, What's new in ceramics sintering? A short report on the latest trends and future prospects, *Current Opinion in Solid State and Materials Science* 24 (2020) 1–23.
- [4] Grand View Research, Market value of ceramics worldwide in 2014 and 2018, with a forecast for 2025, 2019. URL: <https://www.statista.com/statistics/1248928/ceramics-industry-market-size-worldwide/>.
- [5] M. F. Ashby, *Materials Selection in Mechanical Design*, 4th ed., Elsevier, Amsterdam; Boston, 2011. URL: <https://linkinghub.elsevier.com/retrieve/pii/C20090255395>.
- [6] J. N. Coleman, U. Khan, W. J. Blau, Y. K. Gun'ko, Small but strong: A review of the mechanical properties of carbon nanotube-polymer composites, *Carbon* 44 (2006) 1624–1652.
- [7] V. Morales-Flórez, A. Domínguez-Rodríguez, Mechanical properties of ceramics reinforced with allotropic forms of carbon, *Progress in Materials Science* 128 (2022) 100966.

- [8] R. Cano-Crespo, P. Rivero-Antúnez, D. Gómez-García, R. Moreno, A. Domínguez-Rodríguez, The possible detriment of oxygen in creep of alumina and zirconia ceramic composites reinforced with graphene, *Materials* 14 (2021) 1–17.
- [9] E. Zapata-Solvas, D. Gómez-García, R. Poyato, Z. Lee, M. Castillo-Rodríguez, A. Domínguez-Rodríguez, V. Radmilovic, N. P. Padture, Microstructural Effects on the Creep Deformation of Alumina/Single-Wall Carbon Nanotubes Composites, *Journal of the American Ceramic Society* 93 (2010) 2042–2047.
- [10] G. D. Zhan, J. D. Kuntz, J. Wan, A. K. Mukherjee, Single-wall carbon nanotubes as attractive toughening agents in alumina-based nanocomposites, *Nature Materials* 2 (2003) 38–42.
- [11] J. Sun, L. Gao, M. Iwasa, T. Nakayama, K. Niihara, Failure investigation of carbon nanotube/3Y-TZP nanocomposites, *Ceramics International* 31 (2005) 1131–1134.
- [12] C. Muñoz-Ferreiro, A. Morales-Rodríguez, T. C. Rojas, E. Jiménez-Piqué, C. López-Pernía, R. Poyato, A. Gallardo-López, Microstructure, interfaces and properties of 3YTZP ceramic composites with 10 and 20 volnanostructures as fillers, *Journal of Alloys and Compounds* 777 (2019) 213–224.
- [13] A. Gallardo-López, I. Márquez-Abril, A. Morales-Rodríguez, A. Muñoz, R. Poyato, Dense graphene nanoplatelet/yttria tetragonal zirconia composites: Processing, hardness and electrical conductivity, *Ceramics International* 43 (2017) 11743–11752.
- [14] C. B. Mo, S. I. Cha, K. T. Kim, K. H. Lee, S. H. Hong, Fabrication of carbon nanotube reinforced alumina matrix nanocomposite by sol-gel process, *Materials Science and Engineering A* 395 (2005) 124–128.
- [15] M. K. Satam, L. Gurnani, S. Vishwanathe, A. Mukhopadhyay, Development of Carbon Nanotube Reinforced Bulk Polycrystalline Ceramics with Intragranular

- Carbon Nanotube Reinforcement, *Journal of the American Ceramic Society* 99 (2016) 2905–2908.
- [16] L. Esquivias, P. Rivero-Antúnez, C. Zamora-Ledezma, A. Domínguez-Rodríguez, V. Morales-Flórez, Intragranular carbon nanotubes in alumina-based composites for reinforced ceramics, *Journal of Sol-Gel Science and Technology* 90 (2019) 162–171.
- [17] W. H. Wollaston, On a method of rendering platina malleable, *Philosophical Transactions of the Royal Society* 119 (1829) 1–8.
- [18] Z. A. Munir, U. Anselmi-Tamburini, M. Ohyanagi, The effect of electric field and pressure on the synthesis and consolidation of materials: A review of the spark plasma sintering method, *Journal of Materials Science* 41 (2006) 763–777.
- [19] Z. Y. Hu, Z. H. Zhang, X. W. Cheng, F. C. Wang, Y. F. Zhang, S. L. Li, A review of multi-physical fields induced phenomena and effects in spark plasma sintering: Fundamentals and applications, *Materials and Design* 191 (2020) 108662.
- [20] C. Manière, G. Lee, E. A. Olevsky, All-Materials-Inclusive Flash Spark Plasma Sintering, *Scientific Reports* 7 (2017) 1–8.
- [21] P. Rivero-Antúnez, R. Cano-Crespo, F. Sánchez-Bajo, A. Domínguez-Rodríguez, V. Morales-Flórez, Reactive SPS for sol-gel alumina samples: Structure, sintering behavior, and mechanical properties, *Journal of the European Ceramic Society* 41 (2021) 5548–5557.
- [22] E. Zapata-Solvas, D. Gómez-García, A. Domínguez-Rodríguez, Towards physical properties tailoring of carbon nanotubes-reinforced ceramic matrix composites, *Journal of the European Ceramic Society* 32 (2012) 3001–3020.
- [23] X. Wang, N. P. Padture, H. Tanaka, Contact-damage-resistant ceramic/single-

- wall carbon nanotubes and ceramic/graphite composites, *Nature Materials* 3 (2004) 539–544.
- [24] P. Rivero-Antúnez, C. Zamora-Ledezma, F. Sánchez-Bajo, J. C. Moreno-López, E. Anglaret, V. Morales-Flórez, Sol-gel method and reactive SPS for novel alumina-graphene ceramic composites, *Journal of the European Ceramic Society* 43 (2023) 1064–1077.

## **Chapter 3**

# **Intragranular carbon nanotubes in alumina-based composites for reinforced ceramics**

### **The Sol-Gel procedure: boehmite as an alumina precursor**

This chapter consists of the first article published within the framework of the present thesis. In it, the potential of the sol-gel method for the inclusion of carbon nanotubes in a ceramic matrix is explored. Specifically, the manufacturing process of the precursor powder of alumina with nanotubes (which is subjected to sintering in future investigations) as well as its chemical and structural characterization are discussed.

The main idea is to disperse carbon nanotubes in the precursor sol, a boehmite sol, by magnetic stirring and ultrasonic treatment. Once dispersed, in-situ fast gelation of the sol is carried out, trapping the nanotubes and preventing them from re-aggregating during the drying process of the gel. After drying, crushing and sieving, a composite powder of boehmite and CNTs is obtained, which is then



---

calcined in an inert atmosphere to convert boehmite into  $\alpha$ -alumina. The hypothesis is that these  $\alpha$ -alumina particles that “encase” the CNTs will become grains of a compacted piece during sintering, in which the CNTs will reside inside the grains (intragranular localization), strongly bonded to the matrix, adding toughness and resistance to the matrix against crack propagation. The transformation of boehmite into  $\alpha$ -alumina and the position of the CNTs in the composite powder are analyzed using nitrogen physisorption, SEM and TEM microscopy, Raman spectroscopy, thermogravimetry (TGA), and differential scanning calorimetry (DSC) studies.



## Intragranular carbon nanotubes in alumina-based composites for reinforced ceramics

Luis Esquivias<sup>1,2</sup> · Pedro Rivero-Antúnez<sup>1</sup> · Camilo Zamora-Ledezma<sup>3,4</sup> · Arturo Domínguez-Rodríguez<sup>1</sup> · Víctor Morales-Flórez<sup>1,2</sup>

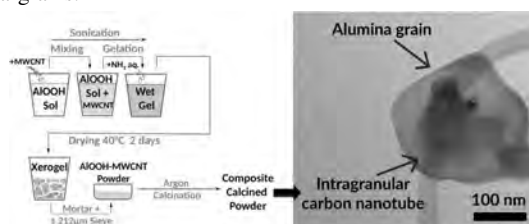
Received: 2 July 2018 / Accepted: 24 September 2018 / Published online: 3 October 2018  
© Springer Science+Business Media, LLC, part of Springer Nature 2018

### Abstract

The traditional methods for the synthesis of reinforced alumina-based matrix composites with carbon nanotubes (CNTs) have presented serious difficulties for obtaining well-dispersed and homogeneously distributed CNTs within the matrix. Besides this, the CNTs are typically found in the grain boundaries of the matrix. These features involve a non-optimal reinforcement role of the CNTs. With the aim of maximizing the efficiency of the reinforcement of the CNT, this work reconsiders a sol-gel-based procedure for ceramic composite fabrication with a two fold objective: to achieve a good dispersion of the CNTs and to promote the intragranular location of the CNTs. The mixing of precursors and CNTs has been developed under the presence of high-power ultrasounds, followed by a rapid in-situ gelation that “froze” the nanotubes inside the gel. The chemical and physical relationships between the ceramic matrix and the embedded reinforcing phase have been researched. First results confirm the success of the synthesis procedure for the preparation of alumina-based composite powders starting from a commercial boehmite sol and multiwalled carbon nanotubes. X-ray diffraction and Raman analyses confirmed the formation of the  $\alpha$ -Al<sub>2</sub>O<sub>3</sub> and the persistence of the non-damaged nanotube structure. N<sub>2</sub> physisorption and electron microscopy were used to check the evolution of the nanostructure and to confirm the presence of intragranular carbon nanotube within the polycrystalline powder. Therefore, the alumina-based composite powder prepared by this new procedure is a good candidate for the preparation of reinforced ceramic matrix composites.

### Graphical Abstract

The new synthesis process based on the controlled gelation of boehmite and MWCNT achieves the intragranular location of the nanotubes inside the alumina grains.



✉ Víctor Morales-Flórez  
vmorales@us.es

<sup>1</sup> Dpto. Física de la Materia Condensada, Universidad de Sevilla, Av. Reina Mercedes s/n, 41012 Seville, Spain

<sup>2</sup> Instituto de Ciencia de Materiales de Sevilla (CSIC/US), Av. Américo Vespucio, 49, 41092 Seville, Spain

<sup>3</sup> Yachay Tech University, School of Physical Sciences and Nanotechnology, 100115 Urcuquí, Ecuador

<sup>4</sup> Instituto Venezolano de Investigaciones Científicas (IVIC), Centro de Física, Laboratorio de Física de la Materia Condensada, Apartado 20632 Caracas 1020-A, Venezuela

## Highlights

- Boehmite sol was considered for  $\alpha$ -Al<sub>2</sub>O<sub>3</sub>-based MWCNT composite powders.
- The average radii of the synthesized alumina grains are ~200 nm.
- The structure of the MWCNT is preserved throughout the synthesis process.
- A good and homogeneous dispersion of the MWCNT is achieved.
- The intragranular MWCNT can be found inside the alumina grains.

**Keywords** Boehmite · MWCNT ·  $\alpha$ -Al<sub>2</sub>O<sub>3</sub> · Ceramic matrix composite · Intragranular reinforcement

## 1 Introduction

Ceramic materials have been a very fruitful field of research in the past decades due to their outstanding physical properties. Their high thermal stability, hardness, and wear resistance, combined with their relatively low densities and the chemical inertness upon a wide range of different environments, promote applications for ceramic materials in a variety of technologies and in very different industrial sectors. Thus, they are currently present in high-temperature superconductors, gas sensors, thermal barriers, shields, cutting tools or tissue engineering, among other sectors [1–3]. However, the inherent fragility of ceramics has always hindered their use as structural materials, so most of the research efforts have been targeted to the increase of their mechanical properties, and especially their fracture toughness.

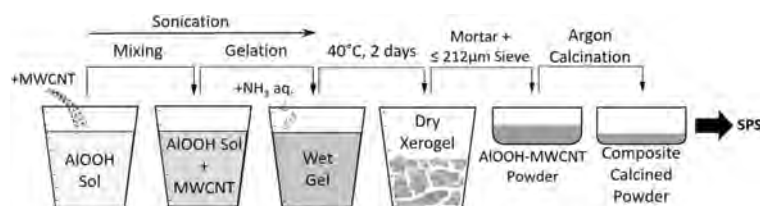
In this framework, the preparation of ceramic matrix composites (CMC) by the inclusion of fibers, or particles, or other embedded elements has been already tested as a strategy for toughening and mechanical enhancement [4, 5]. Besides, the development of low-dimensional carbon allotropes such as nanotubes, nanofibers, or graphene nanoplatelets has motivated their consideration as a reinforcing phase for the CMC. Properties such as superior Young's modulus or tensile strength make them perfect candidates to be included into the ceramic matrix in order to overcome the previously mentioned mechanical constraint [6, 7]. Hence, previous researches have already reported an enhancement in of the mechanical properties of CMC with carbon allotropes [7–10]. Furthermore, it has been proved that embedded graphene nanoplatelets in CMC can act as bridges for the reduction of the crack propagation or as builders of tribofilms for wear protection [11–14].

However, there are also several reports questioning these claimed mechanical enhancements due to the introduction of these embedded phases in the CMC, where significant worsening of the mechanical behavior is remarked [15–18]. Basically, there are three features that cause the worsening of the mechanical properties, namely, (i) inhomogeneous distribution of the reinforcing phase at the nanometer scale, (ii) the inefficient location of the reinforcing phase within the matrix, and (iii) the weak link between them. Firstly,

carbon nanotube (CNT) dispersion in stable suspensions is difficult due to their strong Van der Waals interaction that leads them to form bundles and entanglements [19]. This is an important point since a bad dispersion of the CNTs within the ceramic matrix leads to mechanical weakening. Besides, the presence of non-dispersed graphene platelets forming aggregates in graphene-reinforced CMC has also exhibited residual pores and defects that reduced the mechanical resistance [20]. Secondly, if we take into account that grain boundaries play a major role in the physical properties of the ceramic materials, the paramount relevance of the type of junction between reinforcing phase and ceramic matrix becomes clear [21]. In this regard, there are several investigations focused on how the reinforcing phases are embedded into the ceramic polycrystalline matrix. They concluded that the reinforcing phases are located around the grain boundaries [11, 13, 22] with the grain interiors being nearly completely depleted of CNTs. This feature severely limits the improvements achieved in fracture and wear properties. Finally, weak bonds between CNTs and ceramic matrix have also been stated as a reason for the unsuccessful CNT-based reinforcements [23], so the existence of close interactions between CNTs and alumina such as chemical bonds [24] is desirable. To sum up, a fully homogeneous dispersion of the reinforcing phase is not the only relevant structural feature for an efficient CMC reinforcement; it is also of paramount importance where it is located and how it is bonded to the ceramic matrix.

Up to now, colloidal processing, mixing powders, and in situ growth are the most considered protocols for CMC fabrication. However, the fabrication of composites fulfilling the aforementioned structural pre-requisites deserves special attention to the preparation strategies, as it is, in fact, a major current challenge in the materials science. In this regard, large efforts are being invested in achieving homogeneous and stable liquid suspensions of low-dimensional reinforcing phases [25, 26] to ensure homogeneous dispersion in the precursors. Moreover, though the sol-gel method has been considered since decades for ceramic fabrication [27, 28], only very recently, has it been reconsidered for the fabrication of alumina-based CMC with CNTs [22], and some first hopeful evidences of the intragranular reinforcement have been already found [29].

**Fig. 1** Sketch of the sol-gel synthesis procedure, starting from commercial boehmite (AlOOH) sol and functionalized MWCNT. The controlled addition of aqueous NH<sub>3</sub> prompts the fast gelation



The aim is now to achieve a good dispersion of the CNTs, thanks to the synthesis procedure based on liquid precursors with controlled pH and assisted by high-power ultrasounds [30], and to characterize the chemical and physical relationships between the ceramic matrix and the embedded reinforcing phase. In addition, this procedure may promote the intragranular location of the CNTs as they are present since the very first steps of the ceramic grain formation. Also, it may enhance the formation of chemical bonds between CNTs and the metallic oxide by using functionalized CNTs and the use of metallic hydroxides or alkoxides [22]. In this work, the structural features of the different steps of the fabrication of  $\alpha$ -Al<sub>2</sub>O<sub>3</sub> matrix composites with CNTs by the sol-gel method are researched; that is, the nano- and micro-structure of the as-prepared dry gel, the calcined aluminum oxide, and the polycrystalline powder prior to the sintering were studied by X-ray diffraction, thermogravimetry, Raman spectroscopy, N<sub>2</sub> physisorption, and electron microscopy, to follow up the hybrid particle formation and to confirm the intragranular inclusion of the CNTs into the alumina grains.

## 2 Materials and Methods

### 2.1 Synthesis of the gels

The preparation route is based on the procedure reported by Barrera-Solano et al. [28]. It started with the direct mixing of a commercial boehmite (AlOOH) sol (NYACOL© Nano Technologies, Inc., density = 1.14 g/cm<sup>3</sup>) and the required amount of OH-functionalized multiwalled carbon nanotubes (MWCNT, Nanostructured & Amorphous Materials, Inc., purity > 95%, short length 2.5  $\mu$ m, inner diameter = 3–5 nm, outer diameter = 8–15 nm, specific surface area > 233 m<sup>2</sup>/g, bulk density 0.36–0.42 g/cm<sup>3</sup>) under the application of high-power ultrasounds (15 min, 50 W) to achieve their maximum dispersion into the sol. The quality of dispersion was firstly estimated with the naked eye. Once MWCNT bundles cannot be optically distinguished; NH<sub>3</sub><sup>(aq)</sup> (Panreac, pH = 11.6) was slowly added under sonication, and homogeneous gelation occurred in a matter of minutes. In this step we had a wet boehmite gel in which MWCNT were embedded in the porous structure. After 2 days at 40 °

C in a stove, we obtained a dry fractured xerogel, which was milled in an agate mortar and sieved < 212  $\mu$ m. Boehmite–MWCNT composite powders were labeled “BSEX”, where X is the weight percentage of MWCNT in the final alumina composite powder. In Fig. 1, the complete process is sketched.

Finally, the powders were calcined under an Ar atmosphere for 1 h (heating ramp: 10 °C/min) at two different temperatures: 600 °C, to promote the dehydroxylation temperature of the aluminum hydroxides and to remove moisture and other possible unwished traces present in the as-prepared gels; and 1200 °C, the sintering temperature typically considered in the ceramic composite preparation procedure, above the crystallization temperature of the stable crystalline phase of the alumina ( $\alpha$ -Al<sub>2</sub>O<sub>3</sub>). Calcined samples were labeled with the suffix “@600” or “@1200”, respectively. The sintering of these powders by spark plasma sintering (SPS) to fabricate ceramic composites and their mechanical characterization are out of the scope of this work and will be the subject of a future paper.

### 2.2 Characterization techniques

Crystalline phases present in the samples were identified by X-ray diffraction (XRD Bruker diffractometer D8I-90 Cu-K $\alpha$ ) by the standard powder method. Boehmite commercial sol was dried on a hot plate at 80 °C for XRD characterization. Thermogravimetric analyses (TGA) in flowing Ar or oxidative atmosphere (air) were considered to evaluate the chemical composition of the samples. Using standard TGA procedure (STD Q600, TA Instruments), samples were heated at 10 °C/min from room temperature up to 1000 °C under an air flux (100 mL/min). Special attention was paid to the measurement of the mass losses within the thermal range corresponding to the dehydroxylation of the boehmite (200–450 °C) and within the thermal range in which MWCNT burn out under an oxidative atmosphere (450–650 °C). A specific sample containing 10 wt.% of MWCNT was synthesized in order to check the reliability of the carbon contents. For the sake of comparison, TGA curves were normalized at the sample masses at 200 °C for stoichiometric calculations. Micro-Raman spectra were collected at room temperature using a Horiba Jobin-Yvon LabRam HR800 coupled with a CCD camera and excited

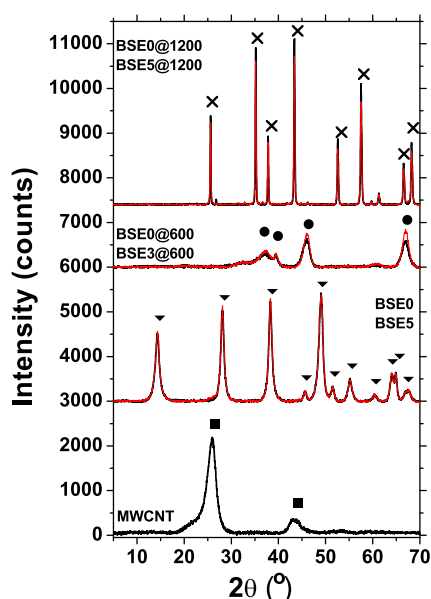


**Fig. 2** XRD patterns from samples series as-received (MWCNT), as-prepared (samples BSE0 and BSE5), and after calcination at the indicated temperatures (600 and 1200 °C). Major peaks were identified according to the following pattern diffraction files: ■ graphite (PDF: 00-003-0401); ▼ Boehmite (AlOOH, PDF: 00-005-0190); ● aluminum oxide ( $\gamma$ -Al<sub>2</sub>O<sub>3</sub>, PDF: 01-077-0396); × corundum ( $\alpha$ -Al<sub>2</sub>O<sub>3</sub>, PDF: 00-043-1484). From bottom to top, the evolution of the phases can be seen, from the starting Al-hydroxide, to transition alumina, and to subsequent corundum formation

by a Nd:YAG laser ( $\lambda_{\text{exc}} = 532$  nm). A microscope with a 100x objective lens (laser spot size of about 1  $\mu\text{m}$ ) was used to focus on the sample and its resolution was set to 0.35  $\text{cm}^{-1}$ . The Raman spectrometer was calibrated using the 520  $\text{cm}^{-1}$  line of a Si wafer. Spectra were recorded in the 100–3000  $\text{cm}^{-1}$  region. In typical measurements we used 3 s and 40 scans in extended mode. All spectra were analyzed by using commercial software.

The nanostructural features of the samples were investigated by N<sub>2</sub> physisorption experiments (Micromeritics ASAP2010, working at 77 K and equipped with pressure transducer resolution of 10<sup>-4</sup> mm Hg). Prior to N<sub>2</sub> physisorption analyses, samples were degasified at 150 °C for 2 h under a N<sub>2</sub> flux. Specific surface area, specific pore volume, pore size, and pore size distribution (PSD) were determined considering standard models for the analysis (BET and BJH, respectively). Scanning electron microscopy (SEM-FEG, Hitachi S5200) using an acceleration voltage of 5 kV and transmission electron microscopy (TEM, Philips CM-200) were also considered to research the nanostructure of the samples. Characteristic sizes from micrographs were measured after analyses of tenths of images with the help of

*ImageJ* software and uncertainties are given by the standard deviations.

## 3 Results and Discussion

### 3.1 X-ray diffraction

The considered precursors, commercial boehmite sol and MWCNT, were analyzed to resolve the structural evolution of the samples throughout the synthesis of the powders. Firstly, as-received MWCNT (Fig. 2) exhibited two broad bands at typical graphite reflections, corresponding to interplanar distances 3.40 and 2.06 Å, as expected for MWCNT. Besides, MWCNT@600 and MWCNT@1200 exhibited identical XRD patterns (not shown) along the calcination processes, which confirm that the structure of the MWCNT is kept constant upon the calcination treatments under inert atmosphere. In addition, the sole presence of crystalline boehmite (aluminum oxyhydroxide) in the boehmite commercial sol was also verified (pattern not shown).

On the other hand, the diffraction patterns of all the gel powder signatures were overlapped, regardless of the content of MWCNT. As an example, in Fig. 2 identical patterns corresponding to samples BSE0 and BSE5 are plotted. Thus, the addition of the MWCNT to the liquid precursor of the gel did not alter the boehmite structure. The crystalline signatures were similar to the signature found in the solid phase present in the precursor boehmite sol, revealing boehmite as the only crystalline phase present in these samples. For the carbon contents considered in this work, the broad peaks observed in the pure MWCNT were not detected in either as-prepared or calcined composites, because the amount of MWCNT was too low.

The calcined samples BSE0@600 and BSE3@600 also exhibited coincident patterns. In this case, poorly crystallized aluminum oxide could be identified. An estimation of the measured interplanar distances and the relative intensities gives the following values: 1.98 Å (100%), 1.40 Å (96%), 2.28 Å (46%), 2.80 Å (22%), similar to the signature of the  $\gamma$ -Al<sub>2</sub>O<sub>3</sub>, as expected for boehmite calcined at 600 °C [31]. These results confirmed the dehydroxylation of the starting boehmite below 600 °C. Finally, the corresponding patterns of the samples calcined at 1200 °C presented a clear corundum ( $\alpha$ -Al<sub>2</sub>O<sub>3</sub>) signature. In Fig. 2 the patterns of samples BSE0@1200 and BSE5@1200 are plotted. Considering these results, the introduced synthesis procedure is confirmed as an easy strategy for the fabrication of powders of  $\alpha$ -Al<sub>2</sub>O<sub>3</sub>-based ceramic matrix composites with embedded MWCNT.

### 3.2 Thermogravimetric analyses

Thermal analyses of the non-calcined samples were performed by TGA in flowing Ar (data not shown). The TGA curve of the as-prepared gels exhibited a major weight loss below 500 °C corresponding to the dehydroxylation of the boehmite gel. The measured weight losses ranged from –17.0 %, in the case of the pure alumina sample, to –16.5 % and –16.0 % in the case of samples BSE5 and BSE10, respectively. Moreover, no significant weight loss was observed in the as-received MWCNT. These values match stoichiometrically the weight loss due to the dehydroxylation of the pure boehmite (–15%), and those of the boehmite composites (within a margin of error below 2%), also according to the composition revealed by XRD (Fig. 2).

On the other hand, TGA analyses under oxidative atmosphere were performed to check the carbon content of the samples. To facilitate the quantification of the phases, a specific sample containing 10 wt.% of MWCNT was specifically prepared. The results of the TGA analyses in samples calcined at 600 °C are plotted in Fig. 3. It should be kept in mind that calcinations of the samples were performed under inert atmosphere in all cases to remove water from boehmite, whereas in this case TGA of calcined samples was performed in air (oxidative atmosphere) in order to permit carbon burnout. Thus, the absence of significant weight loss in the pure alumina sample (BSE0@600) between 400 and 700 °C, as a reference sample can be compared with the weight losses of the BSE5@600 and BSE10@600 samples, with a theoretical carbon content of 5 and 10 wt.%. These two samples exhibited well defined 5.1 and 10.2% weight losses, respectively, due to the carbon burnout, confirming the

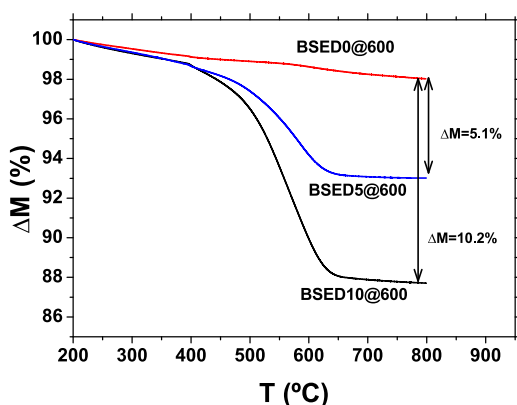


**Fig. 3** TGA analyses under oxidative atmosphere of samples loaded with 0, 5, and 10 wt.% of MWCNT, previously calcined at 600 °C under inert atmosphere. Indicated weight losses due to the burnout of the carbon of the samples are in very close correspondence with the expected carbon contents

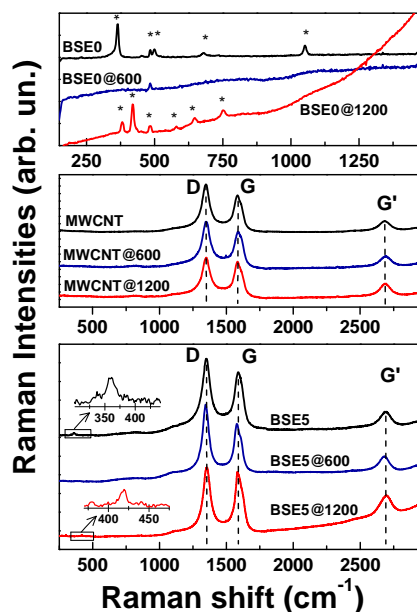


**Fig. 4** Typical Raman spectra excited with a Nd:YAG laser ( $\lambda = 532$  nm) for the sample series: top, alumina BSE0 samples; middle, MWCNT and bottom, composites BSE5, as-prepared and calcined in Ar atmosphere at indicated temperatures. The stars point the observed boehmite signature in the as-prepared BSE0 and BSE5 samples, and alumina signature in the Ar-calcined composites BSE0@1200 and BSE5@1200. Spectra were normalized and shifted along the vertical axis for clarity. Insets in the bottom panel show magnifications of indicated low-frequency areas

good reliability of the synthesis procedure regarding the MWCNT content.

### 3.3 Raman spectroscopy

Raman spectroscopy provides valuable information about the crystalline structures of the matrix and presence of possible disorder or defects in the carbonaceous phases. Firstly, Raman spectra for alumina sample series are shown in Fig. 4-top. The as-prepared sample (BSE0) shows the features typical of polycrystalline boehmite, with very well-defined bands peaking at 369, 497, 676, and 1053  $\text{cm}^{-1}$  [32]. In contrast, the spectrum for the calcined BSE0@600 exhibited a flat spectrum with a very important background (and definitely related to the luminescence centers) [33]. At the same time, occurrence of weak features merging up from the continuum is observed, which must be related to the presence of alumina transition phases such as  $\gamma\text{-Al}_2\text{O}_3$ , as revealed by XRD analysis (Fig. 2). Finally, for the BSE0@1200, the Raman signature corresponds with that of well-crystallized disoriented polycrystalline  $\alpha\text{-Al}_2\text{O}_3$ , with the major peaks located at the expected frequencies 378,

418, 432, 578, 645, and 751  $\text{cm}^{-1}$  [22, 32, 34]. Again, this characterization is in complete coherence with XRD results (Fig. 2).

Secondly, the spectra shown in Fig. 4 middle correspond to the pure as-received MWCNT and after calcinations. All of them exhibit typical features of MWCNT, namely, (i) the absence of visible peaks at low frequencies corresponding to radial breathing modes, as expected for MWCNT with inner radius 2 nm [33, 35–37]; (ii) the strong peak located around 1348  $\text{cm}^{-1}$  (called D band), which is assigned to the presence of disorder in graphitic materials and a measure of it; (iii) the strong peak located around 1588  $\text{cm}^{-1}$  (called G band), which indicates high crystalline graphitic layers and is caused by the tangential stretching modes (in plane vibrational modes) and is often considered as a good measure of the graphitization of the sample; and (iv) the presence of a well-defined band around 2687  $\text{cm}^{-1}$  (called G'), which is a second order harmonic of the D band. This band is often used as indicative of the presence of long-range order in the sample. Thus, considering the similarities between the set of three Raman spectra of the MWCNT samples, it can be stated that the structure of MWCNT is conserved during the whole thermal processes.

Finally, at Fig. 4-bottom, the typical Raman features of the boehmite–MWCNT and alumina–MWCNT composites can be observed. The strong signal of the MWCNT present in all the composites reveals identical features as observed for the MWCNT alone. Besides, the boehmite revealed by XRD gave a comparatively weak signature in the as-prepared sample at low frequencies (inset in Fig. 4-bottom, 359  $\text{cm}^{-1}$ ), which is found to be slightly shifted as a consequence of a different environment surrounding the boehmite due to the presence of MWCNT. On the contrary, no signals of  $\gamma\text{-Al}_2\text{O}_3$  or transition alumina were observed in sample BSE5@600, as expected. And in the case of sample BSE5@1200, the Raman spectrum exhibits, comparatively, a very weak peak attributable to the  $\alpha\text{-Al}_2\text{O}_3$  observed by XRD (418  $\text{cm}^{-1}$ , inset in Fig. 4-bottom), which confirms the phase transition from boehmite to  $\alpha\text{-Al}_2\text{O}_3$  as a function of the calcination [31, 34].

Besides, it is worthy to remark that Raman spectra for all MWCNT samples show a relatively intense D band and a G band of lower intensity, which is a common feature of a highly defective CNT [36] and is typically observed in functionalized MWCNT. As reported in the literature, a decrease in the  $I_D/I_G$  ratio is often an indication of the quality of nanotubes, meaning less defective nanotubes, or the presence of less amorphous carbon in the sample [37]. However, it has been found that differences in the position and intensities of the D band as a function of the excitation wavelength make it difficult to standardize and compare  $I_D/I_G$  ratios. It turns out that the assessment of the  $I_G/I_G$  ratio is a much better indicator of the crystallinity in MWCNT, as

**Table 1** Intensities  $I_D/I_G$  and  $I_G/I_G$  ratios for Raman peaks in as-produced and Ar-annealed MWCNT and Alumina/MWCNT composites

Sample	$I_D/I_G$	$I_G/I_G$
MWCNT	1.26	0.27
MWCNT@600	1.29	0.32
MWCNT@1200	1.10	0.37
BSE5	1.19	0.29
BSE5@600	1.37	0.32
BSE5@1200	1.18	0.43

the defects would reduce the double resonance process resulting in the decrease of the G' band. We have computed both the ratios  $I_D/I_G$  and  $I_G/I_G$  for all MWCNT and BSE5 samples (Table 1). In the case of the set of MWCNT,  $I_D/I_G$  ratio exhibits no defined trend, while  $I_G/I_G$  ratio increases from 0.27 to 0.37 upon calcination, suggesting a decrease in the disorder in our carbonaceous structures—that is, the higher the temperature of the thermal treatment, the higher the growth of the crystallinity [37]. Finally, in the case of the set of BSE5 samples, while  $I_D/I_G$  shows no well defined trend,  $I_G/I_G$  behaves the same as MWCNT, confirming the decrease of defects in the MWCNT embedded in the composite powder.

### 3.4 Nanostructural analyses by $\text{N}_2$ physisorption

As-prepared and calcined samples were analyzed by nitrogen physisorption experiments in order to reveal the representative nanostructural features. The values of the most relevant parameters are listed in Table 2. The analyses of the as-received MWCNT and calcined MWCNT confirmed that the calcination under inert atmosphere does not affect the nanostructure. Though  $S_{\text{BET}}$  results are quite lower than the value supplied by the manufacturer, considering the nanotube dimensions and their uncertainties, they are close to the lower limit of the range of the estimated specific surface area (159  $\text{m}^2/\text{g}$ ), and suggest that the average inner and outer diameters are close to 3 and 15 nm, respectively. Moreover, specific porosity values can be overestimated given that pure MWCNT powder may promote the agglomeration of single nanotubes and the formation of ropes or bundles with nanometric porosity within. On the other hand, in the light of the results of the as-prepared sample series, it can be affirmed that the characteristic values of the nanostructure parameters of the boehmite gels remain almost constant regardless of the MWCNT content. Adsorption–desorption isotherm plots revealed type IV isotherm curves in all cases, corresponding to mesoporous structures. Finally, the nanostructure parameters of the calcined composites exhibit a reduction of more than one order of magnitude in almost all parameters,

**Table 2** Specific surface area obtained from BET analyses ( $S_{BET}$ ) and specific porous volume ( $V_P$ ) of the different sample series obtained by nitrogen physisorption experiments

Samples	$S_{BET}$ (m <sup>2</sup> /g)	$R^{est}$ (nm)	$V_P$ (cm <sup>3</sup> /g)
MWCNT	188	–	1.18
BSE0	173	5.7	0.32
BSE1 BSE1 <sup>a</sup> (discr.)	168 173 (3%)	–	0.31 0.33 (6%)
BSE3 BSE3 <sup>a</sup> (discr.)	168 174 (3%)	–	0.33 0.35 (5%)
BSE5 BSE5 <sup>a</sup> (discr.)	177 174 (2%)	–	0.34 0.36 (7%)
MWCNT@1200	174	–	1.00
BSE0@1200	3.80	198	0.02
BSE5@1200 BSE5@1200 <sup>a</sup> (discr.)	16.9 12 (27%)	–	0.15 0.07 (53%)

“discr.” relative discrepancy between experimental data from composites and calculated expected data, “ $R^{est}$ ” estimated average radii of the basic building particles of the structure derived from  $S_{BET}$ , (–) no relevant data  
 Expected values for composites, calculated from the weighted combination of pure alumina sample and pure MWCNT experimental results

coherently with the expected vanishing of the nanostructure due to thermal treatment of the gel.

Regarding the composite BSE5@1200, its expected values  $S_{BET}$  and  $V_P$  can be calculated by a weighted combination of the pure boehmite gel and pure MWCNT values (Table 2). In addition, the relative discrepancy between experimental values and expected values are also shown in Table 2. The very low discrepancy for as-prepared samples indicates that they can be described as a pure weighted combination of the pure alumina sample and the pure MWCNT. However, calcined composite BSE5@1200 cannot be described like that as the discrepancies are significantly much higher. Thus, regarding the nanostructure, this calcined sample cannot be described as just the combination of the weighted combination of both involved phases. Instead, they suggest the existence of a closer structural relationship in such a way that nitrogen is not capable of accessing some structural features that are available in the samples BSE0@1200 and MWCNT@1200.

The pore size distribution (PSD) curves (Fig. 5) show the distribution of porosity measured by nitrogen in the samples calcined at 1200 °C. Firstly, the bimodal distribution observed in MWCNT@1200, similar to as-received MWCNT (not shown), reveals that the diameter of the inner space of the nanotubes is slightly higher than 3 nm in average (in coherence with estimation from the  $S_{BET}$  result, as explained before). In addition, the high porosity centered in the large pore range above 30 nm in size is an artifact due to the aggregation of the MWCNT. The alumina samples BSE0@1200 and BSE5@1200 presented very low PSD curves due to the vanishing of the nanostructure by calcination, as expected. Moreover, the expected PSD of BSE5@1200<sup>a</sup>, obtained as a weighted combination of BSE0@1200 and MWCNT@1200 experimental curves, is also plotted in Fig. 5. Interestingly, the porosity below 5 nm corresponding to the inner space of the MWCNT that should be observed in BSE@1200<sup>a</sup> has almost disappeared in the actual BSE5@1200 composite. This result suggests

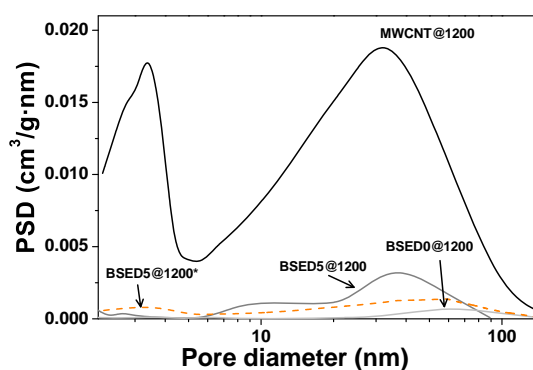


**Fig. 5** Pore size distributions (PSD) from nitrogen physisorption experiments, for sample series calcined at 1200 °C, and expected PSD for composite BSE5@1200 calculated from weighted combination of BSE0@1200 and MWCNT@1200

the idea that the extremes of the nanotubes are located inside alumina grains, making inner nanotube space inaccessible for nitrogen molecules.

Finally, as a rough approach, the average particle size, assuming a very simplified model of spherical particles with radius  $R$  for the boehmite or alumina matrix, can be estimated. Thus, for a bulk sphere of density  $\rho$ , volume  $V$ , mass  $M$  and surface  $S$ , the specific surface area (SSA) is given by

$$SSA = \frac{S}{M} = \frac{S}{\rho V} = \frac{4\pi R^2}{\rho \frac{4}{3}\pi R^3} \quad (1)$$

Assuming the experimental value  $S_{BET}$  as the SSA, Eq. 2 is obtained:

$$R^{est} = \frac{3}{\rho S_{BET}} \quad (2)$$

where  $\rho$  corresponds to the boehmite density in the case of as-prepared samples, and to the alumina density for calcined samples. No  $R^{est}$  was calculated for composites given that



**Fig. 6** Scanning electron microscopy images for BSE5 as-prepared (left, center), and BSE5@1200 (right). Scale bar represents 500 nm in all cases. Arrows point to individual MWCNT

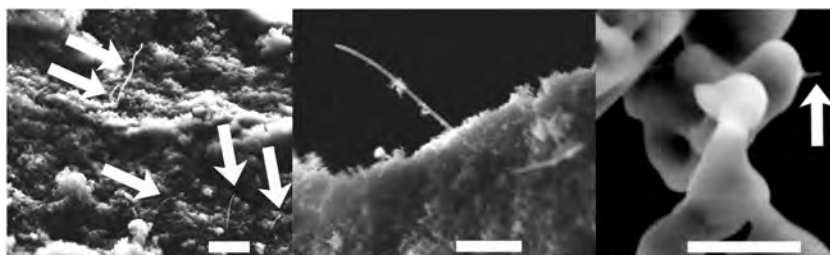
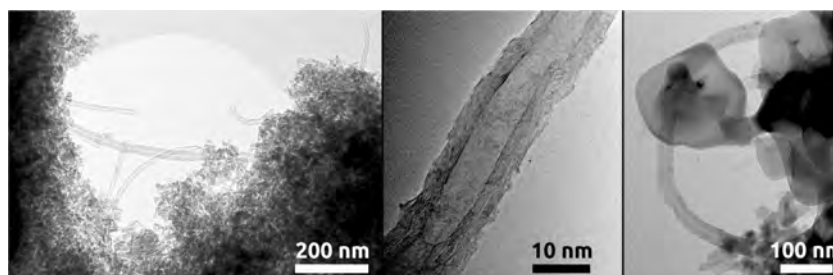


**Fig. 7** TEM images for BSE5 as-prepared (left), MWCNT (middle), and BSE5@1200 (right)



the contribution of the embedded MWCNT has to be removed. The estimated values disclose an increase of almost two orders of magnitude of the particle radii, attaining in the case of the calcined  $\alpha$ - $\text{Al}_2\text{O}_3$  powder particles  $\sim 400$  nm in size.

### 3.5 Electron microscopy

The SEM and TEM helped us to find out the nano/micrometric and sub-micrometric structure of the samples and to assess the quality of the dispersion of the MWCNT population. The SEM micrographies of the as-prepared samples (Fig. 6-left, center) show the typical wrinkled texture of the nanoporous gel where separated MWCNT can be clearly identified. The MWCNT are typically embedded in the boehmite gel (Fig. 6-center), which exhibit the nanosized features revealed by  $\text{N}_2$  physisorption. In the calcined sample BSE5@1200 (Fig. 6-right), a dendritic structure was observed with a characteristic size of hundreds of nm. In this sample, a considerable amount of MWCNT could be found emerging from inside the alumina grains (pointed by the arrow in Fig. 6-right), confirming the intragranular location of many nanotubes.

On the other hand, TEM images (Fig. 7-left) accurately reveal the boehmite nanostructured gel in sample BSE5 (as-prepared), and the dispersed nanotubes within the nanoporous structure. Though bundles have been found, a reasonably good but also improvable dispersion has been achieved with this synthesis process. The basic building blocks of the boehmite gel exhibit the characteristic orthorhombic shape. The average size is  $25 \pm 8$  nm  $\times$   $7 \pm 3$

nm, yielding a characteristic radius of  $R = 7 \pm 2$  nm, in complete coherence with  $\text{N}_2$  physisorption estimations. Besides, the significant differences in the nanotube outer diameter of the nanotubes can be seen. An estimation of the average diameter could be directly performed in tenths of TEM images (e.g., Fig. 7-center), yielding an average outer diameter of  $20 \pm 7$  nm, as typically reported in the literature [38].

An apparent increase of the size of the particles is evident due to calcination. Thus, in the calcined sample BSE5@1200 (Fig. 7-right), grains of typically 200–400 nm in size are seen everywhere. Nevertheless, smaller particles are still present, suggesting that a longer calcination process may be necessary in order to obtain a more homogeneous alumina grain size distribution. Finally, the main target of this research was to synthesize composite powders in which the intragranular location of the MWCNT inside the  $\alpha$ - $\text{Al}_2\text{O}_3$  grains could be corroborated in order to encourage the intragranular reinforcement of the sintered alumina-based ceramic. It was already explained how the nanotubes were embedded inside the fuzzy boehmite as-prepared gel. After calcination (Fig. 7-right), it can be confirmed that the coalescence of the boehmite gel particles promotes the embedding of the MWCNT inside the  $\alpha$ - $\text{Al}_2\text{O}_3$  grains.

## 4 Conclusions

1. The synthesis procedure from boehmite sols is a cheap, simple, and efficient route for the fabrication of

- alumina-based ceramic matrix composite powders.
2. The MWCNT were frozen in the nanostructure of the boehmite gel. Nevertheless, the dispersion of the MWCNT has to be optimized.
3. Calcination of the gel powders involved the formation and growth of alumina grains in the presence of the MWCNT. The intragranular presence of a considerable amount of MWCNT was achieved, as shown by electron microscopy and nitrogen physisorption.
4. The structure of the MWCNT was kept undamaged along the calcination processes.
5. Therefore, the BSE route is confirmed as a solid candidate for the design of new efficient synthesis procedures of CNT-based ceramic matrix composites.

**Acknowledgements** Project P12-FQM-1079 and funding support to FQM163 from Junta de Andalucía are acknowledged. V- M-F. thanks the grant from V Plan Propio de Investigación de la Universidad de Sevilla. Fco. Luis Cumbreira and R. Cano-Crespo are also acknowledged for their help on XRD diffraction patterns and sample preparation. The help from the technical staff from the CITIUS is acknowledged. The authors would like to thank the work by the National Institutes of Health, USA for the development of the *ImageJ* (<https://imagej.nih.gov/ij/>) software. Comercial Química Massó is also acknowledged for supplying the boehmite precursor Nyacol®.

#### Compliance with ethical standards

**Conflict of interest** The authors declare that they have no conflict of interest.

#### References

1. Robinson AL (1987) An oxygen key to the new superconductors *Science* 236:1063–1065. <https://doi.org/10.1126/science.236.4805.1063>
2. Padture NP, Gell M, Jordan EH (2002) Thermal barrier coatings for gas-turbine engine applications *Science* 296:280–284. <https://doi.org/10.1126/science.1068609>
3. Okada A (2008) Automotive and industrial applications of structural ceramics in Japan *J Eur Ceram Soc* 28:1097–1104. <https://doi.org/10.1016/j.jeurceramsoc.2007.09.016>
4. Ko FK (1989) Preform fiber architecture for ceramic matrix composites *Am Ceram Soc Bull* 68:401–414
5. De Arellano-López AR, Domínguez-Rodríguez A, Goretta KC, Routbort JL (1993) Plastic deformation mechanisms in SiC-Whisker-Reinforced alumina *J Am Ceram Soc* 76:1425–1432. <https://doi.org/10.1111/j.1151-2916.1993.tb03921.x>
6. Zhu Y, Murali S, Cai W, Li X, Suk JW, Potts JR, Ruoff RS (2010) Graphene and graphene oxide: synthesis, properties, and applications *Adv Mater* 22:3906–3924. <https://doi.org/10.1002/adma.201001068>
7. Zapata-Solvas E, Gómez-García D, Domínguez-Rodríguez A (2010) On the microstructure of single wall carbon nanotubes reinforced ceramic matrix composites *J Mater Sci* 45:2258–2263. <https://doi.org/10.1007/s10853-009-4126-z>
8. Zapata-Solvas E, Gómez-García D, Poyato R, Lee Z, Castillo-Rodríguez M, Domínguez-Rodríguez A, Radmilovic V, Padture NP (2010) Microstructural effects on the creep deformation of alumina/single-wall carbon nanotubes composites *J Am Ceram Soc* 93:2042–2047. <https://doi.org/10.1111/j.1551-2916.2010.03681.x>
9. Castillo-Rodríguez M, Muñoz A, Morales-Rodríguez A, Poyato R, Gallardo-López Á, Domínguez-Rodríguez A (2015) Influence of the processing route on the carbon nanotubes dispersion and creep resistance of 3YTZP/SWCNTs nanocomposites *J Am Ceram Soc* 98:645–653. <https://doi.org/10.1111/jace.13348>
10. Castillo-Rodríguez M, Muñoz A, Domínguez-Rodríguez A (2016) High-temperature deformation mechanisms in monolithic 3ytzp and 3ytzp containing single-walled carbon nanotubes *J Am Ceram Soc* 99:286–292. <https://doi.org/10.1111/jace.13974>
11. Porwal H, Tatarko P, Grasso S, Khaliq J, Dlouhý I, Reece MJ (2013) Graphene reinforced alumina nano-composites *Carbon N Y* 64:359–369. <https://doi.org/10.1016/j.carbon.2013.07.086>
12. Cano-Crespo R, Malmal Moshtaghion B, Gómez-García D, Domínguez-Rodríguez A, Moreno R (2017) High-temperature creep of carbon nanofiber-reinforced and graphene oxide-reinforced alumina composites sintered by spark plasma sintering *Ceram Int* 43:7136–7141. <https://doi.org/10.1016/j.ceramint.2017.02.146>
13. Wozniak J, Jastrzębska A, Cygan T, Olszyna A (2017) Surface modification of graphene oxide nanoplatelets and its influence on mechanical properties of alumina matrix composites *J Eur Ceram Soc* 37:1587–1592. <https://doi.org/10.1016/j.jeurceramsoc.2016.11.010>
14. Gutiérrez-Mora F, Cano-Crespo R, Rincón A, Moreno R, Domínguez-Rodríguez A (2017) Friction and wear behavior of alumina-based graphene and CNFs composites *J Eur Ceram Soc* 37:3805–3812. <https://doi.org/10.1016/j.jeurceramsoc.2017.02.024>
15. Wang X, Padture NP, Tanaka H (2004) Contact-damage-resistant ceramic/single-wall carbon nanotubes and ceramic/graphite composites *Nat Mater* 3:539–544. <https://doi.org/10.1038/nmat1161>
16. Lee K, Mo CB, Park SB, Hong SH (2011) Mechanical and electrical properties of multiwalled cnt-alumina nanocomposites prepared by a sequential two-step processing of ultrasonic spray pyrolysis and spark plasma sintering *J Am Ceram Soc* 94:3774–3779. <https://doi.org/10.1111/j.1551-2916.2011.04689.x>
17. Ahmad I, Yazdani B, Zhu Y (2015) Recent advances on carbon nanotubes and graphene reinforced ceramics nanocomposites *Nanomaterials* 5:90–114. <https://doi.org/10.3390/nano5010090>
18. Bocanegra-Bernal MH, Domínguez-Rios C, Echeberria J, Reyes-Rojas A, Garcia-Reyes A, Aguilar-Elguezabal A (2016) Spark plasma sintering of multi-, single/double- and single-walled carbon nanotube-reinforced alumina composites: Is it justifiable the effort to reinforce them? *Ceram Int* 42:2054–2062. <https://doi.org/10.1016/j.ceramint.2015.09.060>
19. Torres-Canas FJ, Blanc C, Zamora-Ledezma C, Silva P, Anglaret E (2015) Dispersion and individualization of SWNT in surfactant-free suspensions and composites of hydrosoluble polymers *J Phys Chem C* 119:703–709. <https://doi.org/10.1021/jp5092015>
20. Lee B, Lee D, Lee JH, Ryu HJ, Hong SH (2016) Enhancement of toughness and wear resistance in boron nitride nanoplatelet (BNNP) reinforced Si3N4 nanocomposites *Sci Rep* 6:27609. <https://doi.org/10.1038/srep27609>
21. Chiang Y-M, Birnie DP, Kingery WD (1997) *Physical ceramics: Principles for Ceramic Science and Engineering*. J. Wiley & Sons, New Jersey USA
22. Satam MK, Gurnani L, Vishwanathe S, Mukhopadhyay A (2016) Development of J Am Ceram Soc 99:2905–2908. <https://doi.org/10.1111/jace.14425>
23. Sun J, Gao L, Iwasa M, Nakayama T, Niihara K (2005) Failure investigation of carbon nanotube/3Y-TZP nanocomposites *Ceram Int* 31:1131–1134. <https://doi.org/10.1016/j.ceramint.2004.11.010>

24. Saleh AKT, Gupta V (2012) Characterization of the chemical bonding between  $\text{Al}_2\text{O}_3$  and nanotube in MWCNT/  $\text{Al}_2\text{O}_3$  nanocomposite *Curr Nanosci* 8:739–743. <https://doi.org/10.2174/157341312802884418>
25. Bepete G, Anglaret E, Ortolani L, Morandi V, Huang K, Pénicaud A, Drummond C (2017) Surfactant-free single-layer graphene in water *Nat Chem* 9:347–352. <https://doi.org/10.1038/nchem.2669>
26. Zapata-Solvas E, Gómez-García D, Domínguez-Rodríguez A (2012) Towards physical properties tailoring of carbon nanotubes-reinforced ceramic matrix composites *J Eur Ceram Soc* 32:3001–3020
27. Yoldas BE (1975) A transparent porous alumina *Ceram Bull* 54:289–290
28. Barrera-Solano C, Esquivias L, Messing GL (1999) Effect of preparation conditions on phase formation, densification, and microstructure evolution in La- $\beta$ - $\text{Al}_2\text{O}_3/\text{Al}_2\text{O}_3$  composites *J Am Ceram Soc* 82:1318–1324. <https://doi.org/10.1111/j.1151-2916.1999.tb01914.x>
29. Morales-Flórez V, Cano-Crespo R, Malmal BM, de la Rosa-Fox N, Esquivias L, Domínguez-Rodríguez A (2018) Intragranular reinforcement of alumina-based composites with carbon nanotubes via sol-gel. In: *ImagineNano Int. Composites Conference Bilbao (Spain)*, available at <http://www.imagenano.com>. Accessed 25 Jun 2018
30. Piñero M, Mesa-Díaz M, del M, de los Santos D, Reyes-Peces MV, Díaz-Fraile JA, de la Rosa-Fox N, Esquivias L, Morales-Florez V (2018) Reinforced silica-carbon nanotube monolithic aerogels synthesised by rapid controlled gelation *J Sol-Gel Sci Technol* 86:391–399. <https://doi.org/10.1007/s10971-018-4645-7>
31. Santos PS, Santos HS, Toledo SP (2000) Standard transition aluminas *Electron Microscop Stud Mater Res* 3:104–114. <https://doi.org/10.1590/S1516-14392000000400003>
32. Assih T, Ayrat A, Abenoza M, Phalippou J (1988) Raman study of alumina gels *J Mater Sci* 23:3326–3331. <https://doi.org/10.1007/BF00551313>
33. Zamora-Ledezma C, Añez L, Primera J, Silva P, Etienne-Calas S, Anglaret E (2008) Photoluminescent single wall carbon nanotube-silica composite gels *Carbon N Y* 46:1253–1255
34. Porto SPS, Krishnan RS (1967) Raman effect of corundum *J Chem Phys* 47:1009–1012. <https://doi.org/10.1063/1.1711980>
35. Torres-Canas F, Blanc C, Mašlík J, Tahir S, Izard N, Karasahin S, Castellani M, Dammasch M, Zamora-Ledezma C, Anglaret E (2017) Morphology and anisotropy of thin conductive inkjet printed lines of single-walled carbon nanotubes *Mater Res Express* 4:035037. <https://doi.org/10.1088/2053-1591/aa5687>
36. Murphy H, Papakonstantinou P, Okpalugo TIT (2006) Raman study of multiwalled carbon nanotubes functionalized with oxygen groups *J Vac Sci Technol B Microelectron Nanom Struct* 24:715. <https://doi.org/10.1116/1.2180257>
37. White CM, Banks R, Hamerton I, Watts JF (2016) Characterisation of commercially CVD grown multi-walled carbon nanotubes for paint applications. *Prog Org Coatings* 90:44–53. <https://doi.org/10.1016/j.porgcoat.2015.09.020>
38. Lehman JH, Terrones M, Mansfield E, Hurst KE, Meunier V (2011) Evaluating the characteristics of multiwall carbon nanotubes *Carbon N Y* 49:2581–2602. <https://doi.org/10.1016/j.carbon.2011.03.028>

## Chapter 4

# Mechanical characterization of sol-gel alumina-based ceramics with intragranular reinforcement of multiwalled carbon nanotubes

The following article is the natural continuation of chapter 3, i.e., the sintering, of the obtained composite powders, structural characterization, and measurement of mechanical properties. It investigates the use of multiwalled carbon nanotubes (MWCNTs) for mechanical reinforcement of ceramic matrix composites.

The efficiency of this reinforcement strategy has been subject to debate due to fabrication issues, such as inadequate homogenization and location of the MWCNTs within the matrix. Assuming an acceptable dispersion and promotion of intragranular placement of the MWCNTs through the proposed the sol-gel method, which promotes intragranular location of the MWCNTs. The mechanical properties of the composites synthesized by this method are characterized, revealing crack-bridging as the toughening mechanism. The article also discusses the conventional use of bibliographical Young's modulus of pure alumina for estimating fracture toughness and proposes improvements by considering elastic moduli

---

obtained by nanoindentation. These findings provide insights into optimizing the mechanical properties of MWCNT-reinforced ceramic matrix composites, being the lack of density the major issue affecting the mechanical properties of the sintered samples.



Contents lists available at ScienceDirect

Ceramics International

journal homepage: [www.elsevier.com/locate/ceramint](http://www.elsevier.com/locate/ceramint)



## Mechanical characterization of sol-gel alumina-based ceramics with intragranular reinforcement of multiwalled carbon nanotubes

Pedro Rivero-Antúnez<sup>a,b</sup>, Rafael Cano-Crespo<sup>a</sup>, Luis Esquivias<sup>a,b</sup>, Nicolás de la Rosa-Fox<sup>c</sup>, Camilo Zamora-Ledezma<sup>d,e</sup>, Arturo Domínguez-Rodríguez<sup>a</sup>, Víctor Morales-Flórez<sup>a,b,\*</sup>

<sup>a</sup> Dpto. Física de la Materia Condensada, Facultad de Física, Universidad de Sevilla, Avenida Reina Mercedes s/n, 41012, Sevilla, Spain

<sup>b</sup> Instituto de Ciencia de Materiales de Sevilla, Centro Mixto CSIC-Universidad de Sevilla, 41092, Sevilla, Spain

<sup>c</sup> Dpto. Física de la Materia Condensada, Facultad de Ciencias, Universidad de Cádiz, Avenida República Saharaui, s/n Puerto Real, 11510, Cádiz, Spain

<sup>d</sup> School of Physical Sciences and Nanotechnology, Yachay Tech University, 100119, Urcuquí, Ecuador

<sup>e</sup> Instituto Venezolano de Investigaciones Científicas (IVIC), Centro de Física, Laboratorio de Física de la Materia Condensada, Apartado, 20632, 1020-A Caracas, Venezuela



### ARTICLE INFO

#### Keywords:

$\alpha$ -Al<sub>2</sub>O<sub>3</sub>

MWCNTs

Intragranular reinforcement

Fracture toughness

Crack bridging

### ABSTRACT

Multiwalled carbon nanotubes (MWCNTs) have been widely considered for mechanical reinforcement of ceramic matrix composites. Nevertheless, the efficiency of this reinforcement strategy is under debate due to fabrication issues, such as a good homogenization or the location of the MWCNTs inside the matrix composite. Regarding this, the intragranular location of the MWCNTs has been deemed a crucial feature for optimizing the reinforcement compared to the typical intergranular placement achieved by conventional procedures. Recently, the sol-gel method has been reconsidered, as it promotes the intragranular placement of the MWCNTs. This work presents the mechanical characterization of these composites synthesized by the sol-gel method, where crack-bridging has been revealed as toughening mechanism. Finally, the conventional use of the bibliographical Young's modulus of pure alumina for the estimation of the fracture toughness is discussed, obtaining significant improvements of the fracture toughness when indentation measurements are treated by considering elastic moduli obtained by nanoindentation.

### 1. Introduction

The idea of using pseudo one-dimensional fillers for materials reinforcement dates back to about 4000 BC, where materials, like straw, were used to reinforce mud bricks [1]. Nowadays, the preparation of ceramic matrix composites (CMCs), through the inclusion of low-dimensional materials, such as nanofibers, nanotubes, or nanoplatelets, is being considered as a strategy for toughening and mechanical enhancement of materials [2,3]. The aim of this strategy is to improve the inherent fragility of ceramics that has hindered their use as structural materials. Thus, most research efforts have been especially targeted to increase their fracture toughness. Low-dimensional carbon allotropes, such as carbon nanotubes (CNTs), nanofibers, or graphene nanoplatelets, are very popular for reinforcement purposes, owing to their outstanding mechanical properties, good thermal stability, and chemical inertness [1]. A superior Young's modulus, or tensile strength,

makes CNTs perfect candidates to be incorporated into the ceramic matrix in order to overcome the previously mentioned fragility. For example, CMCs doped with multiwalled carbon nanotubes (MWCNTs) have been reported to exhibit increased room-temperature mechanical properties, such as fracture toughness and wear resistance [4,5]. However, there are also several reports questioning these claims of mechanical enhancements resulting from the introduction of these embedded phases in the CMCs, where significant worsening of the mechanical behavior is observed [3,5–8].

Basically, three specific features cause controversy regarding the mechanical reinforcement of CMCs through the inclusion of carbon allotropes [9,10]. First, the reinforcing phase is often inhomogeneously distributed at the nanometer scale. Stable suspensions of CNT dispersions are difficult to obtain due to strong Van der Waals interactions that lead to the formation of bundles and entanglements [11,12]. These poor CNT dispersions within the ceramic matrix lead to mechanical

\* Corresponding author. Dpto. Física de la Materia Condensada, Universidad de Sevilla, Av. Reina Mercedes s/n, E41012, Sevilla, Spain.

E-mail addresses: [privero@us.es](mailto:privero@us.es) (P. Rivero-Antúnez), [racacres@us.es](mailto:racacres@us.es) (R. Cano-Crespo), [luisquias@us.es](mailto:luisquias@us.es) (L. Esquivias), [nicolas.rosafox@uca.es](mailto:nicolas.rosafox@uca.es) (N.d.l. Rosa-Fox), [czamora@yachaytech.edu.ec](mailto:czamora@yachaytech.edu.ec) (C. Zamora-Ledezma), [adorod@us.es](mailto:adorod@us.es) (A. Domínguez-Rodríguez), [vmorales@us.es](mailto:vmorales@us.es) (V. Morales-Flórez).

<https://doi.org/10.1016/j.ceramint.2020.04.285>

Received 20 March 2020; Received in revised form 27 April 2020; Accepted 29 April 2020

Available online 04 May 2020

0272-8842/ © 2020 Elsevier Ltd and Techna Group S.r.l. All rights reserved.

weakening. Furthermore, the presence of non-dispersed CNTs, which form aggregates in the CNT-reinforced CMCs, have also produced residual pores and defects that reduced the mechanical resistance. Secondly, the reinforcing phase is inefficiently located within the matrix. Typically, the reinforcing phases are located around the grain boundaries [2,13], but this placement severely limits possible improvements achieved in the fracture and wear properties given that the toughening mechanisms of the composite, such as crack-bridging and the CNTs pulling out, may be limited or may not directly appear [9,14,15]. Lastly, weak bonds between the carbon allotropes and the ceramic matrix have been stated as a reason for unsuccessful reinforcements [16]. Therefore, the existence of close interactions between CNTs and alumina, such as strong interfacial bonding [17,18], is desirable.

The fabrication of composites that fulfill the aforementioned structural prerequisites deserves special attention, as synthesis strategies are currently a major challenge in materials science. In this regard, large efforts are being invested into achieving homogeneous and stable liquid suspensions of low-dimensional reinforcing phases to ensure homogeneous dispersion of the precursors [2,19]. Among all the synthesis strategies, the sol-gel method has been considered for ceramic fabrication [20,21], and more recently, for the fabrication of alumina-based CMCs with CNTs [9,14,15]. The aim is to achieve a good dispersion of the CNTs by a rapid, controlled gelation through the use of liquid precursors, control of the pH, and the assistance of high-power ultrasound [22]. In addition, this method may promote intragranular placement of the CNTs, as they are present during the very first steps of the formation of the ceramic grains [9,14,15]. Finally, the sol-gel method may also enhance the formation of bonds between the CNTs and the ceramic matrix through the use of functionalized CNTs and metallic hydroxides or alkoxides as precursors [23].

Hence, the fabrication problems associated with the inclusion of carbon allotropes in CMCs leads to erratic results and disparities regarding the reinforcement effect. Therefore, a very large distribution of reported mechanical results can be found. For example, values of fracture toughness spanning from 2.95 MGf<sup>1</sup> to 9.7 MGf [10,24] have been published, a priori, for similar composites. Surprisingly, an enormous discrepancy is even found for the pure alumina reference samples, in which reported values of fracture toughness span from 2.2 MGf to 5.7 MGf [25,26].

Regarding the measurement of fracture toughness, the possible sources of disparity can be found, not only in the differences among the synthesis processes employed or the different precursors considered, but also in the characterization protocols and models considered for the toughness measurement. The two most popular methods for the measurement of the fracture toughness, namely Single-Edge Notched Beam (SENB) and Vickers Indentation Fracture (VIF), require very different sample sizes, geometries, and models for the interpretation of the experimental results. VIF method assesses the indentation fracture resistance ( $K_{IFR}$ ), a value absolutely correlated [27,28] with fracture toughness ( $K_{IC}$ ), commonly referred as the same thing. This method starts with the measurement of microindentation prints, cracks lengths, and samples hardness, followed by the consideration of a specific fracture model, in which bulk values, such as hardness and elastic modulus, are required. Typically, researchers use the measured hardness value of each sample. However, they typically use the same elastic modulus for all CNT compositions, which may be an oversimplification. In order to improve the reliability of the VIF method, the use of an actual Young's modulus of each sample would be recommended.

<sup>1</sup> Based on Profs. C. Ramadas and A. R. Jadhav's suggestion, the use of the unit "Griffith" (Gf) is proposed in substitution of the awkward classical magnitude Pa·m<sup>1/2</sup>, where 1 Gf = 1 Pa·m<sup>1/2</sup>, as a tribute to the mechanical engineer Alan Arnold Griffith (1893–1963). Griffith was known in the field of fracture mechanics for his pioneering studies on the nature of stress and failure due to crack propagation in brittle materials.

In this work, the mechanical characterization of  $\alpha$ -Al<sub>2</sub>O<sub>3</sub> matrix composites with MWCNTs synthesized by the sol-gel method and structural characterization of the cracked samples is reported. Values of Vickers hardness and indentation fracture resistance, measured by VIF, and elastic modulus and hardness, obtained by nanoindentation, are shown for alumina composites with up to 5 wt% carbon content of MWCNTs. Finally, instead of using the bibliographical Young's modulus for pure alumina, the actual elastic modulus of the composites, obtained by nanoindentation, are used for the assessment indentation fracture resistance, and the classical procedure for the calculation of  $K_{IFR}$  is discussed.

## 2. Materials and methods

### 2.1. Sample synthesis and preparation

Samples were prepared following a procedure based on a report by Barrera-Solano et al. [15,21]. First, a commercial boehmite (AlOOH) sol (Nyacol Nano Technologies, Inc., density = 1.14 g/cm<sup>3</sup>) and the required amount of OH-functionalized MWCNTs (Nanostructured & Amorphous Materials, Inc., purity > 95%, inner diameter: 3–5 nm, outer diameter: 8–15 nm, length: 0.5–2  $\mu$ m, regarding the supplier, confirmed by TEM) were directly mixed. Then, the MWCNTs were dispersed into the sol with the application of high power ultrasounds (~15 min, 50 W) to achieve maximum dispersion. Once the MWCNTs bundles could not be optically distinguished, NH<sub>3</sub><sup>(aq)</sup> (Panreac, pH = 11.6) was added to the dispersion, and rapid homogeneous gelation occurred (~1–2 min), minimizing possible MWCNT aggregation during gelation. Gels were dried (40 °C, 2 days), milled in an agate mortar, and sieved (<212  $\mu$ m). Boehmite-MWCNT composite powders were calcined under an inert argon atmosphere (to prevent MWCNTs burnout) for 1 h (heating ramp: 10 °C/min) at 600 °C to promote dehydroxylation of the aluminum hydroxides and to remove moisture and other possible undesirable traces present in the as-prepared gels. Calcination at 600 °C resulted in  $\gamma$ -Al<sub>2</sub>O<sub>3</sub>, as expected from the thermal transformation sequence of aluminum hydroxides into metastable alumina polymorphs [29]. This feature was monitored by XRD and published in a specific research work and can be accessed in Ref. [15], together with more details about the synthesis procedure and additional structural characterization of the composite powders. Carbon contents of the samples were 0 (pure alumina sample, reference), 1.0, 2.0, and 5.0 wt%. With X describing the carbon content, the samples were named BSE-X. Fig. 1 illustrates the complete process.

The sintering of these powders was performed by Spark Plasma Sintering (SPS), also called Pulsed Electric Current Sintering (PECS) [30], using a Dr. Sinter Lab Inc. device (Model 515 S, Kanagawa, Japan, pulsed high DC current, 0–1500 A) at 1300 °C for 5 min with 75 MPa of constant uniaxial pressure (heating ramp: 100 °C/min, cooling ramp: 50 °C/min). These parameters have previously been successfully used for the sintering of alumina [31]. During the sintering process, shrinkage and temperature were recorded. Sintered samples were extracted from their graphite die of the SPS device, and thoroughly prepared for micro- and nanomechanical characterization following the RCEP protocol (rectifying, cutting, embedding and polishing) (0.5  $\mu$ m diamond slurry), yielding polished surfaces on which micromechanical properties can be measured. In Fig. 2, the samples are shown for the steps described above.

### 2.2. Mechanical characterization

In order to assess the presence of toughening effects due to the addition of CNTs, a proper comparison of the mechanical properties in this set of samples was performed by Vickers indentation tests. These tests were performed in a Buehler Wilson® VH1150 Micro Vickers Hardness Tester device with a load of 10 kp (98 N) and a 5 s dwell time in series of at least ten indentations for statistics. Fracture toughness,

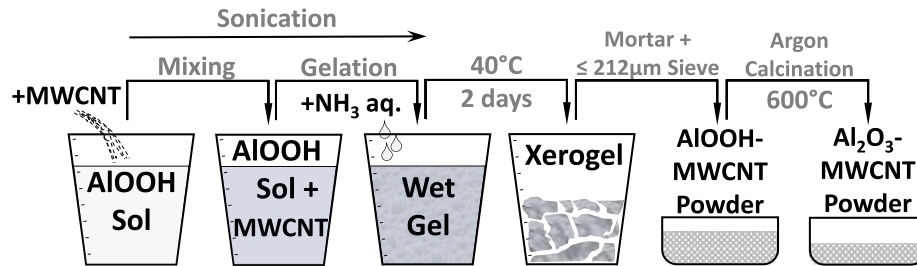


Fig. 1. The synthesis procedure of the precursor powder is summarized in this sketch. More details can be found in Ref. [15].

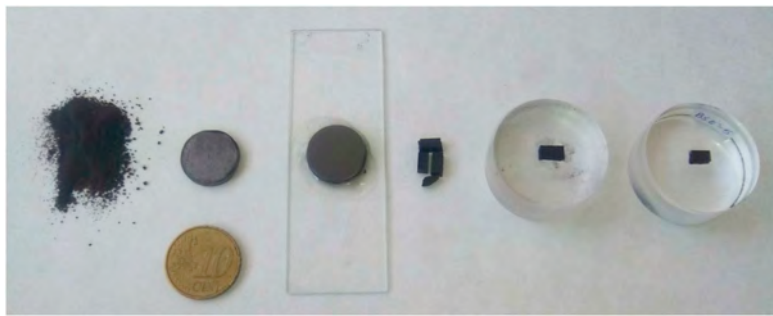


Fig. 2. Samples along the steps of the RCEP preparation protocol. From left to right: CNT-alumina powder after milling and sieving, sintered disc-shaped sample covered with graphite protective wrapping layers for SPS, rectified sample on glass sample holder, rectangular prism sample cuts, embedded sample prism in transparent thermoplastic acrylic mounting material, and polished sample ready to indentation tests. A 1.00 € coin has been used for size reference.

$K_{Ic}$ , was estimated from the indentation fracture resistance,  $K_{IFR}$ . These values were obtained by the VIF method with the help of Shetty's model for median cracks, that has been proved as the most accurate equation for alumina polycrystalline ceramics [28]:

$$K_{Ic} = 0.023 (E/H)^{1/2} P/c^{3/2} \quad (1)$$

in which  $E$  and  $H$  are the elastic modulus and hardness, respectively.  $P$  is the applied load, and  $c$  is the length of the crack from the center of the print. More details of the indentation fracture resistance calculation can be seen in Ref. [32]. The area of the indentation prints and the length of the cracks were measured by optical microscopy with a  $\times 20/0.40$  objective and a CCD camera with digital zoom. Good resolution of the optical microscopes was remarked as a major feature for reliably assessing  $K_{IFR}$  values by VIF tests [28,33]. Scanning electron microscopy (FEG-SEM, Hitachi S5200) with an acceleration voltage of 5 kV, was used to explore the nanostructure of the samples and the cracks due to indentations.

Finally, nanoindentation tests were performed with a Micromaterials Nano Test platform device, using a Berkovich diamond tip. Indentations of depths between 200 and 800 nm were performed in a series of 25 indentations for statistics, using a load/unload ramp of 2 mN/s. Load-depth curves were analyzed using the Oliver and Pharr method [34], and they were used to determine the relative elastic modulus and nanoindentation hardness.

### 3. Results and discussion

#### 3.1. Densities

The density of the synthesized sample series was measured by Archimedes' method, using 3.985 and 2.1 g/cm<sup>3</sup> as the reference theoretical bulk density for pure alumina [35] and the MWCNT content, respectively. The theoretical densities of the biphasic composites have been estimated, weighting the two densities, according to the wt.% of each phase, as shown in eq. (2):

$$\rho_{th} = \frac{\rho_1 \rho_2}{\rho_1 \frac{X}{100} + \rho_2 \left(1 - \frac{X}{100}\right)}, \quad (2)$$

where  $\rho_1$  and  $\rho_2$  are the theoretical densities of the matrix composite and the secondary phase, respectively, and  $X$  is the wt.% of secondary phase in the composite.

The complete sample series exhibited low relative densities, around 85% of theoretical density regardless the MWCNTs content (see Table 1), probably due to the use of nanosized  $\gamma$ -Al<sub>2</sub>O<sub>3</sub> as starting powder. This feature is of major relevance regarding the mechanical properties of bulk materials and should be taken into consideration when performing comparisons with other sample series. Though these relative low densities and high porosities may indicate that lower mechanical values should be expected, the influence of the presence of MWCNTs in the mechanical properties can be explored.

#### 3.2. Vickers hardness

Samples were indented with a Vickers tip at a  $P = 98$  N load (HV10). The prints were examined by optical microscopy, and the typical squared prints were revealed. Additionally, the size of the prints and the length of the cracks at the corners were measured in order to evaluate the Vickers hardness and the indentation fracture resistance, respectively. In Fig. 3, the typical print of Vickers indentations can be seen.

The values of the hardness are shown in Table 2. As seen, hardness

Table 1  
Density of samples.

Sample	MWCNTs content (wt. %)	Weighted theoretical bulk density (g/cm <sup>3</sup> )	Relative density (%)
BSE-0	0	3.985	85.0 ± 1.0
BSE-1	1	3.950	84.2 ± 2.5
BSE-2	2	3.918	86.8 ± 1.1
BSE-5	5	3.814	85.4 ± 2.2



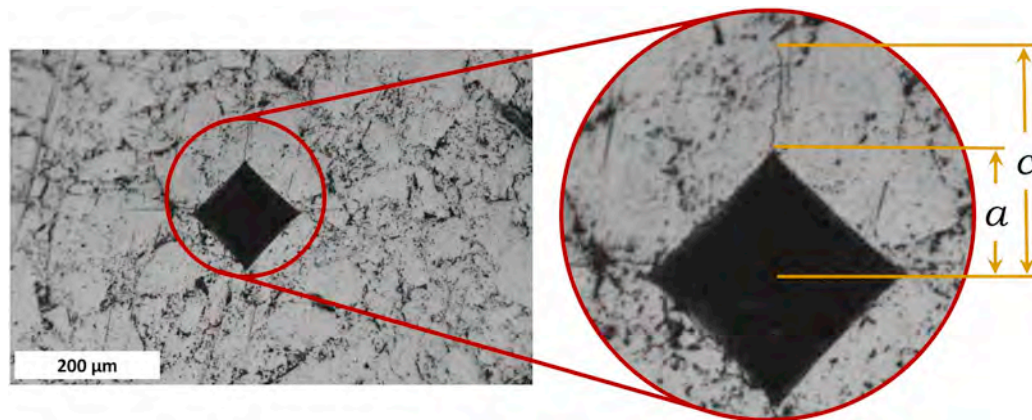


Fig. 3. Left: The optical image of typical squared Vickers indentation print and cracks emerging from print corners. Right: Magnification of indicated area is shown; crack length for  $K_{IFR}$  determination (“c”) and print diagonal (“a”) are also indicated.

values are low in comparison to typical reported values, as expected. Further, hardness is not significantly affected by the presence of the CNTs. As a reference, a pure sample of full, nearly 100% dense monolithic polycrystalline alumina exhibits a hardness between 15 and 20 GPa [4,8,25]. The decisive factor producing the low values for hardness is the lack of densification, which describes the presence of significant porosities that reduces the volume exposed to mechanical stresses. Some models correlate the porosity and the values of several mechanical properties of the porous, brittle solid ceramics [36–38]. Typically, Young's modulus, bending strength, or the hardness of alumina exhibit a drastic decrease with an increase in porosity [39,40]. Using an empirical exponential model, we are able to estimate the expected hardness of fully dense, pure alumina:

$$H = H_0 e^{-bp}, \quad (3)$$

where  $H$  is the hardness for a given porosity fraction  $p$ ,  $H_0$  is the hardness at porosity zero, and  $b$  is a material constant that should be adjusted from the study of different porosities. For the pure alumina sample described in this work,  $H = 8.1$  GPa and  $p = 15\%$ . Therefore, we can estimate that for a sample of zero porosity, the hardness  $H_0$  would be between 18.5 and 24.4 GPa, using the minimum and maximum reported values of  $b = 5.5$  [37] and  $b = 7.35$  [39], respectively. Improvements in densification are, evidently, crucial for hard composites.

### 3.3. Indentation fracture resistance

The measured values of indentation fracture resistance calculated by the VIF method and considering Shetty's formula (1) are listed in Table 2. These values are used to estimate the actual fracture toughness,  $K_{IC}$ . It is worthy to mention that in a porous material, densification under the indenter occurs, which inevitably leads to less plastic deformation and indentation residual stresses, what could invalidate

Shetty's equation. However, we are focused on the comparison of the fracture toughness between this sample series, in order to find its possible correlation with the presence of MWCNTs. As stated above, this indirect fracture toughness measurement method consists of estimating the length of the crack produced at the corner of the Vickers print for a given applied force. In this regard, post-indentation slow crack growth phenomena has been ignored, since the time dependence of the mean crack length after unloading in alumina is negligible (~1%) even one month after the indentation tests [33]. Each  $K_{IFR}$  value resulted from the average of at least ten indentations. In Shetty's formula (1), the considered values of hardness and crack length are those obtained by Vickers tests. On the contrary, the elastic modulus,  $E$ , has been taken from sources [35,41]; for fully dense monolithic alumina,  $E \approx 400$  GPa. Given that the actual Young's modulus should be measured for each individual sample in order to perform a rigorous use of the crack model, this is a questionable practice commonly found in many works. Furthermore, the porosity and/or composition may be crucial parameters affecting the value of  $E$  [41].

As a general consideration, there is no change on this parameter with the addition of the CNTs. Nevertheless, though densities from this set of samples are below 90%, the values of fracture toughness are comparable to the values reported in the literature for these CNTs contents, typically ranging from 3 to 7 MGf [7,42]. This set of results invokes contradictory ideas. On one hand, it may suggest that, given the direct dependence of  $K_{IC}$  versus density [13], improvements in the fabrication procedures that lead to fully dense samples will involve significantly higher fracture toughness values, as expected. On the other hand, however, these values may be also affected by two artifacts: the presence of significant low hardness ( $H$ ) values in the denominator, due, principally, to low densities, and the high elastic modulus ( $E$ ) of pure alumina artificially used in the numerator.

Table 2  
Mechanical values of the sample series.

Sample	MWCNTs content (wt. %)	Vickers Hardness (GPa)	c/a	Indentation Fracture Resistance <sup>a</sup> (MGf)	Young's modulus (GPa)	Nanoindentation Hardness (GPa)	Indentation Fracture Resistance <sup>b</sup> (MGf)
BSE-0	0	8.1 ± 0.5	2.22 ± 0.13	7.4 ± 0.7	121 ± 12	10 ± 2	4.1 ± 0.4
BSE-1	1	7.4 ± 0.6	2.31 ± 0.15	6.8 ± 0.7	171 ± 19	11 ± 3	4.5 ± 0.4
BSE-2	2	7.9 ± 0.8	2.35 ± 0.13	6.8 ± 0.5	161 ± 32	9 ± 4	4.3 ± 0.3
BSE-5	5	7.4 ± 0.5	2.26 ± 0.15	7.1 ± 0.6	260 ± 97	16 ± 6	5.7 ± 0.5

<sup>a</sup> Calculated with Shetty's equation and pure alumina  $E = 400$  GPa for all samples.

<sup>b</sup> Calculated with Shetty's equation and the corresponding measured  $E$  from nanoindentation tests.

### 3.4. Nanoindentation

Nanoindentation, in which hardness and elastic modulus are measured simultaneously, is being considered for the mechanical characterization and the measurement of the fracture toughness of the samples [14,43,44]. In this work, the mechanical properties of the CMCs were also explored by this technique. During the tests, the indentations penetrated between 200 and 800 nm. Considering the porosity shown in Table 1, it is reasonable to think that the indentations have been performed on a surface with pores similar to the tip size, being relatively easy to indent in a pore or bulk material. Nevertheless, this technique has been validated for a large variety of materials, including ultra-porous materials, such as hybrid silica aerogels [45]. Thus, in order to thoroughly assess the properties of the sample, the tests were performed in a repeated series of 25 indentations for statistics.

During an indentation, the total displacement of the tip is the addition of matrix and indenter deformation, so the relative elastic modulus,  $E_r$ , is given by

$$\frac{1}{E_r} = \frac{1 - \nu_i^2}{E_i} + \frac{1 - \nu^2}{E}, \quad (4)$$

where  $\nu_i$  and  $\nu$  are the Poisson's ratios, and  $E_i$  and  $E$  are the elastic moduli of the indenter and sample, respectively. The tip is made of diamond, with  $\nu_i = 0.07$  and  $E_i = 1140$  GPa, and we are working with alumina samples, which have an estimated Poisson ratio of  $\nu \sim 0.20$  for 15% porosity ( $\nu \sim 0.24$  for the best case of fully dense alumina) [41]. These values allow us to roughly ignore the term of the indenter in (4), and assume that  $1 - \nu^2 \approx 1$ . That is, we can consider  $E \approx E_r$ . For more accurate calculations, for example, only considering that  $\nu_i^2 \ll 1$  and retaining  $\nu = 0.20$ , we find that  $E \approx 1.48 \cdot E_r$ , for  $E_r = 400$  GPa, or  $E \approx 1.05 \cdot E_r$ , for  $E_r = 100$  GPa. This is an obvious result: when the elastic modulus of the tested material is a non-negligible fraction of the indenter's elastic modulus, the deviation between  $E_r$  and  $E$  should not be ignored.

As shown in Table 2 and Fig. 4, the hardness values observed by nanoindentation are higher than those obtained by Vickers tests in all cases. The principal cause of this discrepancy between the values may be due to the applied load, which involves very different indentation depths, known as indentation size effect [46]: the lower the load, the smaller the print, the higher the hardness. This effect is something that must be taken into serious consideration when comparing different studies. On the other hand, the relative elastic modulus presents an increasing trend with the carbon content, as it has been stated [14].

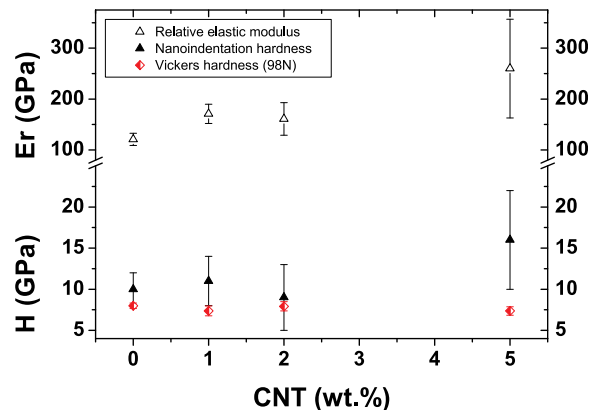


Fig. 4. Relative elastic modulus ( $E_r$ ) and Hardness ( $H$ ) obtained by Berkovich nanoindentations. Vickers Hardness HV10 data from Table 2 is also represented for comparison. Error bars are one standard deviation.

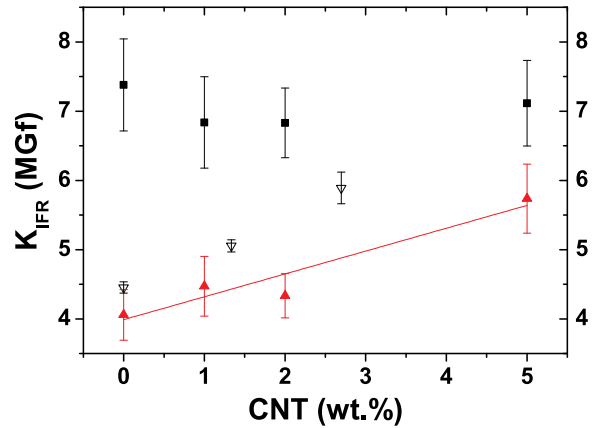


Fig. 5. Indentation fracture resistance values of the alumina-based composites with different MWCNT contents, calculated with Shetty's equation using Young's modulus from bibliography (■) and obtained from nanoindentation tests (▲). The straight line shown is only a visual guide. Values are averaged from at least 10 indentations. Corrected data from Satam et al. [14] is also included (▼). Error bars are one standard deviation in all cases.

### 3.5. Indentation fracture resistance recalculated

As explained in the introduction section, the indentation fracture resistance of alumina-based CMCs is classically obtained by the VIF method, considering Young's modulus of the pure alumina from the literature instead of the actual CMC's modulus. Reliable and representative values of  $K_{Ic}$  are desirable to explore the bulk elastic modulus for each composite. Among the many different procedures to obtain Young's modulus, in this study, we have measured this value for each sample by the nanoindentation technique (see Table 2). Thus, despite the possible controversy due to the different length scales at which the different parameters involved in the calculation are measured, namely hardness ( $H$ ) at the micrometer scale and  $E$  at the nanometer scale, it is feasible to calculate the indentation fracture resistance of samples, obtaining the values shown in Table 2 and Fig. 5.

An increasing behavior of the fracture toughness with the MWCNT concentration has been found using this technique combining a sol-gel route and SPS. Despite the obviously lower values compared to those obtained with a constant  $E = 400$  GPa, the pure alumina  $K_{IFR}$  result is more realistic and closer to the previously reported values for alumina using several measurement methods [28]. Another study on MWCNT-reinforced alumina, which was obtained by sol-gel method and published by Satam et al. [14], also reported increasing values of indentation fracture resistance calculated with Young's modulus from nanoindentation tests (see Fig. 5). Satam et al. used Anstis' formula for the evaluation of indentation fracture resistance, so we have corrected those values using Shetty's expression for a proper comparison of results. This consistency in improving the indentation fracture resistance with the inclusion of carbon allotropes through the sol-gel procedure supports this technique as a promising route for the exploitation of this reinforcing strategy.

### 3.6. Microstructure exploration

The analyses of the cracks in the samples by electron microscopy revealed very interesting features. At first sight, the presence of grey dots in the polished surface (see Fig. 6) proves the high porosity mentioned previously, confirmed by the low densities (Table 1). Besides, a good degree of homogenization was observed as the presence of individual CNTs was easily verified, but it should be mentioned that MWCNT bundles were also found, indicating the necessity of improved

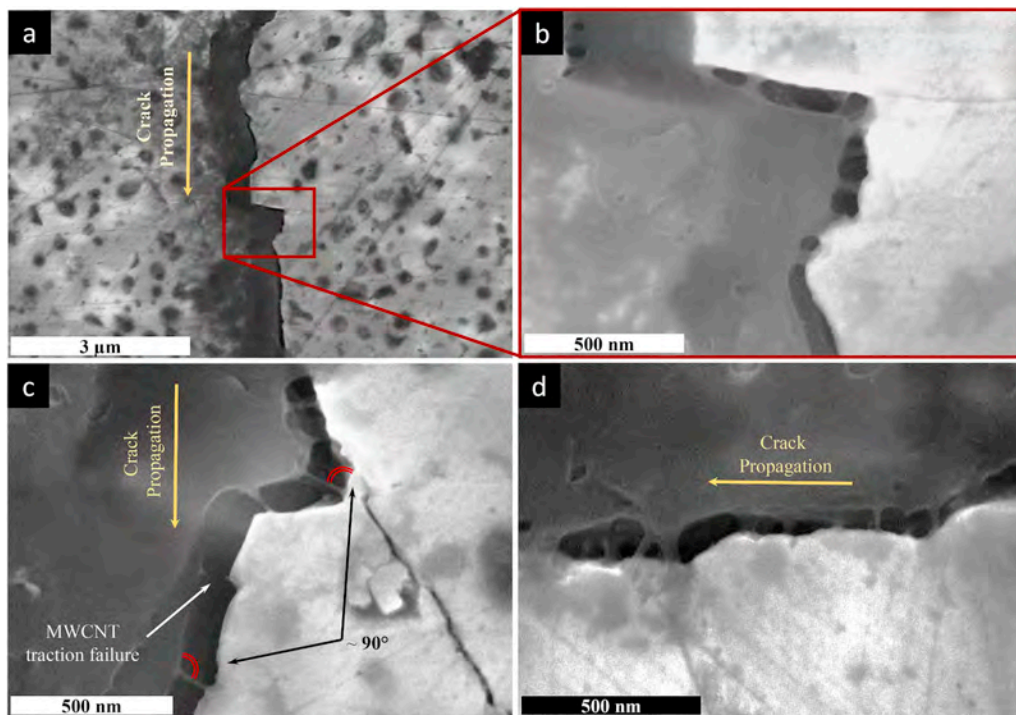


**Fig. 6.** SEM micrographs of different cracks produced during Vickers indentations. **a** shows evident porosity of samples. In **b**, **c**, and **d** pulled-out MWCNTs bridging both sides of the running crack are observed, revealing crack-bridging as a mechanism hindering crack propagation. In **c** and **d**, partial reorientation of MWCNTs perpendicular to the crack sides can be seen and is highlighted by the curved, red double lines. In **c**, tensile-stressed MWCNT failure is shown by the white arrow. (For interpretation of the references to colour in this figure legend, the reader is referred to the Web version of this article.)

sample dispersion. Therefore, developing a tool for real time measurement and quantification of the quality of CNT dispersions during sample preparation is of paramount relevance, especially before and after gelation. This will ensure perfect dispersion and the absence of coils and bundles that will eventually act as defects at the macroscopic scale, affecting densification or fracture toughness.

However, the most startling feature is how intragranular CNTs were clearly seen in fracture surfaces emerging from the bulk samples (Fig. 6). One goal of this kind of strategy for reinforcing composites fabrication is the transfer of tensile loads from the ceramic matrix to the MWCNTs. The toughening mechanisms that may appear, especially in intragranular CMCs, are mainly crack-bridging and crack-deflection [13]. These mechanisms can be found easily in our samples by looking along the cracks produced during the Vickers test, as shown in Fig. 6. MWCNTs are acting as reinforcement bridges, “sewing” both sides of the cracks, forcing the deflection of crack propagation (Fig. 6a and b), and eventually, failing (Fig. 6c), where a significant amount of the crack propagation energy would be released. This is the mentioned crack-bridging effect, and it would be eventually present in the composite response to the fracture propagation independently of the fracture mode. The presence of these toughening phenomena explain the increase of the recalculated indentation fracture resistance (section 3.4) of the samples with nanotubes. Another remarkable fact is that all CNTs found in the cracks seem to be almost perpendicular to the crack propagation direction due to the reorientation of exposed segments of MWCNTs, as indicated in the micrographs in Fig. 6 and sketched in Fig. 7.

#### 4. Conclusions

Sample preparation needs urgent revision to improve the density

and to adequately incorporate the MWCNTs within the ceramic matrix in order to obtain the highest mechanical values. The measurement of every parameter present on an indentation fracture resistance equation is also vital for a realistic comparison, even with samples of the same series. Though typical values of the indentation fracture resistance calculated with the classical Young's modulus of pure alumina from the literature are higher for all samples, the recalculated indentation fracture resistance reveals an increasing behavior when considering the actual elastic moduli of samples, obtained in this case by nanoindentation. Microstructural inspection by SEM reveals the presence of new toughening phenomena such as crack bridging and crack deflection. These mechanisms transfer tensile loads from alumina matrix to the reinforcement nanophase during the propagation of the cracks, which explain the increasing behavior of recalculated  $K_{IR}$  with MWCNT content.

#### Compliance with ethical standards

##### Conflict of interest

The authors declare that they have no conflict of interest.

##### Declaration of competing interest

The authors declare that they have no known competing financial interests or personal relationships that could have appeared to influence the work reported in this paper.

## Chapter 4. Mechanical characterization of sol-gel alumina-based ceramics with intragranular reinforcement of multiwalled carbon nanotubes

P. Rivero-Antúnez, et al.

Ceramics International 46 (2020) 19723–19730

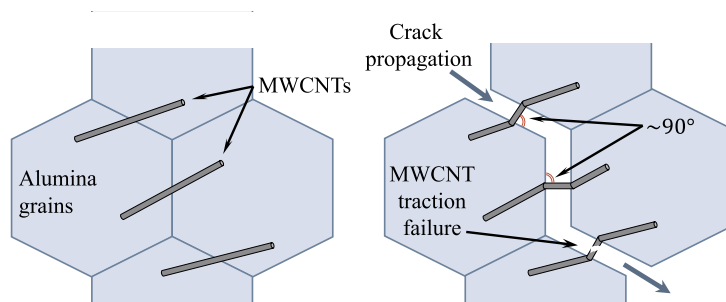


Fig. 7. This sketch highlights partial reorientation and traction failure of CNTs along crack propagation between grains. Only intergranular fracture mode has been sketched, but the same idea is also proposed for intragranular cracks.

### Acknowledgements

Project PGC2018-094952-B-I00 financed by FEDER/Ministerio de Ciencia e Innovación - Agencia Estatal de Investigación and project P12-FQM-1079 from Junta de Andalucía and funding support to FQM393 from Junta de Andalucía are acknowledged. V. M-F. thanks the grant from V Plan Propio de Investigación de la Universidad de Sevilla. P. R-A acknowledge European Social Fund, Empleo Juvenil European Plan and project PGC2018-094952-B-I00 from FEDER/Ministerio de Ciencia e Innovación - Agencia Estatal de Investigación. The help from the technical staff from the CITIUS is acknowledged. The authors would like to thank the work by the National Institutes of Health, USA for the development of the *ImageJ* <https://imagej.nih.gov/ij/software>. Comercial Química Massó is also acknowledged for supplying the boehmite precursor Nyacol®.

### References

- [1] J.N. Coleman, U. Khan, W.J. Blau, Y.K. Gun'ko, Small but strong: a review of the mechanical properties of carbon nanotube-polymer composites, *Carbon N. Y.* 44 (2006) 1624–1652, <https://doi.org/10.1016/j.carbon.2006.02.038>.
- [2] E. Zapata-Solvas, D. Gómez-García, A. Domínguez-Rodríguez, On the microstructure of single wall carbon nanotubes reinforced ceramic matrix composites, *J. Mater. Sci.* 45 (2010) 2258–2263, <https://doi.org/10.1007/s10853-009-4126-z>.
- [3] I. Ahmad, B. Yazdani, Y. Zhu, Recent advances on carbon nanotubes and graphene reinforced ceramics nanocomposites, *Nanomaterials* 5 (2014) 90–114, <https://doi.org/10.3390/nano501090>.
- [4] I. Ahmad, H. Cao, H. Chen, H. Zhao, A. Kennedy, Y.Q. Zhu, Carbon nanotube toughened aluminium oxide nanocomposite, *J. Eur. Ceram. Soc.* 30 (2010) 865–873, <https://doi.org/10.1016/j.jeurceramsoc.2009.09.032>.
- [5] K.S. Lee, B.K. Jang, Y. Sakka, Damage and wear resistance of Al<sub>2</sub>O<sub>3</sub>-CNT nanocomposites fabricated by spark plasma sintering, *J. Ceram. Soc. Japan.* 121 (2013) 867–872, <https://doi.org/10.2109/jcersj2.121.867>.
- [6] G. Yamamoto, M. Omori, K. Yokomizo, T. Hashida, K. Adachi, Structural characterization and frictional properties of carbon nanotube/alumina composites prepared by precursor method, *Mater. Sci. Eng. B Solid-State Mater. Adv. Technol.* 148 (2008) 265–269, <https://doi.org/10.1016/j.mseb.2007.09.013>.
- [7] K. Lee, C.B. Mo, S.B. Park, S.H. Hong, Mechanical and electrical properties of multiwalled CNT-alumina nanocomposites prepared by a sequential two-step processing of ultrasonic spray pyrolysis and spark plasma sintering, *J. Am. Ceram. Soc.* 94 (2011) 3774–3779, <https://doi.org/10.1111/j.1551-2916.2011.04689.x>.
- [8] M.H. Bocanegra-Bernal, C. Domínguez-Ríos, J. Echeberria, A. Reyes-Rojas, A. García-Reyes, A. Aguilar-Elguezabal, Spark plasma sintering of multi-, single- and double-walled carbon nanotube-reinforced alumina composites: is it justifiable the effort to reinforce them? *Ceram. Int.* 42 (2016) 2054–2062, <https://doi.org/10.1016/j.ceramint.2015.09.060>.
- [9] C.B. Mo, S.I. Cha, K.T. Kim, K.H. Lee, S.H. Hong, Fabrication of carbon nanotube reinforced alumina matrix nanocomposite by sol-gel process, *Mater. Sci. Eng.* 395 (2005) 124–128, <https://doi.org/10.1016/j.msea.2004.12.031>.
- [10] G. Yamamoto, T. Hashi, Carbon nanotube reinforced alumina composite materials, *Compos. Their Prop. InTech*, 2012, <https://doi.org/10.5772/48667>.
- [11] F.J. Torres-Canas, C. Blanc, C. Zamora-Ledezma, P. Silva, E. Anglaret, Dispersion and individualization of SWNT in surfactant-free suspensions and composites of hydro-soluble polymers, *J. Phys. Chem. C* 119 (2015) 703–709, <https://doi.org/10.1021/jp5092015>.
- [12] Q. Chen, C. Saliel, S. Manickavasagam, L.S. Schadler, R.W. Siegel, H. Yang, Aggregation behavior of single-walled carbon nanotubes in dilute aqueous suspension, *J. Colloid Interface Sci.* 280 (2004) 91–97, <https://doi.org/10.1016/j.jcis.2004.07.028>.

- [13] G.D. Zhan, J.D. Kuntz, J. Wan, A.K. Mukherjee, Single-wall carbon nanotubes as attractive toughening agents in alumina-based nanocomposites, *Nat. Mater.* 2 (2003) 38–42, <https://doi.org/10.1038/nmat793>.
- [14] M.K. Satam, L. Gurnani, S. Vishwanath, A. Mukhopadhyay, Development of carbon nanotube reinforced bulk polycrystalline ceramics with intragranular carbon nanotube reinforcement, *J. Am. Ceram. Soc.* 99 (2016) 2905–2908, <https://doi.org/10.1111/jace.14425>.
- [15] L. Esquivias, P. Rivero-Antúnez, C. Zamora-Ledezma, A. Domínguez-Rodríguez, V. Morales-Flórez, Intragranular carbon nanotubes in alumina-based composites for reinforced ceramics, *J. Sol. Gel Sci. Technol.* 90 (2019) 162–171, <https://doi.org/10.1007/s10971-018-4834-4>.
- [16] J. Sun, L. Gao, M. Iwasa, T. Nakayama, K. Niihara, Failure investigation of carbon nanotube/3Y-TZP nanocomposites, *Ceram. Int.* 31 (2005) 1131–1134, <https://doi.org/10.1016/j.ceramint.2004.11.010>.
- [17] T.A. Saleh, V.K. Gupta, Characterization of the chemical bonding between Al<sub>2</sub>O<sub>3</sub> and nanotube in MWCNT/Al<sub>2</sub>O<sub>3</sub> nanocomposite, *Curr. Nanosci.* 8 (2012) 739–743, <https://doi.org/10.2174/157341312802884418>.
- [18] J. Yi, W. Xue, T. Wang, Z. Xie, Mechanical and electrical properties of chemically modified MWCNTs/3Y-TZP composites, *Ceram. Int.* 41 (2015) 9157–9162, <https://doi.org/10.1016/j.ceramint.2015.03.008>.
- [19] G. Bepete, E. Anglaret, L. Ortolani, V. Morandi, K. Huang, A. Pénicaud, C. Drummond, Surfactant-free single-layer graphene in water, *Nat. Chem.* 9 (2017) 347–352, <https://doi.org/10.1038/nchem.2669>.
- [20] B.E. Yoldas, A transparent porous alumina, *Ceram. Bull.* 54 (1975) 289–290 <https://ci.nii.ac.jp/naid/10030764894/>, Accessed date: 20 June 2018.
- [21] C. Barrera-Solano, L. Esquivias, G.L. Messing, Effect of preparation conditions on phase formation, densification, and microstructure evolution in La-β-Al<sub>2</sub>O<sub>3</sub>/Al<sub>2</sub>O<sub>3</sub> composites, *J. Am. Ceram. Soc.* 82 (1999) 1318–1324, <https://doi.org/10.1111/j.1151-2916.1999.tb01914.x>.
- [22] M. Piñero, M.M. Mesa-Díaz, D. de los Santos, M.V. Reyes-Peces, J.A. Díaz-Fraile, N. de la Rosa-Fox, L. Esquivias, V. Morales-Flórez, Reinforced silica-carbon nanotube monolithic aerogels synthesised by rapid controlled gelation, *J. Sol. Gel Sci. Technol.* 86 (2018) 391–399, <https://doi.org/10.1007/s10971-018-4645-7>.
- [23] S.R. Inbaraj, R.M. Francis, N.V. Jaya, A. Kumar, Processing and properties of sol gel derived alumina-carbon nano tube composites, *Ceram. Int.* 38 (2012) 4065–4074, <https://doi.org/10.1016/j.ceramint.2012.01.064>.
- [24] G.-D. Zhan, A.K. Mukherjee, Carbon nanotube reinforced alumina-based ceramics with novel mechanical, electrical, and thermal properties, *Int. J. Appl. Ceram. Technol.* 1 (2005) 161–171, <https://doi.org/10.1111/j.1744-7402.2004.tb00166.x>.
- [25] M. Michálek, K. Boďišová, M. Micháľková, J. Sedláček, D. Galusek, Alumina/MWCNTs composites by aqueous slip casting and pressureless sintering, *Ceram. Int.* 39 (2013) 6543–6550, <https://doi.org/10.1016/j.ceramint.2013.01.087>.
- [26] J. Sun, L. Gao, X. Jin, Reinforcement of alumina matrix with multi-walled carbon nanotubes, *Ceram. Int.* 31 (2005) 893–896, <https://doi.org/10.1016/j.ceramint.2004.10.002>.
- [27] H. Miyazaki, Y.I. Yoshizawa, Correlation of the indentation fracture resistance measured using high-resolution optics and the fracture toughness obtained by the single edge-notched beam (SEPB) method for typical structural ceramics with various microstructures, *Ceram. Int.* 42 (2016) 7873–7876, <https://doi.org/10.1016/j.ceramint.2016.01.116>.
- [28] H. Miyazaki, Y. Yoshizawa, A reinvestigation of the validity of the indentation fracture (IF) method as applied to ceramics, *J. Eur. Ceram. Soc.* 37 (2017) 4437–4441, <https://doi.org/10.1016/j.jeurceramsoc.2017.07.027>.
- [29] P. Souza Santos, H. Souza Santos, S.P. Toledo, Standard transition aluminas. Electron microscopy studies, *Mater. Res.* 3 (2000) 104–114, <https://doi.org/10.1590/s1516-14392000000400003>.
- [30] K.Q. Dang, M. Kawahara, S. Takei, M. Nanko, Effects of pulsed current waveforms on sample temperature and sintering behavior in PECS of alumina, *J. Jpn. Soc. Powder Powder Metall.* 56 (2009) 780–787, <https://doi.org/10.2497/jjspm.56.780>.
- [31] R. Cano-Crespo, B. Malmal Moshtaghion, D. Gómez-García, A. Domínguez-Rodríguez, R. Moreno, High-temperature creep of carbon nanofiber-reinforced and graphene oxide-reinforced alumina composites sintered by spark plasma sintering,

- Ceram. Int. 43 (2017) 7136–7141, <https://doi.org/10.1016/j.ceramint.2017.02.146>.
- [32] D.K. Shetty, A.R. Rosenfield, W. Duckworth, Analysis of indentation crack as a wedge-loaded half-penny crack, *J. Am. Ceram. Soc.* 68 (1985) C-65–C-67, <https://doi.org/10.1111/j.1151-2916.1985.tb15288.x>.
- [33] H. Miyazaki, Y.I. Yoshizawa, Refined measurements of indentation fracture resistance of alumina using powerful optical microscopy, *Ceram. Int.* 40 (2014) 2777–2783, <https://doi.org/10.1016/j.ceramint.2013.10.039>.
- [34] W.C. Oliver, G.M. Pharr, An improved technique for determining hardness and elastic modulus using load and displacement sensing indentation experiments, *J. Mater. Res.* 7 (1992) 1564–1583, <https://doi.org/10.1557/JMR.1992.1564>.
- [35] F. Cardarelli, *Materials Handbook*, second ed., Springer London, London, 2008, <https://doi.org/10.1007/978-1-84628-669-8>.
- [36] V.R. Salvini, V.C. Pandolfelli, D. Spinelli, Mechanical properties of porous ceramics, *Recent Adv. Porous Ceram*, IntechOpen, 2018, pp. 171–199, <https://doi.org/10.5772/57353>.
- [37] R.W. Rice, Comparison of physical property-porosity behaviour with minimum solid area models, *J. Mater. Sci.* 31 (1996) 1509–1528, <https://doi.org/10.1007/BF00357860>.
- [38] K.K. Phani, S.K. Niyogi, Young's modulus of porous brittle solids, *J. Mater. Sci.* 22 (1987) 257–263, <https://doi.org/10.1007/BF01160581>.
- [39] N. Miyazaki, T. Hoshide, Influence of porosity and pore distributions on strength properties of porous alumina, *J. Mater. Eng. Perform.* 27 (2018) 4345–4354, <https://doi.org/10.1007/s11665-018-3500-x>.
- [40] R.M. Spriggs, Expression for effect of porosity on elastic modulus of polycrystalline refractory materials, particularly aluminum oxide, *J. Am. Ceram. Soc.* 44 (1961) 628–629, <https://doi.org/10.1111/j.1151-2916.1961.tb11671.x>.
- [41] M. Asmani, C. Kermel, A. Leriche, M. Ourak, Influence of porosity on Young's modulus and Poisson's ratio in alumina ceramics, *J. Eur. Ceram. Soc.* 21 (2001) 1081–1086, [https://doi.org/10.1016/S0955-2219\(00\)00314-9](https://doi.org/10.1016/S0955-2219(00)00314-9).
- [42] M.H. Bocanegra-Bernal, J. Echeberria, J. Ollo, A. Garcia-Reyes, C. Domínguez-Ríos, A. Reyes-Rojas, A. Aguilar-Elguezabal, A comparison of the effects of multi-wall and single-wall carbon nanotube additions on the properties of zirconia toughened alumina composites, *Carbon N. Y.* 49 (2011) 1599–1607, <https://doi.org/10.1016/j.carbon.2010.12.042>.
- [43] L. Melk, J.J. Roa Rovira, F. García-Marro, M.L. Antti, B. Milsom, M.J. Reece, M. Anglada, Nanoindentation and fracture toughness of nanostructured zirconia/multi-walled carbon nanotube composites, *Ceram. Int.* 41 (2015) 2453–2461, <https://doi.org/10.1016/j.ceramint.2014.10.060>.
- [44] M. Sebastiani, K.E. Johanns, E.G. Herbert, G.M. Pharr, Measurement of fracture toughness by nanoindentation methods: recent advances and future challenges, *Curr. Opin. Solid State Mater. Sci.* 19 (2015) 324–333, <https://doi.org/10.1016/j.cossms.2015.04.003>.
- [45] N. de la Rosa-Fox, V. Morales-Flórez, J.A. Toledo-Fernández, M. Piñero, R. Mendoza-Serna, L. Esquivias, Nanoindentation on hybrid organic/inorganic silica aerogels, *J. Eur. Ceram. Soc.* 27 (2007) 3311–3316, <https://doi.org/10.1016/j.jeurceramsoc.2007.02.209>.
- [46] S.J. Bull, T.F. Page, E.H. Yoffe, An explanation of the indentation size effect in ceramics, *Phil. Mag. Lett.* 59 (1989) 281–288, <https://doi.org/10.1080/09500838908206356>.

## Chapter 5

# Reactive SPS for sol–gel alumina samples: Structure, sintering behavior, and mechanical properties

Given the densification problems observed during the sintering of alumina/CNTs composite powders, the research was focused on the sintering of alumina powders obtained via sol-gel. Thus, forgetting about the inclusion of carbonaceous second phases, this chapter is solely devoted to studying the reactive SPS sintering dynamics of pure alumina and its structural and mechanical characterization.

The original idea, as described in previous chapters, is that after obtaining a composite powder of boehmite and graphene or CNTs, it should undergo a thermal treatment to remove the OH groups from boehmite and transform it into alumina, preferably  $\alpha$ -alumina. However, it is observed that this pre-calcination step is counterproductive: as boehmite slowly transforms into alumina, it goes through various meta-stable intermediate phases, such as  $\gamma$ -alumina, resulting in very coarse and packed  $\alpha$ -alumina powders with a vermicular structure that inhibits proper densification during subsequent sintering. Hence, this article studies, for the first

---

time in detail, the benefits of directly subjecting boehmite to the reactive-SPS sintering process.



Contents lists available at ScienceDirect

Journal of the European Ceramic Society

journal homepage: [www.elsevier.com/locate/jeurceramsoc](http://www.elsevier.com/locate/jeurceramsoc)



## Reactive SPS for sol-gel alumina samples: Structure, sintering behavior, and mechanical properties

Pedro Rivero-Antúnez<sup>a,b</sup>, Rafael Cano-Crespo<sup>a</sup>, Florentino Sánchez-Bajo<sup>c</sup>, Arturo Domínguez-Rodríguez<sup>a</sup>, Víctor Morales-Flórez<sup>a,b,\*</sup>

<sup>a</sup> Departamento de Física de la Materia Condensada, Universidad de Sevilla, 41012, Sevilla, Spain

<sup>b</sup> Instituto de Ciencia de Materiales de Sevilla, Centro Mixto CSIC-Universidad de Sevilla, 41092 Sevilla, Spain

<sup>c</sup> Departamento de Física Aplicada, Escuela de Ingenierías Industriales, Universidad de Extremadura, Avda de Elvas s/n, 06006 Badajoz, Spain

### ARTICLE INFO

#### Keywords:

Reactive SPS sintering  
 $\alpha$ -Al<sub>2</sub>O<sub>3</sub>  
Boehmite  
Fracture toughness  
Vickers hardness

### ABSTRACT

This work presents a fast and direct controlled routine for the fabrication of fully dense alumina based on the reactive spark plasma sintering (reactive-SPS) of boehmite ( $\gamma$ -AlOOH) nano-powders obtained by the sol-gel technique. The evolution of the transition aluminas during sintering has been studied. Some boehmite powders were seeded with  $\alpha$ -Al<sub>2</sub>O<sub>3</sub> particles prior to the gelation. Boehmite seeded powders exhibited a direct transition to  $\alpha$ -Al<sub>2</sub>O<sub>3</sub> at 1070 °C, enhancing the transformation kinetics and lowering the required temperature by more than 100 °C. For comparison, other samples were prepared by previously annealing the seeded and unseeded boehmite powders. Thus,  $\alpha$ -Al<sub>2</sub>O<sub>3</sub> powders were obtained and were sintered by standard-SPS. A detailed structural and mechanical characterization is presented, comparing the hardness and indentation fracture resistance for different grain sizes and porosities. Both the reactive-SPSed samples and the standard-SPSed samples showed a high hardness (18–20 GPa), whereas the reactive-SPSed samples exhibited a lower indentation fracture resistance due to a large grain size (~10  $\mu$ m). Improvements of this procedure for obtaining smaller grain size are discussed. In summary, the presented technique brings a revolutionary fast method for the fabrication of fully dense alumina, as this process reduces the time and temperature required for alumina densification.

### 1. Introduction

The fabrication of ceramic matrix composites reinforced by the inclusion of carbon allotropes has been hindered by severe synthesis difficulties such as the proper dispersion of the reinforcing agents. With the purpose of finding the best route for the homogeneous inclusion of carbon allotropes, such as carbon nanotubes, or graphene nanoplatelets inside alumina matrix composites, and to achieve a significant increase of the fracture toughness of the material, the sol-gel route based on aluminum alkoxides or hydroxides, such as boehmite ( $\gamma$ -AlOOH), has been considered a promising procedure [1–3]. The sol-gel method allows the dispersion of the secondary phase in a large liquid volume, the starting sol, where the use of techniques such as the addition of surfactants or the application of ultrasound dissociates the CNTs bundles or GNP agglomerations. Then, the rapid controlled gelation [4] leads to the

formation of a solid network and avoids the re-aggregation of the dispersed carbon allotropes. At the same time, the sol-gel method might promote the intragranular location of the nanotubes inside the alumina grains [1,2,5,6].

It has been verified that a previous annealing of boehmite powders at 600 °C transforms boehmite into  $\gamma$ -Al<sub>2</sub>O<sub>3</sub> (see Fig. 1), and the introduction of  $\gamma$ -Al<sub>2</sub>O<sub>3</sub> (theoretical density = 3.65 g/cm<sup>3</sup> [7]) powders into the SPS inhibited the correct densification during the subsequent spark plasma sintering (SPS) [3], even though the conditions were sufficient for sintering commercial  $\alpha$ -Al<sub>2</sub>O<sub>3</sub> powders [8–10]. Nevertheless, those results have motivated the research of an optimized way for sintering fully dense alumina samples from boehmite nanopowders. A potential way to achieve 100% dense samples is to increase the temperature of the previous annealing to 1200 °C, which ensures the total transformation of boehmite into  $\alpha$ -Al<sub>2</sub>O<sub>3</sub>, with the consequent benefits for the later

\* Corresponding author at: Department of Condensed-Matter Physics, University of Seville, P.O. 1065, 41080 Seville, Spain.

E-mail addresses: [privero@us.es](mailto:privero@us.es) (P. Rivero-Antúnez), [racacres@us.es](mailto:racacres@us.es) (R. Cano-Crespo), [fsanbajo@unex.es](mailto:fsanbajo@unex.es) (F. Sánchez-Bajo), [adorod@us.es](mailto:adorod@us.es) (A. Domínguez-Rodríguez), [vmorales@us.es](mailto:vmorales@us.es) (V. Morales-Flórez).

URL: <http://grupo.us.es/fqm393/> (V. Morales-Flórez).

<https://doi.org/10.1016/j.jeurceramsoc.2021.04.060>

Received 30 December 2020; Received in revised form 1 April 2021; Accepted 30 April 2021

Available online 5 May 2021

0955-2219/© 2021 The Author(s).

Published by Elsevier Ltd.

This is an open access article under the CC BY-NC-ND license

<http://creativecommons.org/licenses/by-nc-nd/4.0/>



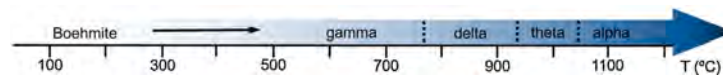


Fig. 1. Evolution of metastable alumina polymorphs (also known as transition aluminas) from boehmite ( $\gamma$ -aluminum oxyhydroxide). Based on data from Ref. [12].

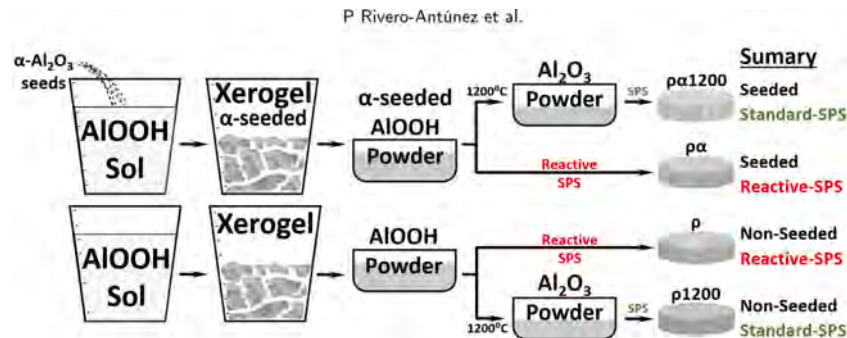


Fig. 2. Sketch summarizing the path followed for each sample. In the last column, the details of each of the four types of samples considered in this work are listed.

sintering. However, one of the major features of SPS is its ability for a fast densification of the sample versus conventional methods like hot pressing, or pressureless sintering, which require several hours for the total densification of ceramics. Given the costs of time and resources involved in the calcination of boehmite powders at 1200 °C for obtaining  $\alpha$ - $\text{Al}_2\text{O}_3$  powders, the suggestion of the direct sintering of boehmite without the previous annealing step is a remarkably captivating idea. In addition, the particle size of the boehmite precursor powders is known to be below 10 nm which may enhance the compaction of the powders and promote a small grain size of the final alumina. According to Prof. J. A. Hedvall's studies on solid-state chemistry [11] published in 1938, this kind of sintering is known as reactive sintering, based on the enhanced reactivity of solids during their decomposition or phase transformation.

Boehmite is an aluminium oxyhydroxide, one of the polymorphs of monohydrated aluminas ( $\text{Al}_2\text{O}_3 \cdot \text{H}_2\text{O}$ ). Boehmite presents an orthorhombic structure of layered deformed octahedra with the aluminum ion close to its center, where the  $[\text{AlO}_6^-]$  octahedra share one edge and the hydroxyl ions hold the layers by hydrogen bonds. Its theoretical density is 3.01 g/cm<sup>3</sup> [13]. The dehydroxylation reaction of boehmite yields alumina and water:



Taking advantage of this reaction, other authors have tried the reactive-sintering route before to obtain dense alumina, but usually with other more time-consuming sintering procedures, such as hot pressing [14–17], cold-pressing [18,19], or pressureless sintering [20]. Using the reactive-SPS procedure has only been tried once before, by Zaman et al. [21], at 1600 °C, a much higher temperature than the one used in the present work. Despite obtaining high density alumina, their work did not highlight the concept of the reactive sintering route based on the SPS technique (reactive-SPS) as an encouraging feature for efficient sintering of dense alumina.

In this work, we explore the performance of a new reactive-SPS route in which the reaction and full densification occur together at lower temperatures. To do so, we use the strategy of seeding the transformation process to enhance the formation of a required phase. Although it is a resource extensively used, it was hardly improved until the 80's [20,22]. The idea is that the  $\alpha$ - $\text{Al}_2\text{O}_3$  seeds will act as nucleation sites so lowering the transformation temperatures of the final  $\alpha$ - $\text{Al}_2\text{O}_3$  and preventing the formation of the vermicular structure due to the phase transformation of boehmite, reducing the residual porosity [23,

24] with the additional help of high pressure. Furthermore, the kinetics of the reactive-SPS processes are discussed and compared with the results obtained by conventional SPS routes (namely, standard-SPS). Structural characterization has been performed at different scales, and the mechanical properties have been measured at different applied loads.

## 2. Materials and methods

### 2.1. Sample synthesis

A route based on the works of Kumagai and Messing [20,23] and Barrera-Solano et al. [25] was employed for the preparation of the powders. In Fig. 2, the synthesis procedure is summarized. A boehmite sol (Nyacal Nano Technologies, Inc., density = 1.14 g/cm<sup>3</sup>, pH = 3.5) was slowly seeded with  $\alpha$ - $\text{Al}_2\text{O}_3$  seeds (30–40 nm particle size, 99% purity), supplied by NanoAmor, Inc. The amount of seeds was chosen in such a way that the mass represented 2 wt.% of the final  $\alpha$ - $\text{Al}_2\text{O}_3$ .

After 24 h of vigorous magnetic stirring, the seeded sol was gelled by adding  $\text{NH}_3^{\text{(aq)}}$  (PanReac, pH = 11.6), until the pH of the sol reached a value of 6.0, approximately, and a rapid gelation occurred. Another set of samples was obtained by exactly the same procedure but without the addition of  $\alpha$ - $\text{Al}_2\text{O}_3$  seeds. The gels were dried in a stove for 48 h at 40 °C. After that, the resulting xerogels were grinded in an agate mortar and sieved (<212  $\mu\text{m}$ ), obtaining white boehmite powders. At this stage, two different samples were present: the unseeded boehmite powders (named  $\rho$ , “rho”), and the boehmite powders seeded with  $\alpha$ - $\text{Al}_2\text{O}_3$  (named  $\rho\alpha$ , “rho-alpha”). Part of each powder was directly considered for reactive-SPS, and the rest was annealed at 1200 °C in a tubular furnace with an argon atmosphere, resulting in  $\alpha$ - $\text{Al}_2\text{O}_3$  powder according to the expected sequence of thermal transformations of aluminum hydroxides into alumina polymorphs [12] (see Fig. 1). The calcined unseeded boehmite powder was named  $\rho1200$ , and the seeded one,  $\rho\alpha1200$ . These annealed powders were submitted to conventional standard-SPS. In summary, the samples with  $\alpha$ - $\text{Al}_2\text{O}_3$  seeds (“seeded samples”) include the character  $\alpha$ ; those sintered via conventional SPS are labeled with the suffix “1200”, i.e.,  $\rho1200$  and  $\rho\alpha1200$ , and will be referred as “standard-SPSed samples”; the samples sintered via reactive-SPS are  $\rho$  and  $\rho\alpha$ , and will be referred as “reactive-SPSed samples”. For the sake of clarity, the types of samples considered in this work are summarized in Fig. 2.

For all cases, the samples were sintered in a Dr. Sinter Lab, Inc., model

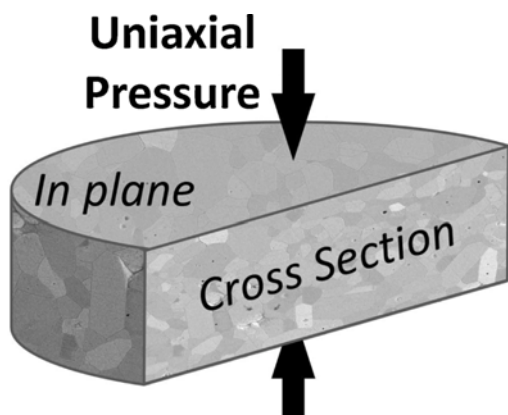


Fig. 3. Scheme of a SPSed sample showing in plane (ip) and cross section (cs) surfaces.

515S (Kanagawa, Japan), at 1300 °C for a dwell time of 5 min (heating ramp: 100 °C/min, cooling ramp: 50 °C/min), applying 75 MPa of constant uniaxial pressure and a squared pulse of current (12 s on and 2 s off). These parameters were chosen because they have previously been successfully used for fully densifying commercial pure  $\alpha$ -Al<sub>2</sub>O<sub>3</sub> powders [8–10,26]. During the sintering, the piston travel (shrinkage) and the temperature of the graphite die were recorded. The temperature was measured with a pyrometer which was capable of obtaining data from 570 °C onwards. The temperature was measured in the exterior wall of the graphite die which might present a time-lag in the automatic temperature adjustment. This was clear when the temperature reached 1300 °C and the thermal inertia overheated the sample by a few degrees Celsius.

The sintered samples were prepared by the classical ceramographics methods, i.e., the “RCEP” protocol [3], namely: rectifying, cutting, embedding, and polishing (up to 1  $\mu$ m diamond slurry), so obtaining polished surfaces for the measurement of micro-structural and mechanical properties. In order to research the anisotropic effects due to the uniaxial compression, two different surfaces were *repped* for each sample: the “in plane” surface (ip), perpendicular to the pressure axis, and the “cross section” surface (cs), parallel to this axis (see Fig. 3).

## 2.2. Chemical and structural characterization

The chemical composition of the samples was analyzed with an X-ray fluorescence (XRF) spectrometer (*Panalytical* model AXIOS). The crystallographic structures of the samples were investigated by XRD (X-ray powder diffraction), using a *Bruker* diffractometer model D81-90, by the step-scanning technique with a range from  $2\theta = 10^\circ$  to  $120^\circ$ , step of  $\Delta\theta = 0.015^\circ$ , counting time of 0.5 s, using Cu-K $\alpha$  radiation (K $\alpha_1$  + K $\alpha_2$  doublet) with no monochromator, 40 kV, 30 mA, and sample rotating at 30 rpm.

For the study of the nanostructural features of the powders, samples were degassed under an N<sub>2</sub> flux at 150 °C for 2 h and analyzed by N<sub>2</sub> physisorption (*Micromeritics* ASAP2010), working at 77 K with a resolution of 10<sup>-4</sup> mm Hg. The specific surface areas (SSA) of the powders were obtained using the curves of gas adsorption and desorption, and the BET model [27]. The micro- and nanostructure were also examined by scanning electron microscopy with SEMFEG, *Hitachi* model S5200 and *FEI* model Teneo, with acceleration voltages of 5 and 2 kV, respectively. Transmission electron microscopy (TEM, *Philips* model CM-200) was also employed. To measure grain size the grain boundaries must be revealed, so the sintered monolithic samples were exposed to a thermal etching of 15 min at 1200 °C (heating ramp: 5 °C/min) in an alumina tubular furnace in the presence of an inert argon atmosphere at

constant flux. After the etching treatment, dozens of SEM micrographs were analyzed with the help of *ImageJ* software [28] (typically, more than 300 grains per surface were studied for the statistics).

Thermogravimetric analyses (TGA) and differential scanning calorimetry (DSC) in flowing air were conducted to evaluate the chemical evolution of samples when they were heated. TGA procedures were performed in a STD Q600 (*TA Instruments*), heating a few milligrams of powder samples at 10 °C/min from room temperature up to 1000 °C, under an air flux of 100 mL/min. Mass losses received special attention in the thermal range corresponding to the dehydroxylation of the boehmite (200–450 °C).

The densities of the monolithic samples were obtained by the Archimedes’ method, submerging the cut pieces of the monolithic samples into distilled water at 25 °C. A set of 5 samples was considered for each type of sample for the statistics.

## 2.3. Surface topographic characterization

To quantify the quality of the polishing of the sintered samples, the roughness is an important value to be considered when measuring mechanical properties [29]. In all the final surfaces, the average arithmetic roughness in the surface,  $S_a$ , was measured. This magnitude is defined as the arithmetic mean of the absolute value of the height  $z$  from the average plane of the surface  $\sigma$  of area  $A$ :

$$S_a = \frac{1}{A} \iint_{\sigma} |z(x, y)| \, dx \, dy \quad (2)$$

The topography of the surfaces was obtained using a 3D optical-confocal microscope-interferometer (*Sensofar* S-NEOX) and the *Senso-Maps* software. The surfaces were photographed with an optical microscope (model *Leica* DMRE, *Leica Microsystems GmbH*, Germany). A magnification of 50 $\times$  was employed with a gaussian filter of 80  $\mu$ m. For the values of  $S_a$ , fifteen different selected areas were studied for each surface. Deeper analyses of the quality of the polishing and other parameters quantifying the roughness from the measurement of  $z(x, y)$ , such as  $S_q$ , a quadratic treatment analogous to the arithmetic average  $S_a$  can be found in the Supplementary Material, Table SM1. This extended discussion includes five different selected areas, and from each area fifteen parallel lines (profiles), and another fifteen parallel lines perpendicular to the first, were used to calculate the values of  $R_a$  and  $R_q$ . Consequently, 30 values for each magnitude were obtained for the same area, that is, 150 values for each examined sample.

## 2.4. Mechanical characterization

The characterization of the hardness was based on Vickers indentation tests at several loads (0.5 to 10 kp) and 10 s of dwell, repeating the test at least ten times for statistical analysis. The tests were performed in a *Buehler Wilson* VH1150 MicroVickers Hardness Tester and a *Struers* Duramin. The applied force:area ratio of the print gives the hardness,  $H$ , of the material. The fracture toughness,  $K_{Ic}$ , was estimated from the indentation fracture resistance,  $K_{IFR}$ , a value obtained from the Vickers Indentation Fractures (VIF) method, and using the Shetty’s equation for median type cracks:

$$K_{IFR} = 0.023(E/H)^{1/2} P / c^{3/2} \quad (3)$$

where  $E$  is the elastic modulus,  $H$  is the Vickers hardness,  $P$  is the applied load, and  $c$  is the length of the crack, measured from the center of the print. More detailed aspects of the equation are given in [30]. We chose this equation after Miyazaki et al. [31,32] proved that, for fully dense alumina ceramics, this equation provides values of  $K_{IFR}$  absolutely correlated with values of  $K_{Ic}$  obtained by standard methods, such as SEPB.

The indentation prints and the length of the cracks were measured using an optical microscope with a  $\times 20/0.40$  objective, a CCD camera

**Table 1**

BET specific surface area of powders, and estimated spherical diameter of the powder particles calculated from SSA. Number of measured grains for the characterization of the grain size on both surfaces, in plane (ip) and cross section (cs). Uncertainties are one standard deviation. Relative densities of sintered samples of the studied materials.

Sample name	BET SSA (m <sup>2</sup> /g)	Estimated diameter (nm)	Measured grains	Grain size (μm)		Relative density (%)
				ip	cs	
$\rho$	163.5	6.0	1002	30 ± 13	24 ± 12	99.6 ± 1.7
$\rho\alpha$	156.5	6.3	916	12 ± 7	10 ± 6	99.4 ± 1.9
$\rho1200$	5.4	140	563	1.3 ± 0.9	1.5 ± 1.0	95.3 ± 0.6
$\rho\alpha1200$	4.7	160	891	1.3 ± 0.8	1.3 ± 1.1	98.9 ± 1.4

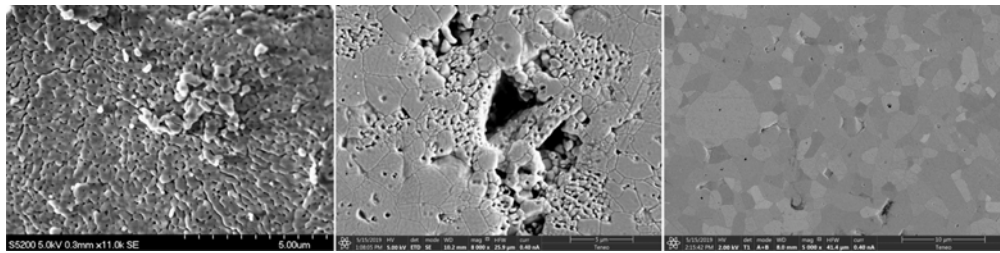


**Fig. 4.** Left:  $\rho1200$  sample at powder stage (prior to sintering). Center: cross section surface of standard-SPSed sample  $\rho1200$ , illustrating the persistence of vermicular structure after sintering, yielding to inter- and intragranular porosities. A hole, probably due to grain chipping during the rectifying and polishing, crowns the center of the image. Right: image of the sample  $\rho\alpha1200$ -ip revealing the fully dense structure of the grains.

with digital zoom, and a traveling stage, as a good optical resolution is a crucial feature for reliable values of  $K_{IFR}$  obtained by VIF tests [32]. Finally, after mechanical characterization, SEM was used again to explore the nano- and microstructure of the polished surfaces of the samples, the indentation prints, and the morphology of the cracks.

### 3. Results and discussion

#### 3.1. Chemical and structural characterization

First of all, the precursor powders of all the types of samples were characterized. The XRF analyses revealed that the composition of all the powders was 98.5% Al in mass, and the rest consisted of impurities of Mg (0.6%), Na (0.2%), Si (0.2%), Ti (0.1%), Fe (0.1%), and Zr (<0.1%). This composition remained mostly the same after the SPS.

The specific surface area (SSA) values from the nitrogen physisorption experiments performed on the powders are listed in Table 1. With these data we can obtain a first estimation of the size of the particles of the precursor powder, using a simple first-approach model based on spherical particles:

$$SSA = \frac{\text{surface}}{\text{mass}} = \frac{4\pi R^2}{\delta \frac{4}{3}\pi R^3} \rightarrow D = 2R = \frac{6}{\delta \cdot SSA}, \quad (4)$$

where  $R$  and  $D$  are the radius and the diameter of the spherical particles, respectively, and  $\delta$  is the theoretical bulk density of the powder. Boehmite powders exhibited an SSA of 163.5 m<sup>2</sup>/g, which involves an estimated particle size of 6.0 nm. Although this approximation underestimates the real size, the results are in accordance with the particles sizes observed using TEM and SEM. Boehmite powders are composed of nanoparticles of dimensions around 7 × 30 nm (see TEM image in Supplementary Material Fig. SM2), that are arranged in clusters of nanoparticles with a wide range of sizes [5]. On the other hand, the addition of 2 wt.% of  $\alpha$ -Al<sub>2</sub>O<sub>3</sub> seeds, which have an SSA of 9.0 m<sup>2</sup>/g, gave to  $\rho\alpha$  powders a quite smaller SSA, and, consequently, a larger estimated particle size.

Regarding the calcined powders for standard-SPS, as expected, they exhibited much lower values of SSA than the non-calcined powders. Moreover, sample  $\rho1200$  presented a smaller particle size than  $\rho\alpha1200$

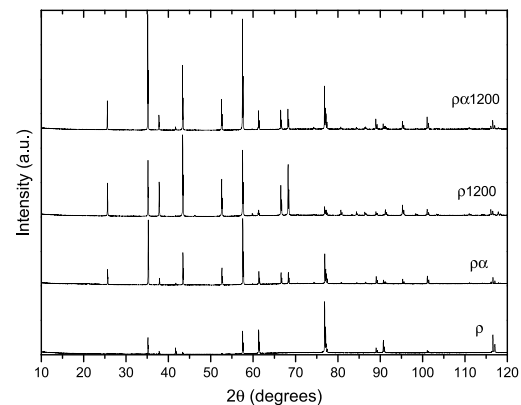


**Fig. 5.** Diffractograms of the sintered samples.

as the  $\rho\alpha1200$  powders contained a 2 wt.% of  $\alpha$ -Al<sub>2</sub>O<sub>3</sub> seeds when they were calcined at 1200 °C to transform boehmite into alumina, leading to an enhanced crystallization. The inspection of the calcined powders with electron microscopy showed that the powder samples  $\rho1200$  and  $\rho\alpha1200$  have much larger characteristic sizes than the estimated particle sizes of 140 or 160 nm, respectively. That difference is principally explained by nanometric vermicular structure of the calcined  $\rho1200$  powder, typically found in  $\alpha$ -Al<sub>2</sub>O<sub>3</sub> obtained from the thermal evolution of transition aluminas (see Fig. 4-left).

The crystallographic characterization of the powders has already been reported [3,5] and clearly showed the expected patterns of boehmite for the non-calcined sample, and  $\alpha$ -Al<sub>2</sub>O<sub>3</sub> for the seeded non-calcined and all the calcined ones. Fig. 5 shows the diffraction patterns of the sintered samples. The peaks displayed in the diffractograms correspond to the X-ray diffraction lines of the  $\alpha$ -Al<sub>2</sub>O<sub>3</sub>, showing that all the samples (reactive-SPSed and standard-SPSed, and with or without  $\alpha$ -Al<sub>2</sub>O<sub>3</sub> seeds) have the same composition. Nevertheless, relative intensities are very different from the ideal structure of  $\alpha$ -Al<sub>2</sub>O<sub>3</sub> for

## Chapter 5. Reactive SPS for sol-gel alumina samples: Structure, sintering behavior, and mechanical properties

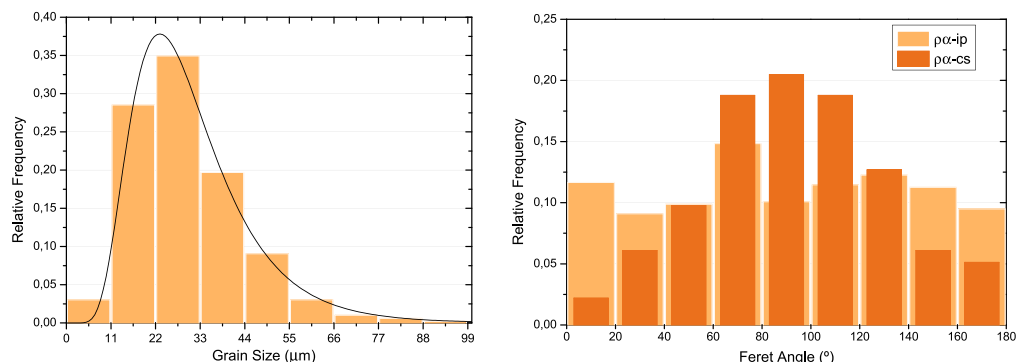


**Fig. 6.** Left: histogram of the grain size for  $\rho$  sample in the ip surface ( $\rho$ -ip), which follows a log-normal distribution (fitting curve, see equation (2)). This is true on both ip and cs surfaces for every sample. Right: in the ip surface of all the samples, the grains do not show any preferential orientation, and a flat distribution is obtained in the histogram number of grains (relative frequency) vs. Feret angle. Alternatively, anisotropic distribution of Feret angle is obtained in the cross section of the sample, indicating the preferential grain growth in the plane perpendicular to the uniaxial pressure direction. Data obtained from  $\rho\alpha$ -ip and  $\rho\alpha$ -cs surfaces of sample  $\rho\alpha$ .

the  $\rho$  sample. In this case, possible texture or preferred orientation effects can be responsible of this behavior. The rest of the samples show relative intensities similar to the ideal case. Therefore, the theoretical density of full-dense pure  $\alpha$ - $\text{Al}_2\text{O}_3$ ,  $3.985 \text{ g/cm}^3$  [7,13] was considered as the reference value for the measurement of the densities of the sintered samples (Table 1). Relative densities above 99.4% were found for the reactive-SPSed samples, while 95.3% and 98.9% were found for samples  $\rho$ 1200 and  $\rho\alpha$ 1200, respectively. According to Delesse's principle of stereology, the fraction of area of pores observed in SEM images was the same as the fraction of volume occupied by that porosity. Thus, the lower density of sample  $\rho$ 1200 is in agreement with the remaining vermicular porosity observed on its surface (as shown in Fig. 4-right, and discussed below).

A qualitative inspection of the X-ray diffraction peaks shows that these are very narrow (Fig. SM3), displaying the doublet components even at low angles ( $2\theta < 40^\circ$ ). This indicates that microstructural effects – especially domain size – are very small in all samples. This can be assessed by measuring the breadths of the peaks. In this way, we have fitted Voigt functions to the peaks with heights greater than 1000 counts, calculating their corresponding Cauchy ( $\beta_c$ ) and Gauss ( $\beta_g$ ) integral breadths. In most cases, the fit was very good, providing Goodness-of-Fit values around 1–2. As an example, Fig. SM4 shows the fit of a Voigt function to the 006 peak of the  $\rho$  sample. Fig. SM5 displays the Cauchy and Gauss integral breadths for the analyzed samples as function of the peak position. Note that, Gaussian integral breadths are similar (for a particular angular position) for the four samples, whereas Cauchy integral breadths are similar for the samples  $\rho$ ,  $\rho\alpha$ , and  $\rho\alpha$ 1200, being greater for the sample  $\rho$ 1200.

Classical microstructural analysis by X-ray diffractometry, especially with respect to the estimation of domain size, is restricted to domain sizes in the nanometric scale. Therefore, domain sizes of about  $1 \mu\text{m}$  and greater cannot be reliably determined, because the widths of the experimental and instrumental-spectral (used as standard) peaks are very similar. This similarity indicates that the experimental line-broadening is mainly due to instrumental-spectral effects, being microstructural effects very small or negligible. In regards to this, shape parameter errors are of the order of the difference between the widths of the experimental and instrumental-spectral peaks and this leads to unacceptable uncertainties.

However, in our case, as the reactive-SPSed samples  $\rho$  and  $\rho\alpha$  seem to have grain sizes of about tens of microns, we have considered the possibility to estimate the domain size of the samples  $\rho$ 1200 and  $\rho\alpha$ 1200 (considering  $\rho$  as standard for the sample  $\rho$ 1200, and  $\rho\alpha$  for the sample  $\rho\alpha$ 1200). Assuming that the domain size effect is approximated by the

Cauchy component of the microstructural profile, only the  $\rho$ 1200 sample can be analyzed, because the Cauchy integral breadths of the  $\rho\alpha$ 1200 sample are the same (within of the uncertainties) that the corresponding to the  $\rho\alpha$  sample. In the case of the  $\rho$ 1200 sample, a classical analysis using the Williamson-Hall plot [33] and the Warren-Averbach method [34] provide a mean apparent volume domain size of  $1.3 \pm 0.8 \mu\text{m}$ , and a mean apparent area domain size of  $0.7 \pm 0.3 \mu\text{m}$ , with a root mean square strain of  $(1.2 \pm 0.2) \cdot 10^{-4}$ . In summary, the domain size values, in spite of the noticeable uncertainties (as we have pointed out above), are in rough agreement with the value derived from the electron microscopy. Note that this suggest that nanometric sub-grains are not present in the  $\rho$ 1200 sample, as the mean values of the domain sizes are about  $1 \mu\text{m}$ . A similar result could be considered for the sample  $\rho\alpha$ 1200 because no significant differences appear between the breadths of the peaks and those corresponding to the sample  $\rho\alpha$ , used as standard.

### 3.2. Surface characterization

The SEM study of the sintered samples allowed the estimation of the typical grain sizes (Table 1). A significant difference was observed between the reactive samples, with typical grain sizes larger than  $10 \mu\text{m}$  (as observed in Figs. SM6, SM7 and SM8), and the standard-SPS ones, with grain sizes lower than  $1.5 \mu\text{m}$  (Fig. 4-center and -right), one order of magnitude smaller. These results are validated by the estimates of crystallite domain size obtained by X-ray diffractometry, discussed previously. In addition, in Fig. 4-center, the SEM image of sample  $\rho$ 1200 shows some details of its microstructure that helps to explain its low density. It can be confirmed that the structure is not totally closed and some residual porosity remains, mainly due to the vermicular network observed in the precursor powder (Fig. 4-left) that persisted when  $\alpha$ - $\text{Al}_2\text{O}_3$  is made by the evolution of transition aluminas [20]. In Fig. 4-right, an image of the sample  $\rho\alpha$ 1200-ip reveals the fully dense structure of the grains, with unusual intragranular porosity. Regarding the reactive-SPSed samples, another relevant result is that the grain size of non-seeded sample  $\rho$ , is twice the grain size of the seeded sample  $\rho\alpha$ . This fact could be explained given the absence of nucleation sites in sample  $\rho$ , what enables a larger grain growth: grain boundaries have more time to expand before they meet another grain boundary. On the contrary,  $\rho\alpha$  has a much larger density of nucleation sites so grain growth is limited by meeting faster grain boundaries.

The statistical analysis of the grain sizes reveals that the grain size (random variable  $D$  which takes values  $d$ ) follows the classically reported log-normal random distribution [35,36] (see Fig. 6-left), whose probability density function is given by:

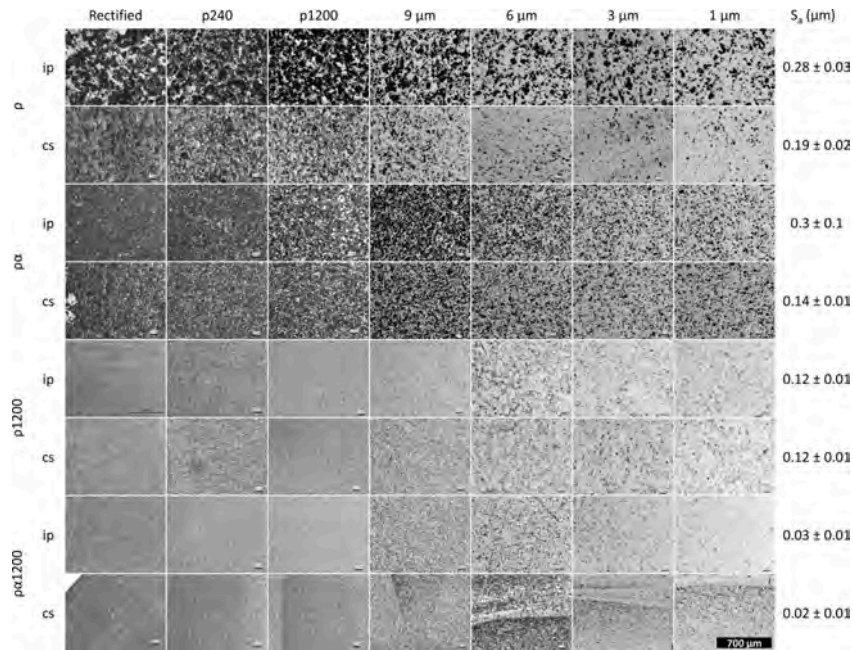


**Fig. 7.** Evolution of surfaces after the different polishing steps. In plane (ip) and cross section (cs) surfaces are shown, as well as average measured roughness ( $S_a$ ). A 3D reconstruction of the polished surface of the sample  $\rho$  obtained by confocal microscopy is shown in Supplementary Material Fig. SM1.

$$f_{\mu,\sigma}(d) = \frac{1}{d\sigma\sqrt{2\pi}} \exp\left(-\frac{[\ln(d) - \mu]^2}{2\sigma^2}\right) \quad (5)$$

where  $\mu$  and  $\sigma$  are the mean and the standard deviation of the variable's natural logarithm. Note that they are not the expectation and standard deviation of random variable  $D$ , as  $D$  is defined as  $D = \exp(\mu + \sigma Z)$ , where  $Z$  is a random variable normally distributed. The arithmetic mean values of  $D$  for the different samples (i.e.  $\bar{d}$ , not  $\mu$ ) are listed as the characteristic grain sizes in Table 1. Additionally, the typical anomalous alumina grain growth [36] was present and is responsible for the relatively large uncertainties of the central values. This behavior is probably enhanced by the tendency for boehmite to grow in a preferred direction, leading to the formation of high aspect ratio alumina crystals [19,37], a process that starts, in the case of the conventionally sintered samples, all along the pre-annealing of boehmite powders at 1200 °C.

The preferential direction of grain growth was quantified by the Feret diameter: it is defined as the maximum diameter that can be drawn between any two points of the boundary of a grain, i.e., the maximum caliper. The Feret angle is then the angle between the Feret diameter and an arbitrary fixed direction. In this work, for the cross section surfaces, the fixed direction to measure the Feret angle was the pressure axis. For the in plane surfaces, the selected direction is any radial direction perpendicular to the loaded axis. All the ip surfaces showed an isotropic distribution of grains (see Fig. 6-right). On the other hand, the cs surfaces of samples  $\rho$ ,  $\rho\alpha$ , and  $\rho\alpha 1200$  presented anisotropies (Fig. 6-right, Figs. SM6 and SM8), that is, during the sintering, the grain growth was inhibited in the direction of the applied pressure. Hence, the grains grew preferentially in the plane perpendicular to the pressure axis [38]. Surprisingly, this phenomenon was not observed at any surface (nor ip nor cs) of the sample  $\rho 1200$  sintered by conventional SPS. This may be explained by the absence of  $\alpha\text{-Al}_2\text{O}_3$  seeds which promoted a retarded formation of grains, and a consequent lack of time for the grains to develop in a preferential direction. Some authors [39] have suggested that what really inhibits the grain growth is the electric field, which could happen during SPS, as the electric field is applied uniaxially in the

same direction as the mechanical load. Nevertheless, is a controversial topic under debate [40,41], and more experiments will be performed in order to elucidate what plays the fundamental role in the inhibition of grain growth.

During the RCEP procedure, the evolution of the surfaces presented significant differences between the reactive-SPSed samples and the standard ones. In Fig. 7, the surfaces were photographed with an optical microscope as the successive sandpapers and diamond slurries were used, from the coarsest p240 sandpaper to finest 1  $\mu\text{m}$  diamond paste. Besides, the results of the topographic characterization of the final polished surfaces present a clear difference between the reactive-SPSed sample and the standard ones.

The higher roughness of the  $\rho$  and  $\rho\alpha$  samples (up to one order of magnitude higher) is attributed to their larger grain size (Table 1) combined with the effect of grain chipping produced during the rectifying and rougher first steps of polishing. Thus, when a grain is chipped out from the surface of a reactive-SPSed sample, the "hole" left by the grain is deeper than in the standard samples. Moreover, some differences between the in plane surfaces (ip) and the cross sections ones (cs) have been appreciated. This fact may be explained attending to how the residual tensions are accumulated in the sintering process, due to anisotropic application of pressure. It is easier for a grain to be chipped out from an ip surface than from a cs surface, as the uniaxial pressure is applied perpendicularly to the ip surfaces, and larger residual tensions are accumulated under grains in ip surfaces, i.e., at the perpendicular plane to the axis of load. Thus, densities do not play the fundamental role determining the roughness of the samples when comparing the reactive-SPSed samples and standard samples. Nevertheless, some effects of the density on the roughness can be appreciated when comparing standard samples:  $\rho\alpha 1200$ , with a density of 98.9%, shows a smoother surface than  $\rho 1200$ , with a density of 95.3% ( $S_a = 0.03 \mu\text{m}$  and  $S_a = 0.12 \mu\text{m}$ , respectively), despite the fact that both samples have the same micrometric grain size.

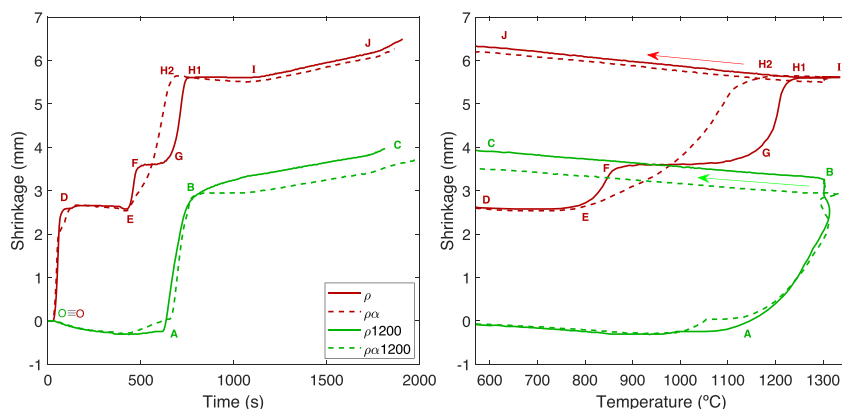


**Fig. 8.** Shrinkage vs. time (left) and vs. temperature (right) curves of the four different samples. Same legend corresponds to both plots. The arrows in the right panel show the direction of the process. Letters indicate similar states (shrinkage, time and temperature) on both figures. Observe that points **O** and **O** cannot be represented in the right plot, as the pyrometer can only measure the temperature above 570 °C. Note that reactive samples exhibited significant shrinkage before temperature data could be acquired, and this causes apparent shifting in Fig. 8-right. (For interpretation of the references to color in the text, the reader is referred to the web version of this article.)

### 3.3. Sintering and structural characterization

During the SPS, the temperature ( $T$ ), and the displacement of the pistons (i.e., the shrinkage of the sample,  $z$ ) were recorded. We took  $z = 0$  after the 75 MPa of uniaxial pressure was applied, at room temperature. These are the points **O** and **O** in Fig. 8-left. Observe that these points cannot be represented in  $z$  vs.  $T$  in Fig. 8-right, given that the pyrometer can only measure temperatures above 570 °C.

The sintering behavior of the conventionally sintered samples,  $\rho_{1200}$  and  $\rho_{\alpha 1200}$ , can be discussed by the real-time collected shrinkage and temperature data, as shown in Fig. 8 (green lines, solid and dashed, respectively). The corresponding sintering curves  $z$  vs.  $t$ , in Fig. 8-left, show the classic densifying process of alumina powders revealed by the sample shrinkages, which start around  $t = 600$  s ( $T = 1150$  °C), and exhibits the maximum slopes at 1220 °C (step from points **A** to **B**). Although both samples,  $\rho_{1200}$  and  $\rho_{\alpha 1200}$ , were basically  $\alpha$ - $\text{Al}_2\text{O}_3$ , the better densification of the seeded one ( $\rho_{\alpha 1200}$ ) with respect to the non-seeded one ( $\rho_{1200}$ ), is revealed by the existence of a plateau during the dwell time at maximum temperature (around  $t = 700$  s to 1000 s) in sample  $\rho_{\alpha 1200}$ , while sample  $\rho_{1200}$  exhibits continuous shrinking. This could be attributed to its increased crystallization during the direct transformation of boehmite into  $\alpha$ - $\text{Al}_2\text{O}_3$  in the previous pre-annealing process thanks to the presence of the seeds, and which also prevents the presence of vermicular structures in the powders and in the sintered sample  $\rho_{\alpha 1200}$ . This difference has been previously reported for a sintering based on pressureless sintering and hot pressing by Kumagai et al. [20,23], using much longer times at higher temperatures. Finally, during the cooling ramp (50 °C/min), beyond  $t = 1000$  s, the shrinkage is produced by the linear thermal contraction (from point **B** to point **C**).

The slight difference in the sintering behavior between  $\rho_{1200}$  and  $\rho_{\alpha 1200}$  once the maximum temperature was reached (at point **B**) can be better visualized in the plot of  $z$  vs.  $T$ , in Fig. 8-right. While the sample  $\rho_{1200}$  continued densifying (vertical increase of  $z$ ) during the dwell time at  $T = 1300$  °C, the seeded sample  $\rho_{\alpha 1200}$  has already densified completely (no variation on  $z$  at maximum  $T$ ). Afterwards, the cooling process from **B** to **C** performs the expected linear behavior of thermal contraction. In fact, this linearity could be used to calculate the linear thermal expansion/contraction coefficient,  $\alpha_L$ , however, for these measurements to be made, the whole system must be calibrated, correcting the plots with the expansion of the die and pistons assembly during heating and cooling, both with and without any powder material, as suggested by Chaklader et al. [14] for hot pressing sintering.

At this point, it is interesting to highlight the differences between the described standard samples and the reactive-SPSed samples. The curve  $z$  vs.  $t$  of the  $\rho$  sample, without  $\alpha$ -alumina seeds, (solid red line in Fig. 8-

left) shows a three-step process. Firstly, from room temperature (**O**) to a temperature below 570 °C (**D**), the shrinkage reveals that the boehmite dehydroxylates and turns into  $\gamma$ - $\text{Al}_2\text{O}_3$ , losing mass in the form of  $\text{H}_2\text{O}$  during topotactic transformations (i.e., the crystal structure transforms without destruction of the original crystal morphology [20]). The transformation is consistent with the TGA and DSC results performed on boehmite  $\rho$  powders (not shown, available in Supplementary Material, Fig. SM9), and this transition is completed at 500 °C, in agreement with the irreversible evolution of alumina polymorphs (Fig. 1). The second densifying step occurs between points **E** and **F**, during which the transition alumina  $\gamma$ - $\text{Al}_2\text{O}_3$  turns into  $\alpha$ - $\text{Al}_2\text{O}_3$ . In the third step, from **G** to **H1**, the  $\alpha$ - $\text{Al}_2\text{O}_3$  densifies, with a maximum slope at 1200 °C. From **H1** to **I**, we observe a little plateau, at which the sample  $\rho$  does not suffer compaction. At the end, the linear thermal contraction happens, from **I** to **J**.

Correspondingly, the inspection of the curve of  $z$  vs.  $T$  of the sample  $\rho$  (solid red line in Fig. 8-right) gives additional relevant information about the sintering behavior, specially at the highest temperatures. At the segment **H1-I**, the temperature rises up from 1250 °C to 1300 °C, is held for 5 min at 1300 °C, and goes back to 1250 °C (back to **H1**), exhibiting a linear behavior. This is a period of time in which the structure suffers an unnecessary grain growth [9], as it was revealed in the grain size measurements (>10  $\mu\text{m}$ , Table 1), which will lead to a decrease in the mechanical properties. This stretch is useless from the point of view of efficient use of time and resources. At the end, the linear thermal contraction happens, from **H1** to **J**, with exactly the same slope that the standard-SPSed samples exhibited (segment from **B** to **C** of the green lines in Fig. 7).

Finally, the last curves to be analyzed, correspond to the reactive-SPSed samples  $\rho_{\alpha}$ , seeded at the sol stage with  $\alpha$ - $\text{Al}_2\text{O}_3$  (red dashed curve in Fig. 8-left and right). During the initial step from **O** to **D**, the dehydroxylation happens and the boehmite transforms into alumina, as the non-seeded sample  $\rho$  did. However, given that  $\rho_{\alpha}$  contains  $\alpha$ - $\text{Al}_2\text{O}_3$  seeds, the boehmite turns directly into  $\alpha$ - $\text{Al}_2\text{O}_3$  because of the effect of nucleation and subsequent growth [20,42]. Thus, this sample does not exhibit the step **E-F-G**. Instead, it jumps directly from **E** to **H2**, a step in which the alumina densifies. This process mimics the way that  $\alpha$ - $\text{Al}_2\text{O}_3$  does in standard samples from **A** to **B**. Interestingly, this step, with a maximum slope at 1070 °C, finishes at 1200 °C at **H2**, more than a minute before **H1** and **B**. The plot of  $z$  vs.  $T$  (Fig. 8-right) confirms that the full densification (point **H2**) at a temperature 50 °C lower. Subsequently, and similarly to the red solid line of sample  $\rho$ , the bounce **H2-I-H2** is a plateau in which the sample does not densify any further, a segment of heating ramp, holding, and cooling, which can be considered a waste of time and energy in which the grain size grows [9]. This is confirmed by

**Table 2**

Vickers Hardness (HV) and Fracture Indentation Resistance ( $K_{IFR}$ ) measured at different loads: 0.5, 1.0, 5.0, and 10 kp. Tests performed in plane (ip) and cross section (cs) surfaces. Uncertainties are given by one standard deviation.

Sample name (relative density)		HV0.5		HV1		HV5		HV10	
		HV (GPa)	$K_{IFR}$ (MGf)	HV (GPa)	$K_{IFR}$ (MGf)	HV (GPa)	$K_{IFR}$ (MGf)	HV (GPa)	$K_{IFR}$ (MGf)
$\rho$ (99.6%)	ip	18.3 ± 1.2	3.0 ± 0.7	–	–	–	–	–	–
	cs	–	–	16.7 ± 1.4	2.5 ± 0.6*	–	–	–	–
$\rho\alpha$ (99.4%)	ip	16.9 ± 0.7	–	–	–	–	–	–	–
	cs	17.9 ± 1.0	–	16.1 ± 1.1	–	–	–	–	–
$\rho1200$ (95.3%)	ip	–	–	15.1 ± 1.4	5.0 ± 0.6	13.3 ± 0.8	5.4 ± 0.9	13.4 ± 0.5	4.4 ± 0.8
	cs	17.8 ± 1.1	–	16.7 ± 1.2	5.8 ± 0.4	14.2 ± 0.5	5.8 ± 1.0	14.4 ± 0.5	5.8 ± 1.2
$\rho\alpha1200$ (98.9%)	ip	19.7 ± 0.5	–	19.4 ± 0.8	5.0 ± 0.5	–	–	16.8 ± 0.8	5.2 ± 0.6
	cs	–	–	18.4 ± 1.2	3.7 ± 0.5	–	–	16.5 ± 0.3	4.4 ± 0.7

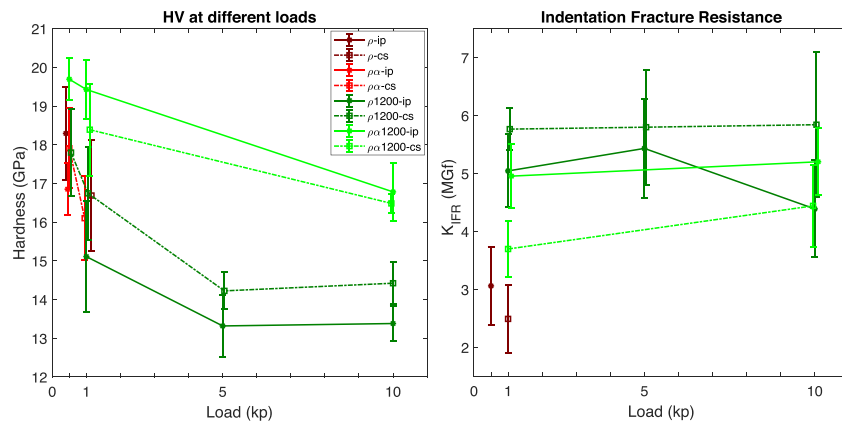


**Fig. 9.** Left: Vickers Hardness of different samples at several loads, illustrating Indentation Size Effect. Error bars are one standard deviation. Right: Indentation Fracture Resistance of samples for different loads. Error bars are one standard deviation. Points have been slightly horizontally shifted so the error bars do not overlap. Legend is the same for both graphics.

the large grain size observed in this sample (>10  $\mu\text{m}$ , Table 1). Finally, the process ends up exactly as all the other samples, with the same linear thermal contraction from H2 to J.

There are many factors that explain the advantages of the reactive

and the standard-SPSed samples in comparison to the standard-SPSed samples, namely, a reduction of time and temperature required for the total densification of alumina. The fundamental role in the densification mechanism is being played by the ability of the particles to rearrange

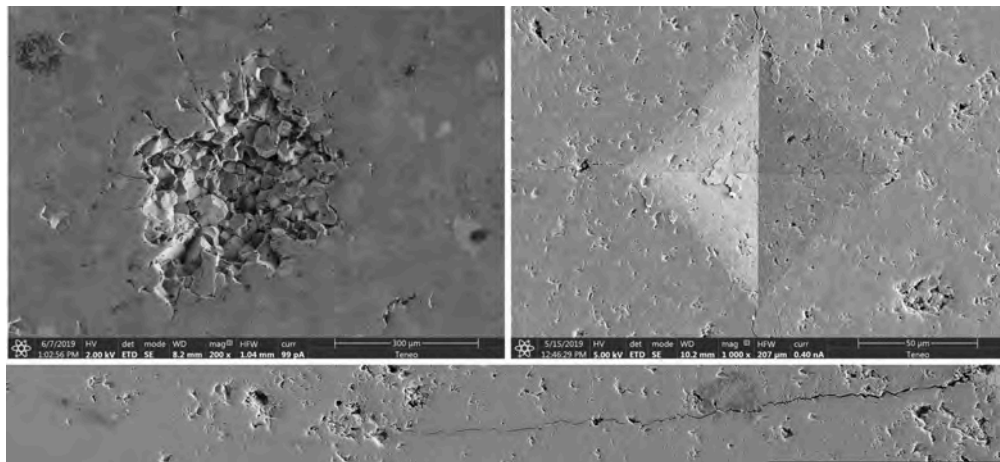


**Fig. 10.** Top-left: indentation HV10 on a reactive-SPSed sample ( $\rho$ -ip). Top-right: indentation HV10 on standard-SPSed sample ( $\rho1200$ -ip). Notice the difference on scale bars. Bottom: (Highly zoom-able image) HR-SEM image of a fracture after a HV10 indentation on the cross section surface sample  $\rho1200$ -cs, coated with 9 nm of carbon for avoiding SEM electronic charging. Scale: the black rectangle at the bottom is 70  $\mu\text{m}$  long. Fracture propagation from a HV10 Vickers indentation tip along its extremely long, approximately 225  $\mu\text{m}$ . This indentation was not considered either in the statistics of hardness, nor  $K_{IFR}$ . Both intergranular and transgranular crack propagation modes are present. Porosity due to vermicular remnants, grain boundaries, and holes produced by grain chipping can also be observed.

## Chapter 5. Reactive SPS for sol-gel alumina samples: Structure, sintering behavior, and mechanical properties

during the transformation phase [42]. During the initial application of pressure, the compaction involves a large scale particle rearrangement and motion. The smaller nanometric particle size of boehmite powders of the reactive-SPSed samples, compared with micrometric  $\alpha$ -Al<sub>2</sub>O<sub>3</sub> calcined powders of the standard-SPSed samples, induces a better initial compaction, leading to a better contact between the particles and a subsequent faster densification, as can be confirmed by the lower times and temperatures of points **H1** and **H2** in comparison to point **B**. Note that, the reactivity of boehmite powders is enhanced by its high SSA (see Table 1), 30 times bigger than the SSA of calcined alumina powders. In addition, the advantages of seeding the reaction with  $\alpha$ -Al<sub>2</sub>O<sub>3</sub> seeds are also clear as it facilitates a faster and cooler full densification. Finally, it is evident that the sintering parameters can be improved for reactive-SPS as the final segment of the process that led to excessive grain growth should be avoided. Thus, once the full density (end of shrinkage) is achieved, the process can be terminated. Probably, more parameters such as the heating ramp, cooling ramp, or the applied pressure, can be tuned and optimized to minimize the costs of alumina sintering.

### 3.4. Hardness and indentation fracture resistance

The monolithic samples were indented in their polished surfaces, and the obtained results of hardness and  $K_{IFR}$  are shown in Table 2 and plotted in Fig. 9. The first particular result is that, given the large grain size of reactive-SPSed samples, it was a hard task to obtain a well-defined print after indentation tests at loads larger than 1 kp. Even applying low loads, such as 0.5 and 1 kp, the prints usually had blurry edges and dozens of measurements were discarded. The grain size of these fully dense samples, larger than 10  $\mu$ m, is synonymous with more brittle ceramics, i.e., the larger the grain size, the worse  $K_{IFR}$ , although not necessarily worse  $K_{IC}$ , calculated by other methods, as reported by Yasuda et al. [43]. The energy applied by the tip is released leading to, in these cases, a multitude of radial cracks, material pile-up, and catastrophic grain chipping, as shown in Fig. 10-left when a load of 10 kp was applied. In contrast, the more fine-structured samples fabricated by standard-SPS, can be indented and measured without a hitch (Fig. 10-right).

In Fig. 9-left, it can be seen that all the samples show a hardness between 17 GPa and 20 GPa when a load of 0.5 kp is applied, 20 GPa being the value typically reported for fully dense  $\alpha$ -Al<sub>2</sub>O<sub>3</sub> [44,45]. The sample  $\rho$ 1200, which did not completely densify, exhibits a lower hardness for every load tested, especially when compared with its fully dense analogous,  $\rho\alpha$ 1200. This is due to the presence of 5% of porosity and the consequent lack of full connection of the whole crystalline microstructure [46].

On the other hand, the indentation fracture resistances measured in these set of samples (Fig. 10-right) were more sensitive to the grain size than the measured hardness, and the reactive-SPSed samples (with grain size above 10  $\mu$ m) showed  $K_{IFR}$  values significantly lower than the standard-SPSed samples (around 3 MGf<sup>1</sup> and 5 MGf, respectively). Moreover, the indentations made on both surfaces of the samples, cs and ip, yielded no relevant differences nor any systematic trend in the hardness and  $K_{IFR}$  values. Even so, all the results are contained in the wide range of fracture toughness reported for dense pure alumina, from 2.2 to 5.7 MGf [47,48].

Regarding the measurement of cracks, defined cracks were only found in the samples with large grain size when low loads were used.

The problem, then, is the difficulty to accurately measure the tiny, short cracks produced when low loads are applied. Given the huge efforts needed to obtain well defined prints and cracks even at low loads,  $K_{IFR}$  was measured in only two surfaces of one of the reactive-SPSed samples: HV-0.5 on  $\rho$ -ip, and HV-1 on  $\rho$ -cs, while the rest of reactive surfaces have been tested several times to confirm that they respond in the same way than their homologous do under the same loads. Respecting the mode of propagation of cracks, we found out that both transgranular and intergranular modes are present, with a preponderance of the latter one, as shown in Fig. 10-bottom. Finally, the indentation size effect [3,29,49], a source of discrepancy when the results of hardness are compared between different studies, is not apparently a crucial issue affecting the  $K_{IFR}$ , as deduced from Fig. 9 and the data in Table 2.

### 4. Conclusions

The proposed reactive-SPS process has been explored as an efficient route for the fabrication of fully dense  $\alpha$ -Al<sub>2</sub>O<sub>3</sub>, starting from a low-cost precursor such as the boehmite sol. It has been demonstrated that the fully dense samples can be obtained faster and at lower temperatures (1200 °C) than starting from  $\alpha$ -Al<sub>2</sub>O<sub>3</sub> powder. However, Vickers hardness of the obtained samples are among the highest reported for fully dense  $\alpha$ -Al<sub>2</sub>O<sub>3</sub>, being affected by the density and the indentation size effect, as expected, but they are independent of the sintering route. On the contrary, indentation fracture resistance is clearly affected by the sintering route as the conditions used in the reactive-SPS produced excessive grain growth, a crucial feature affecting the fragility of the samples, leading to poor values of  $K_{IFR}$ . Nevertheless, it has been shown that this process can be optimized, avoiding the holding time and reducing the maximum temperature, and subsequently avoiding excessive grain growth.

In addition, seeding the initial sol of boehmite with  $\alpha$ -Al<sub>2</sub>O<sub>3</sub> has been proved as a key feature for optimizing the process, as it allows the direct transformation into  $\alpha$ -Al<sub>2</sub>O<sub>3</sub>, lowering temperatures and times required for the full densification of samples via SPS. In this regard, a highly exciting route is to use a sol made of diasporite ( $\alpha$ -AlOOH) nanoparticles instead of boehmite ( $\gamma$ -AlOOH), which would avoid transition aluminas as the diasporite transforms directly to the stable  $\alpha$ -Al<sub>2</sub>O<sub>3</sub> phase by dehydroxylation [12,50], which could simplify the process and further reduce the temperature for a complete reactive sintering and total densification of alumina.

### Conflict of interest

The authors declare no conflict of interest.

### Declaration of Competing Interest

The authors report no declarations of interest.

### Acknowledgments

Project PGC2018-094952-B-I00 funded by FEDER/Ministerio de Ciencia e Innovaci3n – Agencia Estatal de Investigaci3n and project P12-FQM-1079 from Junta de Andaluc3a and funding support to FQM393 from Junta de Andaluc3a are acknowledged. V. M-F. thanks the grant from V Plan Propio de Investigaci3n de la Universidad de Sevilla. P. R-A acknowledge European Social Fund, Empleo Juvenil European Plan and project PGC2018-094952-B-I00 from FEDER/Ministerio de Ciencia e Innovaci3n – Agencia Estatal de Investigaci3n. F.S-B. acknowledges the support provided by a project co-financed by the European Regional Development Fund and the Junta de Extremadura (GR18081). The help from the technical staff from the CITIUS and Jos3 Hidalgo are acknowledged, as well as the fruitful discussions with Dr. Camilo Zamora-Ledezma. The authors would like to thank the work by the National Institutes of Health, USA for the development of the *ImageJ*

<sup>1</sup> Based on Prof. C. Ramadas and Mr. A. R. Jadhav's suggestion, the use of the unit "griffith" (Gf) is proposed in substitution of the awkward classical magnitude Pa · m<sup>1/2</sup>, where 1 Gf = 1 Pa · m<sup>1/2</sup>, as a tribute to the mechanical engineer Alan Arnold Griffith (1893–1963), as already considered in ref. [3]. Griffith was known in the field of fracture mechanics for his pioneering studies on the nature of stress and failure due to crack propagation in brittle materials.



software. *Comercial Química Massó* is also acknowledged for supplying the boehmite precursor Nyacol®.

## Appendix A. Supplementary data

Supplementary data associated with this article can be found, in the online version, at <https://doi.org/10.1016/j.jeurceramsoc.2021.04.060>.

## References

- [1] C.B. Mo, S.I. Cha, K.T. Kim, K.H. Lee, S.H. Hong, Fabrication of carbon nanotube reinforced alumina matrix nanocomposite by sol–gel process, *Mater. Sci. Eng. A* 395 (2005) 124–128.
- [2] M.K. Satam, L. Gurnani, S. Vishwanathe, A. Mukhopadhyay, Development of carbon nanotube reinforced bulk polycrystalline ceramics with intragranular carbon nanotube reinforcement, *J. Am. Ceram. Soc.* 99 (2016) 2905–2908.
- [3] P. Rivero-Antúnez, R. Cano-Crespo, L. Esquivias, N. de la Rosa-Fox, C. Zamora-Ledezma, A. Domínguez-Rodríguez, V. Morales-Florez, Mechanical characterization of sol–gel alumina-based ceramics with intragranular reinforcement of multivalled carbon nanotubes, *Ceram. Int.* 46 (2020) 19723–19730.
- [4] M. Piñero, M.M. Mesa-Díaz, D. de los Santos, M.V. Reyes-Peces, J.A. Díaz-Fraile, N. de la Rosa-Fox, L. Esquivias, V. Morales-Florez, Reinforced silica-carbon nanotube monolithic aerogels synthesised by rapid controlled gelation, *J. Sol–Gel Sci. Technol.* 86 (2018) 391–399.
- [5] L. Esquivias, P. Rivero-Antúnez, C. Zamora-Ledezma, A. Domínguez-Rodríguez, V. Morales-Florez, Intragranular carbon nanotubes in alumina-based composites for reinforced ceramics, *J. Sol–Gel Sci. Technol.* 90 (2019) 162–171.
- [6] V. Verma, S.C. Galaveen, L. Gurnani, T. Venkateswaran, A. Mukhopadhyay, Development of oxidation resistant and mechanically robust carbon nanotube reinforced ceramic composites, *Ceram. Int.* 46 (2020) 21784–21789.
- [7] I. Levin, D. Brandon, Metastable alumina polymorphs: crystal structures and transition sequences, *J. Am. Ceram. Soc.* 81 (1998) 1995–2012.
- [8] R. Cano-Crespo, B. Malmal Moshaghiooun, D. Gómez-García, A. Domínguez-Rodríguez, R. Moreno, High-temperature creep of carbon nanofiber-reinforced and graphene oxide-reinforced alumina composites sintered by spark plasma sintering, *Ceram. Int.* 43 (2017) 7136–7141.
- [9] J.G. Santanach, A. Weibel, C. Estourns, Q. Yang, C. Laurent, A. Peigney, Spark plasma sintering of alumina: study of parameters, formal sintering analysis and hypotheses on the mechanism(s) involved in densification and grain growth, *Acta Mater.* 59 (2011) 1400–1408.
- [10] Z. Shen, M. Johnsson, Z. Zhao, M. Nygren, Spark plasma sintering of alumina, *J. Am. Ceram. Soc.* 85 (2002) 1921–1927.
- [11] J.A. Hedvall, *Reaktionsfähigkeit fester Stoffe*, 1st ed., Leipzig, J.A. Barth, 1938 <https://doi.org/10.1002/bbpc.19380440414>.
- [12] P. Souza-Santos, H. Souza-Santos, S. Toledo, Standard transition aluminas. Electron microscopy studies, *Mater. Res.* 3 (2000) 104–114.
- [13] F. Cardarelli, *Materials Handbook*, 2nd ed., Springer London, London, 2008 <https://doi.org/10.1007/978-1-84628-669-8>.
- [14] A.C.D. Chaklader, R.C. Cook, Kinetics of reactive hot-pressing of clays and hydroxides, *Am. Ceram. Soc. Bull.* 47 (1968) 712–716.
- [15] D.I. Matkin, W. Munro, T.M. Valentine, The fabrication of  $\alpha$ -alumina by reactive hot-pressing, *J. Mater. Sci.* 6 (1971) 974–980.
- [16] P.A. Badkar, J.E. Bailey, H.A. Barker, Sintering behaviour of boehmite gel, in: G. C. Kuczynski (Ed.), *Sintering and Related Phenomena*, 1st ed., Springer US, Boston, MA, 1973, pp. 311–321, [https://doi.org/10.1007/978-1-4615-8999-0\\_27](https://doi.org/10.1007/978-1-4615-8999-0_27).
- [17] A.C.D. Chaklader, Reactive hot-pressing of aluminas, *J. Am. Ceram. Soc.* 61 (1978) 252–257.
- [18] C. Boussquet, C. Elissalde, C. Aymonier, M. Maglione, F. Cansell, J.M. Heintz, Tuning Al<sub>2</sub>O<sub>3</sub> crystallinity under supercritical fluid conditions: effect on sintering, *J. Eur. Ceram. Soc.* 28 (2008) 223–228.
- [19] A.C. Zaman, C.B. Üstündag, C. Kaya, Boehmite derived surface functionalized carbon nanotube-reinforced macroporous alumina ceramics, *J. Eur. Ceram. Soc.* 30 (2010) 2525–2531.
- [20] M. Kumagai, G.L. Messing, Controlled transformation and sintering of a boehmite Sol–Gel by  $\alpha$ -alumina seeding, *J. Am. Ceram. Soc.* 68 (1985) 500–505.
- [21] A.C. Zaman, C.B. Üstündag, A. Çelik, A. Kara, F. Kaya, C. Kaya, Carbon nanotube/boehmite-derived alumina ceramics obtained by hydrothermal synthesis and spark plasma sintering (SPS), *J. Eur. Ceram. Soc.* 30 (2010) 3351–3356.
- [22] R. Bauer, Process for Production of Alpha Alumina Bodies by Sintering Seeded Boehmite Made From Alumina Hydrates, 1987.
- [23] M. Kumagai, G.L. Messing, Enhanced densification of boehmite sol–gels by  $\alpha$ -alumina seeding, *J. Am. Ceram. Soc.* 67 (1984) c230–c231.
- [24] A.C. Zaman, C.B. Üstündag, N. Kuskonmaz, F. Kaya, C. Kaya, 3-D micro-ceramic components from hydrothermally processed carbon nanotube-boehmite powders by electrophoretic deposition, *Ceram. Int.* 36 (2010) 1703–1710.
- [25] C. Barrera-Solano, L. Esquivias, G.L. Messing, Effect of preparation conditions on phase formation, densification, and microstructure evolution in La- $\beta$ -Al<sub>2</sub>O<sub>3</sub>/Al<sub>2</sub>O<sub>3</sub> composites, *J. Am. Ceram. Soc.* 82 (1999) 1318–1324.
- [26] R. Cano-Crespo, P. Rivero-Antúnez, D. Gómez-García, R. Moreno, A. Domínguez-Rodríguez, The possible detriment of oxygen in creep of alumina and zirconia ceramic composites reinforced with graphene, *Materials* 14 (2021) 1–17.
- [27] S. Brunauer, P.H. Emmett, E. Teller, Adsorption of gases in multimolecular layers, *J. Am. Chem. Soc.* 60 (1938) 309–319.
- [28] C.A. Schneider, W.S. Rasband, K.W. Eliceiri, NIH image to ImageJ: 25 years of image analysis, *Nat. Methods* 9 (2012) 671–675.
- [29] M.M. Renjo, L. Čurković, D. Corić, Influence of surface roughness of alumina ceramics on indentation size, *Mater. Test.* 56 (2014) 32–39.
- [30] D.K. Shetty, A.R. Rosenfield, W. Duckworth, Analysis of indentation crack as a wedge-loaded half-penny crack, *J. Am. Ceram. Soc.* 68 (1985) C-65–C-67.
- [31] H. Miyazaki, Y.I. Yoshizawa, Correlation of the indentation fracture resistance measured using high-resolution optics and the fracture toughness obtained by the single edge-notched beam (SEPB) method for typical structural ceramics with various microstructures, *Ceram. Int.* 42 (2016) 7873–7876.
- [32] H. Miyazaki, Y. Yoshizawa, A reinvestigation of the validity of the indentation fracture (IF) method as applied to ceramics, *J. Eur. Ceram. Soc.* 37 (2017) 4437–4441.
- [33] G.K. Williamson, W.H. Hall, X-ray line broadening from filed aluminium and wolfram, *Acta Metall.* 1 (1953) 22–31.
- [34] B.E. Warren, B.L. Averbach, The effect of cold-work distortion on X-ray patterns, *J. Appl. Phys.* 21 (1950) 595–599.
- [35] S.H. Neher, H. Klein, W.F. Kuhs, Determination of crystal size distributions in alumina ceramics by a novel X-ray diffraction procedure, *J. Am. Ceram. Soc.* 101 (2018) 1381–1392.
- [36] I. Nettlehip, R.J. McAfee, W.S. Slaughter, Evolution of the grain size distribution during the sintering of alumina at 1350°C, *J. Am. Ceram. Soc.* 85 (2002) 1954–1960.
- [37] J. Zhang, F. Shi, J. Lin, S.Y. Wei, D. Chen, J.M. Gao, Z. Huang, X.X. Ding, C. Tang, Nanoparticles assembly of boehmite nanofibers without a surfactant, *Mater. Res. Bull.* 43 (2008) 1709–1715.
- [38] B. Ratzker, A. Wagner, S. Kalabukhov, S. Samuha, N. Frage, Non-uniform microstructure evolution in transparent alumina during dwell stage of high-pressure spark plasma sintering, *Acta Mater.* 199 (2020) 469–479.
- [39] J.A. Bejarano-Palma, B.M. Moshtaghiooun, F.L. Cumbre-Hernández, D. Gómez-García, Motrice Forces Involved in the Grain Growth of Ceramics Under Electric Fields Applied During Spark Plasma Sintering, 2020. [https://congreso2020.secv.es/wp-content/uploads/2020/10/IP05142-OV-JA.Bejarano-LVIIICongr201013-193\\_6.pdf](https://congreso2020.secv.es/wp-content/uploads/2020/10/IP05142-OV-JA.Bejarano-LVIIICongr201013-193_6.pdf).
- [40] G. Lee, E.A. Olevsky, C. Manière, A. Maximenko, O. Izhvanov, C. Back, J. McKittrick, Effect of electric current on densification behavior of conductive ceramic powders consolidated by spark plasma sintering, *Acta Mater.* 144 (2018) 524–533.
- [41] Z. Trzaska, A. Couret, J.P. Monchoux, Spark plasma sintering mechanisms at the necks between TiAl powder particles, *Acta Mater.* 118 (2016) 100–108.
- [42] C. Legros, C. Carry, P. Bowen, H. Hofmann, Sintering of a transition alumina: effects of phase transformation, powder characteristics and thermal cycle, *J. Eur. Ceram. Soc.* 19 (1999) 1967–1978.
- [43] K. Yasuda, J. Tatami, K. Asada, Y. Matsuo, S. Kimura, Influence of crack propagation path on the fracture toughness of polycrystalline Al<sub>2</sub>O<sub>3</sub>, *J. Ceram. Soc. Jpn. Int. ed.* 101 (1993) 1349–1355.
- [44] M.H. Bocanegra-Bernal, C. Domínguez-Ríos, J. Echeberria, A. Reyes-Rojas, A. Garcia-Reyes, A. Aguilar-Elguezabal, Spark plasma sintering of multi-, single- and double- and single-walled carbon nanotube-reinforced alumina composites: is it justifiable the effort to reinforce them? *Ceram. Int.* 42 (2016) 2054–2062.
- [45] I. Ahmad, H. Cao, H. Chen, H. Zhao, A. Kennedy, Y.Q. Zhu, Carbon nanotube toughened aluminium oxide nanocomposite, *J. Eur. Ceram. Soc.* 30 (2010) 865–873.
- [46] N. Miyazaki, T. Hoshida, Influence of porosity and pore distributions on strength properties of porous alumina, *J. Mater. Eng. Perform.* 27 (2018) 4345–4354.
- [47] M. Michálek, K. Boďišová, M. Michálková, J. Sedláček, D. Galusek, Alumina/MWCNTs composites by aqueous slip casting and pressureless sintering, *Ceram. Int.* 39 (2013) 6543–6550.
- [48] J. Sun, L. Gao, X. Jin, Reinforcement of alumina matrix with multi-walled carbon nanotubes, *Ceram. Int.* 31 (2005) 893–896.
- [49] J. Gong, J. Wu, Z. Guan, Examination of the indentation size effect in low-load vickers hardness testing of ceramics, *J. Eur. Ceram. Soc.* 19 (1999) 2625–2631.
- [50] R. Demichelis, Y. Noel, B. Civalieri, C. Roetti, M. Ferrero, R. Dovesi, The vibrational spectrum of  $\alpha$ -AlOOH diaspore: an ab initio study with the CRYSTAL code, *J. Phys. Chem. B* 111 (2007) 9337–9346.

## Chapter 6

# Sol–gel method and reactive SPS for novel alumina–graphene ceramic composites

This chapter is about the natural continuation of the main theme of the thesis. In it, the knowledge acquired about how to disperse carbon phases via sol-gel is combined with the advantages of reactive SPS sintering. As a result, a series of alumina composites with different concentrations of graphene oxide (GO) are obtained, and their structural and mechanical properties are studied

The fabrication process was improved employing a “maximum volume” strategy to ensure the lowest graphene concentration and most homogeneous distribution during the liquid stage of the boehmite sol-gel route, prior to gelation. The use of reactive sintering also facilitated the manufacturing process of alumina/GO ceramics by avoiding time-consuming intermediate steps such as pre-calcination under an inert atmosphere. The ceramic samples were produced at a lower sintering temperature (1200 °C), which would allow for further industrial scalability of the process.

The SEM observations revealed the efficacy of this fabrication approach, with no apparent presence of large graphene agglomerations for the lowest concentrations of

---

graphene. Raman mapping analyses confirmed the integrity of the GO along the fabrication process, and the improvement in the dispersion of the GO as a result of the sol-gel based procedure, compared to conventional methods. The mechanical features of the composite, such as hardness, Young's modulus and indentation fracture toughness, were comparable to those of conventional alumina/GO CMCs or pure alumina. Despite there are improvements in the dispersion of the GO and the chemical relationship between the GO and the matrix, the mechanical behavior of the composite is still driven by other factors such as the extremely high content of graphene. However, this approach offers a promising route to fabricate CMCs with better dispersion of the reinforcing phase without compromising their mechanical properties.



Contents lists available at ScienceDirect

Journal of the European Ceramic Society

journal homepage: [www.elsevier.com/locate/jeurceramsoc](http://www.elsevier.com/locate/jeurceramsoc)



## Sol-gel method and reactive SPS for novel alumina-graphene ceramic composites

Pedro Rivero-Antúñez<sup>a,b,\*</sup>, Camilo Zamora-Ledezma<sup>c</sup>, Florentino Sánchez-Bajo<sup>d</sup>,  
Juan Carlos Moreno-López<sup>e</sup>, Eric Anglaret<sup>f</sup>, Víctor Morales-Flórez<sup>a,b</sup>

<sup>a</sup> Departamento de Física de la Materia Condensada, Universidad de Sevilla, Sevilla 41012, Spain

<sup>b</sup> Instituto de Ciencia de Materiales de Sevilla, Centro Mixto CSIC-Universidad de Sevilla, Sevilla 41092, Spain

<sup>c</sup> Tissue Regeneration and Repair Group, Orthobiology, Biomaterials and Tissue Engineering, UCAM - Universidad Católica de Murcia, Campus de los Jerónimos 135, Guadalupe, 30107 Murcia, Spain

<sup>d</sup> Departamento de Física Aplicada, Escuela de Ingenierías Industriales, Universidad de Extremadura, Avda de Elvas s/n, 06006 Badajoz, Spain

<sup>e</sup> Faculty of Physics, University of Vienna, Boltzmanngasse 5, 1090 Vienna, Austria

<sup>f</sup> Université Montpellier 2, Laboratoire Charles Coulomb, UMR 5521 CNRS, 34095 Montpellier, France

### ARTICLE INFO

#### Keywords:

$\alpha$ -Al<sub>2</sub>O<sub>3</sub>-graphene oxide composite  
Reactive SPS  
Sol-gel  
Raman mapping  
Mechanical properties

### ABSTRACT

Reinforced ceramic matrix composites of alumina and graphene oxide have been widely researched, but there are still unresolved issues such as the optimum distribution of the graphene or the presence of efficient bonds between filler and matrix. This work introduces a novel fabrication procedure based on the sol-gel method, using boehmite as an alumina precursor, and graphene oxide nanoplatelets as the reinforcing phase. Full densification of the samples was done through reactive spark plasma sintering under milder conditions than usual. Structural characterization was done by XRD, SEM and micro-Raman among other techniques, and the presence of Al-O-C bonds was studied by XPS. Mechanical characterization was performed by Vickers microindentation and nanoindentation. No significant change was observed concerning the Young's modulus, hardness or fracture toughness, though improvements in the homogeneity of the distribution of the graphene and the chemical bonds between the matrix and the reinforcing phase were confirmed.

### 1. Introduction

The driving force behind the research on alumina-based ceramic matrix composites (CMC) is the development of reinforced materials by the inclusion of toughening additives. In this context, low dimensional carbon allotropes such as graphene or carbon nanotubes (CNT) have gained considerable attention in the last decades [1–3]. Recently, Shah et al. [4] observed substantial improvements in the mechanical properties of alumina with low graphene content obtained by physical dispersion methods and Spark Plasma Sintering (SPS). However, despite some selected reported improvements on the mechanical properties, many other papers show an erratic influence of the graphene on the fracture toughness of the alumina-based composites [2,5,6]. Thus, no significant and unquestionable improvement can be concluded, and even the reinforcing strategy has been questioned itself [7,8]. The main alleged causes of the observed limitations on the mechanical improvements are based on the fabrication process [5,9]. For example, the presence of graphene aggregates acting as defects in the composite

material has been reported, despite the fact that the dispersion of graphene is expected to be relatively easy to control. Moreover, the lack of an appropriate bond between the reinforcing graphene and the alumina matrix may hinder the efficiency of the expected reinforcing mechanisms, such as bridging or crack deflection [10,11].

Generally, improvements of the quality of the spatial distribution of carbon allotropes and the verification of the absence of aggregates have been assessed very often, but usually through local explorations by SEM, TEM or other techniques [3,12–14]. But the statistical representation of the sample through results obtained by these local techniques is questionable and the results continue to be unclear, since, as claimed by some [15,16], there is no standard with which to estimate the quality of the dispersion or to definitively determine the presence (or absence) of agglomerates at the large scale [7,16].

Nevertheless, significant efforts have been made to quantify the quality of the dispersion of carbon allotropes through global measures, instead of local measures such as SEM or TEM. For example, Pal et al.

\* Correspondence to: Department of Condensed-Matter Physics, University of Seville, P.O. 1065, Seville 41080, Spain.

E-mail addresses: [privero@us.es](mailto:privero@us.es) (P. Rivero-Antúñez), [czamora9@ucam.edu](mailto:czamora9@ucam.edu) (C. Zamora-Ledezma), [fsanbajo@unex.es](mailto:fsanbajo@unex.es) (F. Sánchez-Bajo), [juan.moreno@univie.ac.at](mailto:juan.moreno@univie.ac.at) (J.C. Moreno-López), [eric.anglaret@umontpellier.fr](mailto:eric.anglaret@umontpellier.fr) (E. Anglaret), [vmorales@us.es](mailto:vmorales@us.es) (V. Morales-Flórez).  
URL: <http://grupo.us.es/fqm393/> (V. Morales-Flórez).

<https://doi.org/10.1016/j.jeurceramsoc.2022.10.043>

Received 26 July 2022; Received in revised form 7 October 2022; Accepted 15 October 2022

Available online 22 October 2022

0955-2219/© 2022 Elsevier Ltd. All rights reserved.

[17] explored EDAX mapping as a way to clarify the location of 3 wt% CNTs inside an alumina matrix. In addition to these techniques, there has been used Raman spectroscopy, which has been widely considered as a reliable tool to check the integrity of the carbon nanophase throughout the fabrication of the sample [18–21], or to study the distribution of the nano-reinforcements in the matrix [22,23]. In this work, Raman mapping with high spatial resolution is proposed as an appealing alternative for depicting the spatial distribution of the graphene for the first time, and the obtained maps will be considered for assessing an objective quantification of the quality of the dispersion of the graphene in the ceramic matrix.

In this context, CMCs obtained by the sol–gel procedures have been proven as a modern alternative, and appear to be an useful route to fabricate novel alumina-based composites with CNT and/or graphene with tailored physico-chemical properties [4,24,25], and several papers have reported interesting mechanical improvements [5,20,26]. As the sol–gel method starts in the liquid sol phase, it is expected to facilitate the dispersion of the graphene phase and its homogeneous distribution throughout the composite. In addition, it is also expected to enhance the formation of bonds through bridging oxygens between the reinforcing phase and the matrix due to the presence of hydroxyl groups in the graphene oxide during the condensation step. However, the fabrication of alumina-based ceramics with graphene through the sol–gel method has hardly been researched.

In summary, while these fabrication problems are not resolved, fundamental questions such as, to what extent is the reinforcing strategy based on the addition of carbon allotropes being efficiently used? or, what is the maximum toughening that can be expected from this reinforcing strategy?, will remain unanswered and, therefore, the viability of this reinforcing strategy will continue to be subject to debate. Thus, there is still room for improvements of the processing techniques to achieve the most efficient transfer of the outstanding nanomechanical properties of graphene to the macroscopic properties of the composites [27].

With the aim of contributing to solve these fundamental problems, we present a new procedure for the fabrication of fully-dense alumina/graphene ceramic matrix composites (GCMC) based on the innovative combination of the sol–gel method and reactive spark plasma sintering (rSPS), as an alternative route promoting the dispersion of the graphene oxide in the composite, and to improve the formation of efficient bonds between the alumina matrix and the graphene.

## 2. Materials and methods

### 2.1. Materials

Boehmite colloidal dispersion ( $\gamma$ -AlOOH - AL20DW) was acquired from Nyacol Nano Technologies, Inc. (density = 1.19 g/cm<sup>3</sup>, dispersed sizes of 60–90 nm, crystallite size of 15 nm, 23.5 wt% AlOOH). This sol is made with deionized water to reduce the sodium and chlorine levels to less than 10 ppm. Graphene oxide flakes (GO) were purchased from Graphenea Inc., and synthesized by the oxidation of natural graphite powder through a modified Hummers method with two oxidation stages, which guarantees single layer graphene exfoliation. Regarding the supplier, the as-received 4 wt% GO wet slurry has a monolayer content  $\geq 95\%$ , and an average lateral size of about 10  $\mu\text{m}$  and a chemical composition of 49%–56% carbon, 41%–50% oxygen with a remnant sulfur content about 2%–4%. During the preparation of the samples, in order to guarantee the highest percentage of monolayer flakes, our aqueous GO dispersions were systematically bath sonicated prior to use, as they tend to slightly agglomerate with time. Aqueous ammonia (NH<sub>3</sub>) 30% was acquired from Panreac. Powder of  $\alpha$ -Al<sub>2</sub>O<sub>3</sub> seeds (99% purity, particle size = 30–40 nm) came from Nanostructured and Amorphous Materials, Inc.

### 2.2. Fabrication of the alumina/graphene ceramic matrix composites (GCMC)

In order to optimize the homogeneity and dispersion of the GO in the matrix during the fabrication of the GCMC, we adapted an original procedure based on the sol–gel method and the reactive SPS [25]. In a typical procedure, 30 mL of the commercial boehmite sol are mixed with 145 mg of  $\alpha$ -Al<sub>2</sub>O<sub>3</sub> seeds, i.e., the 2 wt% of the total amount of alumina in the final sample, and homogenized for 24 h by mechanical stirring at room temperature to promote direct crystallization of the  $\alpha$ -Al<sub>2</sub>O<sub>3</sub> during the sintering, due to the multiple nucleation sites [25]. Separately, the required amount of GO slurry to obtain the desired graphene wt.% content in the ultimate solid components was slowly poured into a beaker with 350 mL of distilled water. This volume of water was experimentally obtained as the maximum volume in which the required amount of the used boehmite sol will form a gel. Hence, this maximum volume aims to facilitate the dispersion and homogeneous distribution of the GO flakes throughout the whole volume of the liquid sol prior to gelation. The GO suspension was homogenized by a pulsed ultrasound tip-sonication for 7 min, with square pulses (time on: 1.4 s, time off: 0.6 s).

The gel was obtained by pouring the previously described seeded boehmite sol into the GO suspension under high power ultrasound and adding, drop by drop, aqueous ammonia until rapid controlled gelation [28]. All the dispersions were gelled in an ice tank to avoid sample overheating due to the tip sonication. The processes of GO dispersion, boehmite addition, and gelation, typically occur within 20 to 25 min. The obtained gels were dried in a stove at 80 °C for 48 h. Then, dry xerogel powders were pulverized in an alumina mortar, and sieved <212  $\mu\text{m}$ . Sample powders were labeled with the code GRALX-p, where the X indicates the wt.% of GO of the composite after the following sintering, and the suffix “-p” is used to indicate the powder phase prior to sintering. The GO content (X) in the final solid GCMCs varies from 0.0 to 6.0 wt%.

The powders were densified by reactive Spark Plasma Sintering (rSPS) in a Dr. Sinter Lab Inc. equipment, model 515 S machine (Kanagawa, Japan, 0–1500 A pulsed DC current). Under 75 MPa of constant uniaxial pressure, the samples were heated at 100 °C/min up to 1200 °C for 5 min, and cooled at 50 °C/min, reproducing the conditions reported by Rivero-Antúnez et al. [25], but reducing by 100 °C the plateau temperature, in coherence with previous conclusions. This reactive sintering process is an effective protocol to synthesize  $\alpha$ -Al<sub>2</sub>O<sub>3</sub>/GO ceramics avoiding intermediate steps like the pre-calcination of the boehmite-GO powders under inert atmosphere to produce a previous transformation of the boehmite into alumina via the dehydroxylation of the aluminum oxyhydroxide, as this step leads to the formation of intermediate metastable crystalline phases (i.e.  $\gamma$ -Al<sub>2</sub>O<sub>3</sub>) [6,20,29]. The sintered samples were submitted to the rectification–cutting–embedding–polishing (RCEP) protocol in order to display a flat micro-scale polished surface for structural and mechanical characterization. More details can be found in Ref. [25]. The sintered samples were labeled with the code GRALX, where X denotes the wt.% of the GO. Fig. 1 summarizes the experimental process used to fabricate this alumina-based GCMC.

A reference sample with 2.0 wt% of GO was fabricated by a conventional procedure, mixing the  $\alpha$ -Al<sub>2</sub>O<sub>3</sub> powder (the same used as the seeds in the sol–gel samples) directly in a beaker with 350 mL of distilled water, where the pertinent amount of graphene slurry was dispersed with the help of ultrasound. This mix was mechanically stirred in a hot plate until all the water evaporated. Thus, this “fake” sample was obtained without sol–gel process, and was not densified by reactive SPS, but by conventional SPS, as no phase change is happening during the sintering of this sample. The powder was labeled GRAL2F-p and the sintered composite, GRAL2F. This sample was considered for the specific study of the influence of the sol–gel method and reactive sintering on the physical properties of these GCMC.

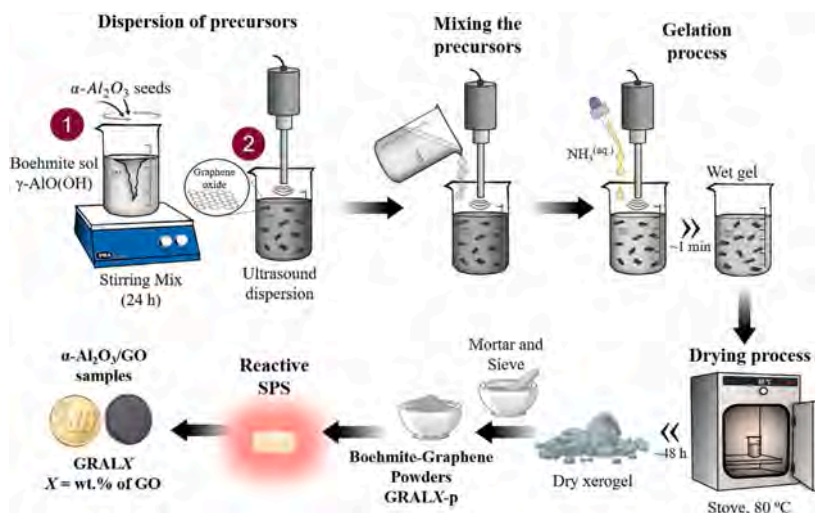


Fig. 1. Sketch summarizing the sol-gel fabrication procedure of alumina/graphene samples.

### 2.3. Experimental characterization

#### 2.3.1. Densities and composition

The densities of all the sintered samples were measured by Archimedes's method using distilled water at 20 °C, and compared with the theoretical densities of the composites estimated through Eq. (1), assuming  $\rho_A = 3.985$  and  $\rho_G = 2.1$  g/cm<sup>3</sup> as the theoretical bulk densities of alumina and GO, respectively [24,30], and with X being the wt.% of GO in the biphasic composite:

$$\rho = \frac{\rho_A \rho_G}{\rho_A \frac{X}{100} + \rho_G \left(1 - \frac{X}{100}\right)} \quad (1)$$

Thermal gravimetric analyses (TGA) were performed in an STD Q600 device from TA Instruments Inc. Under an Ar or an air flux of 100 mL/min, the samples were heated to 1000 °C (heating ramp: 2 or 10 °C/min) from room temperature. The mass losses occurring at two critical ranges were specially examined: from 200 to 450 °C, assigned to the boehmite dehydroxylation, and from 450 to 650 °C, where the carbonaceous phases burn out under an oxidative atmosphere.

#### 2.3.2. Microstructural characterization

The nitrogen adsorption/desorption isotherms of powder composites were obtained with a Micromeritics ASAP 2010 (*Accelerated Surface Area and Porosimetry System*), armed with a pressure transducer that allows a resolution of 10<sup>-4</sup> mm Hg. Prior to an N<sub>2</sub> physisorption analysis at -196 °C, the samples were degassed for 2 h at 150 °C under a N<sub>2</sub> flux. The specific pore volume, pore size, pore size distribution, and specific surface area were obtained using BJH and BET models for the analyses of the isotherms.

The crystallographic structures of the samples were investigated by X-ray powder diffraction (XRD), using a Bruker D8I-90, by the step-scanning technique with a range from  $2\theta = 10^\circ$  to  $120^\circ$ , step of  $\Delta\theta = 0.015^\circ$ , counting time of 0.5 s, using Cu-K $\alpha$  radiation (K $\alpha_1$  + K $\alpha_2$  doublet) with no monochromator, operating at 40 kV and 30 mA, and the sample rotating at 30 rpm. The crystalline phases of our samples were identified following reported patterns diffraction files. The analysis of the XRD data was performed by using the program MAUD (Materials Analysis Using Diffraction, v.2.94; [31]), based on the Rietveld method [32]. A model was fitted to the whole diffractograms using the following parameters as free: the coefficients of a polynomial function describing the background (up to fifth order in most cases);

the scale parameter; the cell parameters of the  $\alpha$ -Al<sub>2</sub>O<sub>3</sub>, *a* and *c*; the *z* fractional coordinate of Al and the *x* fractional coordinate of O; the mean crystallite size and the r.m.s. strain assuming an isotropic model. As the standard for the microstructure analysis, a previously sintered sample [25] of  $\alpha$ -Al<sub>2</sub>O<sub>3</sub> with micrometric grain size was considered, and measured under the same experimental conditions. Further details on the analysis of the samples and the consideration of the effects of the preferred orientations can be found in the Supplementary Material (SM).

Transmission Electron Microscopy (TEM) was performed with a Philips CM-200 device, and Scanning Electron Microscopy (SEM) images were acquired by using two scanning electron microscopes with field emission gun (SEM-FEG) (Hitachi S5200 and FEI Teneo). The SEM operation voltage ranged from 5 to 20 kV, and the magnification from  $\times 4000$  to  $\times 12000$  depending on the samples. To measure the grain size, with the help of ImageJ software, dozens of SEM micrographs were analyzed, and more than 300 grains per surface were studied for the statistics, differentiating between a surface perpendicular to the loaded axis during the sintering (in-plane, "ip"), and a parallel one (cross-section, "cs"). The size of a grain was calculated as the diameter of a circle with equivalent area.

#### 2.3.3. Raman analysis and mapping (RAM)

The Raman spectroscopy measurements were carried with a Renishaw Invia Raman Spectrometer excited by solid-state green/red laser lines ( $\lambda = 532$  nm and 633 nm), and equipped with a  $\times 100$  microscope objective and a CCD camera. Before any acquisitions, the spectrometer was calibrated using as a reference the *T*<sub>2g</sub> mode of a piece of silicon, located at 520.5 cm<sup>-1</sup> at room temperature. The data were treated with manual baselines to remove background signals generated by residual Rayleigh scattering or fluorescence. Regarding the mapping technique, the maps were acquired in square grids of 50  $\times$  50 points, a total of 2500 spectral acquisitions per surface, using green laser and two accumulations per acquisition (with automatic cosmic ray removal), covering a total area of 2500  $\mu$ m<sup>2</sup>. After the acquisitions, a common baseline was applied to all the spectra, and maps were created displaying the ratio between the intensities of selected spectral signatures of GO and alumina. It could be ruled out that there was any significant effect on the results from any heating of the sample due to the long exposure to laser irradiation.

### 2.3.4. X-ray Photoelectron Spectroscopy (XPS)

XPS experiments were performed at normal emission using a PHOIBOS HSA3500 MCD-9 device. All photoemission spectra were treated with the Shirley background subtraction [33], and then fitted by a Gaussian function convolved with a Lorentzian function. The Full Width at Half Maximum (FWHM) of the peaks was calculated using the following equation:

$$FWHM = 0.5346 \cdot w_L + \sqrt{0.2166w_L^2 + w_G^2} \quad (2)$$

where  $w_L$  and  $w_G$  are the Lorentzian and Gaussian FWHM, respectively.

After subtracting the Shirley background, the XPS spectra were fitted using a Voigtian profile, taking into account a Gaussian contribution of 1.60 eV associated with the spectrometer's resolution, while the charging broadening and sample inhomogeneity were convolved with a Lorentzian peak of 0.36 eV. The total FWHM of our peaks used for the fitting was 1.82 eV.

### 2.3.5. Mechanical properties

The hardness and fracture toughness were measured using a Buehler Wilson VH1150 MicroVickers Hardness Tester with a load of 10 kgf applied during 10 s of dwell time. For each surface, at least 10 indentations were made. The fracture toughness ( $K_{Ic}$ ), expressed in  $MGf^{1/2}$ , was estimated by the Vickers Indentation Fracture Resistance ( $K_{IFR}$ ) method, which employs Shetty's median cracks model [34] and Eq. (3). This equation has been proven to be the most accurate for fully-dense polycrystalline alumina [35]:

$$K_{IFR} = 0.023(E/H)^{1/2} P/c^{3/2} \quad (3)$$

where  $E$  is the elastic modulus,  $H$  is the hardness,  $P$  is the applied indentation force, and  $c$  is the length of the crack from the center of the print. SEM and optical imaging were used to assess the propagation of the cracks, fracture surfaces, and microstructures. Nanoindentation experiments were also performed to characterize the Young's moduli,  $E$ , of the samples. A KLA G200X nanoindenter was employed, working with a diamond Berkovich tip and a maximum load of 20 mN, under the NanoBlitz 3D mode, which allowed 2500 indentations on each sample with a 2  $\mu$ m spacing between indents. The standard deviations were used as the uncertainties of the obtained average values.

## 3. Results and discussion

### 3.1. Characterization of the powders

The precursor powders of alumina and graphene oxide obtained by this sol-gel procedure were investigated by TGA, nitrogen physisorption, SEM, and XRD prior to their sintering. The aim of this research was to study how the graphene was distributed within the boehmite gel and to characterize (if possible) the quality of the dispersion, revealing the presence (or absence) of aggregates prior to densification. Firstly, TGA analyses revealed the thermal stability of the GO and the precursor powder series (Fig. SM1). The sample of pure graphene oxide exhibited a 40% mass loss in the range of 100 °C to ~300 °C suggesting the decomposition of oxygen-containing functional groups such as carboxyl (-OOH), hydroxyl (-OH), and carbonyl (-O), in the form of water, CO, and CO<sub>2</sub> [36]. Therefore, reduced graphene oxide (rGO) is expected to appear above this temperature. For temperatures from 400 °C up to 1000 °C, in spite of the inert nature of the Ar atmosphere, a weight loss of 53% was registered. Thus, a significant contribution to the mass loss

during TGA is due to the fact that during the release of gasses due to dehydroxylation and decarboxylation, the argon flux can be dragging some of the outer graphene layers. The TGA curve for GO corroborated this: at a rate of 10 °C/min, a weight loss of 80% abruptly took place at 150 °C (Fig. SM1). On the other hand, the TGA of the composite powder series revealed a weight loss of 18% between 250 and 470 °C corresponding to the dehydroxylation of the boehmite, close to the stoichiometric weight loss of -15% [20,25]. See a representative curve corresponding to the powder of GRAL2-p also plotted in Fig. SM1.

Structural characterization by N<sub>2</sub> physisorption at 77 °C was performed for the boehmite/graphene composite powder series fabricated by the sol-gel method. The obtained isotherms can be seen in Fig. SM2 and the most significant parameters, such as the specific surface area ( $S_{BET}$ ), pore size volume ( $V_p$ ) and diameter ( $D_p$ ), are summarized in Table SM3. There are no important differences between the bare boehmite powders and the as-prepared sample series containing graphene, all of them, except the composite with highest GO wt.% content (GRAL6-p), exhibiting the characteristic values of the basic building blocks of the boehmite gel,  $S_{BET}$  ~160 m<sup>2</sup>/g and  $D_p$  ~7 nm. In addition, these results are similar to the values previously reported in the literature [20,24]. Precursor powder GRAL6-p exhibits a significantly lower specific surface area and higher pore size (99 m<sup>2</sup>/g and 10.5 nm, respectively), revealing a very different spatial arrangement of the boehmite/graphene gel at the microscale, such as some aggregated graphene flakes due to the high graphene content [37].

Electron microscopy images (TEM and SEM) were expected to provide useful information about the level of dispersion of the graphene in the boehmite/GO composite powders, in addition to the morphology and arrangement of the elemental structure of the powder. Firstly, SEM imaging of the lyophilized graphene oxides slurry confirmed the quasi-bidimensional morphology of the platelets, as expected (Fig. 2-a). Moreover, TEM observation (Fig. 2-b, and Fig. SM4) of the boehmite powders showed the orthorhombic shape of the elemental crystallites, whose largest size was below 50 nm [24], as estimated by the N<sub>2</sub> physisorption results previously discussed.

Regarding the composite powders, after several sessions of TEM inspection, the presence of graphene embedded in the powders could not be resolved in an unquestionable way, neither for sample powders with the highest carbon content nor for calcined powders at 1200 °C; there were only images where the presence of graphene could only be barely speculated. SEM was also used for the characterization of the composite powders and the assessment of the quality of the dispersion of the GO. Again, in a disconcerting way, the graphene nanosheets were not found among the boehmite particles after more than ten sessions of SEM inspection, although the powders were clearly black. Nevertheless, the microstructure of the boehmite powder was perfectly resolved (Fig. SM5-left). Hence, graphene oxide nanoplatelets were never found in the black carbonaceous composite boehmite/graphene powders at the microscale. Thus, the total immersion of the graphene nanosheets in the core of the boehmite xerogel and absence of large aggregates of graphene could be guessed (Fig. SM5-right) but the good dispersion of graphene oxide nanosheets among the boehmite particles could not be ascertained.

In order to elucidate the quality of the dispersion of the GO, two additional strategies were also used for the preparation of the powders for microscopic inspection: lyophilization of the wet composite gel to prevent the collapse and compaction of the particulate structure (cryogel-like composite powders), and the calcination of the composite powders at 1200 °C under an inert atmosphere. Although lyophilized composite powders revealed a different microstructure, it was unsuccessful for the revelation of the supposedly embedded graphene nanoplatelets in the gel (not shown). On the contrary, the structure of composite powder GRAL3-p calcined at 1200 °C (GRAL3-p@1200) was observed as the typical vermicules, and graphene wrinkled flakes could be clearly identified (Fig. 2-c), a result comparable to those reported in the literature [18,37].

<sup>1</sup> Based on Profs. C. Ramadas and A. R. Jadhav's suggestion, the use of the unit "griffith" (Gf) was proposed [24] in substitution of the awkward classical magnitude Pa·m<sup>1/2</sup>, where 1 Gf = 1 Pa·m<sup>1/2</sup>, as a tribute to the mechanical engineer Alan Arnold Griffith (1893–1963). Griffith was known in the field of fracture mechanics for his pioneering studies on the nature of stress and failure due to crack propagation in brittle materials.

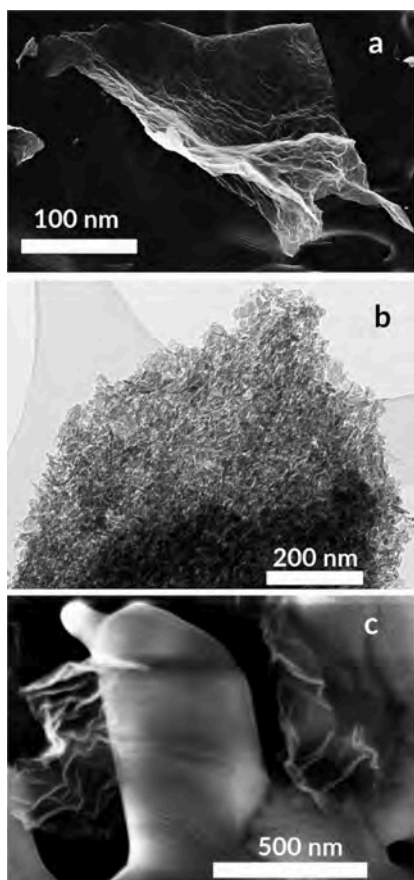


Fig. 2. (a) SEM image of one single lyophilized graphene oxide nanoplatelet. (b) TEM image of powder GRAL3-p showing the typical particulate nanostructure; (c) SEM image of calcined composite powders with 3 wt% graphene oxide, GRAL3-p@1200, where graphene nanosheets can be clearly seen surrounding vermicular particles of alumina.

Finally, the crystallographic nature of the particles observed by electron microscopy was checked by X-ray powder diffraction (XRD), and the exclusive presence of boehmite and  $\alpha$ -Al<sub>2</sub>O<sub>3</sub> seeds precursors was confirmed.

### 3.1.1. Raman analyses of the precursors powders

Firstly, we used Raman spectroscopy to analyze all our precursors: the graphene oxide slurry, the pure boehmite, and the  $\alpha$ -Al<sub>2</sub>O<sub>3</sub> seeds (spectra not shown). The obtained spectra for the graphene oxide flakes exhibited the typical strong peak coming from the D-band (~1350 cm<sup>-1</sup>), which is a second-order double resonant mode activated by defects, and the G and G'-bands located around 1600 cm<sup>-1</sup> and 2700 cm<sup>-1</sup>, respectively [38], where G is a first order mode corresponding to carbon-carbon stretch, and G' is a second-order double resonant mode. In addition, the spectrum for polycrystalline boehmite with well defined signatures at 363, 454, 495, 671, and 1048 cm<sup>-1</sup> [20] was obtained for the dried pure boehmite powder.

On the other hand, the spectra of the crystalline  $\alpha$ -Al<sub>2</sub>O<sub>3</sub> seeds were acquired only in the range from 200 to 1800 cm<sup>-1</sup>, in order to avoid the strong signal attributable to the photoluminescence of the material [20]. Using the green laser, the Raman peaks of the alumina are observed at 378, 418, 645, and 751 cm<sup>-1</sup> [20]. Interestingly, when

the samples are excited with the red laser, the strongest Raman peaks located at 378 and 418 cm<sup>-1</sup> were barely observed, but two extremely strong bands appear at 1368, and 1398 cm<sup>-1</sup> (693 and 694.5 nm for red laser excitation) commonly ascribed to the photoluminescence (PL) of Cr<sup>3+</sup> ions impurities (extrinsic defect) in the  $\alpha$ -Al<sub>2</sub>O<sub>3</sub> seeds. Cr is an element often found as an impurity in alumina materials [39]. Usually, ions with an incomplete 3d shell (such as Cr<sup>3+</sup>) replace some of the Al<sup>3+</sup> ions present in the  $\alpha$ -Al<sub>2</sub>O<sub>3</sub> lattice. The Cr<sup>3+</sup> signatures are referred to as R<sub>1</sub> and R<sub>2</sub> fluorescence lines of ruby, and they are well explained in terms of the transition <sup>2</sup>E→<sup>4</sup>A<sub>2</sub>, from the lowest excited state to the ground state of the Cr<sup>3+</sup>d<sup>3</sup> configuration [40]. In contrast, these PL signals (around 4367.5 and 4397.2 cm<sup>-1</sup>) had not been observed with the green laser because they fall out of the measured range.

When the powder GRAL0-p (reference xerogel powder with no graphene) was exposed to green or red radiation, it presented the typical Raman spectra with the characteristic peaks of boehmite and, when the red laser was used, weak but observable PL signals from Cr<sup>3+</sup> ions impurities in the  $\alpha$ -Al<sub>2</sub>O<sub>3</sub> seeds, located at 1368, and 1398 cm<sup>-1</sup> respectively. Note the very low percentage content of  $\alpha$ -Al<sub>2</sub>O<sub>3</sub> seeds (2 wt% with respect to the final alumina obtained after sintering) in comparison to the boehmite.

Fig. 3 displays the Raman spectra excited with the green laser for the composite powder series fabricated by the sol-gel method (GRALX-p), from X = 0 to 2 wt%. All spectra were normalized with respect to the most intense signal of the boehmite (378 cm<sup>-1</sup>). The Raman spectra of powder samples GRAL3-p and GRAL6-p presented basically the same features as the raw graphene: their graphene signals are so strong that the boehmite signals are in the range of signal noise. As expected, all the spectra exhibited well-defined graphene D, G, and G' peaks around 1350, 1597, and 2706 cm<sup>-1</sup>, respectively, similar to those observed in the as-received raw GO, and with similar intensity ratio I<sub>D</sub>/I<sub>G</sub>, indicating that the structure of the GO is not altered during the sol-gel synthesis process of the powders [20]. In addition, Raman spectra also showed weak but observable characteristic bands of boehmite at 363, 496, 677 and 1050 cm<sup>-1</sup> [20,41,42]. A relative increase of the GO signal with respect to the boehmite is observed for increasing GO concentrations. Thus, the ratio of the intensities of the graphene D and boehmite peaks, I<sub>GO</sub>/I<sub>boeh</sub>, plotted as a function of the GO wt.% (inset in Fig. 3) reveals a clear increasing trend. The sublinear shape is attributed to the increasing self-absorption of the samples with increasing concentrations of the GO. This calibrated trend may be a useful reference for the *a posteriori* estimation of the graphene content for samples obtained by procedures aiming at removing large aggregates of graphene, such as those including filtering and centrifugation.

## 3.2. Structural characterization of the sintered samples

### 3.2.1. Densities

Fully-dense and fine-grained crystalline  $\alpha$ -Al<sub>2</sub>O<sub>3</sub> was readily achieved at lower sintering temperatures, by combining graphene nanoplatelets and boehmite sol seeded with  $\alpha$ -Al<sub>2</sub>O<sub>3</sub> seeds. Table 1 summarizes the theoretical and experimental relative densities of all sintered GCMC (graphene/alumina ceramic matrix composites) with different GO content, obtained through the method of Archimedes. It should be remarked that the phase transformation into stable crystalline  $\alpha$ -Al<sub>2</sub>O<sub>3</sub> happens by nucleation and grain growth under high temperature, and a low density of intrinsic nucleation sites would result in large spaces between them. Many researchers have studied the transformation of alumina-based ceramics paying attention to the microstructure, density and grain size, to increase its mechanical properties. A 2.0 wt% of  $\alpha$ -Al<sub>2</sub>O<sub>3</sub> seeds with respect to the final amount of alumina is equivalent to a 1.7 wt% with respect to the mass of the boehmite. Kumagai and Messing [43] reported that a concentration of 1.5 wt% of  $\alpha$ -Al<sub>2</sub>O<sub>3</sub> seeds (particle size ~ 0.1 μm) in boehmite to be extremely effective for sintering of boehmite gels into fully-dense  $\alpha$ -Al<sub>2</sub>O<sub>3</sub> samples, inspiring the seeding concentrations used in this



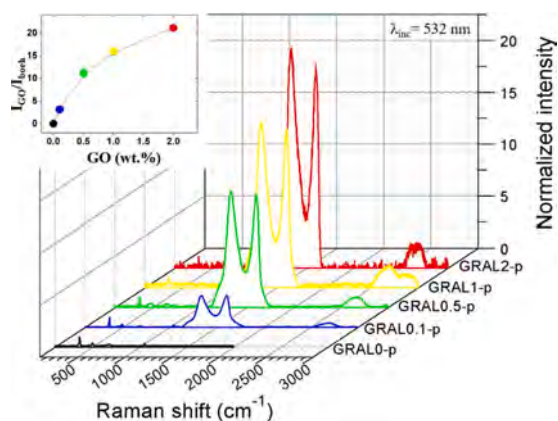


Fig. 3. Raman spectra of the precursor powder series GRALX-p (green laser). “X” indicates the GO wt.% in the samples. Spectra were normalized with respect to the intensity of the boehmite peak at  $418\text{ cm}^{-1}$ . The ratio of the D band of the GO to this peak of the boehmite is plotted in the inset. (For interpretation of the references to color in this figure legend, the reader is referred to the web version of this article.)

Table 1

Theoretical bulk densities estimated with Eq. (1), and relative densities assessed through the method of Archimedes of all sintered GCMC ceramics at different GO contents. Grain size of the two different studied surfaces of each sample (rounded results and uncertainties, not rounded in Fig. 5).

Sample	Theoretical bulk density ( $\text{g/cm}^3$ )	Relative density (%)	Grain size ( $\mu\text{m}$ )	
			in plane	cross section
GRAL0	3.985	$99.7 \pm 0.1$	$0.9 \pm 0.4$	$0.8 \pm 0.4$
GRAL0.5	3.967	$99.7 \pm 0.1$	$1.3 \pm 0.7$	$1.0 \pm 0.6$
GRAL1	3.949	$100.4 \pm 0.7$	$1.0 \pm 0.6$	$0.9 \pm 0.4$
GRAL2	3.914	$100.2 \pm 0.2$	$0.7 \pm 0.4$	$0.7 \pm 0.3$
GRAL3	3.880	$100.1 \pm 0.2$	$0.6 \pm 0.4$	$0.5 \pm 0.3$
GRAL6	3.781	$100.2 \pm 0.4$	$0.5 \pm 0.3$	$0.3 \pm 0.2$

research. In a previous paper [25], we concluded that the considered temperature required for total densification of seeded boehmite by rSPS ( $1300\text{ }^\circ\text{C}$ ) could be significantly reduced. Consequently, in this work, the maximum temperature during the sintering process was set to  $1200\text{ }^\circ\text{C}$  in all samples (with and without graphene). Relative densities  $\sim 100\%$  were achieved in all cases (Table 1), proving that the sintering conditions can be effectively reduced. This is an important feature concerning the microstructure and the mechanical properties of the samples and should be considered for comparisons with other materials.

### 3.2.2. SEM imaging

The investigation of the surface of the composites by SEM provided useful information about the characteristic microstructural features of the samples, and also about the quality of the dispersion of the graphene phase in the sintered ceramic composites. Fig. 4 shows representative SEM images for the sintered samples, and, as expected, a homogeneous micro-sized structure with marked grain boundaries can be seen in all samples, typical of the stable crystalline phase  $\alpha\text{-Al}_2\text{O}_3$  [1,4,18,25,37].

Regarding the grain size of the researched composite materials, one of the most interesting results is the ability of the graphene to inhibit grain growth during sintering. This can be observed in a clear tendency to smaller grain sizes when the GO wt.% increases (see Figs. 4, 5, and Table 1). The grain size in crystalline  $\alpha\text{-Al}_2\text{O}_3$  phases span in a wide range ( $0.1\text{--}10\text{ }\mu\text{m}$ ), and beyond, depending on the nature of the properties of the precursor, the additives, and the sintering conditions [4,18,25,37]. At this scale, GO flakes were found between

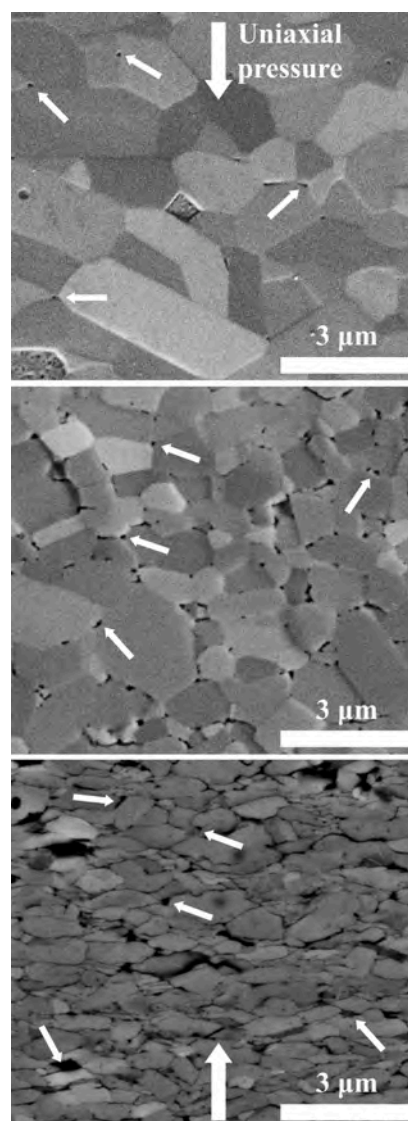


Fig. 4. SEM images of the cross-section surface of sintered composites: GRAL0.5 (top), GRAL2 (center) and GRAL6 (bottom), with 0.5, 2 and 6 wt% GO content, respectively. Large white arrows indicate the direction of uniaxial pressure and pulsed electric field during SPS sintering, as well as the fixed direction for Feret angle measurements. Small arrows point to intergranular graphene.

alumina grains, namely, in intergranular location, acting as barriers that obstruct the growth of the alumina grains [4,18,24,37,44–46].

Interestingly, the addition of GO does not have a continuous effect on decreasing the grain size. The incorporation of small amounts ( $0.5\text{--}1.0\text{ wt}\%$ ) slightly increased the grain size, followed by a reduction of grain size for larger amounts of graphene (Fig. 5). This effect has been previously reported [37,47], although the typically reported behavior is a reduction of grain size, an inhibition of grain growth even with the lowest additions of graphene. Even though the variation of grain size between all the samples could be neglected given the error bars, we think that the clear tendency may be attributed to the competition of a

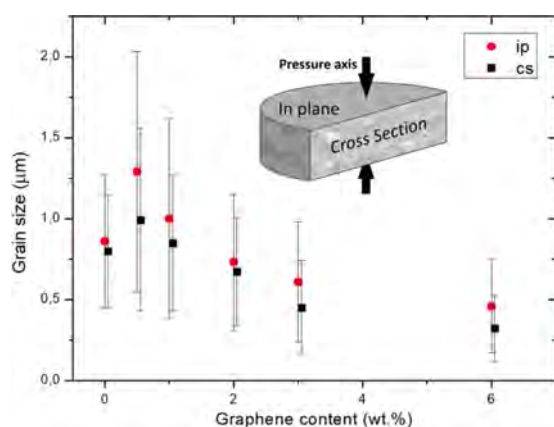


Fig. 5. Grain size of the samples vs. the amount of graphene. Error bars are given for one standard deviation. (Data not rounded, contrary to Table 1). «cross-section» points have been slightly shifted horizontally so they do not overlap with «in-plane» points. Inset: sketch of surfaces studied on each sample, indicating the load axis during sintering.

couple of effects. On the one hand, the inhibition of the growth of the grain size is caused by the intergranular location of graphene blocking grain growth. On the other hand, the addition of graphene increases the electrical and thermal conductivity, improving the heating of the bulk sample and enhancing grain growth. The latter effect seems to be predominant for low concentrations of graphene (<1 wt%), leading to larger grain size than pure alumina without any carbon content.

The sample GRAL6 showed a peculiar grain shape (Fig. 4-bottom). Even though this sample had full density, the gaps or dark regions between grains typically found in low-dense ceramic materials were observed. However, the value of the density leads us to conclude that these dark gaps should be attributed to the presence of graphene agglomerations. This can also be observed in the other samples. For example, in GRAL2 (Fig. 4-center), although the graphene is also located intergranularly and is better dispersed, graphene appears in the form of little black dots located in intergranular positions [45], typically in corners shared by three or more grains (Fig. 4, small white arrows).

Finally, the anisotropy of the samples should be highlighted. The Feret diameter is defined as the maximum segment that can be drawn between any two points of the boundary of a grain, i.e., the maximum caliper. The Feret angle is then the angle between the Feret diameter and an arbitrary fixed direction. In this work, for the cross-section (cs) surfaces, the fixed direction to measure the Feret angle was the pressure axis. For the in-plane (ip) surfaces, the selected direction is any radial direction perpendicular to the loaded axis. All the ip surfaces had an isotropic distribution of grains. On the other hand, the cs surfaces of all the samples presented an anisotropy (Fig. 6), that is, during the sintering, the grain growth was inhibited in the direction of the applied pressure and electric field. Hence, the grains grew preferentially in the plane perpendicular to the pressure axis and/or electric field [25,48].

### 3.2.3. XRD analyses

As a general feature, the intensity of the diffraction peaks on the sintered samples confirmed the presence of the crystalline alpha-alumina (corundum) as the only crystalline phases in the samples. However, clear differences appeared between the large-grain-standard alumina sample and the corundum observed in this sample series. In Fig. 7, an  $\alpha$ -Al<sub>2</sub>O<sub>3</sub> standard sample with coarse-grain (>10 µm) and GRAL2 patterns are compared, revealing strong differences in the intensities of the peaks. In addition, the XRD patterns of all sample series are plotted in Fig. SM6 and it can be seen that, qualitatively, they are all quite

similar, but different from the standard one. These diffractograms indicate the complete phase conversion of boehmite into  $\alpha$ -Al<sub>2</sub>O<sub>3</sub>, i.e., the corundum phase in the baking process, as expected [20,24,25,49]. These results suggest that the rSPS process is an efficient protocol to obtain alumina/GO composites avoiding time-and-money consuming intermediate steps and working with low-cost precursors such as the boehmite sol.

A thorough analysis of the XRD pattern was also performed in order to better explore the microstructure of the crystalline phases. Results such as cell parameters, crystallite size and texture as function of the graphene concentration are included in Fig. 8 (more results and more details are in the supplementary material: Table SM7 and Fig. SM8). These results indicate that the crystallographic structure of the analyzed samples corresponds to that of undistorted corundum (except for the presence of texture effects). The cell parameters and fractional coordinates do not show any clear trend with the carbon concentration and are close to the standard values provided by the literature. Note that, in particular, the cell parameters of the powder GRAL2F sample, with a 2 wt% of graphene, are very close to the reference values as expected for an untreated material. Moreover, the analysis of the positions of the peaks does not show significant displacements as a function of the graphene concentration. These results indicate that the corundum structure of the samples has not been modified by the presence of GO flakes or C atoms. We also noted shifts of the corundum peaks in the alumina-MWCNT composites, which can be explained by the diffusion of small C atoms into the alumina lattice [50]. Otherwise, the diffractograms lack graphite peaks, which can be attributed to the low concentrations of graphene. In this context, for an approximate mass fraction of C about 10%–11%, in CNT-Al<sub>2</sub>O<sub>3</sub> composites, only a very small graphite peak (really indistinguishable from the statistical noise) was observed, as reported by Estili et al. [51].

The mean crystallite size begins by increasing when the graphene content increases up to 2 wt%, and then decreases when this content increases further up to a value of about 300 nm. This increasing-decreasing tendency in the grain size of the sintered samples is in complete agreement with the results obtained by SEM (Fig. 5-Left). The decrease of the domain size with the percentage of graphene has been observed before in CNT-alumina nanocomposites ([53]. Moreover, the texture index does not display any significant trend with the GO concentration, with most of the values ranging between 1.0 to 1.1. As expected, the lower value corresponds to the untreated sintered sample with 2 wt% graphene content powder sample, very close to the random orientation model.

### 3.2.4. Raman analyses

As well as the powder series, the sintered ceramic GRALX series obtained by sol-gel and rSPS were analyzed by Raman spectroscopy.  $X = \{0, 0.5, 1, 2, 3, 6\}$  indicates the GO wt.% in the sample. In contrast with the powder samples, when the green laser ( $\lambda=532$  nm) is used, the expected well-defined D, G, and G' peaks around 1350 cm<sup>-1</sup>, 1597 cm<sup>-1</sup>, and 2706 cm<sup>-1</sup> of the GO are observed only when the GO content is higher than 2 wt% (data not shown). Likewise, weak but noticeable characteristic bands of single crystalline  $\alpha$ -Al<sub>2</sub>O<sub>3</sub> phase located at 378, 418, 578, and 751 cm<sup>-1</sup> are observed in the spectra, as expected from pure  $\alpha$ -Al<sub>2</sub>O<sub>3</sub> [20]. These features confirm that the boehmite is transformed into crystalline  $\alpha$ -Al<sub>2</sub>O<sub>3</sub> phase at 1200 °C, during rSPS.

When the red laser is used ( $\lambda=633$  nm), very intense Raman peaks found at 1370 and 1400 cm<sup>-1</sup> are easily seen (R2 and R1 peaks in Fig. 9), again associated to the PL due to the Cr<sup>3+</sup> ions impurities present in the alumina. This signal, given its photoluminescent nature, is often given in wavelength units [39], being located at 693.0 and 694.5 nm. This strong photoluminescence is responsible for hindering the Raman signal of other species, making it impossible to observe the GO signature in sintered GRAL samples up to a 6 wt% concentration

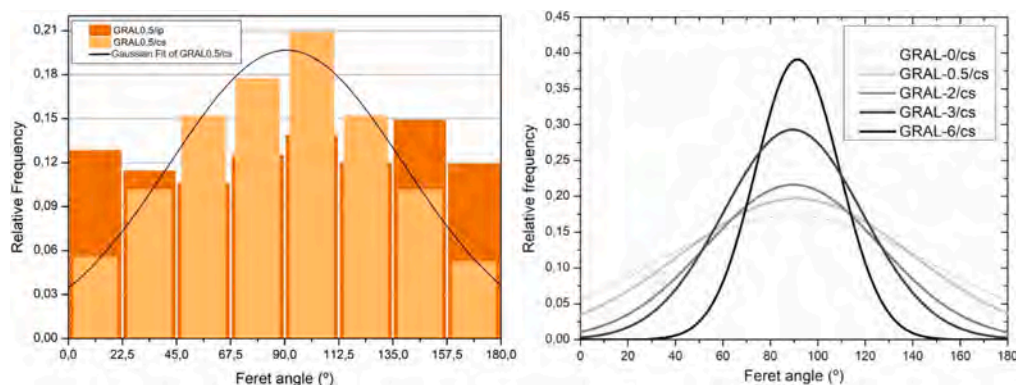


Fig. 6. **Left:** Histogram of the number of grains (relative frequency) vs. Feret angle for sample GRAL0.5. A flat histogram is obtained in the in-plane surface of all the samples, indicating the absence of any preferred orientation, unlike histograms obtained in the cross-section surfaces, which show the preferential grain growth in the plane perpendicular to the direction of the uniaxial pressure and electric field. Note that the fitting Gaussian curve is not a real continuous distribution function, but a Gaussian fitting of the cross-section surface histogram. **Right:** Curves fitting the Feret angle distribution histograms of cross-section surfaces. Note they are not real continuous distribution functions, just Gaussian fittings of histograms.

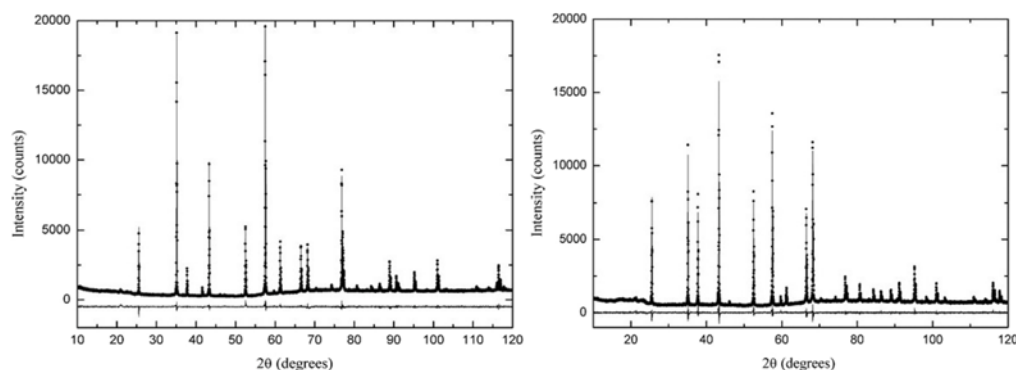


Fig. 7. Diffraction pattern of the standard  $\alpha$ - $\text{Al}_2\text{O}_3$  sintered sample (left) with a larger grain size than the sintered sample GRAL0, and GRAL2 sintered sample (right). Points represent the experimental values and the solid line is the best fit model obtained with the MAUD program. The line at the bottom is the difference plot (observed minus calculated). The shape parameters of the model were included in the models of the analyzed samples in order to extract the microstructural parameters (crystallite size and microstrain).

where, in addition, the R1 and R2 lines overlap in the same region of the GO D-band.

Interestingly, there has been a proposal to use the positions of the PL peak to assess the strain on the surrounding lattice by the shift in the R1 and R2 emissions, namely, the piezospectroscopic effect [54,55]. In the same way, the strain in an alumina crystal induced by the applied stress can also be determined by the shifts in the Raman bands [56,57]. Similarly, a shifting of the G' band of GO (and CNTs) has been reported due to application of stress [27,58,59]. The shift rates (in  $\text{cm}^{-1}/\%$  strain) are found to scale with the Young's modulus of the nanocarbons, which enables such band shifts to be used as a universal stress sensor for composite mechanics.

In this work, to visualize the stored mechanical stress (residual stress), we mapped the region around a crack tip produced by Vickers indentation. With a green laser (532 nm), the spectral shift of the most intense peak of alumina ( $\sim 418 \text{ cm}^{-1}$ ,  $A_{1g}$  vibrational mode [57]) along the path of the crack (Fig. 10) may be assigned to the phonon deformation potential for the  $A_{1g}$  band, related with an induced strain. The shift to larger wavenumbers suggests a stress relaxation occurring in the surroundings of the crack.

### 3.2.5. The issue of the dispersion of the GO assessed by Raman mapping

Although the quality of the dispersion of the nanocarbon is crucial for an efficient reinforcing role, the vast majority of work focusing on

sintered materials reinforced with carbonaceous second phases have determined the quality of the dispersion by SEM or TEM observation. The local character of these techniques could lead to wrong conclusions about the quality of the dispersion, given that a standard SEM image covers a small area, at the most of  $100 \mu\text{m}^2$  (Fig. 4). Although detailed SEM observations could be done by rigorous and patient observation of the surfaces of the samples, electron microscopy is an expensive and time consuming technique. In this work, we propose Raman mapping of the height of the GO peak relative to the alumina peak as a more efficient way to assess the quality of the dispersion of the GO, and even quantify it, by scanning an area of  $500 \times 500 \mu\text{m}^2$  in steps of  $1 \mu\text{m}$ .

Black and white maps have been plotted by assigning the values of the ratio to a gray scale, with black pixels being those in which the concentration of GO is larger (Fig. 11). These maps suggest clear differences in the quality of the dispersion between conventional methods and the new sol-gel based preparation process. Thus, GRAL2-F has dark areas that could be attributed to extensive areas of GO agglomerations, whereas GRAL2 has a more uniform pattern with smaller black regions. The optical resolution of the microscope and the scanning step of one micron could be insufficient given the characteristic size of a GO agglomeration (see, e.g., Fig. 5), nevertheless, just at a glance, the mapping gives useful information about the degree of dispersion of carbonaceous second phases, and confirms the sol-gel method as a promising candidate.

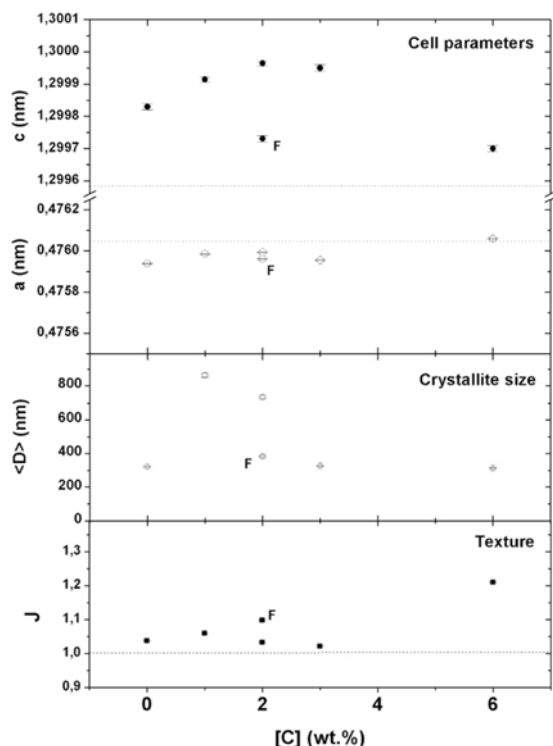


Fig. 8. **Top:** Cell parameters as function of the GO concentration. Dotted lines indicate the values found by Lutterotti and Scardi [52]. **Center:** Mean crystallite size (isotropic) as function of the GO concentration. **Bottom:** Texture index as function of the GO concentration. Dotted line indicates the random orientation value.

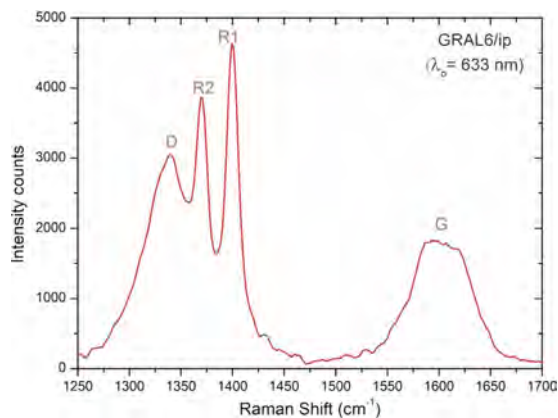


Fig. 9. Raman spectra for the sintered ceramic GRAL6 sintered sample fabricated by the sol-gel method and reactive spark plasma sintering (rSPS), excited with red laser line. D, G and the relevant photoluminescence bands for  $\alpha$ -Al<sub>2</sub>O<sub>3</sub>:Cr<sup>3+</sup> (R1 and R2) are marked.

### 3.2.6. Analysis of the chemical bonds present in the composite: X-ray Photoelectron Spectroscopy (XPS)

The chemical environment of our samples was assessed via XPS analysis. Surface contaminants were removed from all the samples by Ar<sup>+</sup> sputtering under ultra-high vacuum conditions. Survey scans and

Table 2

Fitting details of the C 1s spectrum of GO oxide (Fig. 12-a). FWHM is 1.82 for all the peaks.

Peak index	Max. height	Binding energy (eV)	Area (%)
1	0.18	283.5	9.6
2	0.74	284.4	39.4
3	0.82	286.4	43.4
4	0.12	287.7	6.2
5	0.03	289.1	1.4

a closer inspection of the C 1s, O 1s, and Al 2p regions were performed for all samples. At this point, it is important to highlight that due to the insulating character of the alumina samples, an accumulation of steady-stage charges are expected during the photoemission process [60]. Therefore, all the electron binding energies of the ceramic matrix composites (CMCs) were calibrated against the Al 2p signal, fixed at 74.4 eV as reported for Al in Al<sub>2</sub>O<sub>3</sub> [60].

To test the reliability of our calibration, the binding energy of the corrected O 1s spectra from all the samples was compared. As a result, all the samples showed a main peak centered at the binding energy of  $529.65 \pm 0.03$  eV, in excellent agreement with the expected values after a correct calibration (See the as-obtained spectra in Fig. SM9 in the Supplementary Material). In the following, we will focus our analysis on both the spectral shapes and the relative binding energies of the samples.

Focusing first on the GO present in the CMCs, Fig. 12-a shows the C 1s core level spectra recorded directly on the raw graphene oxide samples. Our C 1s graphene oxide spectrum revealed five main components, which are ascribed to C–N at 283.5 eV [61], to sp<sup>2</sup> carbon at 284.4 eV [61], to C–OH at 286.4 eV, to C–O at 287.7 eV, and to COOH at 289.1 eV, respectively. A detailed report of the fitting is shown in Table 2.

Interestingly, major changes are evident in the C 1s signal for both sintered CMCs samples: the one synthesized via a mixture of powders (GRAL2F, Fig. 12-b), and the one via the sol-gel method (GRAL2, Fig. 12-c).

In particular, the overall aspect of the spectrum narrows significantly, reducing the C–OH component to insignificant contributions. This suggests a chemical reduction of the graphene oxide present into the CMCs, as has already been reported for graphene oxide samples exposed to annealing treatment [62].

Fig. 12-b shows the C 1s core level spectra recorded when the samples are prepared via a conventional mixture of  $\alpha$ -Al<sub>2</sub>O<sub>3</sub> powder and GO (GRAL2F). A main peak at 284.4 eV (46.7% contribution) demonstrates the contributions of sp<sup>2</sup> carbon, with an additional peak at 283.53 eV (34% contribution) which might be ascribed to the presence of C–N bonds originating during the in air annealing process [61]. Furthermore, two minor peaks are observed at 282.1 eV (15% contribution) and 285.7 eV (4% contribution). On the other hand, Fig. 12-c shows the C 1s spectra of the samples prepared via the sol-gel method (GRAL2). Similar to the samples prepared via a conventional mixture of powders, the samples exhibited sp<sup>2</sup> carbon fingerprint as the main contribution of the C 1s spectrum (50% contribution). In addition, a significant component at higher binding energies is observed at 285.7 eV (33% contribution), which can be ascribed to sp<sup>3</sup> carbon [62] (see orange component in Fig. 12-c). In summary, our XPS results show in both samples the reduction of the C–OH component into insignificant contributions and a main contribution of sp<sup>2</sup> carbon in the samples (40%–50%). However, while the samples prepared via conventional mixture of powder show a secondary peak ascribed to the presence of C–N bonds, the samples prepared via sol-gel show an additional peak at higher binding energies ascribed to sp<sup>3</sup> carbon.

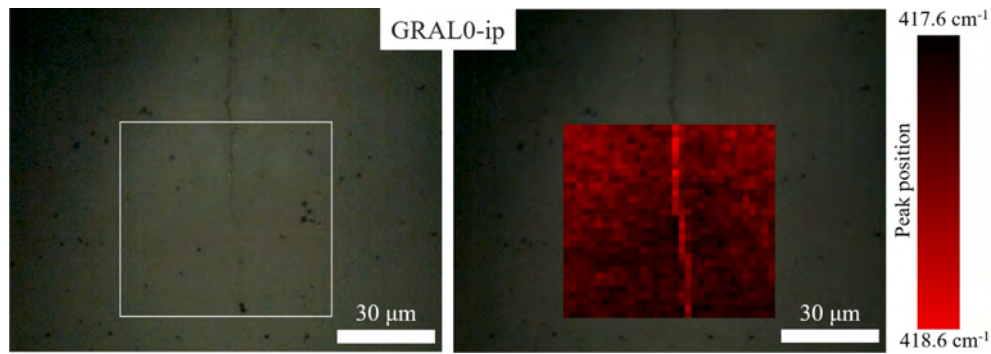


Fig. 10. Left: Optical image of the studied area of the in-plane surface of sample GRAL0. Right: Raman map of GRAL0-ip crack, representing the peak position of Raman band of sapphire belonging to the  $A_{1g}$  vibrational mode.  $\lambda_{inc} = 532$  nm.

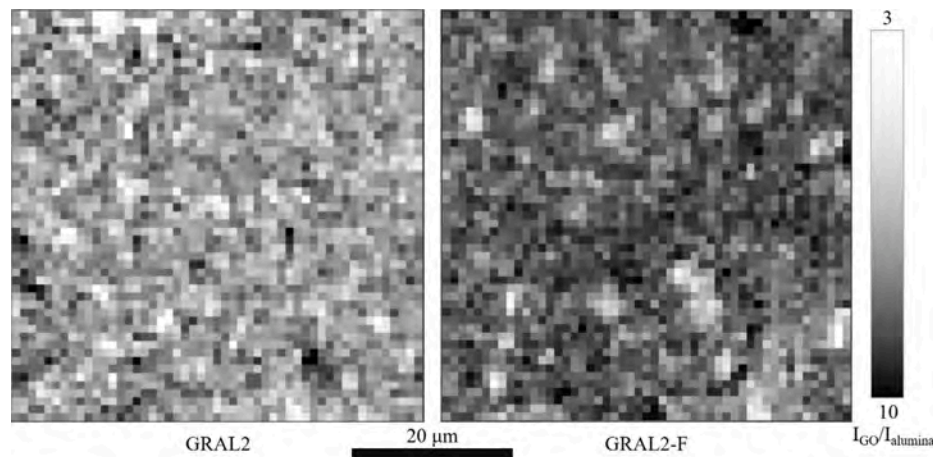


Fig. 11. Raman mapping of in-plane surfaces of sintered samples GRAL2 (left), and GRAL2F (right), where the ratio between the GO signal (intensity of D band) and the alumina signal ( $418\text{ cm}^{-1}$  peak) is represented. Darker regions indicate larger concentrations of GO.  $\lambda_{inc} = 532$  nm.

### 3.3. Mechanical properties

#### 3.3.1. Nanoindentation

The nanoindentation tests allowed the exploration of the micromechanical surface properties, such as the Young’s moduli of the sample series. Three sintered samples were examined by nanoindentation: the pure alumina sample (GRAL0), and the sol-gelled and “fake” samples with a 2.0 GO wt.-%: GRAL2 and GRAL2F, respectively.

All measurements were performed on their ip surfaces. 2500 indentations were performed on a squared area of  $100 \times 100\ \mu\text{m}^2$  for each sample. In Fig. 13-top, the results obtained for GRAL2 sample are summarized. The Young’s moduli of the three mentioned samples are presented in Table 3, and also in Fig. 13-bottom. In addition, dozens of values of Young’s modulus (measured by the ultrasonic pulse method and by nanoindentation) were collected from works focused on alumina and alumina–graphene samples sintered by SPS [1,37,44,45,63–66]. Those results were added to ours, resulting in a cloud of points whose linear fitting helped us to estimate the Young modulus of the rest of the samples (Fig. 13-bottom).

The decreasing behavior of Young’s modulus observed in our samples could be attributed either to the lower elastic modulus of the graphene [64], to the reduction of absolute density of the samples when graphene is added [63,64,66], or to the introduction of defects [37,44]: the large difference of elastic modulus between GRAL2 and GRAL2-F

Table 3

Young’s modulus, Vickers hardness and fracture indentation resistance of the samples series. 1 MGf = 1 MPa  $\text{m}^{1/2}$ .

Sample	Sample surface	E (GPa)	HV10 (GPa)	$K_{IFR}$ (MGf)
GRAL0	ip	$400 \pm 7$	$20.6 \pm 0.9$	$4.3 \pm 0.7$
	cs	–	$20.7 \pm 0.7$	$4.6 \pm 0.6$
GRAL0.5	ip	$381 \pm 11^a$	$17.9 \pm 0.3$	$4.1 \pm 0.5$
	cs	–	$18.2 \pm 0.4$	$4.1 \pm 0.3$
GRAL1	ip	$356 \pm 14^a$	$20.2 \pm 0.4$	$3.7 \pm 0.3$
	cs	–	$18.9 \pm 0.5$	$3.0 \pm 0.3$
GRAL2	ip	$330 \pm 120$	$19.7 \pm 0.4$	$3.1 \pm 0.6$
	cs	–	$19.3 \pm 0.3$	$2.5 \pm 0.4$
GRAL2-F	ip	$250 \pm 90$	$14.5 \pm 2.3$	$2.8 \pm 0.5$
	cs	–	–	–
GRAL3	ip	$260 \pm 30^a$	$20.3 \pm 0.8$	$3.1 \pm 0.6$
	cs	–	$19.9 \pm 0.4$	$2.3 \pm 0.3$
GRAL6	ip	$110 \pm 50^a$	–	–
	cs	–	$10.0 \pm 0.6$	–

<sup>a</sup>Values obtained from linear fitting extrapolation (Fig. 13).

might be explained in terms of the lower quality of the GO’s dispersion, which would lead to a larger concentration of defects, confirming the improvement of the dispersion resulting from the sol–gel procedure.

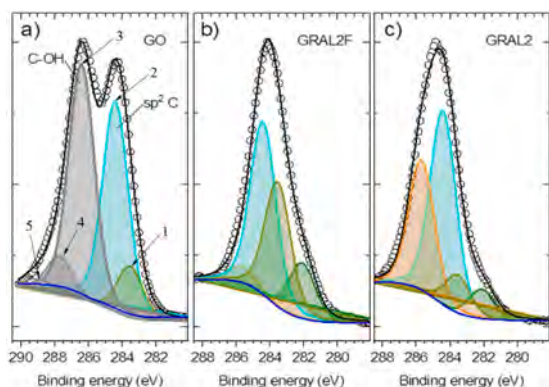


Fig. 12. (a) C 1s XPS spectra of as-received graphene oxide (see Table 2). (b) Sintered GCMCs samples synthesized via a conventional mixture of alumina powders and GO. (c) Sintered GCMC synthesized via sol-gel. The experimental data are represented as open circles, and the fitted data are represented as solid lines. (For interpretation of the references to color in this figure legend, the reader is referred to the web version of this article.)

### 3.3.2. Vickers hardness and indentation fracture resistance

The Vickers hardness of the sintered samples is presented in Table 3 and plotted in Fig. 14, both for the in-plane and cross-section surfaces. It can be seen that the values of the hardness of the in-plane surface do not exhibit significant changes and remain almost constant within the uncertainties, except for the GRAL2F sample. In the case of the hardness values for the cross-section surface, the sample without GO (pure alumina, GRAL0), exhibits a typical value close to 20 GPa. Then, the hardness slightly drops up to 18 GPa for GRAL0.5 and increases afterwards up to 20 GPa with the GO content. Hence, no significant worsening of the hardness was found upon the addition of GO. The subtle decreasing-increasing trend of the hardness could be related with the inverse trend presented by the grain size of the samples (Fig. 5, Table 1). This also suggests the importance of fabricating samples of similar grain size for a strict analysis of the fundamental role of the graphene in the mechanical behavior of ceramic composites.

Regarding the indentation fracture resistance, it is worth mentioning that the use of a bibliographical Young's modulus of 400 GPa in Eq. (3) might promote an underestimation of their concomitant mechanical properties, as has been reported in the literature [24]. Thus, additional characterization through, for example, nanoindentation, is necessary in order to experimentally obtain the most accurate and representative Young's modulus of each one of the samples researched. The values of  $K_{IFR}$  are shown in Fig. 15, computed from Eq. (3), where measured  $H$  values were considered, as well as measured  $E$  values for samples GRAL0, 2 and 2F, and estimated values of  $E$  for the rest of the samples. A slightly decreasing trend is observed, although the average trend remains almost constant within the uncertainties, indicating that the mechanical properties do not show neither appreciable improvement nor worsening.

These results are a bit surprising, given that all the samples are fully densified, the decrease of  $K_{IFR}$  has to be provoked by the effects of the addition of the GO. As revealed through SEM observations (Fig. 4), we noticed the appearance of small black spots in all the samples, which scales with the GO content. These micro/nano-sized pores present in the samples can act like fragile points, being responsible for the decrease of  $K_{IFR}$  observed in the samples.

These results are in total agreement with those reported previously in which the mechanical improvements in similar ceramic matrix composites are only observed below a critical carbonaceous content. For example, Shah et al. [4] reported toughening only for 0.4 wt% of graphene, and typically the critical content is found below 1.0 wt% [5].

Hence, these results may point in the direction highlighted by the simulation results obtained by Garrido-Regife et al. [9]: for the typically used amounts of carbonaceous additives (0.1–2.0 wt%), the spatial distribution of graphene flakes produce, even in the most optimistic case of a perfect dispersion, an absolutely crowded space at the microscale, it then being virtually impossible to achieve a total absence of aggregates, namely, defects.

## 4. Conclusions

In the present work we presented the fabrication of fully-dense alumina/GO ceramic matrix composite (GCMC) by the sol-gel route and reactive spark plasma sintering. In order to optimize the dispersion and homogeneity of GO within the material during the fabrication, a maximum volume strategy was used. This volume ensures the maximum volume in which boehmite will form a physical gel but with the lowest graphene concentration to guarantee the homogeneous distribution and stabilization of the flakes throughout the whole volume. For its part, a reactive sintering process would offer a cost-effective route to produce alumina/GO ceramics, avoiding time-and-money consuming intermediate steps, such as pre-calcination under an inert atmosphere. Our ceramics were manufactured with a lower sintering temperature (1200 °C), which would facilitate any further industrial scalability of the process. SEM observations revealed the apparent absence of large graphene agglomerations for the lowest concentrations of GO used, suggesting the efficacy of this fabrication approach. Raman mapping analyses have confirmed the integrity of the GO along the fabrication process, and the improvement of the dispersion of the GO as a result of the sol-gel based procedure, in comparison to conventional methods. Mechanical features such as hardness, Young's modulus and indentation fracture toughness were comparable with those from conventional alumina/GO CMCs.

Considering that the improvements in the dispersion of the GO, and in the chemical relationship between the GO and the matrix, have not led to clear mechanical improvements, the mechanical behavior of the composite is still being driven by other issues, such as the extremely high content of graphene that makes it impossible to fabricate samples without any aggregates. Nevertheless, this approach offers an appealing route to fabricate GCMC with better dispersion of the reinforcing phase and without worsening their mechanical properties.

## Declaration of competing interest

The authors declare that they have no known competing financial interests or personal relationships that could have appeared to influence the work reported in this paper.

## Acknowledgments

Grant PGC2018-094952-B-I00 funded by MCIN/AEI/ 10.13039/501100011033 and by "ERDF A way of making Europe", Ayuda movilidad internacional VI-PPTIUS funded by the University of Seville, Spain, and grant PAIDI 2020 - 20-01121 funded by Junta de Andalucía, Spain, are acknowledged. F.S-B. acknowledges the support of the Junta de Extremadura, Spain and the ERDF Fund under the grant GR21012. The help from the technical staff from the CITIUS is also acknowledged. The authors would like to thank Comercial Química Massó for supplying the boehmite precursor Nyacol, and the USA National Institutes of Health, for the development of the ImageJ software.

## Appendix A. Supplementary data

Supplementary material related to this article can be found online at <https://doi.org/10.1016/j.jeurceramsoc.2022.10.043>.

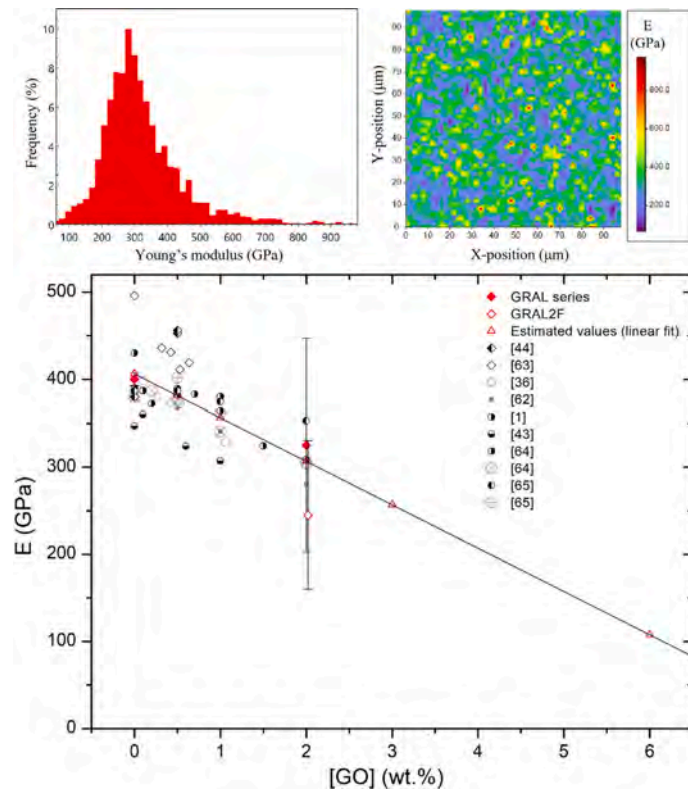


Fig. 13. Young's modulus of alumina-graphene composites fabricated via SPS, measured by Berkovich nanoindentation (squares) and by pulse-echo method (circles). Estimated values for GRAL samples from the linear regression (open red triangles). Source: Non-colored data from [1,37,44,45,63–66].

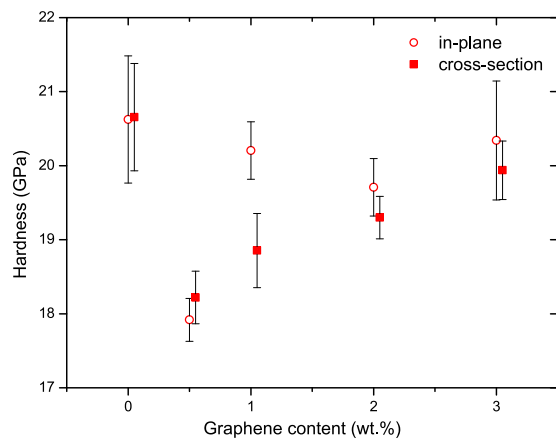


Fig. 14. Vickers hardness for the GCMC sintered samples. In-plane and cross-section data have been slightly shifted so the points do not overlap. Error bars correspond with the standard deviation.

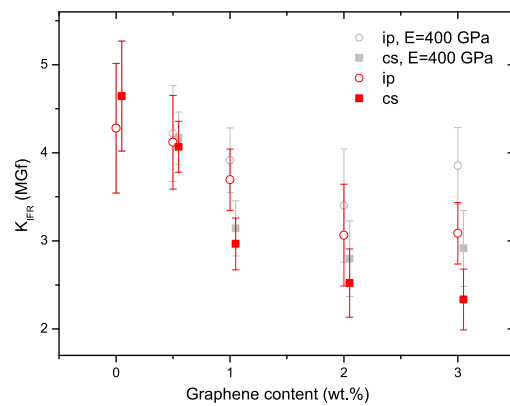


Fig. 15. Red data series: Indentation fracture resistance of GCMC sintered samples calculated with Shetty's equation using the Young's modulus obtained via nanoindentation tests and linear extrapolation (see Fig. 13). Grey data series:  $K_{IFR}$  was also calculated with the bibliographic Young's modulus of pure fully-dense  $\alpha$ - $Al_2O_3$  ( $E=400$  GPa [30]) for all the samples, illustrating the difference of the results. In-plane and cross-section data have been slightly shifted so the points do not overlap. Error bars correspond with the standard deviation.  $1\text{ MGf} = 1\text{ MPa}\cdot\text{m}^{1/2}$ . (For interpretation of the references to color in this figure legend, the reader is referred to the web version of this article.)

## Chapter 6. Sol-gel method and reactive SPS for novel alumina-graphene ceramic composites

P. Rivero-Antúnez et al.

Journal of the European Ceramic Society 43 (2023) 1064–1077

### References

- [1] J.H. Shin, J. Choi, M. Kim, S.H. Hong, Comparative study on carbon nanotube and reduced graphene oxide-reinforced alumina ceramic composites, *Ceram. Int.* 44 (7) (2018) 8350–8357.
- [2] A. Nieto, A. Bisht, D. Lahiri, C. Zhang, A. Agarwal, Graphene reinforced metal and ceramic matrix composites: a review, 2016, pp. 241–302, 62 (5).
- [3] E. Zapata-Solvas, D. Gómez-García, A. Domínguez-Rodríguez, Towards physical properties tailoring of carbon nanotubes-reinforced ceramic matrix composites, *J. Eur. Ceram. Soc.* 32 (12) (2012) 3001–3020.
- [4] W.A. Shah, X. Luo, C. Guo, B.I. Rabiou, B. Huang, Y.Q. Yang, Preparation and mechanical properties of graphene-reinforced alumina-matrix composites, *Chem. Phys. Lett.* 754 (2020) 137765.
- [5] V. Morales-Flórez, A. Domínguez-Rodríguez, Mechanical properties of ceramics reinforced with allotropic forms of carbon, *Prog. Mater. Sci.* 128 (2022) 100966.
- [6] A.M. Abyzov, Research on the Development of High-Quality Aluminum Oxide Ceramic (Review). Part 1. Sintering with Additives, Reactive Sintering, Production of Reinforced Composites, *Glas. Ceram. (English Transl. Steklo I Keramika)* 75 (7–8) (2018) 293–302.
- [7] M.H. Bocanegra-Bernal, C. Domínguez-Ríos, J. Echeberria, A. Reyes-Rojas, A. García-Reyes, A. Aguilar-Elguezabal, Spark plasma sintering of multi-, single/double- and single-walled carbon nanotube-reinforced alumina composites: Is it justifiable the effort to reinforce them? *Ceram. Int.* 42 (1) (2016) 2054–2062.
- [8] R. Cano-Crespo, B. Malmal Moshtaghion, D. Gómez-García, A. Domínguez-Rodríguez, R. Moreno, High-temperature creep of carbon nanofiber-reinforced and graphene oxide-reinforced alumina composites sintered by spark plasma sintering, *Ceram. Int.* 43 (9) (2017) 7136–7141.
- [9] L. Garrido-Regife, P. Rivero-Antúnez, V. Morales-Flórez, Dispersion of carbon nanotubes in composite materials studied by computer simulation of small angle scattering, *Phys. Rev. E (under Revis.)* (2022).
- [10] G.D. Zhan, J.D. Kuntz, J. Wan, A.K. Mukherjee, Single-wall carbon nanotubes as attractive toughening agents in alumina-based nanocomposites, *Nature Mater.* 2 (1) (2003) 38–42.
- [11] A. Azarniya, S. Sovizi, A. Azarniya, M.R. Rahmani Tajiri Boyuk, T. Varol, P. Nithyadharseni, H.R. Madaah Hosseini, S. Ramakrishna, M.V. Reddy, Physicochemical properties of spark plasma sintered carbon nanotube-containing ceramic matrix nanocomposites, *Nanoscale* 9 (35) (2017) 12779–12820.
- [12] M. Estili, Y. Sakka, W.W. Wu, T. Nishimura, H. Yoshida, A. Kawasaki, Perfect high-temperature plasticity realized in multiwalled carbon nanotube-concentrated  $\alpha$ -Al<sub>2</sub>O<sub>3</sub> hybrid, *J. Am. Ceram. Soc.* 96 (6) (2013) 1904–1908.
- [13] O. Hanzel, J. Sedláček, P. Šajgalik, New approach for distribution of carbon nanotubes in alumina matrix, *J. Eur. Ceram. Soc.* 34 (7) (2014) 1845–1851.
- [14] A.M. Zahedi, J. Javadpour, H.R. Rezaie, M. Mazaheri, Analytical study on the incorporation of zirconia-based ceramics with carbon nanotubes: Dispersion methods and mechanical properties, *Ceram. Int.* 42 (1) (2016) 1653–1659.
- [15] N. Song, H. Liu, J. Fang, Fabrication and mechanical properties of multi-walled carbon nanotube reinforced reaction bonded silicon carbide composites, *Ceram. Int.* 42 (1) (2016) 351–356.
- [16] I. Ahmad, B. Yazdani, Y. Zhu, Recent Advances on Carbon Nanotubes and Graphene Reinforced Ceramics Nanocomposites, *Nanomaterials* 5 (1) (2015) 90–114.
- [17] A. Pal, S. Mukherjee, G.C. Das, M.K. Mitra, Synthesis and characterization of CNT reinforced alumina based nanocomposite, *Trans. Indian Ceram. Soc.* 70 (4) (2011) 215–220.
- [18] B.-Y. Zhou, S.-J. Fan, Y.-C. Fan, Q. Zheng, X. Zhang, W. Jiang, L.-J. Wang, Recent progress in ceramic matrix composites reinforced with graphene nanoplatelets, *Rare Met.* 39 (5) (2020) 513–528.
- [19] M.S. Dresselhaus, A. Jorio, M. Hofmann, G. Dresselhaus, R. Saito, Perspectives on Carbon Nanotubes and Graphene Raman Spectroscopy, *Nano Lett.* 10 (3) (2010) 751–758.
- [20] L. Esquivias, P. Rivero-Antúnez, C. Zamora-Ledezma, A. Domínguez-Rodríguez, V. Morales-Flórez, Intragranular carbon nanotubes in alumina-based composites for reinforced ceramics, *J. Sol-Gel Sci. Technol.* 90 (1) (2019) 162–171.
- [21] R. Cano-Crespo, P. Rivero-Antúnez, D. Gómez-García, R. Moreno, A. Domínguez-Rodríguez, The possible detriment of oxygen in creep of alumina and zirconia ceramic composites reinforced with graphene, *Materials (Basel)*. 14 (4) (2021) 1–17.
- [22] J. Stein, B. Lenczowski, N. Fréty, E. Anglaret, Mechanical reinforcement of a high-performance aluminium alloy AA5083 with homogeneously dispersed multi-walled carbon nanotubes, *Carbon N. Y.* 50 (6) (2012) 2264–2272.
- [23] J. Stein, B. Lenczowski, E. Anglaret, N. Fréty, Influence of the concentration and nature of carbon nanotubes on the mechanical properties of AA5083 aluminium alloy matrix composites, *Carbon N. Y.* 77 (2014) 44–52.
- [24] P. Rivero-Antúnez, R. Cano-Crespo, L. Esquivias, N. de la Rosa-Fox, C. Zamora-Ledezma, A. Domínguez-Rodríguez, V. Morales-Flórez, Mechanical characterization of sol-gel alumina-based ceramics with intragranular reinforcement of multiwalled carbon nanotubes, *Ceram. Int.* 46 (12) (2020) 19723–19730.
- [25] P. Rivero-Antúnez, R. Cano-Crespo, F. Sánchez-Bajo, A. Domínguez-Rodríguez, V. Morales-Flórez, Reactive SPS for sol-gel alumina samples: Structure, sintering behavior, and mechanical properties, *J. Eur. Ceram. Soc.* 41 (11) (2021) 5548–5557.
- [26] C.B. Mo, S.I. Cha, K.T. Kim, K.H. Lee, S.H. Hong, Fabrication of carbon nanotube reinforced alumina matrix nanocomposite by sol-gel process, *Mater. Sci. Eng. A* 395 (1–2) (2005) 124–128.
- [27] I.A. Kinloch, J. Suhr, J. Lou, R.J. Young, P.M. Ajayan, Composites with carbon nanotubes and graphene: An outlook, *Science (80-. )*. 362 (6414) (2018) 547–553.
- [28] M. Piñero, M.d.M. Mesa-Díaz, D. de los Santos, M.V. Reyes-Peces, J.A. Díaz-Fraile, N. de la Rosa-Fox, L. Esquivias, V. Morales-Florez, Reinforced silica-carbon nanotube monolithic aerogels synthesised by rapid controlled gelation, *J. Sol-Gel Sci. Technol.* 86 (2) (2018) 391–399.
- [29] L. Liu, Y. Takasu, T. Onda, Z.-C. Chen, Influence of in-situ formed Ba- $\beta$ -Al<sub>2</sub>O<sub>3</sub> on mechanical properties and thermal shock resistance of ZTA/Ba- $\beta$ -Al<sub>2</sub>O<sub>3</sub> composites, *Ceram. Int.* 46 (3) (2020) 3738–3743.
- [30] F. Cardarelli, *Materials Handbook*, second ed., Springer London, London, 2008.
- [31] L. Lutterotti, Total pattern fitting for the combined size-strain-stress-texture determination in thin film diffraction, *Nucl. Instrum. Methods Phys. Res., Sect. B* 268 (3–4) (2010) 334–340.
- [32] H.M. Rietveld, A profile refinement method for nuclear and magnetic structures, *J. Appl. Crystallogr.* 2 (2) (1969) 65–71.
- [33] D.A. Shirley, High-Resolution X-ray Photoemission Spectrum of the Valence Bands of Gold, *Phys. Rev. B* 5 (12) (1972) 4709.
- [34] D.K. Shetty, A.R. Rosenfield, W. Duckworth, Analysis of Indentation Crack as a Wedge-Loaded Half-Penny Crack, *J. Am. Ceram. Soc.* 68 (2) (1985) C-65–C-67.
- [35] H. Miyazaki, Y. Yoshizawa, A reinvestigation of the validity of the indentation fracture (IF) method as applied to ceramics, *J. Eur. Ceram. Soc.* 37 (15) (2017) 4437–4441.
- [36] G. Surekha, K.V. Krishnaiah, N. Ravi, R. Padma Suvarna, FTIR, Raman and XRD analysis of graphene oxide films prepared by modified Hummers method, *J. Phys. Conf. Ser.* 1495 (1) (2020) 012012.
- [37] H. Porwal, P. Tatarko, S. Grasso, J. Khaliq, I. Dlouhý, M.J. Reece, Graphene reinforced alumina nano-composites, *Carbon N. Y.* 64 (2013) 359–369.
- [38] A.C. Ferrari, D.M. Basko, Raman spectroscopy as a versatile tool for studying the properties of graphene, *Nat. Nanotechnol.* 8 (4) (2013) 235–246.
- [39] D. Tuschel, Photoluminescence spectroscopy using a Raman spectrometer, *Spectroscopy* 31 (9) (2016) 14–21.
- [40] V.N. Makhov, A. Lushchik, C.B. Lushchik, M. Kirm, E. Vasil'chenko, S. Vielhauer, V.V. Harutunyan, E. Aleksanyan, Luminescence and radiation defects in electron-irradiated Al<sub>2</sub>O<sub>3</sub> and Al<sub>2</sub>O<sub>3</sub>:Cr, *Nucl. Instrum. Methods Phys. Res., Sect. B* 266 (12–13) (2008) 2949–2952.
- [41] M. Wall, The Raman Spectroscopy of Graphene and the Determination of Layer Thickness, Technical Report, Thermo Electron Scientific Instruments LLC, Madison, 2011, pp. 1–5.
- [42] C.J. Doss, R. Zallen, Raman studies of sol-gel alumina: Finite-size effects in nanocrystalline AlO(OH), *Phys. Rev. B* 48 (21) (1993) 15626.
- [43] M. Kumagai, G.L. Messing, Controlled Transformation and Sintering of a Boehmite Sol-Gel by  $\alpha$ -Alumina Seeding, *J. Am. Ceram. Soc.* 68 (9) (1985) 500–505.
- [44] M. Hrubovčáková, E. Múdra, R. Bureš, A. Kovalčíková, R. Sedlák, V. Girman, P. Hvizdoš, Microstructure, fracture behaviour and mechanical properties of conductive alumina based composites manufactured by SPS from graphenated Al<sub>2</sub>O<sub>3</sub> powders, *J. Eur. Ceram. Soc.* 40 (14) (2020) 4818–4824.
- [45] E.A. Klyatskina, A. Borrell, E.G. Grigoriev, A.G. Zholin, M.D. Salvador, V.V. Stolyarov, Structure features and properties of graphene/Al<sub>2</sub>O<sub>3</sub> composite, *J. Ceram. Sci. Technol.* 9 (3) (2018) 215–224.
- [46] A. Centeno, V.G. Rocha, B. Alonso, A. Fernández, C.F. Gutiérrez-Gonzalez, R. Torrecillas, A. Zurutuza, Graphene for tough and electroconductive alumina ceramics, *J. Eur. Ceram. Soc.* 33 (15–16) (2013) 3201–3210.
- [47] H. Porwal, R. Saggarr, P. Tatarko, S. Grasso, T. Saunders, I. Dlouhý, M.J. Reece, Effect of lateral size of graphene nano-sheets on the mechanical properties and machinability of alumina nano-composites, *Ceram. Int.* 42 (6) (2016) 7533–7542.
- [48] S. Ghosh, A.H. Chokshi, P. Lee, R. Raj, A huge effect of weak DC electrical fields on grain growth in zirconia, *J. Am. Ceram. Soc.* 92 (8) (2009) 1856–1859.
- [49] P. Souza-Santos, H. Souza-Santos, S. Toledo, Standard transition aluminas. Electron microscopy studies, *Mater. Res.* 3 (4) (2000) 104–114.
- [50] N. Sharma, A.N. Syed, B.C. Ray, S. Yadav, K. Biswas, Alumina-MWCNT composites: Microstructural characterization and mechanical properties, *J. Asian Ceram. Soc.* 7 (1) (2019) 1–19.
- [51] M. Estili, A. Kawasaki, Y. Sakka, Highly concentrated 3D macrostructure of individual carbon nanotubes in a ceramic environment, *Adv. Mater.* 24 (31) (2012) 4322–4326.
- [52] L. Lutterotti, P. Scardi, Simultaneous structure and size-strain refinement by the rietveld method, *J. Appl. Crystallogr.* 23 (4) (1990) 246–252.
- [53] S. Sarkar, P.K. Das, Effect of sintering temperature and nanotube concentration on microstructure and properties of carbon nanotube/alumina nanocomposites, *Ceram. Int.* 40 (5) (2014) 7449–7458.
- [54] Q. Ma, D.R. Clarke, Piezospectroscopic Determination of Residual Stresses in Polycrystalline Alumina, *J. Am. Ceram. Soc.* 77 (2) (1994) 298–302.



- [55] H. Mahiou, A. Beakou, R.J. Young, Investigation into stress transfer characteristics in alumina-fibre/epoxy model composites through the use of fluorescence spectroscopy, *J. Mater. Sci.* 34 (24) (1999) 6069–6080.
- [56] W. Zhu, G. Pezzotti, Phonon deformation potentials for the corundum structure of sapphire, *J. Raman Spectrosc.* 42 (11) (2011) 2015–2025.
- [57] W. Zhu, G. Pezzotti, Tensor and spatially resolved analysis of microscopic stress fields in polycrystalline alumina by polarized Raman spectroscopy, *Phys. Status Solidi Appl. Mater. Sci.* 208 (5) (2011) 1141–1150.
- [58] J.E. Lee, G. Ahn, J. Shim, Y.S. Lee, S. Ryu, Optical separation of mechanical strain from charge doping in graphene, *Nat. Commun.* 2012 31 3 (1) (2012) 1–8.
- [59] D.G. Papageorgiou, I.A. Kinloch, R.J. Young, Mechanical properties of graphene and graphene-based nanocomposites, *Prog. Mater. Sci.* 90 (2017) 75–127.
- [60] C.D. Wagner, W.M. Riggs, L.E. Davis, J.F. Moulder, G.E. Muilenberg, *Handbook of X-ray Electron Spectroscopy: A Reference Book of Standard Data for Use in X-Ray Photoelectron Spectroscopy*, Perkin-Elmer Corp., Perkin-Elmer, Minnesota, 1979, p. 192.
- [61] J.C. Moreno-López, F. Fedi, G. Argentero, M. Carini, J. Chimborazo, J. Meyer, T. Pichler, A. Mateo-Alonso, P. Ayala, Exclusive Substitutional Nitrogen Doping on Graphene Decoupled from an Insulating Substrate, *J. Phys. Chem. C* 124 (40) (2020) 22150–22157.
- [62] K. Haubner, J. Murawski, P. Olk, L.M. Eng, C. Ziegler, B. Adolphi, E. Jaehne, The route to functional graphene oxide, *ChemPhysChem* 11 (10) (2010) 2131–2139.
- [63] K. Broniszewski, J. Wozniak, M. Kostecki, A. Olszyna, Properties of Alumina – Graphene Oxide Composites, *Mater. Today Proc.* 2 (1) (2015) 370–375.
- [64] Y. Fan, M. Estili, G. Igarashi, W. Jiang, A. Kawasaki, The effect of homogeneously dispersed few-layer graphene on microstructure and mechanical properties of Al<sub>2</sub>O<sub>3</sub> nanocomposites, *J. Eur. Ceram. Soc.* 34 (2) (2014) 443–451.
- [65] M. Kostecki, M. Grybczuk, P. Klimczyk, T. Cygan, J. Woźniak, T. Wejrzanowski, L. Jaworska, J. Morgiel, A. Olszyna, Structural and mechanical aspects of multilayer graphene addition in alumina matrix composites—validation of computer simulation model, *J. Eur. Ceram. Soc.* 36 (16) (2016) 4171–4179.
- [66] J. Wozniak, A. Jastrzębska, T. Cygan, A. Olszyna, Surface modification of graphene oxide nanoplatelets and its influence on mechanical properties of alumina matrix composites, *J. Eur. Ceram. Soc.* 37 (4) (2017) 1587–1592.

## Chapter 7

# The dispersion of carbon nanotubes in composite materials studied by computer simulation of Small Angle Scattering

After previous work on experimental procedures for the manufacture of alumina-based CMCs, one of the main issues that arises is that, perhaps, for the carbon allotrope (graphene or CNTs) concentrations with which the scientific community usually works (namely, 0.5–2 wt.%), no mechanical reinforcement at room temperature is possible. The premise is that the number of reinforcing elements per unit volume would be such high that achieving good dispersions of the reinforcement phase in the ceramic matrix is impossible, and, therefore, no significant reinforcement in the matrix could be ever achieved at the macroscale. This is where the idea of “visualizing” how a population of reinforcing elements would look like with its reinforcement phase perfectly dispersed comes into play, or with different levels of aggregation.

Small Angle Scattering (SAS) is proposed as a useful tool to study the degree of homogenization of the nanophase in the matrix. The study simulated systems with

---

different CNT concentrations and states of aggregation, proposing two parameters to assess the quality of CNT dispersion in ceramic matrices or other composites. The results suggest that completely avoiding aggregates is impossible if samples are prepared using the typical 0.5–2 wt.% contents. Moreover, the first derivative of the scattering curve is proposed as a useful tool for estimating the quality of nanophase dispersion. The proposed parameters offer a quantitative assessment of the quality of CNT dispersion, which could be useful in designing effective reinforcement strategies for ceramic composites. However, the study also highlights the challenges of completely avoiding CNT aggregates during manufacturing, and suggests that this issue should be carefully reconsidered in future research.



## The dispersion of carbon nanotubes in composite materials studied by computer simulation of Small Angle Scattering

Laura Garrido-Regife<sup>a</sup>, Pedro Rivero-Antúñez<sup>a,b</sup>, Víctor Morales-Flórez<sup>a,b,\*</sup>

<sup>a</sup> Departamento de Física de la Materia Condensada, Universidad de Sevilla, Sevilla 41012, Spain

<sup>b</sup> Instituto de Ciencia de Materiales de Sevilla, Centro Mixto CSIC-Universidad de Sevilla, Sevilla 41092, Spain

### ARTICLE INFO

#### Keywords:

Carbon nanotubes (CNT)  
Dispersion  
Small Angle Scattering (SAS)  
Computer simulation

### ABSTRACT

Although numerous efforts have been made to reinforce ceramic materials by adding a nanostructured phase like carbon nanotubes (CNT), the appearance of aggregates during the manufacturing processes continues to be a problem. Given the size of the CNT (nm– $\mu$ m), techniques such as Small Angle Scattering (SAS) can be a useful tool to study the formation of the aggregates and to quantify the degree of homogenization of the nanophase in the matrix. In this work, systems with different concentrations of CNT have been simulated in different states of aggregation, starting from a perfectly homogeneous dispersion of individualized CNT, and progressively aggregated. A Guinier regime appears in the scattering signal in the range of low values of the modulus of the scattering vector,  $q$ , as the aggregation occurs. Two parameters from the intensity curve are proposed to quantify the quality of the dispersion of the nanophase in the ceramic matrix.

### 1. Introduction

For decades, low-dimensional carbon allotropes, such as carbon nanotubes (CNT) or graphene, have been considered for developing composite materials, due to their remarkable properties [1,2]. Hence, several studies have achieved the improvement of physical properties, such as, e.g., thermal and electrical, or the development of specific functionalities of polymer, metal and ceramic composites by the inclusion of CNT or graphene [3–9]. In addition, such research has allowed the development of a wide variety of possible applications, such as structural reinforcement, aerospace engineering or the creation of new nuclear fuels, among others [10,11]. Due to the outstanding mechanical properties of the low-dimensional carbon allotropes, they have also been considered for the mechanical reinforcement of composite materials [9].

Nevertheless, several fundamental questions are still lacking solid theoretical or experimental responses such as: what is the most efficient type of carbon allotrope? what is the most efficient concentration? what is the best type of bond between the nanophase and the matrix? and, what is the maximum possible reinforcement? Although serious attempts have been made to answer these questions [12], contradictory experimental results are commonly found in the literature, as, for example, the preference of single-wall [1] or multi-wall [13] CNT for mechanical reinforcement, or the better reinforcing efficiency of CNT with high [3,14] or low [15] aspect ratio. In consequence, the scientific

community has been working on a phenomenological basis for the last twenty years in this confusing scenario and, due to this lack of consistency and the large dispersion of the published data, some authors have even questioned the possibility of achieving efficient mechanical reinforcement by adding CNT [14,16]. Undoubtedly, the answers to those questions will help to address the challenge of transferring the outstanding nanomechanical properties of the carbon allotropes to their macroscopic composite hosts [2].

Concerning the problem of the suitable concentration of the reinforcing phase, there is clear agreement on the fact that high CNT concentrations fail to improve the mechanical properties of ceramics. These poor mechanical results are attributed to problems regarding the dispersion of the carbon allotropes in the matrix, since the presence of aggregates of the reinforcing phases acts as defects in the composite material [17]. Thus, coils, entanglements or agglomerates of carbon allotropes lead to accumulations of stress, which promote the propagation of fractures, causing a significant degradation of the mechanical performance [9,14,18]. As a consequence, only samples with a low concentration of CNT (typically  $\leq 1.0$  wt.%) show real improvements of the mechanical properties [8,19,20], and similar behavior has been generally reported in the case of graphene-based composites. Therefore, the tendency of nanostructured carbon allotropes, especially the CNT, to form aggregates may be spoiling the appearance of significant reinforcing phenomena in the composites.

\* Correspondence to: Department of Condensed-Matter Physics, University of Sevilla, P.O. 1065, Seville 41080, Spain.

E-mail address: [vmorales@us.es](mailto:vmorales@us.es) (V. Morales-Flórez).

URL: <http://grupo.us.es/fqm393/> (V. Morales-Flórez).

<https://doi.org/10.1016/j.physb.2022.414450>

Received 4 September 2022; Received in revised form 11 October 2022; Accepted 23 October 2022

Available online 31 October 2022

0921-4526/© 2022 Elsevier B.V. All rights reserved.

In this regard, several studies have been carried out to determine the best techniques to avoid the aggregation of allotropes and to achieve a homogeneous dispersion of the nanophase [21–23]. Very often, the quality of the spatial distribution of carbon allotropes and the absence of aggregates have been assessed very often, but usually through partial explorations by SEM, TEM or other local techniques [4,24–27]. Indeed, a dispersion index has been proposed based on SEM exploration [28]. But the statistical representation of the sample through results obtained by these local techniques is questionable and the results continue to be unclear, since, as claimed by some authors [14,29], there is no standard to estimate the quality of the dispersion or to definitively determine the presence (or absence) of agglomerates at the large scale [14,29].

To perform more rigorous analyses of the dispersion of nanostructured phases, Small Angle Scattering (SAS) techniques (with x-rays, SAXS; light, SALS; or neutrons, SANS as radiation) [30] have the advantage of offering statistically representative information of large volumes of the sample, exploring up to several  $\text{mm}^3$  [31]. In addition, these types of tests are non-destructive and allow monitoring the evolution of the nanophase *in situ*. Biological systems and hybrid organic–inorganic nanomaterials have been widely studied by SAS techniques [32–36], but the use of scattering techniques has been extended to the study of nanomaterials that include carbon nanotubes [11,37–39]. For example, very significant work was carried out by Tomchuk et al. [40], focused on the study of the formation of agglomerates of particles using SAXS in ferrofluids, and verifying that the fractal dimension calculated from the intensity curve decreased from  $D \sim 1.27$  to  $D \sim 1.00$  with increasing temperature from 20 to 70 °C, which indicates a reorganization of the compact aggregates into fibrillar structures. In addition, Ramos et al. [41] published an inspiring paper in which the efficiency of different surfactants on the dispersion of CNT in water was checked. The analysis of the intensity curve revealed a maximum around  $q = 0.16 \text{ \AA}^{-1}$ , corresponding to a characteristic size of 39.3 Å. This value relatively close to the diameter of the CNT used (4–6 nm), and a power law fitting, supported the correct dispersion of the carbon phase.

Furthermore, in order to understand the problem of the dispersion, the visual aspect of how the perfect distributions of carbon allotropes at the microscale could be rendered by computer simulation based on purely geometrical considerations. Hence, the paper by Romanov et al. [42] is, to our knowledge, the only attempt for building realistic images of dispersions for carbon allotropes discussing their influence on the mechanical performance of the composites. These spectacular results give clues about how populated are the typical composites at the microscale. Even for an epoxy matrix with a low 0.5 wt.% of standard sized CNT, the volumetric density of the aggregates is almost 1000 CNT/ $\mu\text{m}^3$ . So, if we consider the case of a ceramic matrix with a grain size of the order of 2  $\mu\text{m}$ , a huge CNT-per-grain ratio is inferred. Moreover, the work by Zhu et al. [43] has faced the problem of the aggregation of nanotubes considering the interaction force between them through Molecular Dynamics simulation.

In the present paper, the results of specific analyses of the spatial distribution of the CNT will be presented, based on geometrical considerations and computer simulations of SAS experiments. Critical features, such as the appearance of aggregates and the characterization of the quality of the dispersion are specifically addressed. To do this, structural models have been built to mimic realistic ceramic composites with CNT under different states of aggregation. Perfectly dispersed sets of CNT have been sequentially aggregated using the Monte Carlo method up to total aggregation. Afterwards, the scattering intensity curves for these systems have been simulated to verify how the formation of aggregates can be revealed by the SAS signals. Finally, intensity curves have been analyzed and discussed in order to quantify the quality of the dispersion and to identify the signature of the appearance of the aggregates.

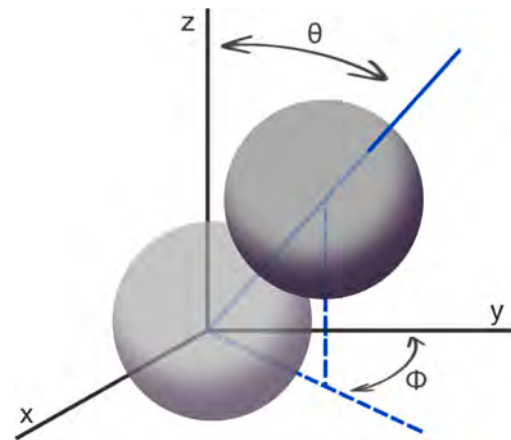


Fig. 1. Scheme for the construction process of the CNT as a concatenation of spheres in hard contact, with a curvature defined by the angles  $\theta$  and  $\phi$ .

## 2. Methods

### 2.1. Modeling one single CNT

Each CNT is modeled as a randomly curved chain of concatenated hard spheres. During the concatenation, the latitude and longitude of the contact point of a new sphere with respect to the previous one is randomly chosen between 0 and two defined limits,  $\theta \in (0, \alpha)$  and  $\phi \in (0, \beta)$ . The limits  $\alpha$  and  $\beta$  ultimately define the curvature of the chain. The geometry of the process is schematically represented in Fig. 1. Before accepting each new sphere, it is checked that it does not overlap with any sphere previously placed.

The number of spheres that make up the CNT is defined by the aspect ratio of the nanotube to be modeled. We have used multi-walled CNT supplied by *NanoAmor, Inc.*, with a length of 1.25  $\mu\text{m}$  and a diameter of 12.5 nm. As a consequence, each chain is made up of 100 spheres. Nevertheless, in the simulations, reduced units are employed in all cases, namely, the spheres have unit diameter. Two other realistic types of CNT with aspect ratios of 20 and 1000 are considered, emulating different multi-walled CNT of dimensions 1  $\mu\text{m} \times 50 \text{ nm}$  and 2  $\mu\text{m} \times 2 \text{ nm}$ , respectively.

### 2.2. Geometrical considerations for the amount of carbon allotropes

The objective of these simulations is to model the dispersion of carbon nanotubes in alumina matrices, the most studied reinforced ceramic system with CNT. Hence, structural models reproducing the set of CNT embedded in the alumina for different carbon concentrations have been generated. For this, it is necessary to find a relation between these concentrations by weight (wt.%) and the numeric density of the nanotubes,  $n_{CNT}$ , namely, the number of CNT per unit volume of the nanocomposite. If we consider a compound formed by two phases,  $a$  and  $b$ , with densities  $\rho_a$  and  $\rho_b$  and occupying volumes  $V_a$  and  $V_b$ , respectively, the volume percentage (vol.%) of phase  $b$  in the compound,  $Y$ , can be expressed as

$$Y = 100 \frac{\rho_a x}{\rho_a x + \rho_b (1 - x)} \quad (1)$$

where  $x = \text{wt.}\%/100$ , namely, the mass ratio of phase  $b$  in the sample. If we assume that the phase  $b$  is the CNT, its total occupied volume will be  $V_b = N_{CNT} \cdot V_{1CNT}$ , where  $N_{CNT}$  is the number of nanotubes and  $V_{1CNT}$  is the volume occupied by one CNT. For a nanotube of length  $l$  and diameter  $d$ ,  $V_{1CNT}$  can be estimated by the volume of a cylinder of

## Chapter 7. The dispersion of carbon nanotubes in composite materials studied by computer simulation of Small Angle Scattering

L. Garrido-Regife et al.

Physica B: Condensed Matter 649 (2023) 414450

these dimensions. In addition,  $Y$  is also defined as 100 times  $V_b$  divided by the total volume of the sample,  $V$ . Hence, the number of CNT per unit volume,  $n_{CNT}$ , is:

$$n_{CNT} = \frac{N_{CNT}}{V} = \frac{V_b/V_{1CNT}}{100V_b/Y} = \frac{Y}{100V_{1CNT}} = \frac{4\rho_a x}{\pi l d^2 [\rho_a x + \rho_{CNT}(1-x)]} \quad (2)$$

where now,  $\rho_a$  and  $\rho_{CNT}$  correspond to the densities of the alumina matrix and CNT, respectively. From this expression,  $n_{CNT}$  can be directly calculated from the wt.%, the geometric parameters of the CNT, and the densities of both phases (the CNT and the host matrix).

The assumed densities are  $\rho_a = 3.99 \text{ g/cm}^3$  [44] and  $\rho_{CNT} = 2.10 \text{ g/cm}^3$ . In this case, the CNT density has been assumed to be equal to the density of the graphite for simplicity, as has been done in experimental work. Nevertheless, this is not a trivial issue, and a more refined calculation can be made taking into account the densities obtained by Laurent et al. [45] for different types of nanotubes as a function of their external diameter and the number of walls. According to these calculations, the density corresponds to multi-walled CNT of an outer diameter between 10 and 20 nm, in accordance with the size of the considered CNT with an aspect ratio of 100. In addition, two other realistic types of CNT were considered with dimensions  $1 \mu\text{m} \times 50 \text{ nm}$  and  $2 \mu\text{m} \times 2 \text{ nm}$ , (aspect ratios of 20 and 1000), the considered densities are  $\rho_{CNT} = 2.10 \text{ g/cm}^3$  and  $\rho_{CNT} = 1.50 \text{ g/cm}^3$ , respectively.

In addition, in order to expand the use of the computational tools developed in this work to explore other systems, an initial approach has also been implemented for systems containing graphene. To do this, similar geometrical considerations have been employed in order to build a structural model representing a typical concentration of graphene microplatelets (GMP) used experimentally. This system has been constructed by modeling each GMP as a parallelepiped of standard dimensions  $2 \mu\text{m} \times 1 \mu\text{m} \times 3.35 \text{ nm}$ . If we take the interplanar distance of graphite,  $0.335 \text{ nm}$ , this model corresponds to a microplatelet made up of 10 layers (few-layer graphene microplatelet). This way, the number of microplatelets  $N_{GMP}$  inside a simulation box of volume  $V$  is given as a function of the vol.% by

$$N_{GMP} = n_{GMP} V = \frac{\text{vol.}\%}{100 V_{1GMP}} V \quad (3)$$

where  $n_{GMP}$  is the numeric density of the nanoplalelets, and  $V_{1GMP}$  is the volume of one GMP.

### 2.3. Creation of the systems of CNT

Once the model of the single CNT has been generated, a cubic simulation box with edge  $L_{box}^*$  (an asterisk stands for magnitudes in reduced units) is built centered on the origin of the coordinates. For the simulations, the total number of spheres has been limited to  $N_{sph} = 5 \cdot 10^5$  in order to keep the computation time below a reasonable limit of 100 hours per system. Hence, considering the aspect ratios of the selected CNT (as explained in Section 2.1), each system will consist of  $N_{CNT} = 25000, 5000,$  and  $500$  CNT, for the CNT with aspect ratios of 20, 100 and 1000, respectively. Therefore, the size of the simulation box,  $L_{box}^*$ , must be adjusted to correspond with the different concentrations of CNT. This is achieved from the wt.%, the densities of the real phases to be simulated, and considering Eq. (2) in order to calculate the density of the CNT,  $n_{CNT}$  (see Section 2.2 for details). If the total volume of the system is  $V = N_{CNT}/n_{CNT}$ , the edge of the box in which it is contained is given, in reduced units, by

$$L_{box}^* = \frac{\sqrt[3]{V}}{d} = \sqrt[3]{\frac{N_{sph}}{n_{CNT}} \frac{\pi [\rho_a x + \rho_{CNT}(1-x)]}{4x\rho_a}} \quad (4)$$

where the relation between the number of CNT and the total number of spheres of the system has been considered, given by  $N_{CNT} = N_{sph} \cdot d/l$ . Thus, the size of the simulation box obtained by this method is independent of the dimensions of the nanotubes.

Knowing the value of  $L_{box}^*$ , the positions of the mass centers of the CNT are generated through a uniform distribution of random points inside the simulation box. Every time a CNT is placed in the system, it is randomly rotated. With this procedure, it is possible to generate a configuration in which the CNT are homogeneously dispersed, that is, the perfect spatial distribution for any carbon concentration.

### 2.4. Similar systems with different degrees of aggregation

Structural models that have different degrees of aggregation of the CNT are subsequently generated by means of a Monte Carlo (MC) algorithm, starting from the homogeneous distributions created as explained in Section 2.3. The MC algorithm begins by generating  $N_{centers}$  random points inside the simulation box that act as "attractor centers" where the future aggregates will be centered. Then, in each aggregation step, the centers of mass of the CNT are randomly moved, accepting only those movements in which the CNT approach the corresponding attractor center. Thus,  $N_{centers}$  agglomerates are progressively formed. This aggregation process ends when the sum of all distances between the centers of mass of the CNT and the closest center of attraction decreases by less than 1.0% compared to the previous configuration. Finally, all the systems were analyzed using an auxiliary code to eliminate those overlapping particles that may have appeared due to the aggregation method, ensuring the hard sphere model in all cases. The negligible effect of these corrections on the validity of the simulation results was verified. As the number of CNT in the system varies with the aspect ratio,  $N_{centers}$  has been adjusted so that each aggregate has at least 100 CNT, taking 10 for the short CNT, and 3 for the CNT with ratio 1000.

In addition, knowing the total number of steps needed to end the process,  $N_{end}$ , a new parameter, %A can be defined to measure the degree of homogenization of a system at any intermediate state, analogous to that proposed by Yazdanbakhsh et al. [46]:

$$\%A = 100 \frac{N_{step}}{N_{end}} \quad (5)$$

where  $N_{step}$  is the aggregation step of the system that is being studied. According to this definition, a degree of aggregation of %A = 0 corresponds to the initial configuration, where the CNT are homogeneously dispersed, while a degree of aggregation of %A = 100 corresponds to the situation where the agglomerates are completely formed.

The size of the final entanglements was estimated from geometrical considerations. Hence, the external radius of the entanglements,  $R_{ext}$ , was calculated as an average of the distances of the center of mass of the most remote CNT to their corresponding center of attraction (the geometrical center of the aggregate). Besides, the gyration radius,  $R_{gyr}$ , was also estimated by the classical expression for a mass distribution with respect to the center of attraction. All the parameters were averaged over all the aggregates and over, at least, three different replicas.

### 2.5. Computer simulation of the small angle scattering intensities

In the simulations of the scattered intensities, the coordinates of all the spheres that form the system of CNT are used as the input data. An ideal ceramic matrix was considered in order to focus the research on the set of CNT, so any possible contribution of the ceramic matrix to the scattering intensity was disregarded. The developed code begins by calculating the pair correlation function from the number of pairs  $N(r)$  of particles located at a relative distance  $r$ . This function is obtained by considering periodic boundary conditions in the simulation box, and is subsequently normalized according to the volume of a spherical shell of radius  $r$  and thickness  $dr$  by the expression

$$g(r) = \frac{N(r)}{4\pi r^2 dr n_0^2} \quad (6)$$

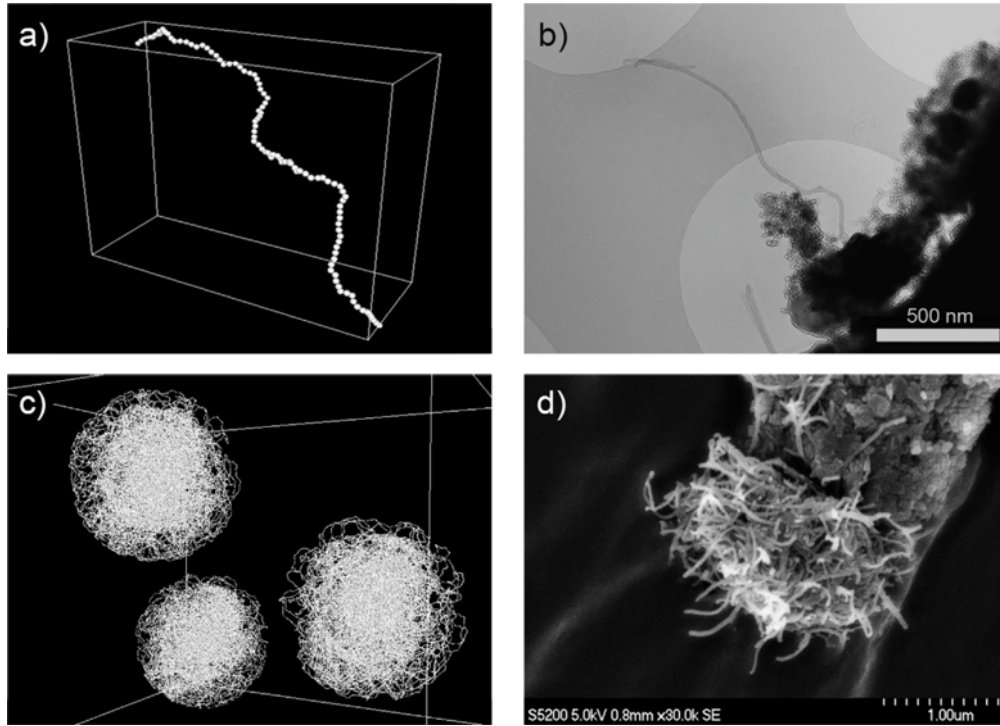


Fig. 2. Comparison between the structural models and the physical systems observed by microscopy techniques: (a) CNT model as a chain formed by a concatenation of 100 spheres; (b) TEM image of an isolated CNT emerging from a cloud of boehmite nanoparticles and  $\gamma$ -Al<sub>2</sub>O<sub>3</sub>; (c) Simulation of the fully-aggregated systems of CNT with an aspect ratio of 1000; (d) SEM image of a CNT agglomerate in a boehmite matrix with 1 wt.% CNT.

where  $n_0^* = N_{sph}/L_{box}^3$  is the numerical density of spheres that make up the system. When the system is formed by identical scattering centers, the scattering intensity is obtained as the product of the form factor,  $P(q)$ , and the structure factor,  $S(q)$ , namely,  $I(q) = P(q)S(q)$ . In this case, as we work with spheres with unit diameter, the form factor is given by Hasmy et al. [47]. The structure factor has been calculated from the pair correlation function  $g(r)$  using the corrected expression defined by Hasmy et al. [47] for finite sized systems:

$$S(q) = 1 + \frac{N_{sph}}{V} \int_0^{r_m} 4\pi r^2 (g(r) - g_0) \frac{\sin(qr)}{qr} dr \quad (7)$$

where  $g_0$  is a parameter whose value is very close but not strictly equal to one, and  $r_m = L_{box}^*/2$  is the cutoff radius used to truncate the integral. Given the random nature of these models, the results have been obtained by averaging the intensity signal over four independent replicas for each concentration.

## 2.6. Analysis of the intensity curves

The intensity curves obtained by simulation were analyzed with the Guinier–Fractal–Porod scheme [30], where, at high values of  $q$ , the flat surface area of the elemental scatterers will lead to a relation  $I \propto q^{-4}$  (linear region in the log–log representation of  $I$  vs.  $q$ ). Decreasing the values of  $q$ , typically, the power law is increased, and, in the case that a well-defined linear region spans for more than one decade, a fractal regime can be identified. At lower values of  $q$ , the Guinier region may appear, which indicates the existence of scatterers of a well-defined size. This characteristic size is estimated by fitting the Guinier model for the intensity (valid for  $qR \ll 1$ ):

$$I(q) = I(0)e^{-\frac{q^2 R_G^2}{3}} \quad (8)$$

where  $R_G$  is the Guinier radius, which is defined as the root mean square distance of the mass of the scatterer to its center of gravity. In the case that the system is formed by spherical structures (or aggregates, which is our case) its radius is related to the Guinier radius by  $R = \sqrt{5/3}R_G$  [30]. This radius can be called the entanglement radius.

In order to verify the ability of the method used in this work to reveal superstructural features of these models based on assemblies of spheres, such as their aggregated or well dispersed states, previous tests were performed by analyzing the Cluster Models [48] (Appendix A).

## 2.7. Electron microscopy images

Some micrographs were acquired in order to exemplify the real appearance of the simulated structures. The images were captured by transmission electron microscopy (TEM), using a Philips model CM-200, and by scanning electron microscopy (SEM), using a Hitachi model S5200 with acceleration voltages of 5 kV. The nanotubes selected for the pictures are multiwall CNT, supplied by *NanoAmor, Inc.*, with a length of 0.5–2  $\mu\text{m}$ , outer diameter 8–15 nm, and inner diameter 3–5 nm, dimensions confirmed by TEM. Those CNT are hosted in clouds of boehmite nanoparticles, which, after heating or sintering treatments, are transformed into alumina [44].

## 3. Results and discussion

### 3.1. Composites at the microscale

The construction algorithm of the CNT gives randomly curled chains as shown in Fig. 2. The simulated CNT obtained by this algorithm recall the typical images of tortuous threads observed by electron microscopy, both isolated CNT and aggregated CNT in the alumina–CNT composites.

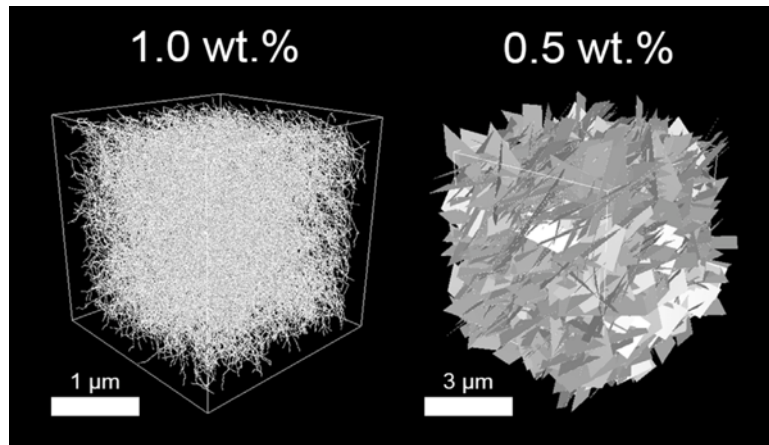


Fig. 3. Simulation of homogeneous distributions of CNT (left) and graphene nanoplatelets (right) for 1.0 wt.% and 0.5 wt.%, respectively, in an alumina matrix.

In addition, in Fig. 2, a fully-aggregated system of CNT of aspect ratio of 1000 forming three entanglements, is also shown. It can be confirmed that the CNT agglomerates obtained by this method are similar to the CNT entanglements found in the composites.

Moreover, the amount of carbon allotropes typically considered in experimental research deserves some comments with the help of this simulation tool. Fig. 3 shows two systems of homogeneous (perfectly random) dispersions of different individualized carbon allotropes, namely, CNT and GMP, corresponding to alumina composites with a carbon concentration of 1.0 wt.% and 0.5 wt.% respectively. This way, the microscopic aspect of composites with typical values of carbon content is rendered. The first impressive feature is how crowded the composite is at the microscale when the carbon allotropes are perfectly distributed. In fact, the volumetric densities of nanostructured allotropes in these systems are  $\sim 122.6$  CNT and  $\sim 1.5$  GMP per  $\mu\text{m}^3$ . Thus, if ceramic matrix with a micrometric average grain size are considered, the volumetric densities indicate a very significant allotrope-per-grain ratio. Therefore, the aim of fabricating ceramic composites with 1.0 wt.% of nanotubes or graphene without aggregates seems naïve. In addition, when the quality of the dispersion of the reinforcing phase is assessed by electron microscopy, if large areas appear absolutely empty of allotropes in the composite, there are necessarily other non-observed areas of the composite that have plenty of aggregated carbon allotropes.

Taking these ideas into account, concentration values of 0.10, 0.05 and 0.01 wt.% have been used for the simulations in this work and Table 1 shows the construction parameters of the generated CNT systems. Note that, since  $N_{sph}$  is fixed for computing limitations,  $L_{box}^*$  does not depend on the dimensions of the CNT used as a reference (Eq. (4)). The aspect of the systems with 0.05 wt.% of CNT at the microscale can be seen in the first row of Fig. 4 for different types of CNT (different aspect ratios). It can be observed that, even for these low carbon contents, the representations of the homogeneous distributions of the CNT reveal a very crowded space at the microscale.

### 3.2. Systems with different aggregation states

Fig. 4 shows the different aggregation states of the systems with the three different aspect ratios studied in this work, corresponding to a concentration of 0.05 wt.%. The initial homogeneous states, namely, the perfectly distributed configurations, were subjected to the Monte Carlo aggregation algorithm explained in Section 2.4 and snapshots for intermediate and full aggregation states are included in Fig. 4.

Hence, it can be seen how the initial homogeneous spatial distribution of CNT is gradually abandoned and selected areas of the simulation

box start to become more crowded while others become more empty. The progressive formation of aggregates can be seen as the aggregation numerical procedure runs (increasing aggregation index, %A), finishing with extremely populated regions of the space that simulate the typical CNT coils or entanglements observed experimentally (Fig. 2c and last row of Fig. 4). It is worth remarking that the densities of the agglomerates obtained with this method are in coherence with those previously reported by Romanov et al. [42]. An animation of the aggregation process can be seen in the *Supplementary Content*.

In Table 1, the calculated values of the numeric density for the different types of CNT and for different carbon contents are shown. It can be confirmed that the number of CNT per cubic micron increases with the carbon content, as expected, and even for the simulated low carbon concentrations (0.01, 0.05 and 0.10 wt.%), if a ceramic matrix with micron-sized grains is considered, the homogeneous distribution implies that all the grains will contain CNT. Again, this suggests that obtaining composites with perfectly dispersed individualized CNT for the considered carbon contents is almost impossible. Moreover, the apparent paradox of increasing the numeric density with the increasing aspect ratio is explained by the real dimensions and densities of the considered CNT (see Section 2.1), with the  $V_{CNT}$  of the CNT with aspect ratio of 20 being more than 300 times higher than the  $V_{CNT}$  for CNT with a ratio of 1000. Consequently, very different numbers of CNT are needed to contribute with the same mass in  $1 \mu\text{m}^3$ .

The final configurations of the systems were used to directly measure the gyration radius,  $R_{g,yp}$ , and the external radius,  $R_{ext}$ , of the aggregates. The obtained data are collected in Table 1. It can be confirmed that, systematically, the gyration radius is smaller than the geometrical size in all cases, as expected. Moreover, the sizes of the aggregates increase with the aspect ratio of the CNT, but not with the carbon content. This result reveals that the aggregation algorithm creates intermediate agglomeration states that may be realistic representations of the considered aggregates of CNT in the composites, but it also reveals the fact that the size of the entanglement in the fully-aggregated state depends on the aspect ratio of the CNT. Nevertheless, this effect is determined by the arbitrary selection of the number of aggregates and the restrictions of the aggregation algorithm, such as the condition of identical size of the aggregates and the absence of folding during aggregation. Thus, these parameters should be thoroughly tuned and calibrated whenever the simulations are intended to reproduce specific real composites.



**Table 1**

Construction parameters of the systems of CNT with different concentrations and aspect ratios ( $l/d$ ), and calculated characteristics: numeric density of nanotubes,  $n_{CNT}$ , and size of the simulation box,  $L_{box}^*$ . Geometric sizes of the entanglements obtained from the fully-aggregated configuration of each system: gyration radius,  $R_{gyr}^*$ , and external radius,  $R_{ext}^*$ . Characteristic sizes obtained from the fitting of the intensity curves to the Guinier model using the fully-aggregated configuration: Guinier radius,  $R_G^*$ , and derived entanglement radius,  $R^* = \sqrt{5/3}R_G^*$ . Asterisks indicate that reduced units are considered, being the reduced unit the diameter of the elemental sphere. Uncertainties have been obtained by averaging over three different replicas.

Parameters of the models			Geometric sizes			Characteristic sizes from $I(q)$	
wt.%	ratio $l/d$	$n_{CNT}$ (CNT/ $\mu\text{m}^3$ )	$L_{box}^*$	$R_{gyr}^*$	$R_{ext}^*$	$R_G^*$	$R^*$
0.01	100	1.24	$1300.94 \pm 0.09$	$22.4 \pm 0.4$	$40.5 \pm 0.9$	$19.3 \pm 0.5$	$24.9 \pm 0.6$
	20	0.48	$751.00 \pm 0.02$	$6.6 \pm 0.1$	$8.5 \pm 0.1$	$7.1 \pm 0.2$	$9.1 \pm 0.2$
0.05	100	6.18	$750.97 \pm 0.04$	$22.5 \pm 0.5$	$38.4 \pm 0.5$	$18.1 \pm 0.5$	$23.4 \pm 0.6$
	1000	211.24	$671.00 \pm 0.04$	$66.7 \pm 2.3$	$113.2 \pm 6.2$	$45.3 \pm 1.1$	$58.5 \pm 1.4$
0.10	100	12.36	$600.96 \pm 0.07$	$22.8 \pm 0.2$	$38.1 \pm 0.4$	$18.3 \pm 0.5$	$23.7 \pm 0.6$

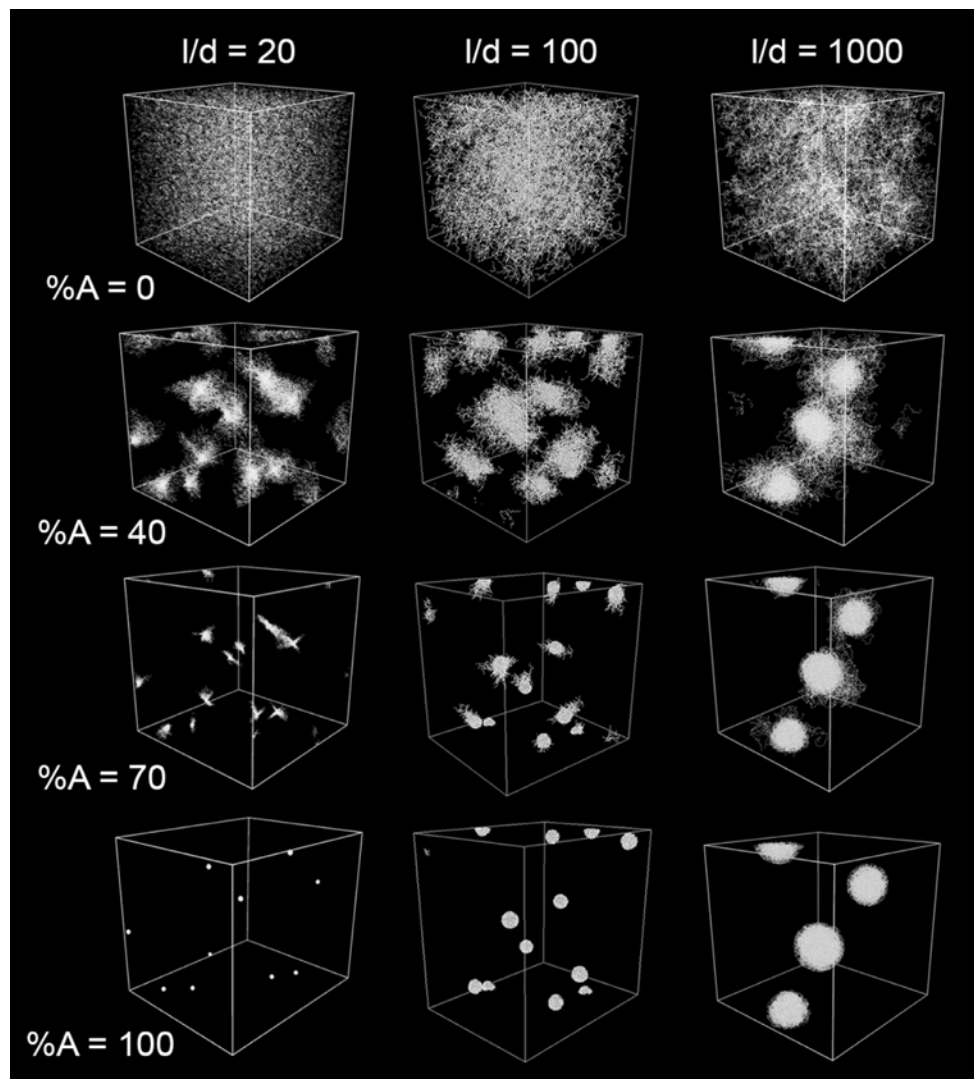


**Fig. 4.** Systems that simulate the sets of CNT with different aspect ratios ( $l/d$ ) for a carbon concentration of 0.5 wt.% distributed in a alumina matrix corresponding to different degrees of dispersion, indicated by the parameter  $\%A$  (see Section 2.4 for details). The first row shows the initial configuration of each system ( $\%A = 0$ , homogeneously dispersed CNT). The second and third rows correspond to intermediate aggregate states with  $\%A = 40$  and  $\%A = 70$  aggregation respectively. Finally, the last row shows the CNT forming agglomerates ( $\%A = 100$ , fully aggregated state). Note that periodic boundary conditions are considered.

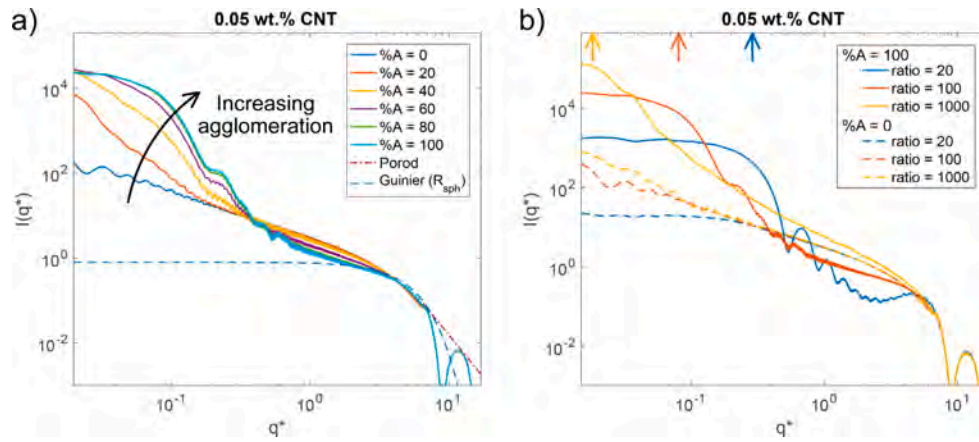


Fig. 5. (a) Scattering intensity curves obtained for systems with a concentration values of 0.05 wt.% of CNT throughout the aggregation process. A shoulder/knee appears in the intensity signal around  $q^* = 0.1$  when the system evolves towards the formation of the entanglements. (b) Comparison between the intensities obtained for systems with nanotubes of different aspect ratios (20, 100 and 1000) for the states with homogeneously dispersed CNT ( $\%A = 0$ ) and fully aggregated CNT ( $\%A = 100$ ). The arrows mark the  $q$  values associated with the size of the CNT aggregates.

### 3.3. The scattering intensity of the systems of CNT for different aggregation states

From each of the generated systems of CNT, the initial homogeneous state, the fully-aggregated configuration, and four intermediate configurations have been selected to obtain the simulated scattering signal. The scattered intensities measured for the systems with 0.05 wt.% of CNT are shown in Fig. 5a. The intensity scattered by systems with different carbon concentrations were also studied but no significant change was found (data not shown).

In the initial configuration ( $\%A = 0$ , CNT homogeneously dispersed), the intensity decreases linearly in the regime of small values of  $q^*$  (in the log-log representation), defining a fractal region spanning for more than one decade. It can be observed that the intensity presents significant variations below  $q^* \sim 0.3$  as the CNT aggregation process occurs. Hence, the aggregation of the CNT leads to the disappearance of the well-defined fractal region, and the intensity in the low- $q^*$  zone shows an increasing shoulder as the percentage of aggregation of the system increases, that is, as the agglomerates of CNT are formed. Then, for the fully-aggregated configuration ( $\%A = 100$ ), a second Guinier regime is fully formed, revealing the presence of well-defined entanglements acting as scatterers.

In the range  $1.5 < q^* < 6.5$ , all the curves follow similar trends, fitting the Guinier model associated with the elementary spheres that make up the system, with radius  $R_{sph}^* = 0.5$ . For  $q^* > 6.5$ , the intensities fall according to Porod's law with a slope  $I(q) \propto q^{-4}$ , where the typical sharp oscillations due to the mathematical monodispersity of the spheres can be seen.

The fully-aggregated systems have been analyzed and the characteristic size of the scatterers that lead to the observed changes in the intensity were estimated. To do this, the curves have been fitted to the Guinier model in the range  $0.02 < q^* < 0.13$ , to obtain the Guinier radius,  $R_G^*$ , and the radius,  $R^*$ , of the entanglements (Table 1). The good correspondence between the size  $R^*$  obtained from the Guinier fittings with the average gyration radius of the entanglements in the maximum agglomeration configuration of the CNT,  $R_{gyr}^*$ , can be verified. That is, the appearance of large scatterers, such as the agglomerates formed by the entanglement of CNT, is clearly revealed by the changes in the scattering curve. Thus, the presence of these aggregates of CNT could be found by Small Angle Scattering, or, eventually, Ultra-Small Angle Scattering.

To check the effect of the aspect ratio of CNT on the scattering signal and the feasibility of detecting the existence of aggregates through

Small Angle Scattering, the three systems with a concentration of 0.05 wt.% of the nanophase have been studied. Fig. 5b shows the intensity curves of these three systems in the initial configuration (dashed line,  $\%A = 0$ ) and the fully-aggregated configuration (solid line,  $\%A = 100$ ). It can be confirmed that, independently of the aspect ratio, perfectly dispersed CNT yields scattering curves that smoothly decrease with increasing  $q^*$ , up to the sizes corresponding to the elemental spheres, namely,  $q^* \sim 6.5$ . Moreover, well-defined Guinier regions appeared at low  $q^*$  in the fully-aggregated systems. On the upper axis, the arrows indicate the positions where the Guinier regimes appear. These characteristic values of  $q^*$  correspond to the values of the size of the agglomerates,  $q^* = \pi/R^*$  (see Table 1), which confirms that the appearance of this Guinier regime indicates the formation of aggregates of size  $R^*$ , regardless of the aspect ratio of the CNT. In addition, the position of this Guinier regime shifts to the left as the aspect ratio increases, in coherence with the increasing measured sizes,  $R^*$ , as discussed in Section 3.2.

### 3.4. The assessment of the quality of the distribution of the CNT

Considering the results obtained for the intensity curves displayed in Fig. 5, the appearance of the Guinier regime in the range of low- $q^*$  values can be established as a first qualitative standard to detect the formation of aggregates. Another qualitative rule to qualitatively assess the dispersion of the nanophase is the presence or not of a fractal regime that extends more than a decade, as occurs in the homogeneous distributions of CNT (curves  $\%A = 0$  in Fig. 5).

Further analyses allow establishing a quantitative relation between the degree of aggregation of CNT systems ( $\%A$ ) and two parameters that can be experimentally calculated from the scattering signals. The first parameter considered to quantify the quality of the dispersion is a relative intensity,  $I_{rel}$ , defined as the quotient between the value of the intensity at the minimum value of  $q$  and the intensity  $I_0$  obtained from the fitting of the intensity to the Guinier model associated with the diameter of the CNT (the diameter of the elemental sphere size in the simulations). An example of this Guinier fitting is shown in Fig. 5a (dashed line). The second studied parameter is the minimum of the derivative of the intensity curve, in absolute value, in the regime of  $q^*$  where the Guinier region associated to the aggregates appears (low- $q^*$  values). This analysis aims to reflect the fact that major changes appeared in the scattering curves in the first stages of the aggregation, namely, from  $\%A = 0$  to  $\%A = 20$ , when the fractal regime is abandoned, as seen in Fig. 5a.

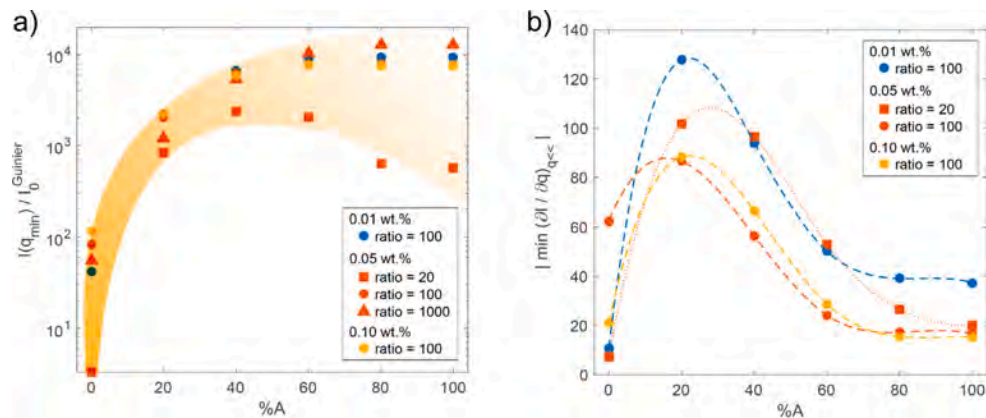


Fig. 6. Dependence of the parameters  $I_{rel}$  (a) and minimum of the derivative of the intensity (b) with the degree of aggregation ( $\%A$ ) of the CNT systems for three concentrations of the nanophase and different aspect ratios. The trend lines (dashed) have been obtained using a spline.

The dependence of these two parameters on the degree of aggregation  $\%A$  for the studied systems can be observed in Figs. 6(a) and 6(b). In both cases, the greatest variation in the experimental parameter is obtained around 20% aggregation, while above 60%, both remain practically constant. These analyses show that the intensity of scattering is highly sensitive to partial aggregations of the nanophase, which is specially relevant for reinforcing strategies because, as stated by Romanov et al. “even partial CNT agglomeration provokes vast matrix stress concentrations that could facilitate an earlier damage onset in a composite” [42].

#### 4. Conclusions

The present work has explored the potentialities of Small Angle Scattering techniques to analyze the dispersion of nanostructured carbon allotropes. Realistic structural models of homogeneously dispersed nanostructured carbon allotropes were built for this purpose, simulating different typical concentrations and CNT with different aspect ratios. Firstly, the aspect of the distributions of carbon nanotubes in alumina-based systems with the usually considered carbon contents showed that, at the microscale, the space is extremely populated, reaching numerical densities as high as several hundreds of CNT per cubic micron. Therefore, the fabrication of carbon-reinforced composites completely lacking in aggregates seems impossible for carbon contents like those. Thus, considering the crucial requirement of avoiding aggregates for the efficiency of reinforcing composites by adding CNT, this strategy should be thoroughly reconsidered.

Moreover, the differences in the scattering intensity from the simulated systems of carbon nanotubes with different degrees of aggregation in an alumina matrix were discussed. It was confirmed that the intensities progressively lose the well-defined fractal regime when the CNT aggregate, and a Guinier regime appears in the range of low- $q^*$  values. The corresponding Guinier radius corresponds to the size of the aggregates. Despite the limitations of the agglomeration algorithm, the consideration of CNT with different aspect ratios shows that the position of this Guinier region shifts according to the size of the aggregates. In addition, the analyses confirmed that the SAS techniques may be suitable to reveal agglomeration problems of reinforcing nanophases such as carbon nanotubes in composites.

Finally, the analyses of the scattering intensity curves of systems that progressively aggregate allow the definition of two parameters to assess the quality of the CNT dispersion: the ratio between the value of the intensity at minimum  $q$  and the intensity  $I_0$  obtained from the Guinier model associated with the diameter of the CNT; and the minimum of the derivative of the intensity curve, in absolute value,

in the regime of low- $q^*$ . It was observed that the greatest relative change in the intensity curve is found between the totally homogeneous distribution and the first stages with partial agglomeration. This characteristic can be explored by studying the first derivative of the scattering curve, and it may be of special interest to quantitatively estimate the quality of the dispersion of the embedded nanophases in ceramic matrices and other composites.

#### CRediT authorship contribution statement

**Laura Garrido-Regife:** Design of the algorithms, Programming, Exploitation of the simulations, Analyses of the correlation between simulation and experiments, Writing – original draft. **Pedro Rivero-Antúñez:** Electron microscopy images, Analyses of the correlation between simulation and experiments, Writing – original draft. **Víctor Morales-Flórez:** Design of the algorithms, Analyses of the correlation between simulation and experiments coordination of the team, Writing – original draft.

#### Declaration of competing interest

The authors declare that they have no known competing financial interests or personal relationships that could have appeared to influence the work reported in this paper.

#### Data availability

Data will be made available on request.

#### Acknowledgments

Project PGC2018-094952-B-I00 funded by FEDER/Ministerio de Ciencia e Innovación - Agencia Estatal de Investigación, Spain is acknowledged. Project P20-01121 (FRAC) funded by Junta de Andalucía (Consejería de Transformación económica, Industria, Conocimiento y Universidades), Spain. Profs. A. Hasmy and E. Anglaret are acknowledged for their help and discussions. All the members of the FQM393 research group and the Knights of the Alumina are greatly acknowledged for their support to this research. M. Gimeno del Valle is also acknowledged for his help with the concept of “quantity” of reinforced concrete.

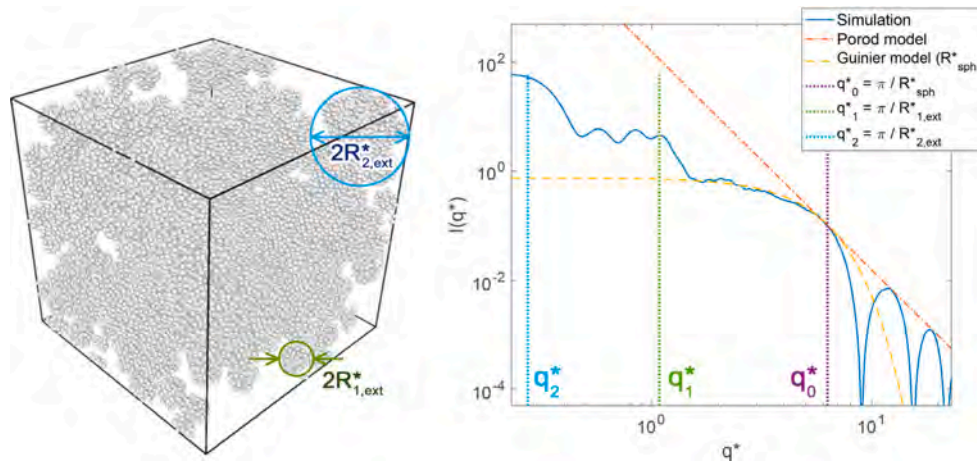


Fig. 7. Left: Cluster model with three different hierarchical levels. The characteristic size of the first level corresponds to the radius of the elementary spheres,  $R_{sph}^*$ , equal to 0.5 in reduced units. The characteristic size of the second and the third level is indicated. Right: Scattering intensity obtained for the cluster model in the Fig. 7(a). In addition to the curve obtained by simulation, the fitted Guinier and Porod models are represented. The vertical lines indicate the values of  $q$  associated with the different characteristic sizes of the system, and their correspondence with real sizes is indicated in the legend.

#### Appendix A. Validation of the scattering intensity algorithm

Cluster Models [48] are structural models with a given superstructure perfectly known from geometrical premises. These systems are built using a hard sphere random packing algorithm. The process starts by surrounding a starting sphere with randomly distributed spheres maintaining the hard contact condition until it is completely covered. Then, each new sphere is randomly surrounded as well until completing the formation of a cluster of a given size and with an approximately spherical shape. This cluster is then used as a structural element instead of spheres, to build the next hierarchical level by the similar procedure. These steps are repeated until  $n$  hierarchical levels have been built. Note that the actual size of the clusters of the different hierarchical levels, namely, the different characteristic sizes, can be geometrically estimated. More details about the construction of these systems can be found in the work done by Morales-Flórez et al. [48]. In Fig. 7(a), one Cluster Model with three hierarchical level is shown.

Several Cluster Models have been constructed and characterized to verify that the sizes of the different hierarchical levels present in these structures are adequately revealed in the scattering intensity curve. Figs. 7(a) and 7(b) show a cluster model with three hierarchical levels and its corresponding scattering intensity. In the regime of high values of  $q$ , the maxima of the intensity fit adequately to the Porod model. The abrupt drops in intensity in this regime are a consequence of the monodispersity of the spheres considered in the construction of the systems. For values of  $q$  between  $\sim 2$  and  $\sim 7$  (reduced units are considered), the simulated intensity fits the Guinier model corresponding to a sphere of radius  $R_{sph}^* = 0.5$ ; however, this correspondence disappears for smaller values of  $q$ . This is due to, by exploring smaller values of  $q$ , the system is observed at greater sizes in real space and, therefore, the intensity begins to be sensitive to the characteristic sizes of higher order structures. The positions of these increments in the intensity coincide with the values of  $q$  associated with the different characteristic sizes of the hierarchical structure, which indicates a correct functioning of the developed code. In Fig. 7(a), the typical sizes of the hierarchical model are indicated, and the corresponding scattered intensity curve is also shown. In the plot, the correspondence between the characteristic sizes of the model and the corresponding  $q$ -values are also highlighted. It could be verified that the characteristic  $q$ -values revealed by the features of the intensity curve correspond reasonably well with the theoretical real characteristic values of the system, with regard to the relationship  $q_i = \pi / R_i$ .

#### Appendix B. Supplementary data

Supplementary material related to this article can be found online at <https://doi.org/10.1016/j.physb.2022.414450>.

#### References

- [1] G.D. Zhan, J.D. Kuntz, J. Wan, A.K. Mukherjee, Single-wall carbon nanotubes as attractive toughening agents in alumina-based nanocomposites, *Nature Mater.* 2 (2003) 38–42.
- [2] I.A. Kinloch, J. Suhr, J. Lou, R.J. Young, P.M. Ajayan, Composites with carbon nanotubes and graphene: An outlook, *Science* 362 (2018) 547–553.
- [3] A.M. Esawi, K. Morsi, A. Sayed, M. Taher, S. Lanka, The influence of carbon nanotube (CNT) morphology and diameter on the processing and properties of CNT-reinforced aluminium composites, *Composites A* 42 (2011) 234–243.
- [4] E. Zapata-Solvas, D. Gómez-García, A. Domínguez-Rodríguez, Towards physical properties tailoring of carbon nanotubes-reinforced ceramic matrix composites, *J. Eur. Ceram. Soc.* 32 (2012) 3001–3020.
- [5] J. Stein, B. Lenczowski, N. Fréty, E. Anglaret, Mechanical reinforcement of a high-performance aluminium alloy AA5083 with homogeneously dispersed multi-walled carbon nanotubes, *Carbon* 50 (2012) 2264–2272.
- [6] S. Parveen, S. Rana, R. Fanguero, A review on nanomaterial dispersion, microstructure, and mechanical properties of carbon nanotube and nanofiber reinforced cementitious composites, *J. Nanomater.* 2013 (2013).
- [7] C. Guo, X. Luo, W.A. Shah, B. Huang, J.K. Li, M.A. Umer, Y.Q. Yang, Mechanical and electrical properties of carbon nanotube-reinforced Al<sub>2</sub>O<sub>3</sub> nanocomposites, *J. Mater. Sci.* 55 (2020) 8728–8740, <http://dx.doi.org/10.1007/s10853-019-04173-5>.
- [8] C. Guo, X. Luo, W.A. Shah, J.K. Li, B. Huang, M.A. Umer, Y.Q. Yang, Mechanical and thermal properties of multiwalled carbon-nanotube-reinforced Al<sub>2</sub>O<sub>3</sub> nanocomposites, *Ceram. Int.* 46 (2020) 17449–17460.
- [9] V. Morales-Flórez, A. Domínguez-Rodríguez, Mechanical properties of ceramics reinforced with allotropic forms of carbon, *Prog. Mater. Sci.* 128 (2022) 100966.
- [10] V.B. Mohan, K.T. Lau, D. Hui, D. Bhattacharyya, Graphene-based materials and their composites: A review on production, applications and product limitations, *Composites B* 142 (2018) 200–220.
- [11] P.T. Rao, J. Prakash, R. Alexander, A. Kaushal, J. Bahadur, D. Sen, K. Dasgupta, Innovative design and fabrication of generation IV nuclear fuel embedded with carbon nanotube, *Ceram. Int.* 46 (2020) 14591–14596.
- [12] P. Greil, Perspectives of nano-carbon based engineering materials, *Adv. Energy Mater.* 17 (2015) 124–137.
- [13] A. Aguilar-Elguézabal, M.H. Bocanegra-Bernal, Fracture behaviour of a-Al<sub>2</sub>O<sub>3</sub> ceramics reinforced with a mixture of single-wall and multi-wall carbon nanotubes, *Composites B* 60 (2014) 463–470.
- [14] M.H. Bocanegra-Bernal, C. Domínguez-Ríos, J. Echeberria, A. Reyes-Rojas, A. García-Reyes, A. Aguilar-Elguézabal, Spark plasma sintering of multi-, single- and double-walled carbon nanotube-reinforced alumina composites: Is it justifiable the effort to reinforce them? *Ceram. Int.* 42 (2016) 2054–2062.

- [15] N. Song, H. Liu, J. Fang, Fabrication and mechanical properties of multi-walled carbon nanotube reinforced reaction bonded silicon carbide composites, *Ceram. Int.* 42 (2016) 351–356.
- [16] R. Cano-Crespo, B.M. Moshaghuioun, D. Gómez-García, R. Moreno, A. Domínguez-Rodríguez, Graphene or carbon nanofiber-reinforced zirconia composites: Are they really worthwhile for structural applications? *J. Eur. Ceram. Soc.* 38 (2018) 3994–4002.
- [17] J.W. McCauley, Proceedings of the 5th Annual Conference on Composites and Advanced Ceramic Materials: Ceramic Engineering and Science Proceedings, Vol. 2, The American Ceramic Society, Inc., Hoboken, NJ, USA, 1981, <http://dx.doi.org/10.1002/9780470291092>, URL <https://ceramics.onlinelibrary.wiley.com/doi/book/10.1002/9780470291092>, Issue 7/8.
- [18] M. Estili, Y. Sakka, Recent advances in understanding the reinforcing ability and mechanism of carbon nanotubes in ceramic matrix composites, *Sci. Technol. Adv. Mater.* 15 (2014).
- [19] J.H. Shin, J. Choi, M. Kim, S.H. Hong, Comparative study on carbon nanotube- and reduced graphene oxide-reinforced alumina ceramic composites, *Ceram. Int.* 44 (2018) 8350–8357.
- [20] P. Rivero-Antúnez, R. Cano-Crespo, L. Esquivias, N. de la Rosa-Fox, C. Zamora-Ledezma, A. Domínguez-Rodríguez, V. Morales-Flórez, Mechanical characterization of sol-gel alumina-based ceramics with intragranular reinforcement of multiwalled carbon nanotubes, *Ceram. Int.* 46 (2020) 19723–19730.
- [21] C.B. Mo, S.I. Cha, K.T. Kim, K.H. Lee, S.H. Hong, Fabrication of carbon nanotube reinforced alumina matrix nanocomposite by sol-gel process, *Mater. Sci. Eng. A* 395 (2005) 124–128.
- [22] R. Poyato, A.L. Vasiliev, N.P. Padture, H. Tanaka, T. Nishimura, Aqueous colloidal processing of single-wall carbon nanotubes and their composites with ceramics, *Nanotechnology* 17 (2006) 1770–1777.
- [23] L. Esquivias, P. Rivero-Antúnez, C. Zamora-Ledezma, A. Domínguez-Rodríguez, V. Morales-Flórez, Intragranular carbon nanotubes in alumina-based composites for reinforced ceramics, *J. Sol-Gel Sci. Technol.* 90 (2019) 162–171.
- [24] A. Mukhopadhyay, B.T. Chu, M.L. Green, R.I. Todd, Understanding the mechanical reinforcement of uniformly dispersed multiwalled carbon nanotubes in alumino-borosilicate glass ceramic, *Acta Mater.* 58 (2010) 2685–2697.
- [25] M. Estili, Y. Sakka, W.W. Wu, T. Nishimura, H. Yoshida, A. Kawasaki, Perfect high-temperature plasticity realized in multiwalled carbon nanotube-concentrated  $\alpha$ - $\text{Al}_2\text{O}_3$  hybrid, *J. Am. Ceram. Soc.* 96 (2013) 1904–1908.
- [26] O. Hanzel, J. Sedláček, P. ajgálík, New approach for distribution of carbon nanotubes in alumina matrix, *J. Eur. Ceram. Soc.* 34 (2014) 1845–1851.
- [27] A.M. Zahedi, J. Javadpour, H.R. Rezaie, M. Mazaheri, Analytical study on the incorporation of zirconia-based ceramics with carbon nanotubes: Dispersion methods and mechanical properties, *Ceram. Int.* 42 (2016) 1653–1659.
- [28] G. Yamamoto, K. Shirasu, Y. Nozaka, W. Wang, T. Hashida, Microstructure-property relationships in pressureless-sintered carbon nanotube/alumina composites, *Mater. Sci. Eng. A* 617 (2014) 179–186.
- [29] I. Ahmad, B. Yazdani, Y. Zhu, Recent advances on carbon nanotubes and graphene reinforced ceramics nanocomposites, *Nanomaterials* 5 (2014) 90–114.
- [30] O. Glatter, O. Kratky, Small Angle X-Ray Scattering, Academic Press Inc. (London) LTD., London, 1982.
- [31] S.S. Welborn, E. Detsi, Small-angle X-ray scattering of nanoporous materials, *Nanoscale Horiz.* 5 (2020) 12–24.
- [32] V. Morales-Flórez, N.D.L. Rosa-Fox, M. Piñero, L. Esquivias, Hybrid aerogels and bioactive aerogels under uniaxial compression: An in situ SAXS study, *Rev. Metal.* 46 (2010) 143–148.
- [33] B. Nagy, A. Tóth, I. Savina, S. Mikhalovsky, L. Mikhalovska, I. Grillo, E. Geissler, K. László, Small angle neutron scattering study of globular proteins confined in porous carbons, *Carbon* 106 (2016) 142–151.
- [34] I. Patmanidis, A.H. de Vries, T.A. Wassenaar, W. Wang, G. Portale, S.J. Marrink, Structural characterization of supramolecular hollow nanotubes with atomistic simulations and SAXS, *Phys. Chem. Chem. Phys.* 22 (2020) 21083–21093.
- [35] T. Rosén, R. Wang, C. Zhan, H. He, S. Chodankar, B.S. Hsiao, Cellulose nanofibrils and nanocrystals in confined flow: Single-particle dynamics to collective alignment revealed through scanning small-angle X-ray scattering and numerical simulations, *Phys. Rev. E* 101 (2020) 032610.
- [36] A. Okuda, M. Shimizu, K. Morishima, R. Inoue, N. Sato, R. Urade, M. Sugiyama, Solution structure of multi-domain protein ER-60 studied by aggregation-free SAXS and coarse-grained-MD simulation, *Sci. Rep.* 11 (2021) 5655.
- [37] B.N. Wang, R.D. Bennett, E. Verploegen, A.J. Hart, R.E. Cohen, Characterizing the morphologies of mechanically manipulated multiwall carbon nanotube films by small-angle X-ray scattering, *J. Phys. Chem. C* 111 (2007) 17933–17940.
- [38] X. Yang, L. Yuan, V.K. Peterson, A.I. Minett, M. Zhao, N. Kirby, S. Mudie, A.T. Harris, Pretreatment control of carbon nanotube array growth for gas separation: Alignment and growth studied using microscopy and small-angle x-ray scattering, *ACS Appl. Mater. Interfaces* 5 (2013) 3063–3070.
- [39] J.C. Fernández-Toribio, A. Mikhalchan, C. Santos, A. Ridruejo, J.J. Vilatela, Understanding cooperative loading in carbon nanotube fibres through in-situ structural studies during stretching, *Carbon* 156 (2020) 430–437.
- [40] O.V. Tomchuk, M.V. Avdeev, V.L. Aksenov, A.V. Shulenina, O.I. Ivankov, V. Ryukhtin, L. Vékás, L.A. Bulavin, Temperature-dependent fractal structure of particle clusters in aqueous ferrofluids by small-angle scattering, *Colloids Surf. A* 613 (2021) 126090.
- [41] E. Ramos, W.A. Pardo, M. Mir, J. Samitier, Dependence of carbon nanotubes dispersion kinetics on surfactants, *Nanotechnology* 28 (2017).
- [42] V.S. Romanov, S.V. Lomov, I. Verpoest, L. Gorbatikh, Stress magnification due to carbon nanotube agglomeration in composites, *Compos. Struct.* 133 (2015) 246–256.
- [43] H. Zhu, A.J. Whittle, R.J. Pellenq, K. Ioannidou, Mesoscale simulation of aggregation of imogolite nanotubes from potential of mean force interactions, *Mol. Phys.* 117 (2019) 3445–3455.
- [44] P. Rivero-Antúnez, R. Cano-Crespo, F. Sánchez-Bajo, A. Domínguez-Rodríguez, V. Morales-Flórez, Reactive SPS for sol-gel alumina samples: Structure, sintering behavior, and mechanical properties, *J. Eur. Ceram. Soc.* 41 (2021) 5548–5557.
- [45] C. Laurent, E. Flahaut, A. Peigney, The weight and density of carbon nanotubes versus the number of walls and diameter, *Carbon* 48 (2010) 2994–2996.
- [46] A. Yazdanbakhsh, Z. Grasley, The theoretical maximum achievable dispersion of nano-inclusions in cement paste, *Cem. Concr. Res.* 42 (2012) 798–804.
- [47] A. Hasmy, M. Foret, E. Anglaret, J. Pelous, R. Vacher, R. Jullien, Scattering measurements small-angle neutron scattering of aerogels: simulations and experiments, *J. Non-Cryst. Solids* 186 (1995) 118–130.
- [48] V. Morales-Flórez, N.D.L. Rosa-Fox, M. Piñero, L. Esquivias, The cluster model: A simulation of the aerogel structure as a hierarchically-ordered arrangement of randomly packed spheres, *J. Sol-Gel Sci. Technol.* 35 (2005) 203–210.

## Chapter 8

# The Possible Detriment of Oxygen in Creep of Alumina and Zirconia Ceramic Composites Reinforced with Graphene

This chapter gathers the results of a collaboration with members of the research group in which this thesis has been developed. It addresses the effect of graphene incorporation on the high-temperature plasticity of ceramics such as alumina and zirconia. This work does not belong to the research line of composite fabrication via sol-gel, as the precursor powders were manufactured through a colloidal route.

Overall, the study suggests that reduced graphene oxide has potential as a reinforcement for high-temperature alumina composites, but its effectiveness depends on the specific application and operating conditions. In addition, high temperature mechanical properties of zirconia does not seem to be affected by the inclusion of graphene. The results also highlight the importance of understanding the underlying deformation mechanisms and microstructural changes that occur at high temperatures in these composites. By examining the rheological behavior, fracture surfaces, and Raman spectra peaks, we were able to gain insights into


---

the carbon phase's role in improving plasticity and overall performance. These findings could have important implications for the development of new materials and composites for use in high-temperature applications.



Article

# The Possible Detriment of Oxygen in Creep of Alumina and Zirconia Ceramic Composites Reinforced with Graphene

Rafael Cano-Crespo <sup>1,\*</sup>, Pedro Rivero-Antúnez <sup>1</sup>, Diego Gómez-García <sup>1,2</sup> , Rodrigo Moreno <sup>3</sup> and Arturo Domínguez-Rodríguez <sup>1</sup>

<sup>1</sup> Departamento de Física de la Materia Condensada, Universidad de Sevilla, Apartado 1065, 41080 Sevilla, Spain; privero@us.es (P.R.-A.); dgomez@us.es (D.G.-G.); adorod@us.es (A.D.-R.)  
<sup>2</sup> Instituto de Ciencia de Materiales de Sevilla, CSIC-USE, Avenida Américo Vespucio 49, 41092 Sevilla, Spain  
<sup>3</sup> Instituto de Cerámica y Vidrio, CSIC, 28049 Madrid, Spain; rmoreno@icv.csic.es  
\* Correspondence: racacres@us.es



**Citation:** Cano-Crespo, R.; Rivero-Antúnez, P.; Gómez-García, D.; Moreno, R.; Domínguez-Rodríguez, A. The Possible Detriment of Oxygen in Creep of Alumina and Zirconia Ceramic Composites Reinforced with Graphene. *Materials* **2021**, *14*, 984. <https://doi.org/10.3390/ma14040984>

Academic Editor: Lei Zhai

Received: 8 January 2021  
Accepted: 12 February 2021  
Published: 19 February 2021

**Publisher's Note:** MDPI stays neutral with regard to jurisdictional claims in published maps and institutional affiliations.



**Copyright:** © 2021 by the authors. Licensee MDPI, Basel, Switzerland. This article is an open access article distributed under the terms and conditions of the Creative Commons Attribution (CC BY) license (<https://creativecommons.org/licenses/by/4.0/>).

**Abstract:** This paper aims to give an answer to the following question: is the oxidation of graphene a critical issue for high-temperature plasticity in graphene-reinforced ceramics? To give a convincing reply, we will focus on two very different graphene-based ceramic composites: reduced graphene oxide (rGO)-reinforced alumina ( $\alpha$ -Al<sub>2</sub>O<sub>3</sub>) and reduced graphene oxide (rGO)-reinforced yttria tetragonal zirconia (t-ZrO<sub>2</sub>). The processing of the powders has been made using a colloidal route, and after that, a spark plasma sintering process was performed in order to densify the samples. Creep tests were performed at temperatures between 1200–1250 °C in an argon atmosphere. The microstructure obtained by SEM of the sintered and tested specimens was characterized quantitatively to elucidate the deformation mechanism. Raman spectroscopy was carried out to check the integrity of the graphene. The average grain size was in the order of 1  $\mu$ m and the shape factor was 0.7 for all the studied materials. The integrity of the graphene was checked before and after the creep experiments. The careful analysis of the creep tests shows that graphene oxide or its reduced version are not efficient phases for creep resistance improvement in general, contrary to what is reported elsewhere. However, the results permit the suggestion of a creep improvement in nanocomposites at a very high temperature regime due to an enhanced reactivity of oxygen between carbon and alumina interfaces. In the case of zirconia, the results give us the conclusion that the oxidation of graphene is a highly detrimental issue regarding the improvement of high-temperature plasticity.

**Keywords:** ceramic; composite; high temperature; microstructural characterization; plasticity

## 1. Introduction

Traditionally, a secondary phase is used in the world of materials to reinforce them and to try and change its mechanical properties. The result is a composite with enhanced properties [1,2]. In the last few years, carbon materials such as carbon nanotubes (CNTs) [3], carbon fibers (CFs) [4], carbon nanofibers (CNFs) [5], graphite, graphene (G) [6,7] or graphene oxide (GO) [6] have become very interesting materials due to their very good properties and the employment of them to optimize the mechanical properties. For example, in the case of graphene, Yang et al. [8] fabricated carbon/graphene/carbon composites and found an improvement of the mechanical properties (flexural strength, interlaminar shear strength, interfacial debonding strength, internal friction and storage modulus) compared to the carbon/carbon composite. These authors also found that these properties were strongly influenced by the fiber/matrix interface which was modified by graphene. One important use of these new materials is as a reinforcement phase of advanced ceramic materials at high temperatures [9].

Concerning alumina, (Al<sub>2</sub>O<sub>3</sub>) there are a lot of studies trying to improve the creep behavior by adding a secondary phase. For example, Lessing et al. [10] found that the pure material has worse mechanical properties than alumina doped with transition metal



ions. Weidner et al. [11] studied the high temperature mechanical properties of alumina-based composites reinforced with a 11 or 21 vol.% of refractory metal Ta and Nb, respectively. These materials did not fail in a completely brittle manner during compression tests between 1300–1500 °C. Tamura et al. [12] sintered by spark plasma sintering an alumina-whisker-reinforced alumina composite and achieved an improvement of the creep resistance by around one order of magnitude compared to the pure material. On the other hand, Zapata-Solvas et al. [13] and Padture [14] found that Al<sub>2</sub>O<sub>3</sub> doped with a 10 vol.% of carbon nanotubes had a better creep behavior than the pure material with a similar microstructure. In another study, Zapata-Solvas et al. [15] found an improvement of the creep resistance in Al<sub>2</sub>O<sub>3</sub>/single-wall carbon nanotube composites. An extensive variety of alumina exists, with a large scatter in the diffusion kinetics processes which can also affect the mechanical properties [16–18]. More recently, Cano-Crespo et al. [19] sintered by spark plasma sintering carbon nanofibers reinforced with alumina and graphene oxide reinforced with alumina composites, respectively. Using a concentration of 2 vol.%, they studied the creep at high temperatures and at 1200 °C the creep resistance of the Al<sub>2</sub>O<sub>3</sub>/carbon nanofiber composite decreased with respect to pure alumina, but at 1250 °C they found a similar behavior of the composite and the pure material. The same authors reported that the Al<sub>2</sub>O<sub>3</sub>/graphene oxide composite has a better creep resistance than the pure material. Zapata-Solvas et al. [20] employed graphite as a secondary phase using a concentration of 10 vol.% and found an improvement of creep resistance.

In the case of zirconia, several researches have been performed in the field of the study of the creep behavior of zirconia-reinforced composites. Grain boundary sliding (GBS) is the most important mechanism of deformation at high temperatures of yttria-stabilized-tetragonal zirconia (3YTZP) [21,22]. Some authors [23,24] reported research about the creep behavior of zirconia reinforced with ceria. Calderón-Moreno et al. [25] sintered a composite alumina/zirconia and studied its creep behavior. Lorenzo-Martín et al. [26] found that grain boundary sliding was the predominant deformation mechanism in a composite of zirconia with a glassy phase, and they also found that the creep rate depended critically on the content of the secondary phase added. Whiskers of SiC have been employed for years, as was the case of Calderón-Moreno et al. [27]; these authors sintered and researched the mechanical properties of ZrO<sub>2</sub>-Al<sub>2</sub>O<sub>3</sub>/SiC composites at high temperatures. A review summarizes the most important features of the research in carbon nanotube reinforced zirconia composites [28]. Cano-Crespo et al. [29] found that carbon nanofiber reinforced zirconia composites were less creep resistant than the same material without the secondary phase. The same authors also reported that graphene oxide reinforced zirconia composites were systematically less creep resistant than pure zirconia. The difference between this study and the present study is the secondary phase employed. In the previous study, graphene oxide was used in order to reinforce zirconia, but in the present study, reduced graphene oxide, a graphene with some defects in its lattice, has been used in two different concentrations to check the possible change in the creep behavior.

The scientific problem is the comprehension of the importance of the reactivity of oxygen between the graphene and the alumina or zirconia grains, and if this reaction is detrimental in the mechanical properties at high temperatures. In order to give an answer, several creep experiments at very elevated temperatures using graphene as the secondary phase were performed for the first time of our knowledge. Consequently, the main goal of this study is to prepare a homogeneous dispersion of reduced graphene oxide (rGO) into alumina and zirconia matrices and to obtain nearly full density compacts by spark plasma sintering with enhanced creep resistance at high temperatures compared to pure materials. To achieve this aim, several experimental techniques were employed: scanning electron microscope, Raman spectroscopy, and creep at high temperatures. The creep experiments were analyzed according to the Equations (1)–(3) presented in the Section 2.5.

## 2. Experimental Procedure

### 2.1. Starting Materials

The starting powders of  $\alpha$ -alumina and tetragonal zirconia used were the same as in [19,29]. The powder of  $\alpha$ -Al<sub>2</sub>O<sub>3</sub> (Celarox, Condea HPA05, Sasol, Lake Charles, LA, USA) has an average particle size of 0.35  $\mu$ m and a specific surface area of 9.5 m<sup>2</sup>/g. The powder of tetragonal-ZrO<sub>2</sub> stabilized with 3% mol of Y<sub>2</sub>O<sub>3</sub> (TZ-3YSE, Tosoh, Tokyo, Japan) has an average particle size of 90 nm and a specific surface area of 6.7 m<sup>2</sup>/g. Both kinds of powders have a high purity and higher than 99.9%.

Reduced graphene oxide (Nanoinnova Technologies, Toledo, Spain) with a length of 1–4  $\mu$ m, a thickness of 0.7–1.2 nm and a surface area of 103 m<sup>2</sup>/g was used as the secondary phase [30,31]. Particle sizes were measured by laser diffraction using a Mastersizer S apparatus (Malvern, UK) and the surface area was measured by single point adsorption (Monosorb, Quantachrome, Boynton Beach, FL, USA).

### 2.2. Powder Processing Methods

First of all, reduced graphene oxide was dispersed in N-methyl-2-pyrrolidone (NMP) with magnetic stirring, as this is considered elsewhere an excellent non-aqueous vehicle to achieve the highly efficient dispersion of reduced graphene oxide. Alumina was dispersed in water using an ammonium salt of poly(acrylic) acid (Duramax D3005, Rohm and Haas, Dow Chemicals, Midland, MI, USA) in a concentration of 0.5 wt.% on a dry solids basis and sonicated with different sonication times. Concentrated suspensions of alumina-reduced graphene oxide were prepared to solid loadings of 30 vol.% and homogenized with 1 min of ultrasonication.

To obtain a homogeneous dispersion of reduced graphene oxide in zirconia, both materials were dispersed independently and furtherly mixed. Zirconia was dispersed in water to a concentration of 30 vol.% using an ammonium salt of poly(acrylic) acid (Duramax D3005, Rohm and Haas, Dow Chemicals, Midland, MI, USA) in a concentration of 0.5 wt.% on a dry solid basis. Reduced graphene oxide was dispersed in 1-methyl-2-pyrrolidone at the same solids content (30 vol.% reduced graphene oxide) and both slurries were subjected to mechanical homogenization and sonication for 1 min (Dr. Hielscher UP400S, Teltow, Germany). Once dispersed, proper fractions of both suspensions were mixed altogether to obtain two relative contents of reduced graphene oxide in the zirconia matrix of 2 and 6.7 vol.%, applying 1 min of additional sonication. The rheological behavior of the different suspensions was analyzed using a rotational rheometer.

The optimized suspensions of the mixture were frozen in a rotatory chamber using liquid nitrogen as refrigerant (−196 °C). The frozen suspensions were introduced in a freeze-dryer for 24 h. The condenser temperature was −50 °C, and the conditions of the storage camera were 20 °C and 0.050 mbar [30].

The following resultant mixtures of powders were obtained:

- A2rGO: 98 vol.%  $\alpha$ -alumina and 2 vol.% reduced graphene oxide.
- A6.7rGO: 93.3 vol.%  $\alpha$ -alumina and 6.7 vol.% reduced graphene oxide.
- Z2rGO: 98 vol.% t-zirconia and 2 vol.% reduced graphene oxide.
- Z6.7rGO: 93.3 vol.% t-zirconia and 6.7 vol.% reduced graphene oxide.

As reference materials, pure alumina and pure zirconia commercial powders were used for the sake of comparison. These powders are named A and Z, respectively.

### 2.3. Sintering

The sintering process employed was the same as in [19,29]. The consolidation of the samples was performed in a spark plasma sintering machine and employed a vacuum in order to prevent the damage of the carbon phase. The resultant mixtures of powders were introduced in a graphite die. The maximum temperature was 1300 °C, using a holding time of 5 min. The applied pressure during all the process was 75 MPa and the heating and cooling rate were 100 °C/min, respectively.

#### 2.4. Microstructural Characterization

Raman spectroscopy was performed in order to note the integrity of the reduced graphene oxide. Measurements were performed in the same way as described in [19,29].

The microstructural characterization was performed by scanning electron microscopy. The surfaces of the samples were polished with diamond paste. The microstructure was described by measuring the grain size and the shape factor. Fracture surfaces were also observed to check the presence and distribution of reduced graphene oxide; to this end a high resolution scanning electron microscope (Model FEI TENE0, Hillsboro, Washington, OR, USA) was employed in the mode secondary electrons.

#### 2.5. High-Temperature Mechanical Tests

The creep at high temperatures of these new materials was investigated in the same way as explained in [19,29]. It measured the stationary strain rate as a function of the stress (the applied load) and the temperature. In general, the creep experiments obey the following phenomenological equation:

$$\dot{\epsilon} = A \frac{Gb}{kT} \left(\frac{b}{\bar{d}}\right)^p \left(\frac{\sigma}{G}\right)^n D \quad (1)$$

where  $\dot{\epsilon}$  is the strain rate,  $A$  is a dimensionless constant,  $G$  is the shear modulus,  $b$  is the magnitude of the Burgers vector,  $k$  is the Boltzmann constant,  $T$  is the absolute temperature,  $d$  is the grain size,  $p$  is the inverse of the exponent of the grain,  $\sigma$  is the stress,  $n$  is the stress exponent and  $D$  a diffusion coefficient [32].

The characteristics parameters of the creep experiments were the stress exponent ( $n$ ) and the activation energy ( $Q$ ). A value of stress exponent was obtained by changing the applied load as it can be seen in the Equation (2) and a value of the activation energy was obtained by modifying the temperature (3).

$$n = [\partial(\ln\dot{\epsilon}_{ss})/\partial(\ln\sigma_{ss})]_T = \left(\ln\frac{\dot{\epsilon}_2}{\dot{\epsilon}_1}\right) / \left(\ln\frac{\sigma_{ss2}}{\sigma_{ss1}}\right) \quad (2)$$

$$Q_c = -k[\partial(\ln\dot{\epsilon}_{ss})/\partial(1/T)]_{\sigma_{ss}} \approx -k \left(\frac{\ln\frac{\dot{\epsilon}_1}{\dot{\epsilon}_2}}{\frac{1}{T_1} - \frac{1}{T_2}}\right) \quad (3)$$

In the previous equations  $ss$  denotes the stationary state. The measuring of  $n$  and  $Q$ , together with the characterization of the microstructure, give us an idea of the predominant deformation mechanism in the material.

A chamber containing argon was employed in all the experiments to avoid the combustion of reduced graphene oxide. Two values of temperature were used: 1200 °C and 1250 °C. The interval of stress applied was between 9–300 MPa.

### 3. Results and Discussion

#### 3.1. Characterization of the Mixtures of Powders

In a first step, the powders of the mixtures were prepared. The starting suspensions of alumina with reduced graphene oxide showed a Newtonian behavior and very low viscosity (7 mPa·s) demonstrating their good dispersibility. Zirconia was dispersed in water, whereas reduced graphene oxide was dispersed in a non-aqueous medium (NMP) in order to improve the dispersion. The final suspensions had a solid loading of 30 vol.%. Figure 1 shows the rheological behavior for the suspensions of zirconia with reduced graphene oxide (Z2rGO and Z6.7rGO). The slope in the two cases is almost constant. The curves exhibit a slightly shear thinning behavior with a small thixotropy and viscosity values at a maximum shear rate of around 12 mPa·s, low enough to ensure stability. Those suspensions were freeze dried to obtain the powders of the reduced graphene oxide/zirconia mixtures. After the spark plasma sintering process, all the samples were fully dense with a value

of density near-to theoretical density, measured by the Archimedes method with distilled water, higher than 99 % and consequently they were optimal to study their mechanical properties at high temperatures (creep experiments).

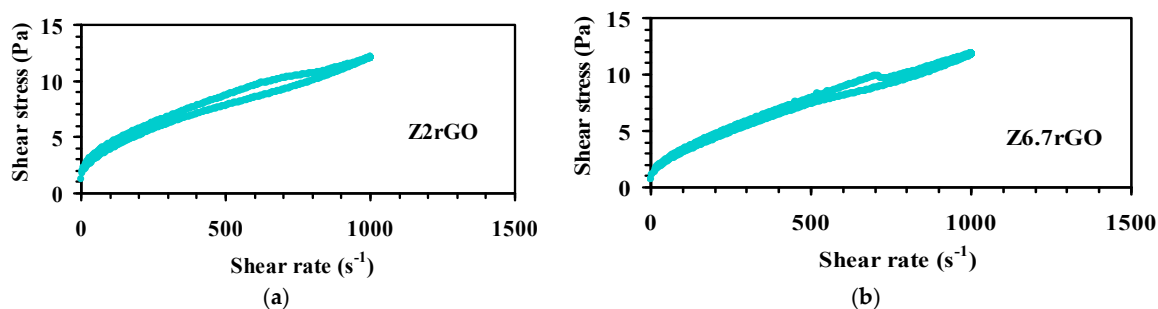


**Figure 1.** Flow curves of 30 vol.% solids suspensions of zirconia with (a) 2 vol.% of reduced graphene oxide (rGO) and (b) 6.7 vol.% of rGO. For both suspensions the shear stress (Pa) is plotted versus the shear rate ( $s^{-1}$ ).

### 3.2. Microstructural Characterization

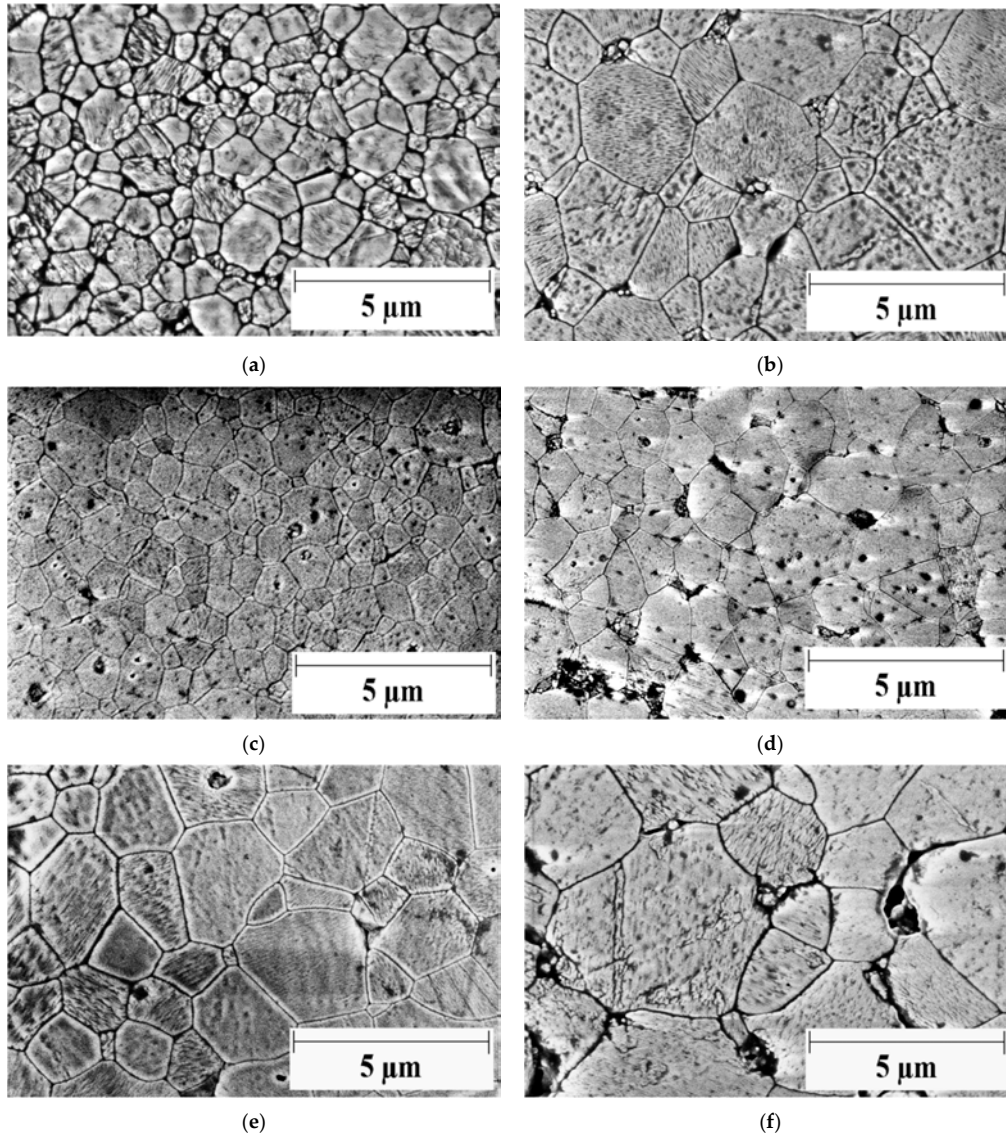
Figure 2 displays the thermal etched surfaces of A, A2rGO and A6.7rGO before and after creep experiments at high temperatures. The grain boundaries between the grains can be seen, a typical image of a ceramic polycrystal. Some little holes can be appreciated due to the polish process which removes some particles from the surface. All the images were obtained using the mode of secondary electrons and with the same scale in order to obtain a better comparison between the samples. Table 1 summarizes some magnitudes of the microstructures. The shape factors have the same value for all the cases: 0.7, which constated that the microstructure is constant during the experiments at high temperatures. Some grain growth was observed in alumina and A6.7rGO, in the first case due to the absence of the secondary phase and in the second case the reason was the high concentration of reduced graphene oxide which provoked percolation of the grains. For A2rGO, the grain size was the same before and after creep within the experimental uncertainty. Rarely, there are some grains with an abnormal size, but they are not important due to their low quantity, which means that they are insignificant to the influence on the mechanical behavior. The presence of reduced graphene oxide inhibits the grain growth at low concentrations, but at higher concentrations is not efficient to this end.

**Table 1.** Grain sizes and shape factors for all the samples of alumina and its composites before and after deformation.

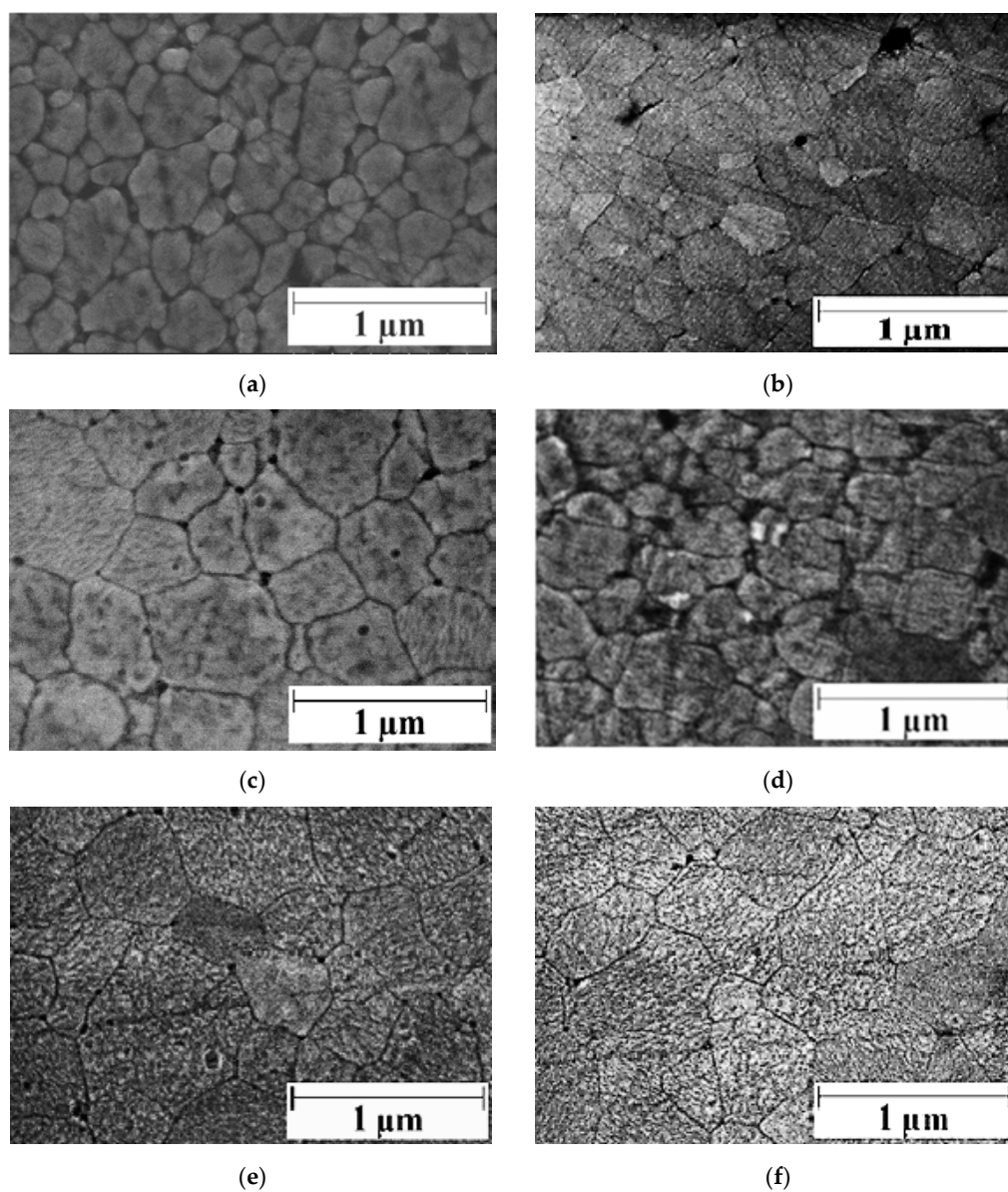
Sample	Grain Size ( $\mu\text{m}$ ) As-Sintered	Grain Size ( $\mu\text{m}$ ) After Creep	Shape Factor As-Sintered	Shape Factor After Creep
A	$0.6 \pm 0.3$	$1.7 \pm 0.8$	$0.7 \pm 0.1$	$0.7 \pm 0.1$
A2rGO	$0.7 \pm 0.3$	$1.0 \pm 0.4$	$0.7 \pm 0.1$	$0.7 \pm 0.1$
A6.7rGO	$1.4 \pm 0.6$	$2.4 \pm 1.2$	$0.7 \pm 0.1$	$0.7 \pm 0.1$

Figure 3 displays the thermal etched and polished surfaces of zirconia, Z2rGO and Z6.7rGO, before and after creep experiments. The same facts were observed as in Figure 2: the grain boundaries and the little holes. Again, the mode of secondary electrons and the same scale were employed for a better comparison. The average grain sizes have values between 0.2–0.3  $\mu\text{m}$  and the shape factor is also the same and equal to 0.7, which means that the microstructure was independent of the secondary phase added and constant during creep experiments. Figure 4 shows high resolution scanning electron microscopy images of fracture surfaces corresponding to Z6.7rGO as sintered; it can be seen surrounded by red circles with some laminates of reduced graphene oxide. From these images, it can be

deduced that the distribution of reduced graphene oxide around all the microstructure is optimum and another important fact is the absence of agglomerates.



**Figure 2.** HRSEM (High resolution scanning electron microscopy) micrographs of (a) as-sintered monolithic  $\text{Al}_2\text{O}_3$ , (b) monolithic  $\text{Al}_2\text{O}_3$  after creep, (c) as-sintered 98 vol.%  $\text{Al}_2\text{O}_3$ -2 vol.% rGO, (d) 98 vol.%  $\text{Al}_2\text{O}_3$ -2 vol.% rGO after creep, (e) as-sintered 93.3 vol.%  $\text{Al}_2\text{O}_3$ -6.7 vol.% rGO and (f) 93.3 vol.%  $\text{Al}_2\text{O}_3$ -6.7 vol.% rGO after creep. The same scale was used for all the cases, 5  $\mu\text{m}$ . The accelerating voltage of electrons was equal to 5 kV.



**Figure 3.** High resolution scanning electron microscopy micrographs of (a) as-sintered pure zirconia, (b) pure zirconia after creep, (c) as-sintered Z2rGO, (d) Z2rGO after creep, (e) as-sintered Z6.7rGO and (f) Z6.7rGO after creep. The same scale was used for all the cases, 1  $\mu\text{m}$ . The accelerating voltage of electrons was equal to 5 kV.

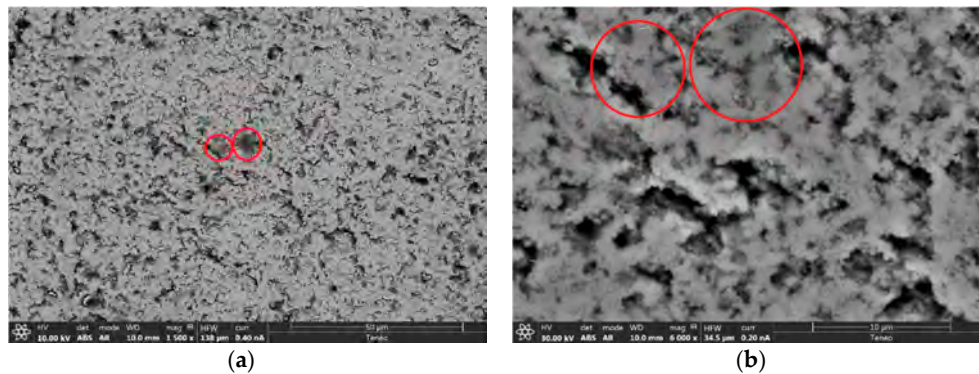


**Figure 4.** High resolution scanning electron microscopy micrographs of fracture surfaces corresponding to as-sintered Z6.7rGO. The accelerating voltage is 10 kV for (a) and 30 kV for (b). The electrical current is 0.40 nA for (a) and 0.20 nA for (b). The scale for (a) is 50  $\mu\text{m}$  and for (b) is 10  $\mu\text{m}$ . For both cases, an angular backscattered detector is employed; in other words, the detector receives the backscattered electrons. In these cases, the image is built with all the surface of the detector, removing the topographic contrast and enhancing the contrast due to the difference in the atomic number.

Figure 5a–f shows the Raman spectra of the reduced graphene oxide-reinforced alumina materials: the powders, as sintered and after creep. Table 2 displays the positions of the peaks. The presence of the two first peaks is due to main phase of  $\alpha$ -alumina, the next peaks correspond to the secondary phase added of reduced graphene oxide [33–35] and they are due to the D mode (longitudinal optical phonons), the G mode (tangential shear mode of carbon atoms) and the second order band 2D (number of layers of graphene or reduced graphene oxide), respectively. Figure 6a–f shows the Raman spectra of the reduced graphene oxide-reinforced zirconia materials: the powders, as sintered and after creep. The positions of the different peaks of the previous Raman spectra are in Table 3. The four first peaks are due to tetragonal zirconia [36,37]. The next peaks correspond to reduced graphene oxide, as explained previously. The growth in the peak at  $\sim 2700\text{ cm}^{-1}$  observed in Figure 5b,c,e,f and in Figure 6b,c,e,f is related to the oxidation of the carbon phase; this phase is almost intact but has oxidized at least partially [38]. It can be constated that the position of the peaks is constant. The intensity ratios between the peak D and G for the starting materials and the fabricated composites are shown in Tables 2 and 3. This magnitude gives us an idea of the damage of the carbon phase after sintering and after creep at high temperatures. The values of the positions of the peaks from Figures 5 and 6 and also from the Tables 2 and 3 permit us to affirm that graphene remains intact during the sintering process and also during creep experiments at high temperatures, and no degradation could be observed.

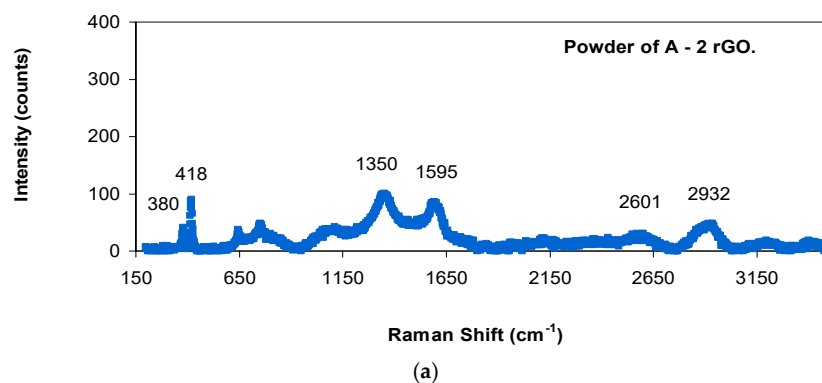


**Figure 5.** Cont.

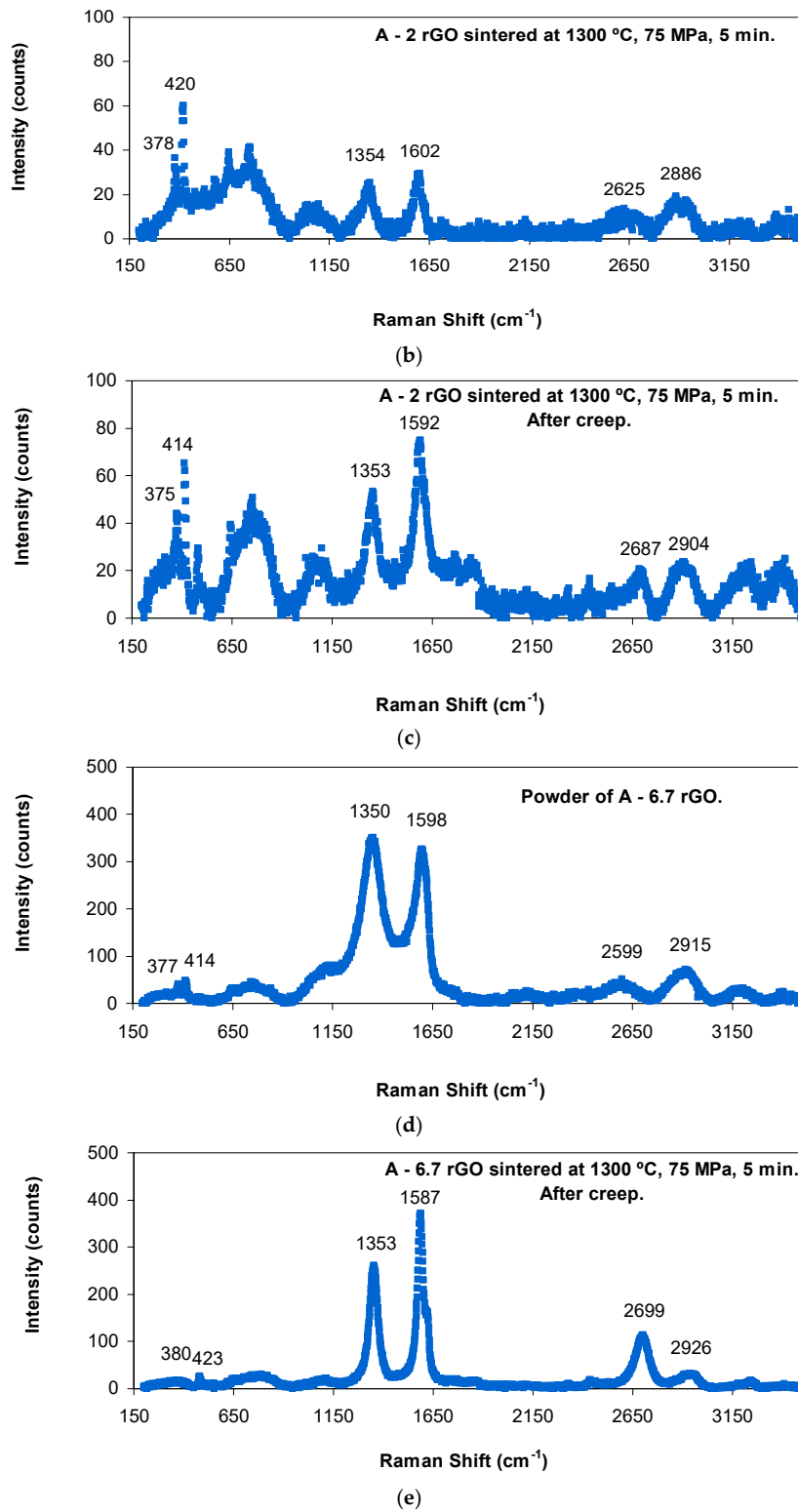
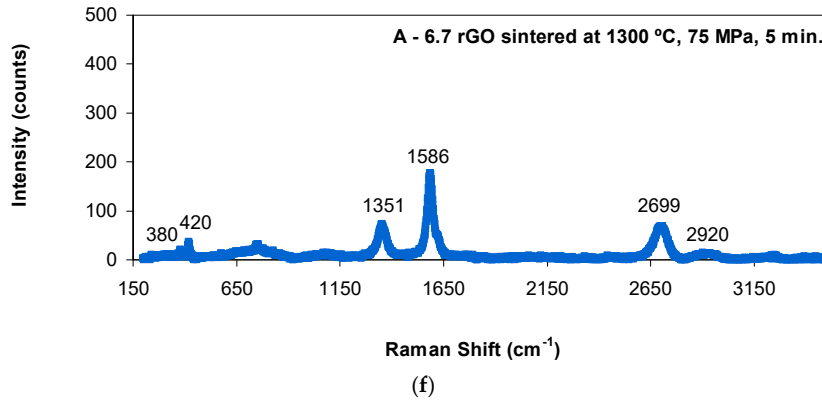


Figure 5. Cont.





**Figure 5.** Raman spectra of (a) powder of 98 vol.% Al<sub>2</sub>O<sub>3</sub>-2 vol.% rGO, (b) sample of 98 vol.% Al<sub>2</sub>O<sub>3</sub>-2 vol.% rGO before creep, (c) sample of 98 vol.% Al<sub>2</sub>O<sub>3</sub>-2 vol.% rGO after creep deformation, (d) powder of 93.3 vol.% Al<sub>2</sub>O<sub>3</sub>-6.7 vol.% rGO, (e) sample of 93.3 vol.% Al<sub>2</sub>O<sub>3</sub>-6.7 vol.% rGO before creep and (f) sample of 93.3 vol.% Al<sub>2</sub>O<sub>3</sub>-6.7 vol.% rGO after creep deformation. It is plotted the intensity (counts) versus the Raman shift (cm<sup>-1</sup>).

**Table 2.** Raman shifts (in cm<sup>-1</sup>) of the different peaks in the Raman spectra of alumina composites and ratio of the intensities of the D and G peaks.

Samples	$\alpha$ -Al <sub>2</sub> O <sub>3</sub> Peak (cm <sup>-1</sup> )	$\alpha$ -Al <sub>2</sub> O <sub>3</sub> Peak (cm <sup>-1</sup> )	D Peak (cm <sup>-1</sup> )	G Peak (cm <sup>-1</sup> )	2D Peak (cm <sup>-1</sup> )	D + G Peak (cm <sup>-1</sup> )	I <sub>D</sub> /I <sub>G</sub>
A2rGO powder	380	418	1350	1595	2601	2932	1.18 ± 0.03
A2rGO sintered specimen	378	420	1354	1602	2625	2886	0.86 ± 0.06
A2rGO after creep	375	414	1353	1592	2687	2904	0.71 ± 0.02
A6.7rGO powder	377	414	1350	1598	2599	2915	1.07 ± 0.01
A6.7rGO sintered specimen	380	420	1351	1586	2699	2920	0.41 ± 0.01
A6.7rGO after creep	380	423	1353	1587	2699	2926	0.70 ± 0.01

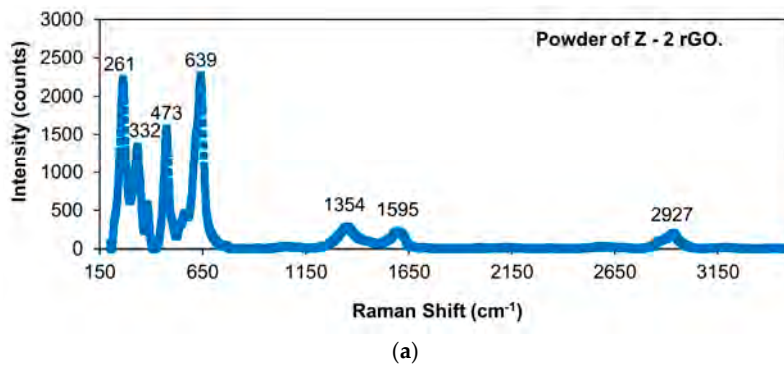
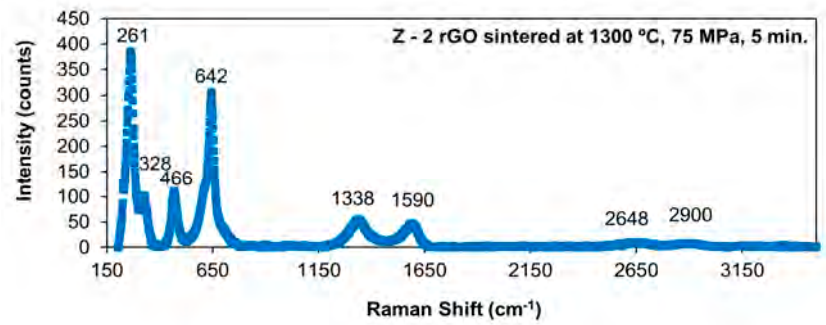
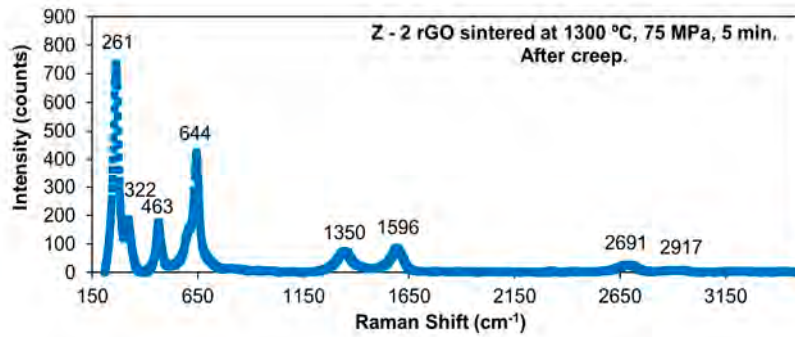


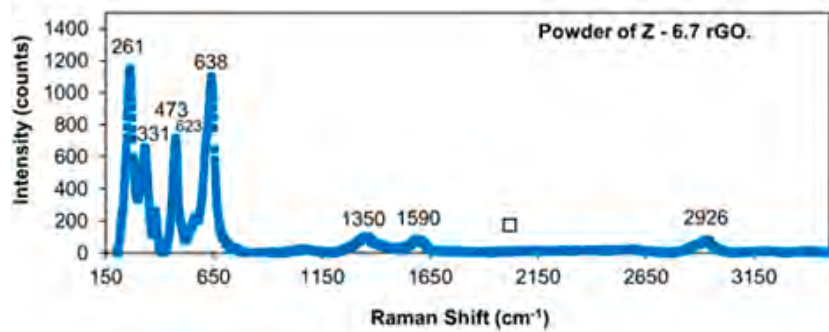
**Figure 6.** Cont.



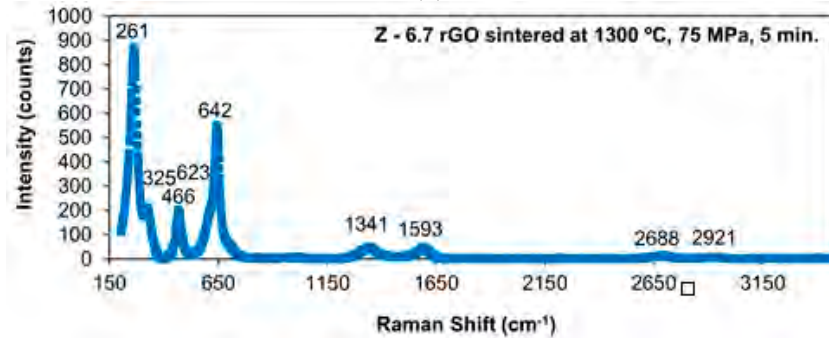
(b)



(c)

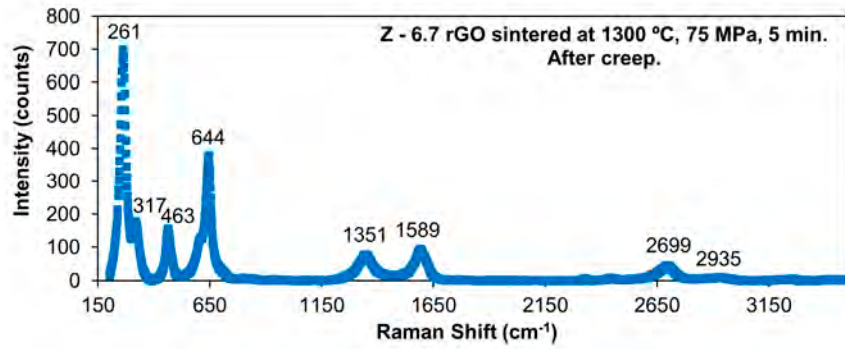


(d)



(e)

Figure 6. Cont.



(f)

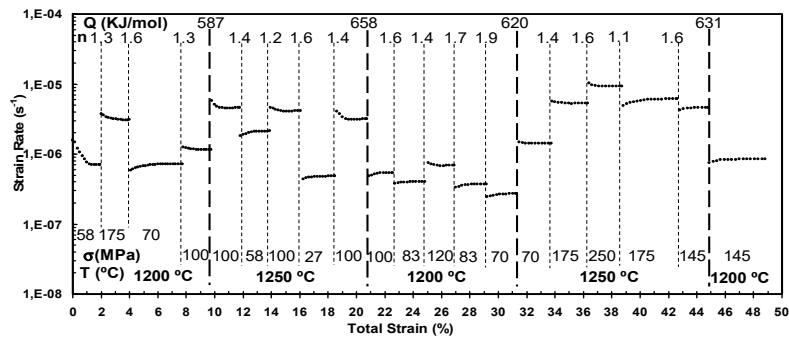
**Figure 6.** Raman spectra of (a) powder of Z2rGO, (b) sample of Z2rGO before creep, (c) sample of Z2rGO after creep deformation, (d) powder of Z6.7rGO, (e) sample of Z6.7rGO before creep and (f) sample of Z6.7rGO after creep deformation. It is plotted the intensity (counts) versus the Raman shift ( $\text{cm}^{-1}$ ).

**Table 3.** Raman shifts (in  $\text{cm}^{-1}$ ) of the different peaks in the Raman spectra of zirconia composites and ratio of the intensities of the D and G peaks.

Samples	ZrO <sub>2</sub> Peak ( $\text{cm}^{-1}$ )	ZrO <sub>2</sub> Peak ( $\text{cm}^{-1}$ )	ZrO <sub>2</sub> Peak ( $\text{cm}^{-1}$ )	ZrO <sub>2</sub> Peak ( $\text{cm}^{-1}$ )	D Peak ( $\text{cm}^{-1}$ )	G Peak ( $\text{cm}^{-1}$ )	2D Peak ( $\text{cm}^{-1}$ )	D + G Peak ( $\text{cm}^{-1}$ )	I <sub>D</sub> /I <sub>G</sub>
Z2rGO powder	261	332	473	639	1354	1595	-	2927	1.25 ± 0.01
Z2rGO sintered specimen	261	328	466	642	1338	1590	2648	2900	1.14 ± 0.04
Z2rGO after creep	261	322	463	644	1350	1596	2691	2917	0.86 ± 0.02
Z6.7rGO powder	261	331	473	638	1350	1590	-	2926	1.19 ± 0.02
Z6.7rGO sintered specimen	261	325	466	642	1341	1593	2688	2921	1.02 ± 0.04
Z6.7rGO after creep	261	317	463	644	1351	1589	2699	2935	0.81 ± 0.02

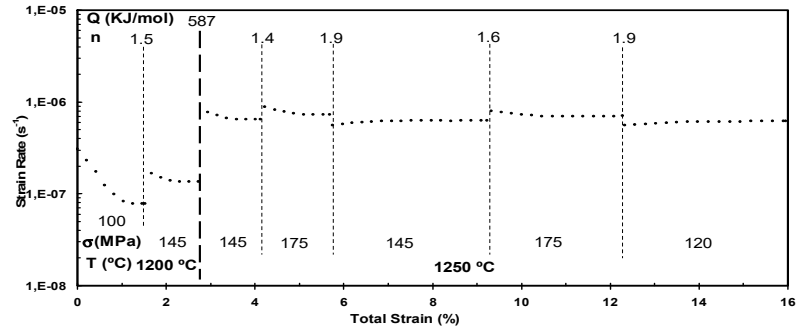
### 3.3. Analysis of the Creep Experiments

Figure 7 displays all the creep experiments which were performed. The stress exponents are in the interval 1.5 and 2.0 for all the composites of alumina, but for zirconia and its composites, these values are in the interval 2.5 and 3.0. The activation energy for A2rGO and for A6.7rGO are around 600 kJ/mol, which are in good agreement with the average values achieved for pure alumina polycrystals [16]. For Z2rGO and Z6.7rGO, the magnitude is around 700 kJ/mol. The reduced graphene oxide is almost intact during creep experiments at high temperatures.

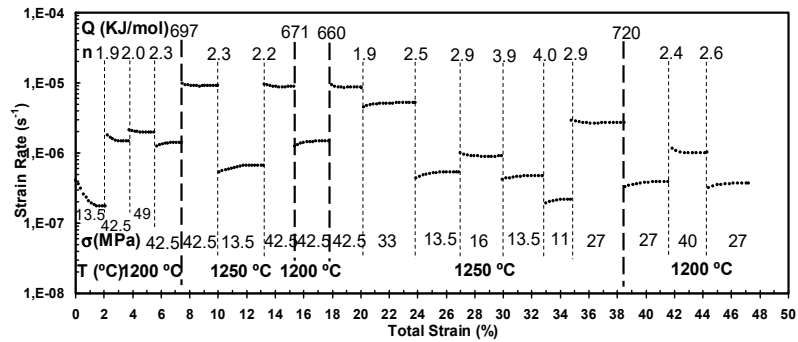


(a)

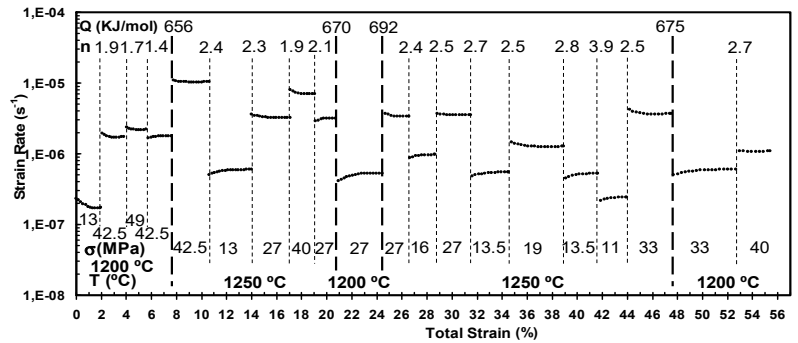
**Figure 7.** Cont.



(b)



(c)



(d)

**Figure 7.** Creep curves of (a) 98 vol.%  $\text{Al}_2\text{O}_3$ -2 vol.% rGO, (b) 93.3 vol.%  $\text{Al}_2\text{O}_3$ -6.7 vol.% rGO, (c) 98 vol.%  $\text{ZrO}_2$ -2 vol.% rGO and (d) 93.3 vol.%  $\text{ZrO}_2$ -6.7 vol.% rGO. It is plotted the strain rate ( $\text{s}^{-1}$ ) versus the total strain (%). Dashed vertical lines separate the different stages in the experiments. Each stage is characterized with a value of stress ( $\sigma$  (MPa)) and a value of temperature ( $T$  ( $^\circ\text{C}$ )). A value of stress exponent ( $n$ ) is obtained with a change of the applied stress and a value of activation energy ( $Q$ ) is also obtained if the temperature is modified.  $1, \text{E}-0n$  denotes  $10^{-n}$ .

All these experimental facts are in good concordance with a general model of the creep deformation in  $Y_2O_3$  stabilized  $ZrO_2$  and in  $Al_2O_3$  ceramics in which there is grain boundary sliding with diffusion as an accommodation mechanism [21,39]. The final strain of A2rGO is ~50%, in contrast, when the concentration of reduced graphene oxide is higher; in the case of A6.7rGO the final strain is in between 15–20 %. The reason can be twofold: this second type of material has a higher grain size (2.4  $\mu m$  for 6.7 vol.% of reduced graphene oxide versus 1.0  $\mu m$  for 2 vol.% of reduced graphene oxide) and the higher concentration of reduced graphene oxide can produce cavitation and cracks during the creep. Given the fact of the limited plasticity of A6.7rGO, several independent creep tests had to be performed to increase the number of  $\dot{\epsilon}$ ,  $T$  and  $\sigma$  data. Therefore, additional values of the stress exponents and activation energies were obtained. These facts and the same microstructure before and after creep permit us to affirm that the most important deformation mechanism is grain boundary sliding accommodated by diffusion [16,39]. The secondary phase added of reduced graphene oxide changes the grain motion, but they do not modify the diffusion, which means the accommodation mechanism [19]. The stress exponents in pure zirconia samples are approximately the same as that found in the composites reinforced with reduced graphene oxide. These experimental results, the obtained values of stress exponents and the same microstructure before and after the creep experiments permit us to say that the deformation mechanism at high temperatures must be grain boundary sliding [39]. The reduced graphene oxide seems to be a lubricant which does not limit the grain boundary mobility. The reduced graphene oxide “wets” the boundaries in a very efficient way.

One aspect which that is very important is the analysis of the creep resistance due to the introduction of this carbon phase. To this end, and assuming that the grain size exponent is three because the accommodation process is the diffusion along the grain boundary, we are using this value to normalize strain rate versus stress plots in log–log scales in Figure 8a,b for pure alumina (A), reduced graphene oxide reinforced alumina composites (A2rGO and A6.7rGO) and graphene oxide reinforced alumina composites (A2GO) from data of previous work [19]. The values for pure zirconia and its composites are in Figure 8c,d (Z, Z2rGO, Z6.7rGO and Z2GO from the literature [29]). It was not necessary to normalize the values of the strain rate due to the fact that all the samples after creep had the same grain size inside the experimental uncertainty and were equal to 0.2–0.3  $\mu m$ . The experimental data fit to lines according to the equation proposed by Dorn. From these plots, it can be seen that the differences between alumina and the two composites (A2rGO and A6.7rGO) are very close, since the difference is around one order of magnitude at 1200 °C and half an order of magnitude at 1250 °C. A2rGO and A2GO have a similar creep behavior at 1200 °C and 1250 °C, being more similar than pure alumina since the difference between these composites and pure alumina is around half an order of magnitude, again inside the experimental scattering. However, there is an interesting point which must be pointed out: Figure 8a,b display that the extrapolation to the low stress range would predict a significant increase in the creep improvement. In both cases, the increment in the creep resistance must be related to the enhanced reactivity of graphene oxide with the grain boundaries of alumina, a fact which is not surprising according to the literature [40]. Should it happen, the grain mobility is restricted due to the interconnected network of carbon layers and grains. From these plots, it can be seen that all composites (Z2rGO, Z6.7rGO and Z2GO) have a similar behavior to that of pure zirconia. At 1200 °C and 1250 °C, there is the same behavior of the materials studied.

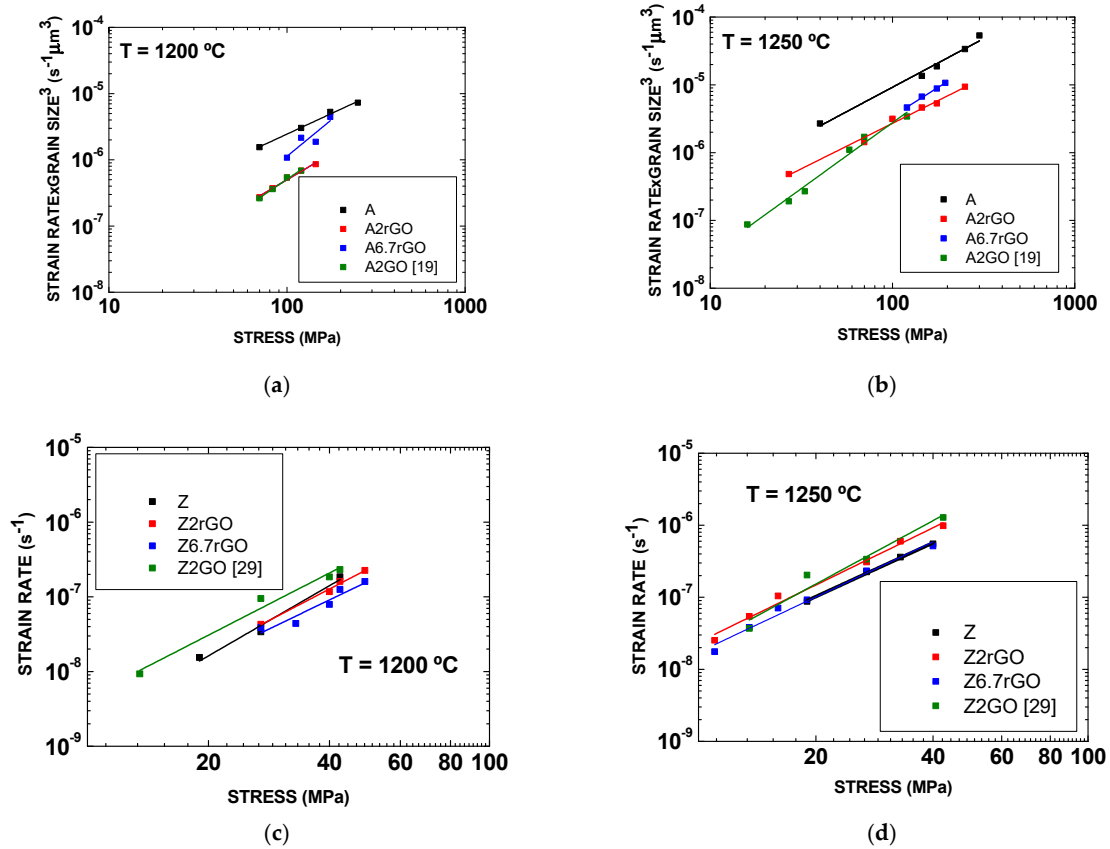


**Figure 8.** The plots of the steady-state creep rate times the cubed of the average grain size after creep versus applied uniaxial compressive stress data for A, A2rGO, A6.7rGO and A2GO [19] at (a) 1200 °C and (b) 1250 °C. The plots of the steady-state creep rate versus applied uniaxial compressive stress data for pure Z, Z2rGO, Z6.7rGO and Z2GO [29] at (c) 1200 °C and (d) 1250 °C. The stress exponents in (a) are: A-1.3, A2rGO-1.5, A6.7rGO-2.1 and A2GO-1.8. The stress exponents in (b) are: A-1.5, A2rGO-1.4, A6.7rGO-1.7 and A2GO-2.0. The stress exponents in (c) are: Z-3.1, Z2rGO-2.6, Z6.7rGO-2.8 and Z2GO-2.9. The stress exponents in (d) are: Z-2.5, Z2rGO-2.7, Z6.7rGO-2.6 and Z2GO-3.1.

The reactivity of oxygen, present in the lattice of graphene, could be a crucial issue for the prediction of high-temperature creep resistance. Further work must be conducted to elucidate the local chemistry bonds involved in the ceramic composite at high temperatures.

#### 4. Conclusions

The microstructure is constant during the creep at high temperatures and the deformation mechanism is grain boundary sliding.

The analysis of the high temperature mechanical properties allows for the conclusion that reduced graphene oxide does not provide an improvement of more than an order of magnitude in comparison to pure alumina, but it is potentially attractive in the range of nanocomposites or very high temperatures (from 1250 °C).

The reduced graphene oxide reinforced zirconia composites are, inside the experimental uncertainty, similar to pure zirconia regarding high-temperature creep properties.

The ability of the carbon phase to “wet” the grain boundaries and distribute homogeneously (watching the rheological behavior, the fracture surfaces and the same positions of the peaks of the Raman spectra in different points of the samples) during deformation is a critical element to predict the high-temperature plasticity.

**Author Contributions:** Conceptualization: D.G.-G. and A.D.-R.; data curation: R.C.-C., P.R.-A. and R.M.; formal analysis: R.C.-C., D.G.-G. and A.D.-R.; funding acquisition: D.G.-G. and A.D.-R.; investigation: R.C.-C., P.R.-A. and R.M.; methodology: A.D.-R.; project administration: A.D.-R.; supervision: D.G.-G. and A.D.-R.; writing—original draft: R.C.-C.; writing—review and editing: P.R.-A., D.G.-G., R.M. and A.D.-R. All authors have read and agreed to the published version of the manuscript.

**Funding:** The authors acknowledge the financial support awarded by the Regional projects of Excellence of “Junta de Andalucía” P12-FQM-1079 and P18-RTJ1972 and the Spanish “Ministerio de Economía y Competitividad” and “Fondo Europeo de Desarrollo Regional” funds through the projects MAT2015-71411-R and RTI2018-099033-B-C33 (MCIU/AEI/FEDER, UE). The authors also acknowledge the financial support awarded by the “VI Plan Propio de Investigación y Transferencia” of the University of Seville (II.3. Ayudas puente posdoctorales). The projects PGC2018-094952-B-I00 (MCIU/AEI/FEDER, UE) and PID2019-103847-RJ-I00 from the “Ministerio de Ciencia, Innovación y Universidades” from Spain are also acknowledged.

**Institutional Review Board Statement:** Not applicable.

**Informed Consent Statement:** Not applicable.

**Data Availability Statement:** The data presented in this study are available on request from the corresponding authors.

**Acknowledgments:** The authors acknowledge the financial support awarded by the Regional projects of Excellence of “Junta de Andalucía” P12-FQM-1079 and P18-RTJ1972 and the Spanish “Ministerio de Economía y Competitividad” and “Fondo Europeo de Desarrollo Regional” funds through the projects MAT2015-71411-R and RTI2018-099033-B-C33 (MCIU/AEI/FEDER, UE). The authors also acknowledge the financial support awarded by the “VI Plan Propio de Investigación y Transferencia” of the University of Seville (II.3. Ayudas puente posdoctorales). The projects PGC2018-094952-B-I00 (MCIU/AEI/FEDER, UE) and PID2019-103847-RJ-I00 from the “Ministerio de Ciencia, Innovación y Universidades” from Spain are also acknowledged.

**Conflicts of Interest:** The authors declare no conflict of interest.

## References

1. Rivero-Antúnez, A.; Cano-Crespo, R.; Esquivias, L.; de la Rosa-Fox, N.; Zamora-Ledezma, C.; Domínguez-Rodríguez, A.; Morales-Flórez, V. Mechanical characterization of sol-gel alumina-based ceramics with intragranular reinforcement of multiwalled carbon nanotubes. *Ceram. Int.* **2020**, *46*, 19723–19730. [[CrossRef](#)]
2. Curtin, W.A.; Sheldon, B.W. CNT-reinforced ceramics and metals. *Mater. Today* **2004**, *7*, 44–49. [[CrossRef](#)]
3. Iijima, S. Helical microtubules of graphitic carbon. *Nat. Cell Biol.* **1991**, *354*, 56–58. [[CrossRef](#)]
4. Endo, M.; Kim, Y.; Hayashi, T.; Nishimura, K.; Matusita, T.; Miyashita, K.; Dresselhaus, M. Vapor-grown carbon fibers (VGCFs). *Carbon* **2001**, *39*, 1287–1297. [[CrossRef](#)]
5. Rodríguez, N.M. A review of catalytically grown carbon nanofibers. *J. Mater. Res.* **1993**, *8*, 3233–3250. [[CrossRef](#)]
6. Zhu, Y.; Murali, S.; Cai, W.; Li, X.; Suk, J.W.; Potts, J.R.; Ruoff, R.S. Graphene and Graphene Oxide: Synthesis, Properties, and Applications. *Adv. Mater.* **2010**, *22*, 3906–3924. [[CrossRef](#)]
7. Geim, A.K.; Novoselov, K.S. The rise of graphene. *Nat. Mater.* **2007**, *6*, 183–191. [[CrossRef](#)] [[PubMed](#)]
8. Yang, W.; Luo, R.; Hou, Z. Effect of Interface Modified by Graphene on the Mechanical and Frictional Properties of Carbon/Graphene/Carbon Composites. *Materials* **2016**, *9*, 492. [[CrossRef](#)] [[PubMed](#)]
9. Vajtai, R. *Springer Handbook of Nanomaterials*; Springer International Publishing: Heidelberg, Germany, 2013.
10. Lessing, P.A.; Gordon, R.S. Creep of polycrystalline alumina, pure and doped with transition metal impurities. *J. Mater. Sci.* **1977**, *12*, 2291–2302. [[CrossRef](#)]
11. Weidner, A.; Ranglack-Klemm, Y.; Zienert, T.; Aneziris, C.G.; Biermann, H. Mechanical High-Temperature Properties and Damage Behavior of Coarse-Grained Alumina Refractory Metal Composites. *Materials* **2019**, *12*, 3927. [[CrossRef](#)] [[PubMed](#)]
12. Tamura, Y.; Moshtaghion, B.M.; Zapata-Solvas, E.; Gomez-Garcia, D.; Domínguez-Rodríguez, A.; Cerecedo-Fernández, C.; Valcárcel-Juárez, V. Is an alumina-whisker-reinforced alumina composite the most efficient choice for an oxidation-resistant high-temperature ceramic? *J. Eur. Ceram. Soc.* **2018**, *38*, 1812–1818. [[CrossRef](#)]
13. Zapata-Solvas, E.; Poyato, R.; Gómez-García, D.; Domínguez-Rodríguez, A.; Radmilovic, V.; Padture, N.P. Creep-resistant composites of alumina and single-wall carbon nanotubes. *Appl. Phys. Lett.* **2008**, *92*, 111912. [[CrossRef](#)]
14. Padture, N.P. Multifunctional Composites of Ceramics and Single-Walled Carbon Nanotubes. *Adv. Mater.* **2009**, *21*, 1767–1770. [[CrossRef](#)]

15. Zapata-Solvas, E.; Gómez-García, D.; Poyato, R.; Lee, Z.; Castillo-Rodríguez, M.; Domínguez-Rodríguez, A.; Radmilovic, V.; Padture, N.P. Microstructural Effects on the Creep Deformation of Alumina/Single-Wall Carbon Nanotubes Composites. *J. Am. Ceram. Soc.* **2010**, *93*, 2042–2047. [[CrossRef](#)]
16. Castillo-Rodríguez, M.; Muñoz, A.; Domínguez-Rodríguez, A. Creep study on alumina and alumina/SWCNT nanocomposites. *J. Eur. Ceram. Soc.* **2018**, *38*, 5497–5502. [[CrossRef](#)]
17. Heuer, A. Oxygen and aluminum diffusion in  $\alpha$ -Al<sub>2</sub>O<sub>3</sub>: How much do we really understand? *J. Eur. Ceram. Soc.* **2008**, *28*, 1495–1507. [[CrossRef](#)]
18. Bretheau, P.T.; Castaing, J.; Rabier, J.; Veyssi re, P. Mouvement des dislocations et plasticit    haute temp rature des oxydes binaires et ternaires. *Adv. Phys.* **1979**, *28*, 835–1014. [[CrossRef](#)]
19. Cano-Crespo, R.; Malmal-Moshtaghion, B.; G mez-Garc a, D.; Dom nguez-Rodr guez, A.; Moreno, R. High-temperature creep of carbon nanofiber-reinforced and graphene oxide-reinforced alumina composites sintered by spark plasma sintering. *Ceram. Int.* **2017**, *43*, 7136–7141. [[CrossRef](#)]
20. Zapata-Solvas, E.; Poyato, R.; Garc a, D.G.; Dom nguez-Rodr guez, A.; Padture, N.P. High-temperature mechanical behavior of Al<sub>2</sub>O<sub>3</sub>/graphite composites. *J. Eur. Ceram. Soc.* **2009**, *29*, 3205–3209. [[CrossRef](#)]
21. Dom nguez-Rodr guez, A.; Garc a, D.G.; Wakai, F. High temperature plasticity in yttria stabilised tetragonal zirconia polycrystals (Y-TZP). *Int. Mater. Rev.* **2013**, *58*, 399–417. [[CrossRef](#)]
22. Jim nez-Melendo, M.; Dom nguez-Rodr guez, A.; Bravo-Le n, A. Superplastic Flow of Fine-Grained Yttria-Stabilized Zirconia Polycrystals: Constitutive Equation and Deformation Mechanisms. *J. Am. Ceram. Soc.* **2005**, *81*, 2761–2776. [[CrossRef](#)]
23. De Bernardi-Mart n, S.; Zapata-Solvas, E.; Garc a, D.G.; Dom nguez-Rodr guez, A.; Guzm n-V zquez, F.; G mez-Herrero, J. On the High-Temperature Plasticity of Ceria-Doped Zirconia Nanostructured Polycrystals. *Key Eng. Mater.* **2009**, *423*, 61–66. [[CrossRef](#)]
24. De Bernardi-Mart n, S.; Garc a, D.G.; Dom nguez-Rodr guez, A.; De Portu, G. A first study of the high-temperature plasticity of ceria-doped zirconia polycrystals. *J. Eur. Ceram. Soc.* **2010**, *30*, 3357–3362. [[CrossRef](#)]
25. Calder n-Moreno, J.; De Arellano-L pez, A.R.; Dom nguez-Rodr guez, A.; Routbort, J.L. Microstructure and creep properties of alumina/zirconia ceramics. *J. Eur. Ceram. Soc.* **1995**, *15*, 983–988. [[CrossRef](#)]
26. Lorenzo-Mart n, C.; Flores-V zquez, J.; G mez-Garc a, D.; Mu oz-Bernab , A.; Dom nguez-Rodr guez, A.; Xueming, D.; Gomez-Herrero, J. Mechanical behaviour of yttria tetragonal zirconia polycrystalline nanoceramics: Dependence on the glassy phase content. *J. Eur. Ceram. Soc.* **2002**, *22*, 2603–2607. [[CrossRef](#)]
27. Moreno, J.C.; DeArellano-L pez, A.; Dom nguez-Rodr guez, A.; Routbort, J. High-temperature deformation of ZrO<sub>2</sub>Al<sub>2</sub>O<sub>3</sub>/SiC whisker composites fabricated by two techniques. *Mater. Sci. Eng. A* **1996**, *209*, 111–115. [[CrossRef](#)]
28. Zapata-Solvas, E.; G mez-Garc a, D.; Dom nguez-Rodr guez, A. Towards physical properties tailoring of carbon nanotubes-reinforced ceramic matrix composites. *J. Eur. Ceram. Soc.* **2012**, *32*, 3001–3020. [[CrossRef](#)]
29. Cano-Crespo, R.; Moshtaghion, B.M.; G mez-Garc a, D.; Moreno, R.; Dom nguez-Rodr guez, A. Graphene or carbon nanofiber-reinforced zirconia composites: Are they really worthwhile for structural applications? *J. Eur. Ceram. Soc.* **2018**, *38*, 3994–4002. [[CrossRef](#)]
30. Rinc n, A.; Chinelatto, A.S.; Moreno, R. Tape casting of alumina/zirconia suspensions containing graphene oxide. *J. Eur. Ceram. Soc.* **2014**, *34*, 1819–1827. [[CrossRef](#)]
31. Rinc n, A.; Moreno, R.; Chinelatto, A.S.A.; Guti rrez-Gonz lez, C.F.; Ray n, E.; Salvador, M.D.; Borrell, A. Al<sub>2</sub>O<sub>3</sub>-3YTZP-Graphene multilayers produced by tape casting and spark plasma sintering. *J. Eur. Ceram. Soc.* **2014**, *34*, 2427–2434. [[CrossRef](#)]
32. Poirier, J.-P. *Creep of Crystals. High-Temperature Deformation Processes in Metals, Ceramics and Minerals*; Cambridge University Press: Cambridge, UK, 1985.
33. Dresselhaus, M.S.; Jorio, A.; Hofmann, M.; Dresselhaus, G.; Saito, R. Perspectives on Carbon Nanotubes and Graphene Raman Spectroscopy. *Nano Lett.* **2010**, *10*, 751–758. [[CrossRef](#)] [[PubMed](#)]
34. Centeno, A.; Rocha, V.G.; Alonso, B.; Fern ndez, A.; Gonz lez, C.F.G.; Torrecillas, R.; Zurutuza, A. Graphene for tough and electroconductive alumina ceramics. *J. Eur. Ceram. Soc.* **2013**, *33*, 3201–3210. [[CrossRef](#)]
35. Malard, L.M.; Pimenta, M.A.; Dresselhaus, G.; Dresselhaus, M.S. Raman spectroscopy in graphene. *Phys. Rep.* **2009**, *473*, 51–87. [[CrossRef](#)]
36. Durand, J.-C.; Jacquot, B.; Salehi, H.; Fages, M.; Margerit, J.; Cuisinier, F.J. Confocal Raman microscopic analysis of the zirconia/feldspathic ceramic interface. *Dent. Mater.* **2012**, *28*, 661–671. [[CrossRef](#)] [[PubMed](#)]
37. Nazarpour, S.; L pez-G ndara, C.; Zamani, C.; Fern ndez-Sanju n, J.M.; Ramos, F.M.; Cirera, A. Phase transformation studies on YSZ doped with alumina. Part 2: Yttria segregation. *J. Alloy. Compd.* **2010**, *505*, 534–541. [[CrossRef](#)]
38. Kim, H.J.; Lee, S.-M.; Oh, Y.-S.; Yang, Y.-H.; Lim, Y.S.; Yoon, D.H.; Lee, C.; Kim, J.-Y.; Ruoff, R.S. Unoxidized Graphene/Alumina Nanocomposite: Fracture- and Wear-Resistance Effects of Graphene on Alumina Matrix. *Sci. Rep.* **2015**, *4*, 5176. [[CrossRef](#)] [[PubMed](#)]
39. Garc a, D.G.; Zapata-Solvas, E.; Dom nguez-Rodr guez, A.; Kubin, L.P. Diffusion-driven superplasticity in ceramics: Modeling and comparison with available data. *Phys. Rev. B* **2009**, *80*, 2141071–2141078. [[CrossRef](#)]
40. Papageorgiou, D.G.; Kinloch, I.A.; Young, R.J. Mechanical properties of graphene and graphene-based nanocomposites. *Prog. Mater. Sci.* **2017**, *90*, 75–127. [[CrossRef](#)]



## Chapter 9

# Rietveld analysis and mechanical properties of in situ formed La- $\beta$ -Al<sub>2</sub>O<sub>3</sub>/Al<sub>2</sub>O<sub>3</sub> composites prepared by sol-gel method

This chapter is the result of a collaboration with team members in which the research deviates slightly from the main topic (ceramics + carbon allotropes). However, at no time do the main themes of the thesis, such as sintering and characterization of ceramics, sol-gel preparation, or measurement of mechanical properties, lose sight.

In particular, this chapter presents the findings of a research study conducted to investigate the effects of using sol-gel processes to create  $\alpha$ -Al<sub>2</sub>O<sub>3</sub> composites reinforced with LBA (LaAl<sub>11</sub>O<sub>18</sub>) platelets from a sol-gel process of alumina-seeded-boehmite sol and lanthanum nitrate. The study focused on monitoring the crystal evolution of the composites using XRD Rietveld, as well as researching the mechanical properties of the specimens through Vickers and Knoop indentations.

The study found that using the sol-gel method was more efficient in promoting the precipitation of LBA platelets at lower temperatures than other solid-state reaction methods. The Rietveld analyses and SEM imaging revealed that LBA

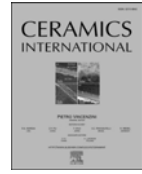
micrometric platelets were found in the sol-gel samples at temperatures as low as 1050 °C, which is 250 °C lower than in samples prepared by solid-state reaction.

However, the formation of platelets at low temperatures hindered the densification process, resulting in poor density for samples sintered at temperatures lower than 1450 °C in the sol-gel sample, and even impeded its full densification up to 1600 °C. The study also found that the growth of these platelets controlled the densification process: the geometry of the platelets disfavored packing, which restrained the densification. Moreover, the influence of the homogeneous distribution of the LBA on the mechanical properties of the samples was also researched. The LBA-alumina composites exhibited lower values of hardness and Young's moduli compared to pure alumina samples, but the indentation fracture resistance increased by up to 30% in the sol-gel sample. This increase was found to be especially significant in the sol-gel sample due to the homogeneous distribution of LBA platelets.



Contents lists available at ScienceDirect

Ceramics International

journal homepage: [www.elsevier.com/locate/ceramint](http://www.elsevier.com/locate/ceramint)

## Rietveld analysis and mechanical properties of in situ formed La-β-Al<sub>2</sub>O<sub>3</sub>/Al<sub>2</sub>O<sub>3</sub> composites prepared by sol-gel method

Pedro Rivero-Antúnez<sup>a,b,\*</sup>, Víctor Morales-Flórez<sup>a,b</sup>, Francisco Luis Cumbreira<sup>a</sup>, Luis Esquivias<sup>a,b</sup>

<sup>a</sup> Departamento de Física de la Materia Condensada, Universidad de Sevilla, Sevilla, 41012, Spain

<sup>b</sup> Instituto de Ciencia de Materiales de Sevilla, Centro Mixto CSIC-Universidad de Sevilla, Sevilla, 41092, Spain

### ARTICLE INFO

#### Keywords:

Alumina  
Reinforced ceramics  
Boehmite  
Ceramic matrix composites  
LaAl<sub>11</sub>O<sub>18</sub>  
Rietveld

### ABSTRACT

In this work, the crystal evolution of α-Al<sub>2</sub>O<sub>3</sub> composites reinforced with LBA platelets were monitored by XRD Rietveld. In addition, the mechanical properties of totally densified specimens were researched by Vickers and Knoop indentations. These composite materials were prepared by a sol-gel process from alumina seeded boehmite sol and lanthanum nitrate. X-ray diffraction data have been studied by Rietveld refinements and line profile analyses, paying attention to the LBA formation, the evolution of vol%, and crystallite size of the different phases. It has been observed that the appearance of the LBA phase happens at a lower temperature than in samples prepared by a conventional solid state reaction. Indentation tests revealed that the presence of LBA microplatelets in the sol-gel samples leads to a significant increase of their indentation fracture resistance, in comparison to the conventional samples.

### 1. Introduction

Resistance to chemical corrosion and wear, extreme hardness, or thermodynamic stability even at high temperatures are the essential characteristics of alumina ceramics. However, they present a major limitation since catastrophic failure occurs under mechanical or thermal stress due to their low fracture toughness. This is a serious drawback when replacing metallic alloys in some structural applications in advanced technology. Over the last forty years, structural ceramics have been intensively studied, and the improvements on their mechanical reliability are still an open source of discussion [1,2]. In more recent years, considerable emphasis has been done on the fabrication of composites where the crack propagation can be deflected and slowed down. It is common to find ceramics reinforced with second phases that present a extremely low dimensionality, such as graphene platelets, nanotubes or fibers [3–5], but they are expensive, hard to mix homogeneously, and need pressure-assisted densification. In this context, the growth of anisotropic second-phase grains formed *in situ*, is being proposed as a profitable alternative for microstructural reinforcement [6–12], as this procedure enhances homogeneity of phases, and thermal stability and electrical insulating properties [13,14].

The microstructure of rare-earth/Al<sub>2</sub>O<sub>3</sub> ceramic systems sintered at temperatures beyond the eutectic point depends on the nature of the additives [15,16]. When La<sub>2</sub>O<sub>3</sub> is added to alumina, a solid state reaction occurs, and a layered hexagonal aluminate with a defective magnetoplumbite structure appears [17]: LaAl<sub>11</sub>O<sub>18</sub>, also known as lanthanum hexa-aluminate, La-β-alumina, or LBA. Ropp and Carroll [18] studied the kinetics of this reactions, reporting a two-step process: initially, at 800 °C, a perovskite-type aluminate (LaAlO<sub>3</sub>) forms (reaction 1); at higher temperatures (>1400 °C), this aluminate slowly reacts with Al<sub>2</sub>O<sub>3</sub> to form elongated LBA grains (reaction 2).



In a former paper [19], it was demonstrated how the development of the crystalline phases and the evolution of the microstructure are influenced by the processing route for 30 vol% LaAl<sub>11</sub>O<sub>18</sub>/Al<sub>2</sub>O<sub>3</sub> composites. The sol-gel method restrains densification because the geometry of the platelets disfavors packing. This fact, combined with the inhibited alumina grain growth, lead to poor density for samples sintered at <1450 °C. However, shrinkage took place in a narrower temperature

\* Corresponding author. Department of Condensed-Matter Physics, University of Sevilla, P.O. 1065, Seville, 41080, Spain.

E-mail addresses: [privero@us.es](mailto:privero@us.es) (P. Rivero-Antúnez), [vmorales@us.es](mailto:vmorales@us.es) (V. Morales-Flórez), [fcumbreiras@us.es](mailto:fcumbreiras@us.es) (F.L. Cumbreira), [luisesquivias@us.es](mailto:luisesquivias@us.es) (L. Esquivias).

URL: <http://grupo.us.es/fqm393/> (V. Morales-Flórez).

<https://doi.org/10.1016/j.ceramint.2022.05.058>

Received 8 March 2022; Received in revised form 21 April 2022; Accepted 5 May 2022

Available online 10 May 2022

0272-8842/© 2022 The Authors. Published by Elsevier Ltd. This is an open access article under the CC BY license (<http://creativecommons.org/licenses/by/4.0/>).

# Chapter 9. Rietveld analysis and mechanical properties of *in situ* formed La- $\beta$ -Al<sub>2</sub>O<sub>3</sub>/Al<sub>2</sub>O<sub>3</sub> composites prepared by sol-gel method

P. Rivero-Ant3nez et al.

Ceramics International 48 (2022) 24462–24470

interval and the formation of LBA platelets occurs at lower temperature than by other preparation methods. Almost identical XRD patterns are obtained for all samples after heating at 1450 °C for 5 h, independently of the preparation method, but the relative phase concentration evolution does depend on the preparation routine. Therefore, it was concluded that the growth of platelets controlled the densification process.

A revision of the bibliographical background reveals that the first application of *in situ* formed anisometric  $\beta$ -alumina grains was for the fabrication of abrasive grits [20]: through the incorporation of small amounts of La<sub>2</sub>O<sub>3</sub> into Al<sub>2</sub>O<sub>3</sub> by coprecipitation, the microstructural uniformity and the formation of LaAl<sub>11</sub>O<sub>18</sub> were improved. In 1992, Kang et al. [21] added different concentrations of LaAl<sub>11</sub>O<sub>18</sub> for the fabrication of self-reinforced  $\alpha$ -Al<sub>2</sub>O<sub>3</sub>, obtaining an increase of fracture toughness from 2.5 to 3.5 MGf<sup>1</sup> when raising the content of LaAl<sub>11</sub>O<sub>18</sub>. In the same year, Chen et al. [22] achieved a peak of fracture toughness of 4.3 MGf for alumina composites reinforced with a 30 vol% of LBA. A few years later, Yasuoka et al. [23] reported high flexural strength and high fracture toughness (630 MPa and 6 MGf, respectively) for silica-doped 20 vol% LBA/Al<sub>2</sub>O<sub>3</sub> composites. Since then, LBA as well as many other  $\beta$ -aluminate with elongated grain morphologies, have been used as reinforcements for ceramic compounds, such as SrAl<sub>12</sub>O<sub>19</sub> or LaMgAl<sub>11</sub>O<sub>19</sub> [22,24], as they may lead to improvements in strength and fracture toughness compared to monolithic ceramic [22,25].

In this work, the basic knowledge on the formation of LBA/Al<sub>2</sub>O<sub>3</sub> composites and their structure is examined. The crystallization and densifying process were studied by rigorous Rietveld analyses of XRD patterns. The effect of the sol-gel method on the formation of the LBA platelets was researched, emphasizing their formation and the effect of the temperature. Finally, the role of LBA as a mechanical reinforcing agent in alumina matrix is discussed.

## 2. Materials and methods

### 2.1. Sample synthesis

Two batches of samples were prepared for this work: a series prepared by sol-gel route, and another one by solid state reaction. The preparation routes of the powders of these two types of samples are summarized as follows (full details can be found in Ref. [19]):

#### 2.1.1. Sol-gel route

Inspired in the steps of Kumagai et al. [26], a boehmite ( $\gamma$ -AlO(OH)) sol (Disperal Sol P2, Condea, Germany, crystallite size 4.5 nm, dispersed particle size 20 nm, viscosity 10 mPa·s) was dispersed at pH = 4.5, and slowly seeded with 1.75 wt% of 100 nm diameter pure  $\alpha$ -Al<sub>2</sub>O<sub>3</sub> particles. The seeded sol and La(NO<sub>3</sub>)<sub>3</sub>·6H<sub>2</sub>O (Johnson Matthey Electronics, Wayne, USA) were mixed resulting in a volume ratio Al<sub>2</sub>O<sub>3</sub>/LBA = 7/3. The mixture was stirred for 24 h at room temperature, and then heated at 80 °C until gellation occurred. The dried xerogel was milled in an alumina mortar, and the resulting powder was sieved to <354  $\mu$ m. Pellets were uniaxially pressed at 70 MPa, in order to conform handleable pieces, and then cold isostatically pressed at 275 MPa. Finally, the green bodies were calcined at 750 °C for 2 h. This series of samples were named SG. The whole process is summarized in Fig. 1.

#### 2.1.2. Solid-state reaction

Despite the samples prepared by the previous sol-gel process also will

involve a solid-state reaction during its later sintering, this second method is referred to as a solid-state reaction, as it consists of a standard mixing of  $\alpha$ -Al<sub>2</sub>O<sub>3</sub> powders and a La<sub>2</sub>O<sub>3</sub> precursor.

High-purity (>99.99%, particle diameter = 0.3  $\mu$ m)  $\alpha$ -Al<sub>2</sub>O<sub>3</sub> powder (Baikalox SM8, Baikowski International Corp., Charlotte, USA) was dispersed in distilled water with HNO<sub>3</sub> (pH 3) in presence of high power ultrasound and a magnetic stirrer, leading to a slurry texture. La(NO<sub>3</sub>)<sub>3</sub>·6H<sub>2</sub>O was poured to the  $\alpha$ -Al<sub>2</sub>O<sub>3</sub> to yield a mixture of 30 vol% LBA and 70 vol%  $\alpha$ -Al<sub>2</sub>O<sub>3</sub> (same ratio of SG series). The mixture was mechanically stirred for 24 h while it dried on a hot plate at 100 °C. These powders were calcined in air at 750 °C for 2 h, and hand-grounded in an alumina mortar before and after calcination. Finally, the calcined powders were uniaxially pressed at 160 MPa. The resultant series of samples was designated as SSR.

#### 2.1.3. Calcination and sintering

The mentioned calcination at 750 °C for 2 h ensured the elimination of traces and the transformation of the La(NO<sub>3</sub>)<sub>3</sub> into La<sub>2</sub>O<sub>3</sub>. At the same time, in the SG samples, the boehmite releases the hydroxyl groups, going into transition aluminas. After this calcination, samples were sintered by conventional pressureless sintering at 60 °C/h, with several dwell times at different temperatures, from 1050 up to 1650 °C.

Finally, pure commercial  $\alpha$ -Al<sub>2</sub>O<sub>3</sub> nanopowders (same powders than the used in SSR samples) were sintered as a reference sample also through conventional pressureless sintering procedure under the same conditions used for SSR samples.

## 2.2. Structural and chemical characterization

The shrinkage of the pellets during heating was specifically monitored by thermal mechanical analysis (TMA), performed at 300 °C/h up to 1500 °C, with a dwell time of 3 h at this temperature. Samples were pre-heated at 800 °C for 2 h before TMA. Phase development was characterized with this method, and also by XRD/Rietveld analyses performed on the different stages of sintering of the samples.

The densities of the samples were determined by geometry, or by Archimedes' method if density >92% of the theoretical density. Sintered samples were polished by conventional ceramographics methods [27] up to 1  $\mu$ m diamond slurry, and thermally etched for the study of their microstructures by scanning electron microscopy (SEM).

The XRD data were obtained with a Philips PW-1800 diffractometer (40 kV, 30 mA) equipped with a graphite mono-chromator and an automatic system of step-scanning. The wavelength was the corresponding to the Cu K $\alpha$  ( $\lambda$  = 0.15483 nm). The range  $2\theta \in (20^\circ, 80^\circ)$  was scanned at steps of 0.02° and 10 s. The profiles were refined with a recent version of the program FullProf for Rietveld analysis. The modified Thompson-Cox-Hasting pseudo-Voigt function was assumed as profile shape function [28]. Initial values for the parameters of the structure were taken from the Powder Diffraction File database (International Centre for Diffraction Data). The scale factors were obtained from the relation of Hill and Howard [29] and the completion of Rietveld protocol of refinement, which takes account for structural, profile and global parameters. These factors were used for the determination of relative abundances.

The conventional agreement indices were below  $R_{wp}$  = 13.7,  $R_e$  = 8.4,  $\chi^2$  = 2.64. The volume-weighted distribution of different particle sizes was determined with the aid of software BREADTH. This program implement the "double-Voigt" method [30,31], equivalent to the classical Warren-Averbach approach [32]. In such a way, the program evaluates the column-length distribution parallel to the reciprocal [hkl] direction by choosing a hkl reflection of the pure profile and its harmonics.

#### 2.3. Mechanical characterization

Mechanical characterization was performed on samples densified at

<sup>1</sup> Based on Profs. C. Ramadas and A. R. Jadhav's suggestion, the use of the unit "griffith" (Gf) was proposed [4] in substitution of the awkward classical magnitude Pa·m<sup>1/2</sup>, where 1 Gf = 1 Pa m<sup>1/2</sup>, as a tribute to the mechanical engineer Alan Arnold Griffith (1893–1963). Griffith was known in the field of fracture mechanics for his pioneering studies on the nature of stress and failure due to crack propagation in brittle materials.

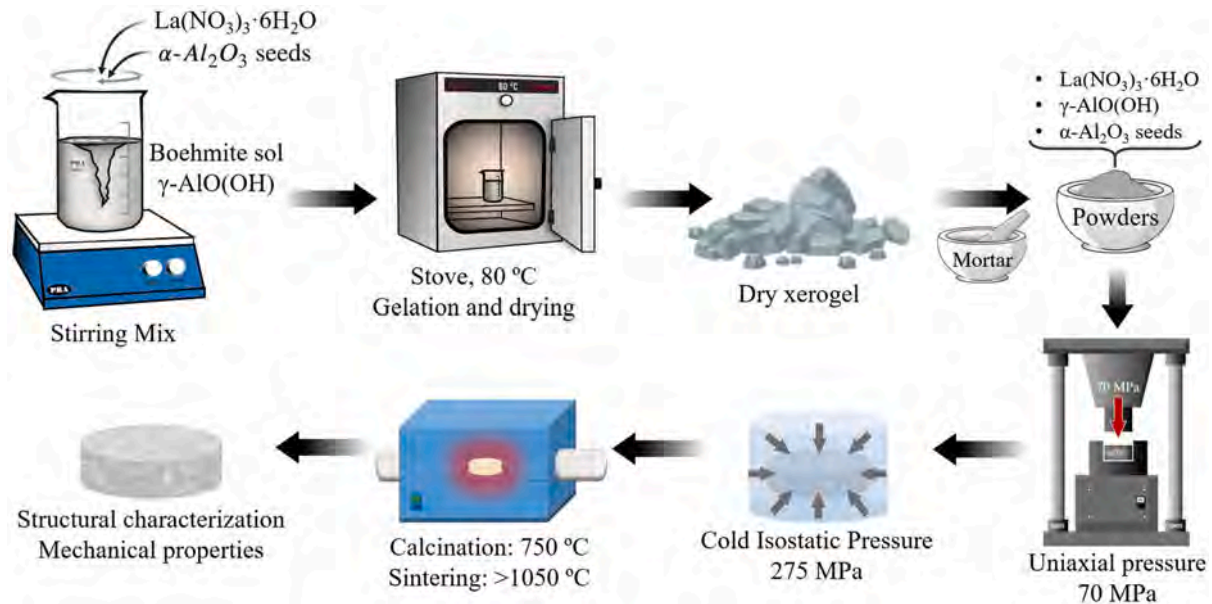


Fig. 1. Sketch summarizing the fabrication procedure of Sol-Gel samples.

1500 and 1600 °C. For the measurement of hardness, Vickers indentation tests were performed on mirror-finished surfaces. A load of 20 kp (196 N) was applied during a dwell time of 20 s using a *Buehler Wilson VH1150 MicroVickers Hardness Tester*. For the proper statistic treatment, the test was repeated at least ten times for each sample. Miyazaki et al. [33] proved that for dense alumina ceramics, Shetty's equation for median cracks [34] provides values of indentation fracture resistance ( $K_{IFR}$ ) totally correlated with values of fracture toughness ( $K_{IC}$ ) measured by standardized methods, such as SEPB. Taking advantage of the Vickers indentation tests, the resultant radial cracks were measured, and  $K_{IFR}$  was calculated to estimate the  $K_{IC}$ , and elucidate differences between the toughness of the reference pure alumina sample and the composites. Shetty's equation for half-penny (median) cracks is expressed as follows:

$$K_{IFR} = 0.023(E/H)^{1/2} P / c^{3/2} \quad (3)$$

where  $E$  is the Young's modulus,  $H$  is the Vickers hardness,  $P$  is the load applied by the tip, and  $c$  is the length of the crack, measured from the center of the print. For the calculation of Young's modulus, Knoop indentations (load = 20 kp) were made in polished surfaces, and the procedure suggested by Marshall et al. [35] was followed. Given the geometry of the Knoop indenter, the relationship between the large diagonal ( $D$ ) and the short diagonal ( $d$ ) of the diamond tip is  $D/d = 7.11$ . However, after the indentation, the elastic recovery of the indented material shorten the length of the minor diagonal, whilst longer diagonal remains almost the same. Thus, when the unload is completed and the indenter is withdrawn, the ratio between the printed diagonals  $d'/D'$ , give us a way to measure the Young's modulus:

$$\frac{d'}{D'} \approx \frac{d}{D} = \frac{d}{D} - \alpha \frac{H}{E} \quad (4)$$

$$\Rightarrow E = \frac{\alpha H}{1/7.11 - d'/D'} \quad (5)$$

where  $\alpha = 0.45$  is a well known constant obtained from the fitting of several test performed on a wide type of ceramic materials [35], and  $H$  is the hardness, obtained from Vickers tests.

### 3. Results and discussion

#### 3.1. Structural evolution

##### 3.1.1. Rietveld analysis

In this work, Rietveld analyses were performed, so XRD data do not just give qualitative information about the existence of the different species, but we have also calculated the volume concentration of these phases and their grain size distributions, studying how those parameters evolve with the different sintering temperatures. In this sense, the qualitative description of the process was already reported in a previous paper, based on the first approach by XRD and SEM [19]. The results of volume concentrations and average grain sizes are summarized in Table 1.

As it was shown, in SSR samples, peaks of  $\text{LaAlO}_3$  were not observed up to 1000 °C [19]. At 1050 °C  $\text{LaAlO}_3$  represents a ~7 vol% (see Table 1). This phase increases its presence according to reaction 1 up to 10 vol%, at 1100 °C. At  $1200 < T \leq 1250$  °C, LBA appears [19]. Despite the onset of this transformation (reaction 2) is expected at  $T \sim 1250$  °C, LBA does not represent a significant amount of the volume of the sample up to 1400 °C. At this temperature,  $\alpha\text{-Al}_2\text{O}_3$  is the ~90 vol% of the sample, whereas perovskite  $\text{LaAlO}_3$  still exists, meaning a 5.1 vol%, and LBA represents the 4.5 vol%. At 1500 °C, all the perovskite has been consumed and LBA jumps to be almost the 30 vol% of the composite, as planned during the preparation stage. With respect to the grain size of LBA, the average grain size ( $d$ ) experiments a significant increase, from 90 nm at 1300 °C to 350 nm at 1650 °C (Table 1). Simultaneously, the grain size distribution becomes flatter, wider, and shifts to larger values (Fig. 2).

Regarding SG samples, it was reported that, at 750 °C, they are basically composed of  $\gamma\text{-Al}_2\text{O}_3$  and incipient  $\alpha\text{-Al}_2\text{O}_3$ , without any signal of  $\text{LaAlO}_3$ , similar to the behavior of SSR samples. However, unlike SSR,  $\text{LaAlO}_3$  was not found at 1000 °C in SG samples (although some  $\gamma\text{-Al}_2\text{O}_3$  was present) [19]. It has been confirmed that, after 10 h at 1050 °C, a 3.5 vol% of perovskite appeared, as well as a 6.0 vol% of LBA (Table 1). Therefore, reaction 2 started at a temperature at least 200 °C lower than the required for SSR samples (Table 1). In Fig. 3, the identification of the

## Chapter 9. Rietveld analysis and mechanical properties of in situ formed $\text{La-}\beta\text{-Al}_2\text{O}_3/\text{Al}_2\text{O}_3$ composites prepared by sol-gel method

P. Rivero-Ant3nez et al.

Ceramics International 48 (2022) 24462–24470

**Table 1**

Phase volume concentration (vol%) and crystallite average size ( $\bar{d}$ ) resulting from the Rietveld analysis of the X-ray diffraction patterns of the SSR and SG samples sintered at different temperatures.

Sample	Phase		1050 °C	1100 °C	1150 °C	1300 °C	1350 °C	1400 °C	1500 °C	1650 °C	
SSR	$\alpha\text{-Al}_2\text{O}_3$	vol%	93.1	90.0							
		$\bar{d}$ (nm)		240	260	290	290				
	$\text{LaAlO}_3$	vol%	6.9	10.0					5.1	0.0	0.0
		$\bar{d}$ (nm)		310							
	LBA	vol%	0.0	0.0					4.5	27.3	27.1
		$\bar{d}$ (nm)					90	140	270		350
SG	$\alpha\text{-Al}_2\text{O}_3$	vol%	90.5	86.8	83.3	78.1	72.2	68.5	70.4	71.6	
		$\bar{d}$ (nm)		450	480	510	540	540	540	540	590
	$\text{LaAlO}_3$	vol%	3.5	2.2	1.2	0.8	0.2	0.0	0.0	0.0	0.0
		$\bar{d}$ (nm)		220							
	LBA	vol%	6.0	11.0	15.5	21.1	27.6	31.5	29.6	28.4	28.4
		$\bar{d}$ (nm)		240				430	440		480

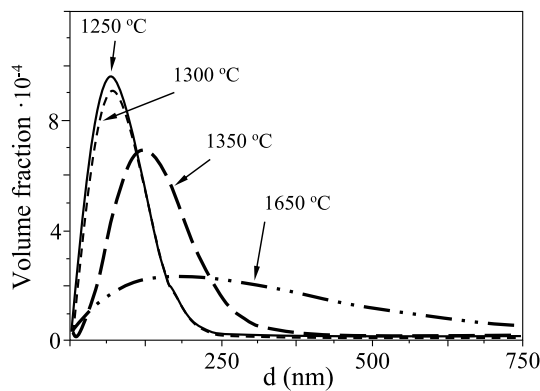


**Fig. 2.** Evolution of the volume fraction of LBA during sintering of SSR samples.  $\text{La-}\beta\text{-aluminate}$  crystallite size distribution for different sintering temperatures.

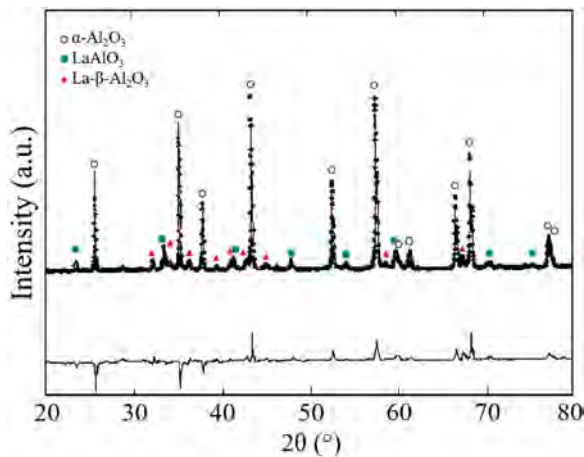


**Fig. 3.** Rietveld plot for diffraction data collected for SG sample heat-treated at 1050 °C during 10 h. The observed data are indicated by dots and the calculated pattern by the solid line overlying them. The line at the bottom of the pattern is the difference between the observed and calculated profile.

peaks and the fitting of the spectrum corresponding to the SG sample at 1050 °C can be seen. In addition,  $\text{LaAlO}_3$  is present in a narrower range of temperatures: it appears at  $T \leq 1050$  °C, then it represents a 2.2 vol% at 1100 °C, and is rapidly consumed in the formation of LBA, with a residual content at 1300 °C (see Table 1).

The evolution of the grain size distribution of LBA in SG samples is shown in Fig. 4. The distributions do not reach the same heights than in SSR, but are wider, spanning over a wider range of grain sizes. In addition, the grain size distribution of SG suffers a less severe evolution than in the case of SSR samples (compare, e.g., the change in the average size or in the full width half maximum) given that in SG samples this phase is formed gradually since the first steps of sintering at lower temperatures in SG samples. Thanks to this faster reactivity, the ratio 7/3 of  $\alpha\text{-Al}_2\text{O}_3/\text{LBA}$  is reached quite earlier in samples prepared by sol-gel method.

In the composite samples, the alumina grain growth is inhibited by two mechanisms: on the one hand, the frictional (pinning) effect of LBA platelets with the migrating grain boundaries, which opposes to grain movements [36]; on the other hand,  $\text{La}^{3+}$  cations segregate at grain boundaries, increasing the Al–O ionic bonding at grain boundaries, decreasing grain boundary diffusivities [37], and hindering the transformation of transition aluminas into  $\alpha\text{-Al}_2\text{O}_3$  [38].

The precipitation of LBA has been also confirmed by SEM analysis. In

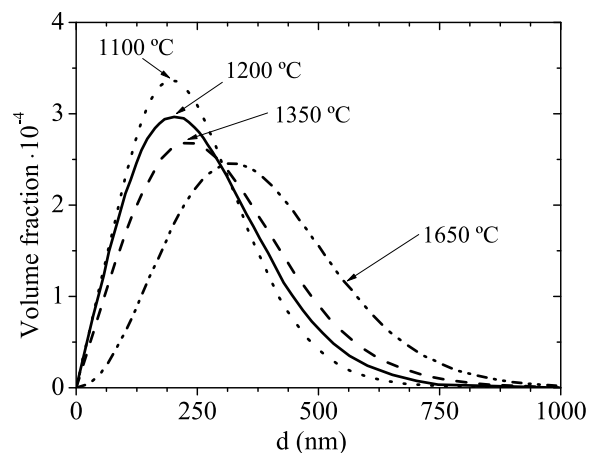


**Fig. 4.** Evolution of the volume fraction of LBA during sintering of SG samples. LBA crystallite size distribution for different sintering temperatures.

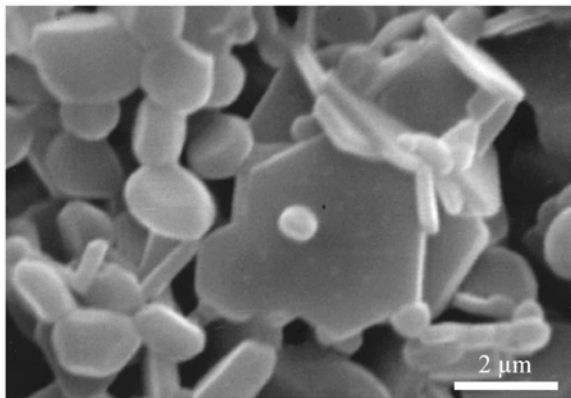


Fig. 5. Evidence of platelet-like structure of the anisometric phase LBA. Micrograph corresponding to the SG sample sintered at 1050 °C for 10 h.

the literature, LBA grains have been described as platelets [39–41], also referred as plate-like or needle-like, as well as barium or other rare-earth  $\beta$ -aluminate ceramic systems [15,25]. SEM images taken on the sample calcined at 1050 °C certainly show the plate-like shape of the LBA grains, confirming the existence of LBA at this temperature only when samples are prepared via sol-gel (see Fig. 5-left). In accordance to the Rietveld results (Fig. 2), LBA platelets have not been observed by SEM in SSR samples calcined at temperatures below 1250 °C.

### 3.1.2. Thermal mechanical analysis

The TMA tests gives information about the temperatures and times required for the densification of the samples, as well as the temperatures at which phase transformations could happen. The data obtained from this analysis is represented in Fig. 6. The densification rate of pure  $\alpha$ -Al<sub>2</sub>O<sub>3</sub> (green data, squares) started increasing at approximately 950 °C, decelerating at ~1300 °C, being completely null after 20 min at 1500 °C. The maximum shrinkage rate was found at T = 1350 °C (t = 250 min).

On the other hand, due to the presence of a second phase, SSR samples (red data, solid circles) required more time and temperature before the shrinkage started, and it does not occur until ~1275 °C are reached, almost coinciding with the transformation of perovskite into LBA. Thus, the precipitation of the perovskite occurs without densification. The densification stopped some later than pure  $\alpha$ -Al<sub>2</sub>O<sub>3</sub>, 35 min after 1500 °C were reached, when all the LaAlO<sub>3</sub> has reacted.

As the samples were calcined at 750 °C before TMA analysis, the boehmite of SG suffered an endothermic transformation into  $\gamma$ -Al<sub>2</sub>O<sub>3</sub>, as expected from the evolution of transition aluminas [42], and its associated loss of mass and contraction. During the TMA (blue data, triangles), a first shrinkage started around 950 °C and stopped at ~1250 °C due to the transformation of transition aluminas (mostly  $\gamma$ -Al<sub>2</sub>O<sub>3</sub>) into  $\alpha$ -Al<sub>2</sub>O<sub>3</sub>. Note that shrinkage rate completely stopped (back to zero) before a second densification process started, revealing two well differentiated processes. This first step of densification suppose the transition from the density of  $\gamma$ -Al<sub>2</sub>O<sub>3</sub> (3.65 g/cm<sup>3</sup> [43]) to the density of  $\alpha$ -Al<sub>2</sub>O<sub>3</sub> (3.985 g/cm<sup>3</sup> [44]), an increase of 9.18%, thus, a theoretical shrinkage of 8.4% of the height of a cylindrical sample of fixed basal section, which coincides with the shrinkage that SG sample suffered during this first step of densification (area enclosed by the blue curve in Fig. 6 in the first step). Nevertheless, this coincidence is the result of two facts: not all the sample is made of alumina, and the  $\alpha$ -Al<sub>2</sub>O<sub>3</sub> reached after this first step is not completely densified. Anyway, it can be considered as signature of the physics running in this process.

The next step of shrinkage occurs between 1350 °C and 1500 °C, and

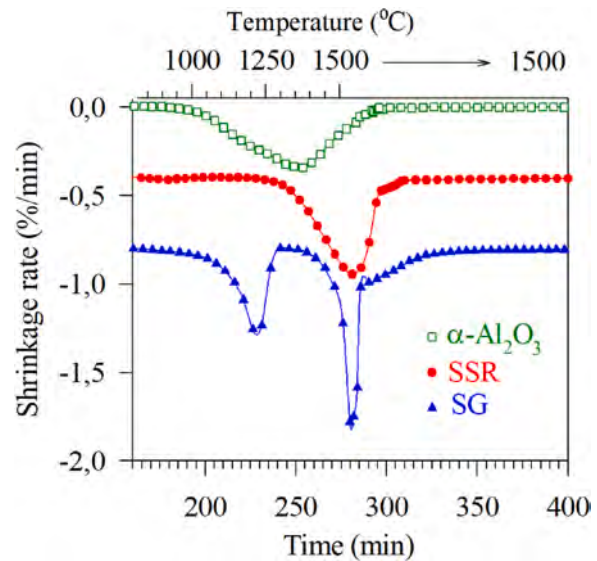


Fig. 6. Shrinkage behaviour versus temperature for heating ramp of 300 °C/h ( $\sim$ 5 °C/min) and a 3 h dwell at 1500 °C. Samples were pre-heated at 800 °C for 2 h. The red circles and the blue triangles curves have been vertically shifted so they do not overlap at the origin. (For interpretation of the references to colour in this figure legend, the reader is referred to the web version of this article.)

it is due to the rearrangement and densification of  $\alpha$ -Al<sub>2</sub>O<sub>3</sub>, analogously to the densification of SSR and pure  $\alpha$ -Al<sub>2</sub>O<sub>3</sub> samples, exhibiting the maximum shrinkage rate at exactly the same instant that in SSR sample: T = 1500 °C, t = 280 min. Thus, the presence of La<sub>2</sub>O<sub>3</sub> and LaAlO<sub>3</sub> (precursors of LBA) is retarding the temperatures and times necessary for  $\alpha$ -Al<sub>2</sub>O<sub>3</sub> densification.

Furthermore, in a sample of boehmite seeded with  $\alpha$ -Al<sub>2</sub>O<sub>3</sub>, those seeds play a crucial role accelerating the transformation of boehmite into  $\alpha$ -Al<sub>2</sub>O<sub>3</sub>, acting as nucleation sites, and reducing the required time and temperature [26,27]. This effect, nevertheless, is hindered in this sol-gel boehmite sample by the presence of LBA precursors. Schaper et al. [38] described that the sintering of alumina proceed via surface diffusion. This diffusion decreases by the formation of LaAlO<sub>3</sub> at the surface of alumina grains [45], postponing 100 °C the  $\gamma \rightarrow \alpha$  phase transformation and the densification, results that are in complete agreement with those described in this work.

### 3.1.3. Sintering behavior and densification

The densities were measured for the determination of the composition and the level of densification. The densities are registered in Table 2 and in Fig. 7, expressed as the fraction of the theoretical density, i.e., 3.985 g/cm<sup>3</sup> for pure  $\alpha$ -Al<sub>2</sub>O<sub>3</sub> [44], and 4.04 g/cm<sup>3</sup> for SG and SSR samples. This density is obtained by considering the theoretical 30 vol% of LBA (4.17 g/cm<sup>3</sup> [17]) present in these composites, supposing all the LaAlO<sub>3</sub> perovskite has reacted with alumina (reaction 2). Nevertheless, this criterion introduces an overestimation in the relative density of samples in stages in which they still contain LaAlO<sub>3</sub> (theoretical density = 6.53 g/cm<sup>3</sup> [46]) that has not reacted with  $\alpha$ -Al<sub>2</sub>O<sub>3</sub> to form LBA. For example, a sample with a remaining 10 vol% of LaAlO<sub>3</sub> will show a relative density ~6% larger than the actual one.

At 1200 °C, the pure  $\alpha$ -Al<sub>2</sub>O<sub>3</sub> sample is the most densified (73%), while the SSR sample is the least (53%). At this temperature, the SG sample is more densified (61%) than the SSR thanks to the first step of shrinkage observed at ~1150 °C in the TMA experiments, related to transition aluminas transforming into  $\alpha$ -Al<sub>2</sub>O<sub>3</sub>. This feature was explained in the previous section 3.1.2, but note that data cannot be

## Chapter 9. Rietveld analysis and mechanical properties of in situ formed La- $\beta$ -Al<sub>2</sub>O<sub>3</sub>/Al<sub>2</sub>O<sub>3</sub> composites prepared by sol-gel method

P. Rivero-Ant3nez et al.

Ceramics International 48 (2022) 24462–24470

**Table 2**

Evolution of the densities of the samples, expressed as a fraction of the theoretical densities: 3.985 g/cm<sup>3</sup> for pure  $\alpha$ -Al<sub>2</sub>O<sub>3</sub>, and 4.04 g/cm<sup>3</sup> for SG and SSR composites.

Temperature (°C)	1100	1200	1250	1300	1400	1450	1500	1550	1650
$\alpha$ -Al <sub>2</sub> O <sub>3</sub>	0.65	0.73	0.81	0.93	0.98	0.98	0.98	0.99	0.99
SSR	–	0.53	0.57	0.72	0.90	0.92	0.94	0.95	0.99
SG	–	0.61	0.60	0.62	0.73	0.73	0.92	0.92	0.96

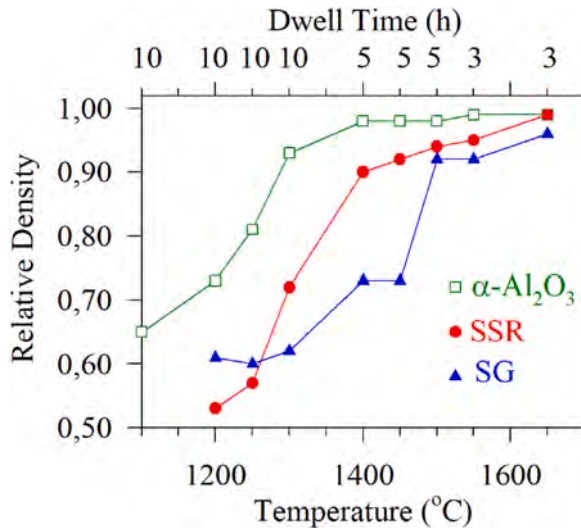


**Fig. 7.** Evolution of the densities of pure  $\alpha$ -Al<sub>2</sub>O<sub>3</sub>, SSR and SG samples for different temperatures and dwell times. Adapted with permission from Ref. [19].

completely correlated as density measurements were made at each indicated temperature after specific dwell times, while TMA were dynamic measurements. At 1300 °C, the differences between the samples becomes more pronounced: the pure  $\alpha$ -Al<sub>2</sub>O<sub>3</sub> samples reaches 93% density at 1300 °C, while the SG sample is 61% dense, and the SSR is 71%. The formation of LBA platelets inhibits densification because their geometry disfavors packing. In SSR samples, LBA platelets appear at ~1250 °C and they form gradually. This slow appearing allows the rearrangement of particles, and subsequent densification. LBA represents just the 4.5 vol% at 1400 °C (Table 1), temperature at which the samples already exhibited a 90% of densification (Fig. 7 and Table 2). On the other hand, a significant amount of LBA platelets are already present in the SG sample since early stages, and their formation occurs rapidly, in a short interval. This fact hinders densification, allowing just a 73% of densification at 1400 °C. Notice that, at this temperature, pure  $\alpha$ -Al<sub>2</sub>O<sub>3</sub> samples has already reached almost its maximum density.

In SSR sample, at ~1500 °C, when all the lanthanum has reacted and the vol. ratio LBA/ $\alpha$ -Al<sub>2</sub>O<sub>3</sub> is 7/3, densities are in 94%, and densification continues till 99% after 3 h at 1650 °C, apparently unaffected by the existence of LBA platelets. On the other hand, the early appearance of anisometric structures in SG samples allows a major development of the platelets that reached bigger sizes (see Fig. 4), reducing the surface available for contact between particles during the sintering. This fact frustrates the densification: even after 3 h at 1650 °C, the SG sample did not obtain full density (Fig. 7 and Table 2).

The SEM micrographs reveal important differences between the samples after the treatment at the highest temperature of 1650 °C (Fig. 8). At this stage, pure  $\alpha$ -Al<sub>2</sub>O<sub>3</sub> and SSR have obtained almost the 100% of theoretical densities, and SG the 96%. Given the large times and

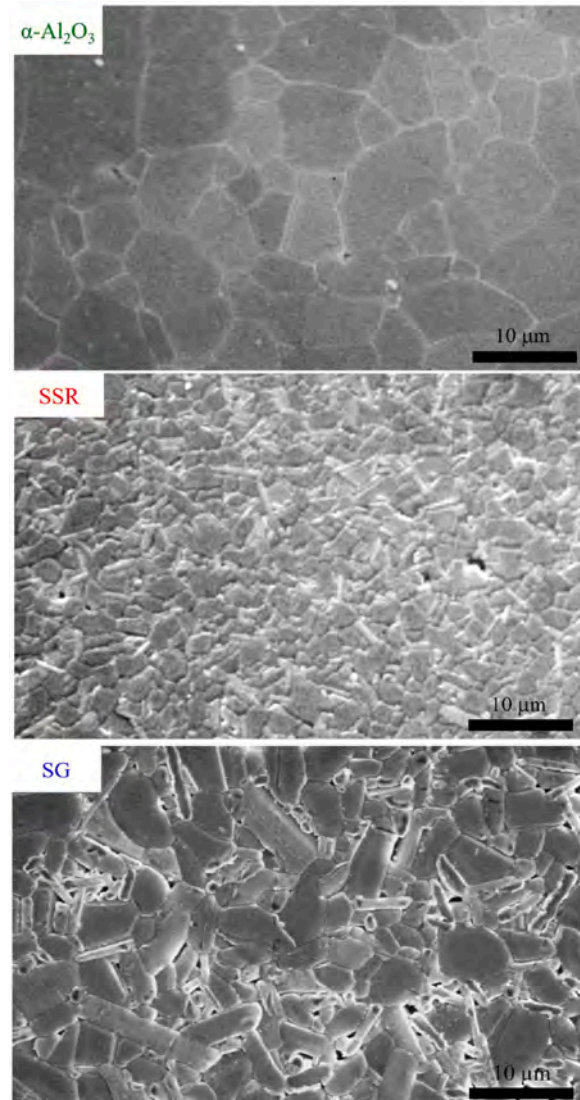


**Fig. 8.** SEM micrographs regarding the microstructures of samples sintered 3 h at 1650 °C. **Top:** fully dense commercial pure  $\alpha$ -Al<sub>2</sub>O<sub>3</sub> sample. **Center:** fully dense SSR sample, exhibiting the finest structure. Adapted with permission from Ref. [19]. **Bottom:** SG sample, with a coarser grain structure and not fully densified (96%). Adapted with permission from Ref. [19].



temperatures of sintering, the grains of the pure  $\alpha$ -Al<sub>2</sub>O<sub>3</sub> samples grew considerably. SSR exhibited the finest structure, while SG sample showed the larger platelets that obstructed rearrangement of particles, forced the densification to occur via grain growth, and resulted in a coarser microstructure. The apparent grain size of LBA observed by SEM confirms that the addition of LBA precursors reduces the ability to densify, as well as the alumina grain size. Note the discrepancies between SEM and XRD results regarding grain size that may arise from the fact that crystallite size (XRD) and grain size (SEM) are not the same. Finally, the homogeneous distributions of the LBA platelets can be also highlighted in the samples regarding SEM micrographies (Fig. 8).

### 3.2. Mechanical properties

The analysis of the mechanical properties of the different samples via Vickers and Knoop indentations allowed for the estimation of the Vickers Hardness, Young's modulus, and indentation fracture resistance,  $K_{IFR}$  (results listed in Table 3). Firstly, there are not differences in the Vickers hardness of samples sintered at 1500 °C and 1650 °C. The highest value is achieved by the classical sample made of pure  $\alpha$ -Al<sub>2</sub>O<sub>3</sub>, as well as the largest value of Young's modulus, which are, besides, both in agreement with the values typically reported for fully dense  $\alpha$ -Al<sub>2</sub>O<sub>3</sub> [22, 44]. On the other extreme, the sample with the lowest Vickers hardness is the SSR sample, despite it is fully dense at 1650 °C. The Hall-Petch effect predicts an increase of hardness as grain size decreases, however, the low hardness of LBA (~9 GPa [22]) plays a critical role, reducing the hardness of composites samples when a 30 vol% of LBA is used.

Young's modulus suffers significant increase of ~30% in all samples due to the last calcination step, from 1500 °C to 1650 °C, being grain growth and densifying decisive elements. Nevertheless, when monolithic sample is compared with the composites, the reduction may be attributed to the lower value of Young's modulus of LBA (~230 GPa [22]). To sum up, both hardness and elastic modulus decreases ~20% when a 30 vol% of LBA platelets is intercalated within the alumina matrix, mainly due to intrinsic lower values of the LBA [22,47].

Regarding the fracture resistance, the reliability of indirect methods, such as the indentation-based crack resistance, to estimate the fracture toughness or ceramics is widely discussed. Eventhough many authors claim that  $K_{IFR}$  gives a good estimation of  $K_{Ic}$  [33,48], these works are focused on fully dense ceramics, which is not exactly the case of SG sample sintered at 1500 °C nor 1650 °C (densification = 96%). In that case, densification may occur below the indenter, compromising the results. Nevertheless, we can find many works focused on LBA/Al<sub>2</sub>O<sub>3</sub> systems which have reported an increase in fracture toughness measured by  $K_{IFR}$  [22,49,50], as well as measured by standardized methods such as SEPB [23,51,52], all of them attributing the increase to crack deflection, a behavior also reported for other self-reinforced alumina matrix with elongated second phases [25].

The measured values of  $K_{IFR}$  are shown in Table 3. Classical pure  $\alpha$ -Al<sub>2</sub>O<sub>3</sub> sample showed the expected values, lower than those measured in SSR and SG samples. Thus, it can be inferred that the addition of LBA contributed to the increase of the indentation fracture resistance of the

Table 3

Mechanical properties of the samples: Vickers Hardness (HV20), Young's modulus (E), and indentation fracture resistance ( $K_{IFR}$ ).

Sample	HV20 (GPa)	E (GPa)	$K_{IFR}$ (MGf)
$\alpha$ -Al <sub>2</sub> O <sub>3</sub> -1500	15.6 ± 0.2	350 ± 20	4.3 ± 0.7
$\alpha$ -Al <sub>2</sub> O <sub>3</sub> -1650	16.1 ± 0.6	440 ± 30	5.1 ± 0.4
SSR-1500	11.1 ± 0.3	290 ± 20	4.9 ± 0.4
SSR-1650	11.3 ± 0.3	360 ± 20	5.6 ± 0.3
SG-1500	12.4 ± 0.7	280 ± 20	5.6 ± 0.3
SG-1650	12.0 ± 0.5	380 ± 10	6.5 ± 0.4

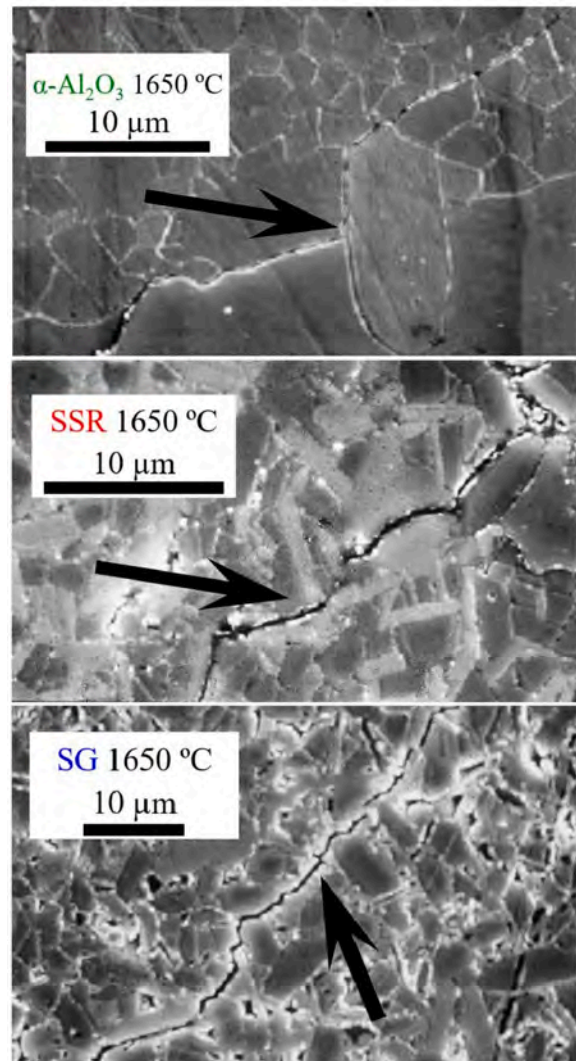


Fig. 9. Propagation of cracks produced after Vickers indentations on the different samples sintered at their max. Densities. The arrows show the crack paths.

sample. In particular, sample SG exhibited the highest values of indentation fracture resistance, at 1500 °C and 1650 °C, an interesting result considering that it was less densified than the other samples in both cases. Two aspects may explain this feature: firstly, SG sample showed lower values of hardness; and, secondly, the existence of LBA platelets inhibited the growth of the matrix grains and led to a more tortuous path of the crack, helping to the dissipation of the energy of the crack through the crack deflection mechanism [23,49].

SEM images of the cracks (Fig. 9) revealed the increase of the path of the crack. On the top image, the big grains of the pure  $\alpha$ -Al<sub>2</sub>O<sub>3</sub> sample allow the rapid propagation of the fracture. In the center and bottom images, LBA platelets can be easily distinguished by their brighter tonality due to their larger atomic mass. The smaller grains and the presence of the LBA platelets make more tortuous the intergranular crack path, leading to the observed increase of the indentation fracture resistance of the composite samples.

## Chapter 9. Rietveld analysis and mechanical properties of in situ formed La- $\beta$ -Al<sub>2</sub>O<sub>3</sub>/Al<sub>2</sub>O<sub>3</sub> composites prepared by sol-gel method

P. Rivero-Antúnez et al.

Ceramics International 48 (2022) 24462–24470

### 4. Conclusions

The sol-gel method has been proven as an efficient method to enhance the precipitation of the LBA at lower temperatures than other solid-state reaction methods. Hence, as revealed by the Rietveld analyses and SEM imaging, LBA micrometric platelets were found in the sol-gel samples at temperatures as low as 1050 °C, 250 °C lower than in samples prepared by solid state reaction. Moreover, it was also observed that the growth of these platelets controls the densification process. Thus, the formation of platelets at low temperature, as it happens using the sol-gel method, restrains the densification because their geometry disfavours packing. This fact, combined with the inhibition of the alumina grain growth, involves a poor density for samples sintered at temperatures lower than 1450 °C in the sol-gel sample, and even impeded its full densification up to 1600 °C.

Finally, the influence of the homogeneous distribution of the LBA on the mechanical properties of the samples was assessed. In comparison to the pure alumina sample, LBA-alumina composites exhibited lower values of hardness and Young's moduli, but the indentation fracture resistance increased. This is specially significant in the case of the sol-gel sample, with an observed increase of 30% of the indentation fracture resistance.

### Declaration of competing interest

The authors declare that they have no known competing financial interests or personal relationships that could have appeared to influence the work reported in this paper.

### Acknowledgments

Project PGC2018-094952-B-I00 financed by FEDER /Ministerio de Ciencia e Innovación - Agencia Estatal de Investigación - FEDER, UE, and project P20-01121 financed by PAIDI2020 Junta de Andalucía are acknowledged. P. R-A acknowledge project PGC2018-094952-B-I00 from FEDER /Ministerio de Ciencia e Innovación - Agencia Estatal de Investigación. The authors would like to thank the work by the National Institutes of Health, USA for the development of the *ImageJ* software.

### References

- [1] V. Morales-Florez, A. Dominguez-Rodriguez, Mechanical properties of ceramics reinforced with allotropic forms of carbon, *Prog. Mater. Sci.* (2021), <https://doi.org/10.1016/j.pmatsci.2022.100966> (accepted).
- [2] E. Zapata-Solvas, D. Gómez-García, A. Domínguez-Rodríguez, Towards physical properties tailoring of carbon nanotubes-reinforced ceramic matrix composites, *J. Eur. Ceram. Soc.* 32 (2012) 3001–3020.
- [3] L. Esquivias, P. Rivero-Antúnez, C. Zamora-Ledeza, A. Domínguez-Rodríguez, V. Morales-Florez, Intragranular carbon nanotubes in alumina-based composites for reinforced ceramics, *J. Sol. Gel Sci. Technol.* 90 (2019) 162–171.
- [4] P. Rivero-Antúnez, R. Cano-Crespo, L. Esquivias, N. de la Rosa-Fox, C. Zamora-Ledeza, A. Domínguez-Rodríguez, V. Morales-Florez, Mechanical characterization of sol-gel alumina-based ceramics with intragranular reinforcement of multiwalled carbon nanotubes, *Ceram. Int.* 46 (2020) 19723–19730.
- [5] E. Zapata-Solvas, D. Gómez-García, A. Domínguez-Rodríguez, On the microstructure of single wall carbon nanotubes reinforced ceramic matrix composites, *J. Mater. Sci.* 45 (2010) 2258–2263.
- [6] X. Xiong, Z. Wang, X. Wang, H. Liu, Y. Ma, Enhancing mechanical properties and air permeability of corundum porous materials by in situ formation of LaAl<sub>11</sub>O<sub>18</sub> in bonding phase, *J. Rare Earths* 38 (2020) 195–202.
- [7] S.A. Basha, K.S. Chandra, D. Sarkar, Salient features of SrO doping in Al<sub>2</sub>O<sub>3</sub> – 5 wt.% ZrO<sub>2</sub> reaction sintered composite ceramics, *J. Alloys Compd.* 829 (2020), 154559.
- [8] L. Liu, Y. Takasu, T. Onda, Z.C. Chen, Influence of in-situ formed Ba- $\beta$ -Al<sub>2</sub>O<sub>3</sub> on mechanical properties and thermal shock resistance of ZTA/Ba- $\beta$ -Al<sub>2</sub>O<sub>3</sub> composites, *Ceram. Int.* 46 (2020) 3738–3743.
- [9] Y.L. Xin, H.F. Yin, Y. Tang, H.D. Yuan, X.H. Ren, K. Gao, Q.F. Wan, Y.C. Liu, Formation mechanism of MgSrAl<sub>10</sub>O<sub>17</sub> and its effect on the mechanical performance of lightweight Al<sub>2</sub>O<sub>3</sub>-MgAl<sub>2</sub>O<sub>4</sub> refractories, *Ceram. Int.* 46 (2020) 11075–11079.
- [10] A.P. Luz, J.H. Gagliarde, C.G. Aneziris, V.C. Pandolfelli, B4C mineralizing role for mullite generation in Al<sub>2</sub>O<sub>3</sub>-SiO<sub>2</sub> refractory castables, *Ceram. Int.* 43 (2017) 12167–12178.
- [11] J.-F. Tsai, U. Chon, N. Ramachandran, D.K. Shetty, Transformation plasticity and toughening in CeO<sub>2</sub>-partially-stabilized Zirconia-alumina (Ce-TZP/Al<sub>2</sub>O<sub>3</sub>) composites doped with MnO, *J. Am. Ceram. Soc.* 75 (1992) 1229–1238.
- [12] P.F. Becher, Microstructural design of toughened ceramics, *J. Am. Ceram. Soc.* 74 (1991) 255–269.
- [13] R.R. Rao, L. Mariappan, Combustion synthesis and characterisation of lanthanum hexa-aluminate, *Adv. Appl. Ceram.* 104 (2005) 268–271.
- [14] R. Gadow, M. Lischka, Lanthanum hexaaluminate - novel thermal barrier coatings for gas turbine applications - materials and process development, *Surf. Coating Technol.* 151–152 (2002) 392–399.
- [15] J. Zhang, M. Fang, Z. Huang, Y.G. Liu, X. Min, X. Wu, Preparation and mechanical properties of ReAl<sub>11</sub>O<sub>18</sub> ceramics, *Key Eng. Mater.* 602–603 (2014) 345–348.
- [16] K. Hamano, S. Ohta, Y. Ozaki, Effects of rare earth oxides on sintering of alumina, *J. Ceram. Soc. Jpn.* 87 (1979) 632–641.
- [17] N. Iyi, Z. Inoue, S. Takekawa, S. Kimura, The crystal structure of lanthanum hexaaluminate, *J. Solid State Chem.* 54 (1984) 70–77.
- [18] R.C. Ropp, B. Carroll, Solid-state kinetics of LaAl<sub>11</sub>O<sub>18</sub>, *J. Am. Ceram. Soc.* 63 (1980) 416–419.
- [19] C. Barrera-Solano, L. Esquivias, G.L. Messing, Effect of preparation conditions on phase formation, densification, and microstructure evolution in La- $\beta$ -Al<sub>2</sub>O<sub>3</sub>/Al<sub>2</sub>O<sub>3</sub> composites, *J. Am. Ceram. Soc.* 82 (1999) 1318–1324.
- [20] W.P. Wood, L.D. Monroe, S.L. Conwell, Abrasive Grits Formed of Ceramic Containing Oxides of Aluminum and Rare-Earth Metal, Method of Making and Products Made Therewith, U.S. Pat. No. 4 881 951, Nov. 21, 1989.
- [21] S.W. Kang, J.W. Ko, H.D. Kim, formation of La-beta-Aluminate in alpha-alumina matrix and its influence on mechanical properties, *J. Kor. Chem. Soc.* 29 (1992) 23–28.
- [22] P.L. Chen, I.W. Chen, In-situ alumina/aluminate platelet composites, *J. Am. Ceram. Soc.* 75 (1992) 2610–2612.
- [23] M. Yasuoka, K. Hirao, M.E. Brito, S. Kanzaki, High-strength and high-fracture-toughness ceramics in the Al<sub>2</sub>O<sub>3</sub>/LaAl<sub>11</sub>O<sub>18</sub> systems, *J. Am. Ceram. Soc.* 78 (1995) 1853–1856.
- [24] R.A. Cutler, R.J. Mayhew, K.M. Prettyman, A.V. Virkar, High-toughness Ce-TZP/Al<sub>2</sub>O<sub>3</sub> ceramics with improved hardness and strength, *J. Am. Ceram. Soc.* 74 (1991) 179–186.
- [25] Z.-C. Chen, S. Nugroho, M. Ezumi, T. Akao, T. Onda, In situ synthesis of alumina-matrix oxide/oxide composites by reactive sintering, *Mater. Sci. Eng.* 557 (2012) 59–68.
- [26] M. Kumagai, G.L. Messing, Controlled transformation and sintering of a boehmite sol-gel by  $\alpha$ -alumina seeding, *J. Am. Ceram. Soc.* 68 (1985) 500–505.
- [27] P. Rivero-Antúnez, R. Cano-Crespo, F. Sánchez-Bajo, A. Domínguez-Rodríguez, V. Morales-Florez, Reactive SPS for sol-gel alumina samples: structure, sintering behavior, and mechanical properties, *J. Eur. Ceram. Soc.* 41 (2021) 5548–5557.
- [28] P. Thompson, D.E. Cox, J.B. Hastings, Rietveld refinement of Debye-Scherrer synchrotron X-ray data from Al<sub>2</sub>O<sub>3</sub>, *J. Appl. Crystallogr.* 20 (1987) 79–83.
- [29] R. Hill, C. Howard, B. Reichert, Quantitative phase Abundance in Mg-PSZ by Rietveld analysis of neutron and X-ray diffraction data, *Mater. Sci. Forum* 34–36 (1988) 159–163.
- [30] D. Balzar, Breadth – a program for analyzing diffraction line broadening, *J. Appl. Crystallogr.* 28 (1995) 244–245.
- [31] D. Balzar, X-ray diffraction line broadening: modeling and applications to high-Tc superconductors, *J. Res. Natl. Inst. Stand. Technol.* 98 (1993) 321.
- [32] B.E. Warren, B.L. Averbach, The effect of cold-work distortion on x-ray patterns, *J. Appl. Phys.* 21 (1950) 595–599.
- [33] H. Miyazaki, Y. Yoshizawa, A reinvestigation of the validity of the indentation fracture (IF) method as applied to ceramics, *J. Eur. Ceram. Soc.* 37 (2017) 4437–4441.
- [34] D.K. Shetty, A.R. Rosenfield, W. Duckworth, Analysis of indentation crack as a wedge-loaded half-penny crack, *J. Am. Ceram. Soc.* 68 (1985). C-65–C-67.
- [35] D.B. Marshall, T. Noma, A.G. Evans, A simple method for determining elastic-modulus-to-hardness ratios using Knoop indentation measurements, *J. Am. Ceram. Soc.* 65 (1982) c175–c176.
- [36] Z. Negahdari, M. Willert-Porada, Tailoring the microstructure of reaction-sintered alumina/lanthanum hexaaluminate particulate composites, *J. Eur. Ceram. Soc.* 30 (2010) 1381–1389.
- [37] H. Yoshida, S. Hashimoto, T. Yamamoto, Dopant effect on grain boundary diffusivity in polycrystalline alumina, *Acta Mater.* 53 (2005) 433–440.
- [38] H. Schaper, E.B. Doesburg, L.L. Van Reijen, The influence of lanthanum oxide on the thermal stability of gamma alumina catalyst supports, *Appl. Catal.* 7 (1983) 211–220.
- [39] T. Fujii, H. Muragaki, H. Hirano, Microstructure development and mechanical properties of Ce-TZP/La- $\beta$ -Alumina composites, in: S. Hirano, G.L. Messing, H. Hausner (Eds.), *Ceramic Powder Science IV*, vol. 22, (Ceramic Transactions), American Ceramic Society, Westerville, OH, 1991, pp. 693–698.
- [40] B.-K. Jang, T. Kishi, Fabrication and microstructure of Al<sub>2</sub>O<sub>3</sub> matrix composites by in-situ reaction in the Al<sub>2</sub>O<sub>3</sub>-La<sub>2</sub>O<sub>3</sub> system, *J. Ceram. Soc. Jpn.* 106 (1998) 739–743.
- [41] P. Jana, P.S. Jayan, S. Mandal, K. Biswas, Effect of seeding on the formation of lanthanum hexaaluminates synthesized through advanced sol gel process, *J. Cryst. Growth* 408 (2014) 7–13.
- [42] P. Souza-Santos, H. Souza-Santos, S. Toledo, Standard transition aluminas. Electron microscopy studies, *Mater. Res.* 3 (2000) 104–114.

- [43] I. Levin, D. Brandon, Metastable Alumina polymorphs: crystal structures and transition sequences, *J. Am. Ceram. Soc.* 81 (1998) 1995–2012.
- [44] F. Cardarelli, *Materials Handbook*, second ed., Springer London, London, 2008 <https://doi.org/10.1007/978-1-84628-669-8>.
- [45] W. Huang, G. Liu, X. Li, T. Qi, Q. Zhou, Z. Peng, Structural variation in improving thermal stability of transition alumina with La dopant, *J. Alloys Compd.* 824 (2020) 153905.
- [46] F.S. Galasso, *Structure, Properties, and Preparation of Perovskite-type Compounds*, first ed., Pergamon, Oxford, 1969 <https://doi.org/10.1016/C2013-0-02117-2>.
- [47] Z. Negahdari, M. Willert-Porada, C. Pfeiffer, Mechanical properties of dense to porous alumina/lanthanum hexaaluminate composite ceramics, *Mater. Sci. Eng., A* 527 (2010) 3005–3009.
- [48] H. Miyazaki, Y.I. Yoshizawa, Correlation of the indentation fracture resistance measured using high-resolution optics and the fracture toughness obtained by the single edge-notched beam (SEPB) method for typical structural ceramics with various microstructures, *Ceram. Int.* 42 (2016) 7873–7876.
- [49] Y.Q. Wu, Y.F. Zhang, X.X. Huang, J.K. Guo, In-situ growth of needlelike LaAl<sub>11</sub>O<sub>18</sub> for reinforcement of alumina composites, *Ceram. Int.* 27 (2001) 903–906.
- [50] Y.Q. Wu, Y.F. Zhang, X.X. Huang, B.S. Li, J.K. Guo, Preparation, sintering and fracture behavior of Al<sub>2</sub>O<sub>3</sub>/LaAl<sub>11</sub>O<sub>18</sub> ceramic composites, *J. Mater. Sci.* 36 (2001) 4195–4199.
- [51] I. Yamashita, K. Tsukuma, T. Kusunose, Translucent Al<sub>2</sub>O<sub>3</sub>/LaAl<sub>11</sub>O<sub>18</sub> composite, *J. Am. Ceram. Soc.* 92 (2009) 2136–2138.
- [52] M. Yasuoka, K. Hirao, M.E. Brito, S. Kanzaki, Microstructure and mechanical properties of alumina based ceramics with changed amounts of  $\beta$ -lanthanaluminate, *J. Ceram. Soc. Jpn.* 105 (1997) 641–644.

# Chapter 10

## General conclusions

The individual conclusions of each article have already been presented in detail. In this section, we describe the conclusions that can be drawn by combining the experiences presented here. This research line, namely, the sol-gel manufacturing of ceramic matrices reinforced with carbon allotropes and their structural and mechanical characterization through experiments and modelling, has undoubtedly resulted in a prolific topic that has led to multiple publications. Major conclusions are summarized below.

1. The process of synthesizing alumina-based ceramic matrix composite powders from boehmite sols is efficient, inexpensive, and simple.
2. The liquid stage of the sol-gel process emerges as a promising technique for the proper dispersion of second phases in ceramic precursors.
3. The potential of the rapid gelation process in the sol-gel method has been demonstrated to prevent the reaggregation of the dispersed phase, in contrast to other colloidal methods where the liquid removal is slower and allows for reaggregation. Furthermore, both CNTs and graphene preserve their structure throughout the entire process of dispersion (magnetic stirring and ultrasonication), gelation, mortar mixing, and sieving.

- 
4. During the calcination process of boehmite gel powders in the presence of MWCNTs, alumina grains underwent formation and growth, and a quantity of MWCNTs was discovered within these grains (intragranular location), as verified through electron microscopy (SEM and TEM) and nitrogen physisorption.
  5. While the enhancements in GO dispersion and chemical interaction with the matrix did not result in significant mechanical improvements, this approach presents an appealing pathway for producing GCMCs with superior dispersion of the reinforcing phase without compromising their mechanical properties.
  6. Although SEM analysis of the microstructure reveals the occurrence of toughening mechanisms like crack bridging and crack deflection, none of the employed methods have successfully achieved a significant population of reinforcing nanophase within the intragranular position. These findings suggest that the pursued notion of such intragranular nanophase incorporation may need to be reconsidered.
  7. Although the boehmite gel effectively incorporated the MWCNTs and graphene within its nanostructure, the dispersion of these components required optimization. This improvement was achieved through the implementation of the “Max-Vol” route (Chapter 6), which increased the available volume for dispersing the second phase while reducing its concentration in the liquid stage without affecting the concentration in the final composite.
  8. In contrast to the traditional approach of pre-calcining boehmite powders to obtain  $\gamma$ -Al<sub>2</sub>O<sub>3</sub> and/or  $\alpha$ -Al<sub>2</sub>O<sub>3</sub> by subsequent sintering, the reactive-SPS route emerges as the clear winner. Rapid densification of samples occurred at lower temperatures (1200 °C) compared to sinterings starting with  $\alpha$ -Al<sub>2</sub>O<sub>3</sub> powder derived from the prior calcination of boehmite powders. This advancement holds promise for enhancing the industrial scalability of the process.

9. The optimization of the reactive-SPS technique to obtain  $\alpha$ -Al<sub>2</sub>O<sub>3</sub> from boehmite involves eliminating the holding time, lowering the maximum temperature, and introducing  $\alpha$ -Al<sub>2</sub>O<sub>3</sub> seeds into the initial boehmite sol. This was demonstrated in chapter 6, where the SPS parameters were fine-tuned to achieve fully dense composites of alumina and graphene.
10. It is suggested that employing a sol comprising diasporite nanoparticles ( $\alpha$ -AlOOH), instead boehmite ( $\gamma$ -AlOOH), would streamline the process and would result in further temperature reduction for achieving complete sintering and total densification of alumina.
11. The samples exhibited Vickers hardness values that ranked among the highest recorded for fully dense  $\alpha$ -Al<sub>2</sub>O<sub>3</sub>. These values were influenced primarily by density and the indentation size effect, rather than the presence of nanotubes or graphene.
12. The sintering method had a pronounced impact on the indentation fracture resistance ( $K_{IFR}$ ), as the reactive-SPS conditions resulted in significant grain growth, a critical factor contributing to sample fragility and resulting in unfavorable  $K_{IFR}$  values.
13. It is essential to assess all the parameters involved in an equation for indentation fracture resistance to ensure a reliable comparison, even when analyzing samples from the same series. The conventional approach employing the Young's modulus of pure alumina typically yields higher values for indentation fracture resistance, while reevaluated values considering the real elastic moduli obtained through nanoindentation demonstrate an upward trend with carbon allotrope content. This can be attributed to the mechanisms that transfer tensile loads from the alumina matrix to the nanophase reinforcement during crack propagation, elucidating the observed modest increase in recalculated  $K_{IFR}$  with MWCNT content (chapter 4).

- 
14. The distribution patterns of carbon nanotubes within alumina-based systems, with carbon contents typically used ranging from (0.1 – 2 wt.%), indicate a densely populated microscale space, with volumetric densities reaching several hundreds of CNTs per cubic micron. Consequently, achieving aggregate-free carbon-reinforced composites appears to be highly challenging with such carbon contents.
  15. In the light of structural simulation, working with carbon allotrope concentrations in the range of 0.5 – 2 wt.%, the number of reinforcing elements per unit volume is so high that good dispersions and the absence of aggregations are impossible. Therefore, given the crucial importance of avoiding aggregates for the effective reinforcement of composites through CNT/graphene addition, a comprehensive reassessment of this strategy is required.
  16. The potential applications of Small Angle Scattering (SAS) techniques for analyzing the dispersion of nanostructured carbon allotropes were proposed. It was observed that the most significant variations in the SAS intensity curve occurred during the initial stages of partial agglomeration, compared to the completely homogeneous distribution. This characteristic can be investigated by examining the first derivative of the scattering curve and may be particularly valuable for quantitatively assessing the dispersion quality of embedded nanophases in ceramic matrices and other composites.
  17. With regard to the mechanical properties at high temperatures discussed in chapter 8, it can be inferred that, for alumina composites, the enhancement provided by reduced graphene oxide is not significantly greater than that of pure alumina. However, it does exhibit potential appeal in the realm of nanocomposites or under extremely high temperatures above 1250 °C.
  18. The high-temperature creep properties of pure zirconia are comparable to those of zirconia composites reinforced with reduced graphene oxide.

19. The carbon phase's capacity to effectively permeate (to "wet") the interfaces between grains and evenly disperse itself during deformation plays a pivotal role in forecasting the plasticity at elevated temperatures.
20. Ultimately, based on the findings in Chapter 9 regarding  $\alpha$ -Al<sub>2</sub>O<sub>3</sub> composites reinforced with LBA platelets fabricated through the sol-gel process, it is evident that the sol-gel method has demonstrated its effectiveness in promoting the precipitation of LBA at lower temperatures compared to alternative solid-state reaction approaches. This has resulted in a significant temperature reduction of 250 °C on the attainment of LBA micrometric platelets.
21. The LBA-alumina composites demonstrated reduced levels of hardness and Young's moduli, while the indentation fracture resistance showed an improvement. This is particularly noteworthy in the sol-gel sample, where a remarkable 30% increase in the indentation fracture resistance was observed.